ESCORT TUG HYDRODYNAMICS: ANALYSIS OF FLOW AROUND SHIPS AT LARGE YAW ANGLES

WILLIAM DAVID MOLYNEUX

ESCORT TUG HYDRODYNAMICS: ANALYSIS OF FLOW AROUND SHIPS AT LARGE YAW ANGLES

by

© William David Molyneux B. Sc., M. A. Sc.

A thesis submitted to the
School of Graduate Studies
in partial fulfilment of the
requirements for the degree of
Doctor of Philosophy

Ocean and Naval Architectural Engineering
Faculty of Engineering and Applied Science
Memorial University of Newfoundland

November 2006

Your file Votre référence
ISBN: 978-0-494-31325-1
Our file Notre référence
ISBN: 978-0-494-31325-1

ABSTRACT

The ship hydrodynamics literature contains little information on a hull at a yaw angle greater than that commonly encountered in ship manoeuvring. New ship types, such as escort tugs with very low aspect ratio fin keels, will benefit from an analysis of the hydrodynamics that occurs at yaw angles between 20 and 45 degrees. Computational Fluid Dynamics (CFD) is an important technique that could be used for this analysis, but the accuracy of predicted forces and flow patterns at high yaw angles was unknown prior to this research.

A new data set of three-dimensional flow vectors in planes around an escort tug model was obtained using Particle Image Velocimetry (PIV). These data were used to validate the flow vectors predicted by a commercial CFD code. As part of the validation study, a method for numerically analyzing the difference between measured and predicted flow vectors was developed. The method was used to evaluate CFD predictions of flow patterns around a conventional hull (at 10 and 35 degrees yaw) against published experimental results.

The type of computational mesh was found to affect the accuracy of the forces predicted for a hull with a yaw angle, but different hull types needed different meshing approaches. The forces at 10 degrees yaw for a typical high-speed merchant ship were predicted to within 5% of experimental results using an

unstructured tetrahedral mesh, whereas a structured hexahedral mesh gave force predictions accurate to within 15%. For the escort tug model, which was a wider and shallower hull shape, the situation was reversed, and the structured mesh gave force predictions accurate to within 5% of the experimental data up to 40 degrees yaw. There was no noticeable difference in the predicted flow patterns between meshing approaches for the tug model. Mean flow vector magnitudes were within 10% of measured values.

As a result of this research PIV has been developed into a practical technique for measurements around a hull with a yaw angle and CFD has been shown to give insights into the flow around an escort tug and its appendages, within a specified level of accuracy.

Table of Contents

List of Tables

List of Tables (continued)

List of Figures

List of Figures (continued)

List of Figures (continued)

List of Figures (continued)

List of Figures (continued)

List of Figures (continued)

ACKNOWLEDGEMENTS

The work described in this thesis would not have been possible without the help and support of many people, which is gratefully acknowledged:

Professor Neil Bose, Canada Research Chair in Offshore and Underwater Vehicles Design at Memorial University for his continuing support and encouragement of my efforts to understand PIV and develop it into a practical experiment technique for ocean engineering and naval architecture research.

Dr. Fabio Di Felice of INSEAN and Dr. Joseph Longo of the Iowa Institute for Hydraulic Research who provided computer files of data from their experiments on the Series 60 models, which were compared with the CFD predictions. In each case this required a significant effort on their part to recover and reformat the original test data, and their willingness to do this is gratefully appreciated.

Mr. Robert Allan, President of Robert Allan Ltd., Vancouver, British Columbia, for permission to use the model of the escort tug in the PIV experiments and for the use of the experimental data on the force components to compare with the CFD simulations. His enthusiasm for the subject of tug design and encouragement for me to carry out this work is also very much appreciated.

The Canada Foundation for Innovation and the Newfoundland and Labrador Department of Innovation, Trade and Rural Development for financial support of the purchase of the PIV system.

Ms. Jie Xu, research laboratory coordinator in the Department of Ocean and Naval Architectural Engineering, for her leadership, continuous dedication and attention to detail that was necessary for making successful PIV experiments.

Mr. Jim Gosse, Laboratory Technician in the Fluids Laboratory at Memorial University is for all his help during the set-up and carrying out the experiments in the OERC Towing Tank at MUN.

The staff at IOT for preparing the model for testing and assisting with the many tasks required during experiments at IOT.

The management of IOT is thanked for their financial support.

The author previously published substantial portions of Chapters 2, 3, 4 and 5 as NRC-IOT reports TR-2006-11, TR-2006-12, TR-2006-18 and TR-2006-20 respectively.

I would like to dedicate this publication to my father, William Henry Molyneux, who passed away while the research was being carried out. His faith in my ability to be educated was always much greater than my own.

CHAPTER 1

INTRODUCTION

'Classical' ship hydrodynamics generally considers a relatively slender ship, moving in a straight line. The ship is propelled by a screw propeller (or propellers), whose thrust acts along the centreline of the ship. The ship is kept on a straight course by using small adjustments of a foil-like rudder. In this situation, the flow around the hull is symmetrical with the slight exception for a single screw ship, where the flow influenced by the propeller is biased by its direction of rotation. When a constant rudder angle is applied, the ship will develop a steady rate of turn, and the flow will no longer be symmetrical, but the degree of asymmetry will depend on the speed of the ship and the rudder angle applied. The angle of the hull to the flow during a steady turn will be less than 10 degrees for most ships. These conditions can be referred to as 'design conditions' in ship hydrodynamics.

'Off design' cases in ship hydrodynamics can include the case when the required propeller thrust is much greater than the hydrodynamic resistance of the hull, propulsion systems that are not aligned with the ship's centreline or yaw angles much more than 10 degrees. Small ships, such as tugs and commuter ferries, are frequently required to operate in what are usually considered to be 'off-design' conditions in classical ship hydrodynamics. To improve manoeuvrability, these ships often have propulsion systems that can be vectored off the ship's centreline. This can result in the ship's hull being at much higher angles of attack to the flow than can be obtained from rudder initiated manoeuvres.

An escort tug is an extreme example of a small ship operating in 'off-design' hydrodynamic conditions. In this situation, the tug uses its hull and propulsion system to create a hydrodynamic force, which is used to bring a loaded oil tanker under control in an emergency. The tug is attached to a towline at the stern of the tanker, and by using vectored thrust, it is held at a yaw angle of approximately 45 degrees. The maximum practical speed of operation for escort tugs is about 10 knots, resulting in a maximum Froude number based on ship length of around 0.30, for a tug approximately 40 m long.

Escort tug research to date (Hutchison et al. (1993), Allan et al. (2000), Allan and Molyneux, (2004)) has focused on predicting the total force and the limits of safe operation for specific combinations of hull and propulsion system using physical model experiments. The problem has not been approached from the point of view of trying to analyze the hydrodynamics of the situation and its influence on the resulting solution. However, to obtain this knowledge will require a more sophisticated approach than has been used to date, which must include numerical prediction of the flow patterns around a hull and the forces that result. Without this data, it is unlikely that escort tugs can be developed to their full potential.

Computational Fluid Dynamics (CFD) has been applied to a wide range of ship hydrodynamics analysis, including a ship's hull at an angle of attack to the undisturbed flow. Reynolds Averaged Navier-Stokes (RANS) solutions for a Series 60 C_B=0.6 hull at 10 degrees of yaw have been carried out (Alessandri and Delhommeau (1996), Cura Hochbaum (1996), Campana et al. (1998), Tahara et al. (2002)). The ability of RANS type CFD codes to predict flow patterns and forces at yaw angles outside the range of 'design' hydrodynamics has not been evaluated. The major advantage of analyzing flow conditions with CFD should be the relative simplicity of assessing the effect of changes in the flow patterns around the hull and the resulting forces that are generated as a result of changes to the ship geometry. Accurate predictions using CFD would remove the need for model experiments at each step. However, to prove the practicality of the technique it will be necessary to compare forces and flow patterns predicted by CFD with experimental measurements for the same ship geometry and flow conditions.

Commercial CFD codes are now available with all of the features necessary for making predictions of the flow patterns around a ship at a large yaw angle. One code that was available for this research was *Fluent* (Fluent Inc., 2005a). This code was a volume of fluid approach to solving the Reynolds Averaged Navier-Stokes (RANS) equations of fluid motion, which also allowed for the presence of a free surface at the interface between two fluids. Computational meshes can be created for Fluent using a variety of techniques, but the code that was used for the research described here was *Gambit* (Fluent Inc. 2005b).

The type of mesh required for a hull with a large yaw angle has not previously been evaluated. Most of the previous application of CFD to ship hydrodynamics has used a hexahedral mesh. This type of mesh is defined by elements that have six four-sided faces. At the boundary to the hull, one face of the element is fitted exactly to the hull surface. An alternative approach, that is sometimes simpler to create, is to use a tetrahedral mesh, consisting of elements made of four three-sided faces. This type of mesh is also fitted to the hull at the boundary condition. The hexahedral mesh is potentially better at resolving drag forces due to viscous shear within the boundary layer than the tetrahedral mesh, but the significance of this force component is likely to decrease as the yaw angle of the hull increases. *Gambit* allowed for both meshing approaches. To determine the most appropriate meshing strategy, it was necessary to compare predictions for forces and flow patterns predicted with CFD against measured data for the same flow conditions.

Two sets of model data were identified within the literature that presented measured flow velocities around a ship's hull. One set was for the Series 60 C_B=0.6 hull at a yaw angle of 10 degrees (Longo and Stern, 1996, 2002). This data set was very complete, since it included measurements at nine sections relative to the hull geometry, but the yaw angle was below the range of interest for escort tug operation. Another data set was for the same hull form at 35 degrees (Di Felice and Mauro, 1999). This data set was less complete than the set for 10 degrees yaw since it only contained two sections, but the yaw angle was large enough to be of interest for escort tug operation.

CFD predictions of the forces and flow patterns were made for the Series 60 C_B=0.6 hull at yaw angles of 10 degrees and 35 degrees using the two alternative meshing approaches. It was relatively easy to assess the accuracy of the predicted force components against the measured data (when it was available) because a single numerical value can be used. It was more complex to compare the flow patterns around the hull, since both the CFD predictions and the experiment data sets included hundreds or thousands of points distributed over relatively large geometric areas.

The data from the Series 60 hull was used to develop a method of comparing CFD predictions of flow patterns at a plane within the fluid with experiment data at the same plane. This method enables the analyst to visualize the differences between the CFD predictions and experiments and identify the areas with the highest and lowest accuracy. It also gave numerical measures to the overall degree of fit between the CFD predictions and the measured data, which could also be used in assessing the accuracy of the predictions. The CFD predictions for the Series 60 hull, the development of the method for comparison of flow patterns and the analysis of the predicted flow patterns against the experiment data are described in Chapter 2.

The main conclusion from Chapter 2 was that there was relatively little difference in the accuracy of the predicted flow patterns between the two meshing approaches when the hull had a yaw angle. However, the Series 60 hull was designed based on 'classical' assumptions of ship hydrodynamics, and was not designed to operate at the yaw angles required for escort tugs. The Series 60 hull was long, narrow and relatively deep, with no appendages. Compared to the Series 60, a typical escort tug would be wider, shallower and have a large fin or keel, which was a significant feature of the design. Also, the Series 60 data was incomplete, since force data was only available for the hull at 10 degrees yaw. It was necessary to confirm the findings for the Series 60 hull against a hull shape more typical of those used in practice for large yaw angle operation. An escort tug model was made available for this research, for which force measurements (over a yaw angle range for zero to 45 degrees) had been carried out as part of a commercial project, but no flow measurements were available.

Within the time frame of this research, Memorial University purchased a Stereoscopic Particle Image Velocimetry (PIV) system, which could be used for making measurements of underwater flow patterns. PIV is a fluid flow measurement method that calculates flow vectors within a plane illuminated by a laser light sheet. Pairs of digital pictures of small, reflective particles are used to analyze the flow, and the results are given as three dimensional velocity vectors at grid points within the measurement space. The commissioning of this equipment and the preparation needed to ensure that flow around a hull with a large yaw angle could be successfully seeded with particles and analyzed was a major element of the required research, and so it has been described in detail. The PIV system, the analysis methods and the development of the necessary seeding delivery system are described in Chapter 3.

Flow measurements were successfully carried out on the escort tug model for a yaw angle of 45 degrees, at two different locations around the hull. The two locations were upstream and downstream planes normal to the undisturbed flow direction, intersecting the model at midships. Two different model geometries (with and without the low aspect ratio fin typical of many escort tugs) were tested. The results revealed many detailed flow patterns, such as the vortex generated by the fin and the separation of the flow at the bilge on the upstream side of the hull, which had not been observed before. The results of the PIV experiments are described in Chapter 4.

The CFD predictions for the tug and the comparison of the predicted forces and flow patterns against the experiment data are described in Chapter 5. CFD predictions for the tug were made using *Fluent* at the yaw angles for which experiment data on forces and flow patterns were available. The tetrahedral and hexahedral meshing strategies were used to predict the forces and flow patterns for yaw angles from 10 to 50 degrees. The results from the two different meshes were compared against the experimentally measured forces (Molyneux, 2003) and the results of the PIV experiments described in Chapter 4, using the same methods developed in Chapter 2. Based on the predicted force components and the flow patterns around the hull, the CFD solution using the hexahedral mesh was found to be superior throughout the range of flow conditions considered for the escort tug (with and without the fin fitted).

Chapter 6 describes the results of some CFD simulations for different hull shapes with a yaw angle, and discusses how the shape of the hull affected the resulting forces and flow patterns. The four hull shapes used for discussion were the Wigley hull, a simplified geometric shape used for validation of numerical ship hydrodynamics (Tahara and Longo, 1994), the Series 60 hull, and the escort tug hull, with and without the fin. The CFD simulations were also used to analyze the flow patterns around the low aspect ratio fin typical of many escort tugs. Some discussion on where the CFD simulations may be limited is also given in Chapter 6. The limitations discussed were the assumptions of steady flow and the absence of consideration of the free surface. The conclusions derived from the research are described in Chapter 7.

CHAPTER 2

EVALUATION OF CFD MESHING STRATEGIES FOR A HULL WITH A YAW ANGLE, BASED ON SERIES 60 C_B=0.6 HULL FORM

2.1 INTRODUCTION

Commercial RANS based CFD programs have become an accepted method of making predictions of flow patterns, pressures and the forces resulting from water flow around a ship's hull. The main advantages of using a commercial code are that the user interfaces are flexible and well designed and the codes are validated by a large number of users in many fields of fluid dynamics and thermodynamics. The disadvantages are that they are very general in their application, and may be more complicated or less reliable to use than a custom made code for a very specific application.

The commercial RANS based CFD program used at Memorial University of Newfoundland is *Fluent* (Fluent Inc., 2005a). Meshes for this program can be created in a number of different ways, but *Gambit* (Fluent Inc., 2005b) is the product supplied by the same company for this purpose, and was the program used for this study.

Within *Gambit*, there are two distinct approaches for creating a mesh. The simplest type of mesh to generate is a tetrahedral mesh, where four points define individual cells and four triangular faces define a volume. This type of mesh can be generated very quickly using Gambit, once the basic size of the elements has been specified. The disadvantage of this approach is that the user has relatively little control over the size of the elements, beyond the definition of faces attached to boundaries within the mesh.

An alternative approach is to use a hexahedral mesh, where eight points and six faces define individual cells. When using Gambit, this type of mesh is much harder to define when boundaries of the cells must be fitted to the surface of the ship's hull. It requires the complete definition of the hull surface with four sided faces, and the definition of construction planes radiating out from the hull surface, which can also be defined by elements with four sided faces. The result is that the user has much more control over the definition of the mesh, but the time and effort required for this type of definition is much higher than that required for the tetrahedral mesh.

There are several trade-offs to be considered when developing the most appropriate mesh for a CFD prediction of the flow around a ship with a yaw angle. These are:

1) Accuracy of results
    a) Hydrodynamics Forces
    b) Flow patterns (including free surface waves)
2) Level of operator skill and time required for creating the mesh
3) Computer power required for solving the problem

The best meshing strategy for predicting the forces and flow patterns around a hull with a yaw angle has not been established. Hexahedral meshes are used frequently for ship hydrodynamic studies at zero or small yaw angles, but tetrahedral meshes may be equally effective as the yaw angle increases, and the importance of the viscous terms decreases. A major objective of this research was to determine the methods for making the most accurate CFD predictions of forces and flow patterns around a hull with a yaw angle.

The most effective way to evaluate the different meshing strategies was to compare the results of the CFD predictions against measured data for the same flow conditions. Comparing forces predicted by CFD programs against experiment data was relatively straight forward, but evaluation of the predicted flow patterns was more complicated. Most published research comparing CFD predictions of flow patterns with experiment results is done in a subjective way, and does not put numerical values on the comparison. A numerical index of the goodness of fit for the flow patterns was an important step in determining if one CFD model was better than another, but there was not an accepted method of doing this. A method was developed which allowed graphical and numerical comparison of CFD predictions against measured data, and in turn, enabled the selection of the CFD method that gave the most accurate predictions of the flow patterns.

In reviewing the available cases for measurements of flow around a hull with a yaw angle in the literature, two examples were found. Each case was for the Series 60 hull, with a block coefficient of 0.6 (Todd, 1963). Data was collected for a yaw angle of 10 degrees (Longo and Stern, 1996 and 2002) and a yaw angle of 35 degrees (Di Felice and Mauro, 1999). The bodyplan for this ship is shown in Figure 2-1. The hull has very fine waterlines in the bow and stern and a midship section with a relatively large bilge radius. A summary of the principal particulars is given in Table 2-1.

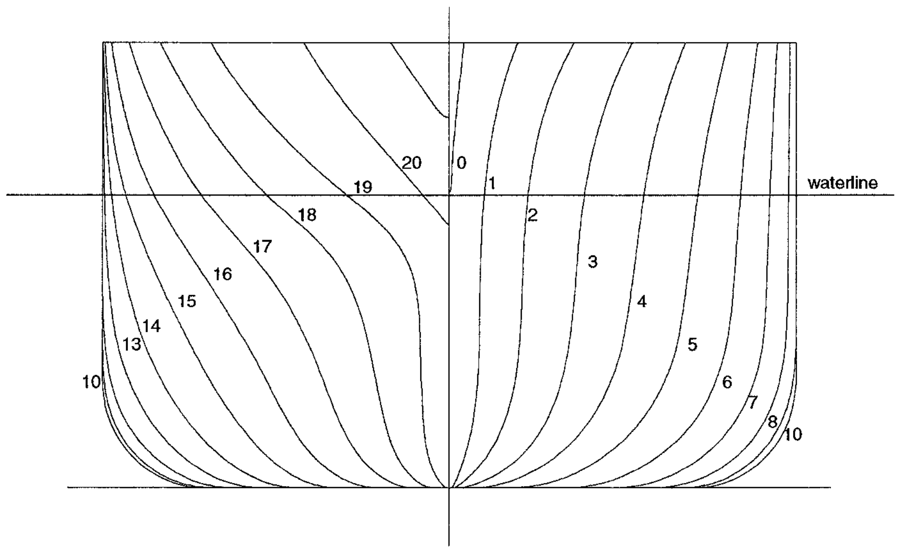

Figure 2-1, Series 60, C_B=0.6, Body plan for hull showing 21 equally spaced sections along waterline length

Table 2-1, Principal Dimensions for Series 60, C_B=0.6 hull form

	Full scale	Iowa model (Longo & Stern, 1996, 2002))	INSEAN model (Di Felice & Mauro, 1999)
Length, BP, m	121.92	3.048	1.219
Beam, m	16.256	0.406	0.163
Draft, m	6.502	0.163	0.065
Wetted area, m^2	2526.4	1.579	0.253
C_B	0.6	0.6	0.6
C_M	0.977	0.977	0.977
Scale		1:40	1:100

2.2 DESCRIPTION OF SERIES 60 C_B=0.6 MODEL EXPERIMENTS

2.2.1 Pitot Tube Data for Yaw Angle of 10 Degrees

An extensive flow survey around a model of the Series 60, C_B=0.6 hull was made using five-hole pitot tubes for zero yaw angle (Toda et al., 1992, Longo et al., 1993) and with a 10 degree yaw angle (Longo and Stern, 1996, 2002). The experiments were carried out to determine the influence of waves created by a surface-piercing hull on its wake and boundary layer and to provide detailed measurements of the flow field for validating CFD methods. Mean velocity and pressure measurements were made for two Froude numbers (0.160 and 0.316) at multiple sections from the bow to the stern, and into the near wake at the stern. The two speeds were chosen to give the effects of waves on the flow.

A Cartesian measurement grid was used with the origin at the intersection of the forward perpendicular and the static waterline. The x-axis was positive towards the stern, the y-axis was positive to starboard and the z-axis was positive upwards. Velocities in the x, y and z direction were referred to as u, v and w respectively. Results were non-dimensionalized using model length (between perpendiculars) L, carriage velocity U and fluid density ρ. Two models were tested, at scales of 1:40 and 1:66.7.

Data from the experiments was presented as total pressure head and axial (u) velocity contours, cross plane (v, w) velocities and pressures and axial vorticity contours. The y-z planes were at locations of 0, 0.1, 0.2, 0.4, 0.6, 0.8, 0.9, 1.0, 1.1 and 1.2L for each of the two Froude numbers. Wave profiles at the hull surface, contours of wave elevation and wave slope were also measured. Pressure measurements with the pitot tubes were made at between 200 and 350 locations per section.

Wave profiles at the hull were measured at more locations than the pressures. Wave elevation was measured using an array of wave probes fixed in the tank axis system, referred to in the paper as global elevations. Wave elevation close to the model was measured from a moving wave probe on the towing carriage, and this was referred to as local elevation. For the zero yaw case, the results presented were based on the combination of approximately 4000 carriage runs.

The work at 1:40 scale was expanded to include steady yaw angles up to 10 degrees (Longo & Stern, 1996, 2002). Forces and moments were measured for yaw angles from zero to 10 degrees at intervals of 2.5 degrees. Wave profiles at the hull surface and wave elevations were measured at yaw angles of zero, 5 and 10 degrees. Detailed pressure measurements were made at 10 degrees only. The methods used were essentially similar to the ones discussed above, with some minor changes. The biggest difference was that the range of the local wave surface measurements had to be extended, since the projected beam of the ship was wider, due to the yaw angle. Also, measurements were required on both sides of the hull, since the flow was no longer symmetric about the centerline.

The more complex flow around the yawed hull required a more precise spatial definition than the symmetric flow, and so data density for measurements was increased to between 800 and 1500 points per y-z plane. Data was collected for the upstream and downstream sides of the hull. The measurement grid for the case with 10 degrees yaw is given in Figure 2-2.

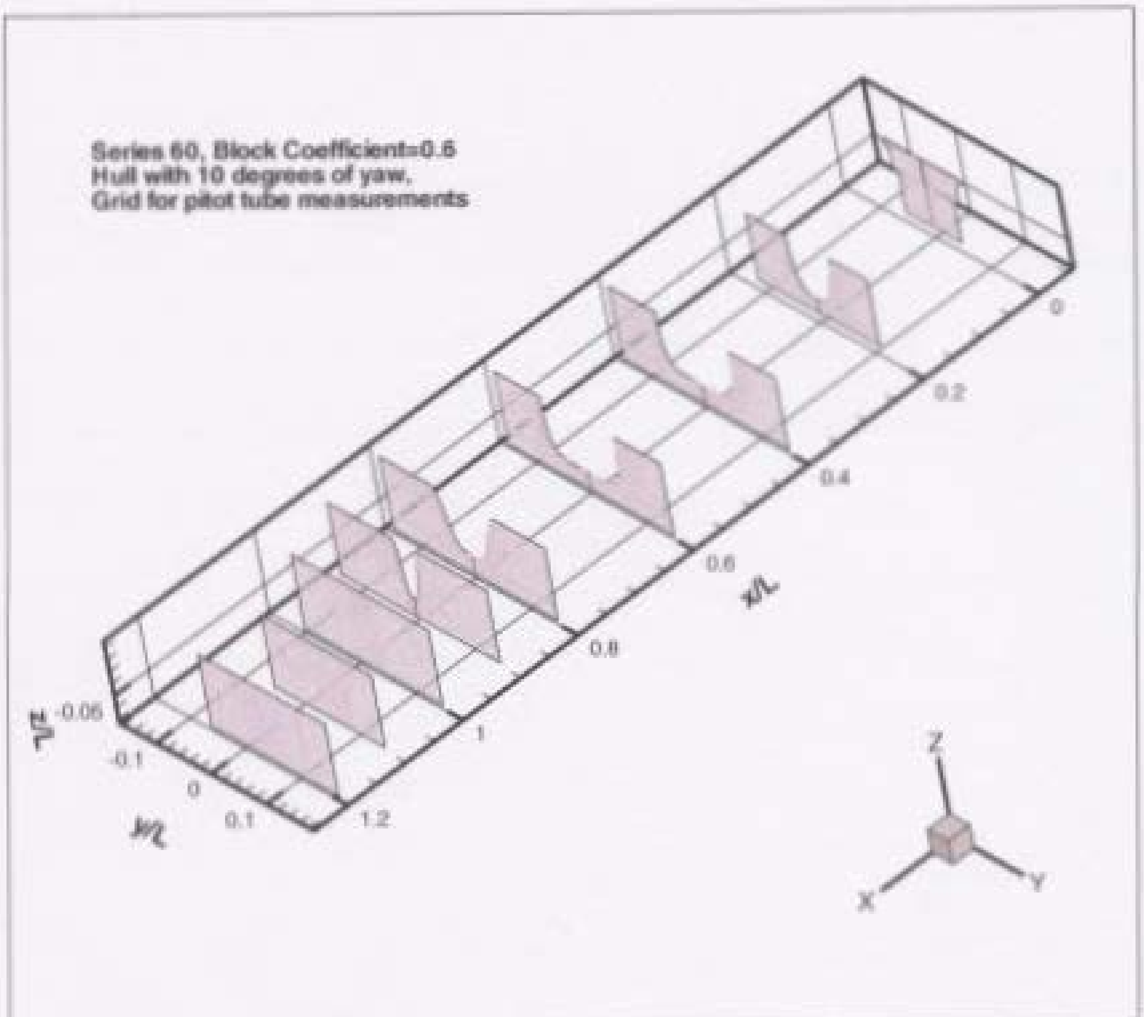

Figure 2-2, Measurement grid for Series 60, C_B=0.6 at 10 degrees yaw

The results of the experiments for the zero yaw and the yawed case are available from the web site of the IIHR Hydroscience and Engineering Ship Hydrodynamics Website at the University of Iowa (http://www.iihr.uiowa.edu/~shiphydro/efd.htm). For the purposes of this research, these data were re-plotted as contours of longitudinal flow velocity, u (non-dimensionalized by the free stream speed, U) and vectors of in plane flow components (v-w, also non-dimensionalized by the free stream speed, U) for selected sections along the hull.

For evaluation of the CFD predictions, only three of the sections were chosen. These were 20%L, 60%L and 90%L aft of the fore perpendicular. The data from Longo and Stern for these sections are shown plotted in Figures 2-3 to 2-5. These sections were picked because they showed the development of a vortex within the flow, and this vortex moved, relative to the centreline of the ship, as the section location was changed. It was important for the CFD code to be able to predict the flow patterns at different positions along the ship's hull.

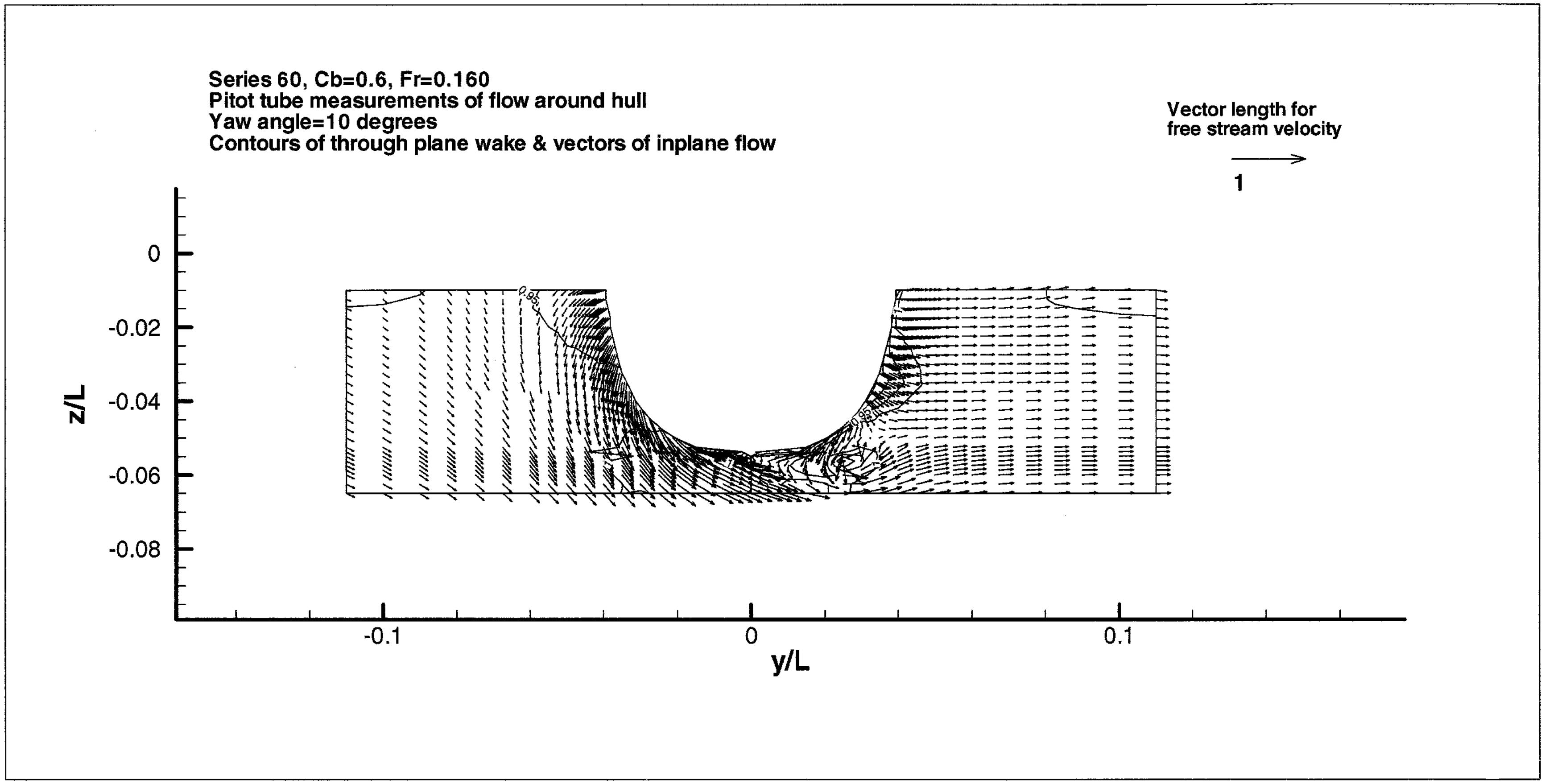

Figure 2-3, Results of pitot tube survey for flow around Series 60, C_B=0.6, section at 20%*L*

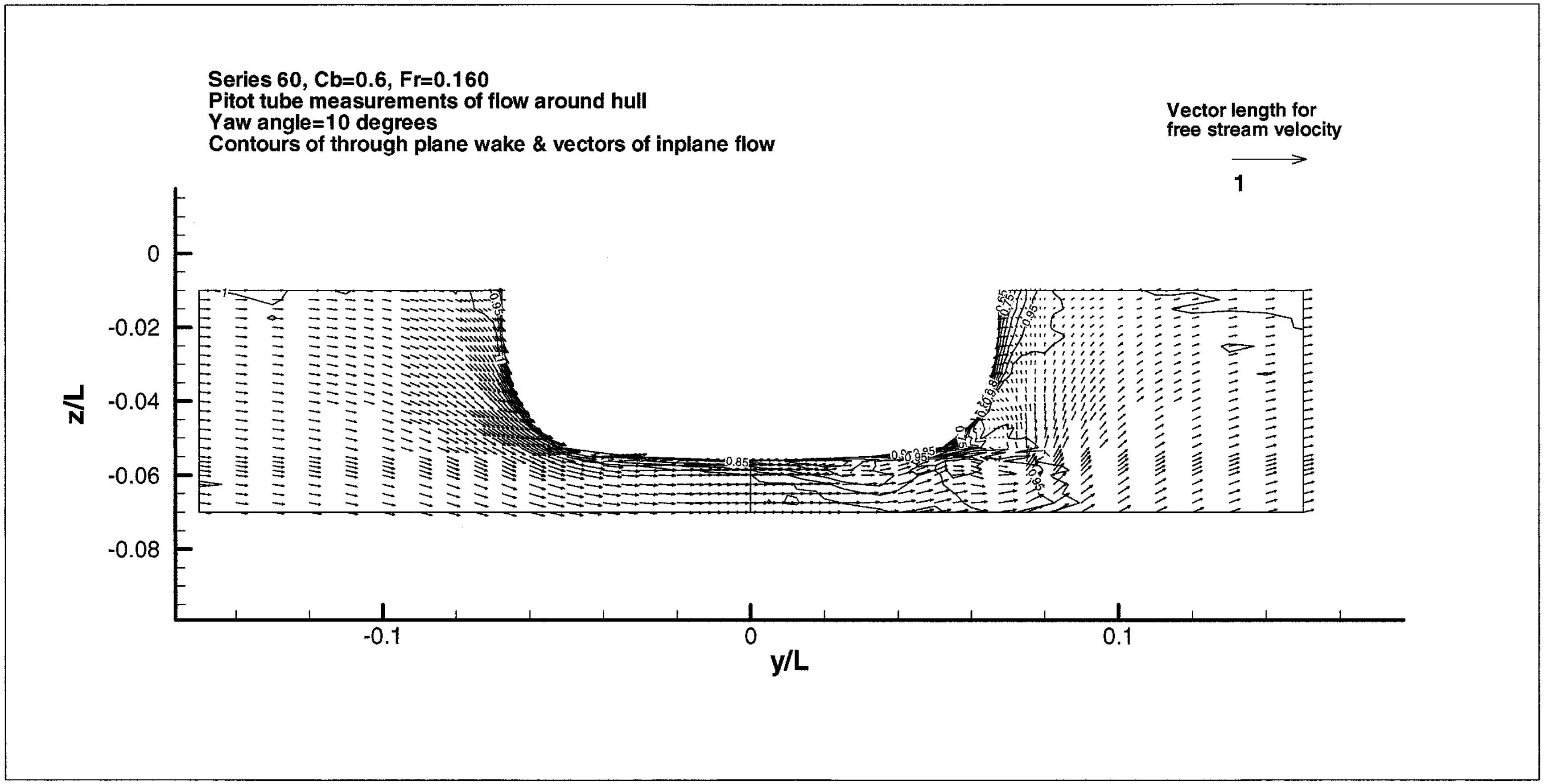

Figure 2-4, Results of pitot tube survey for flow around Series 60, C_B=0.6, section at 60%*L*

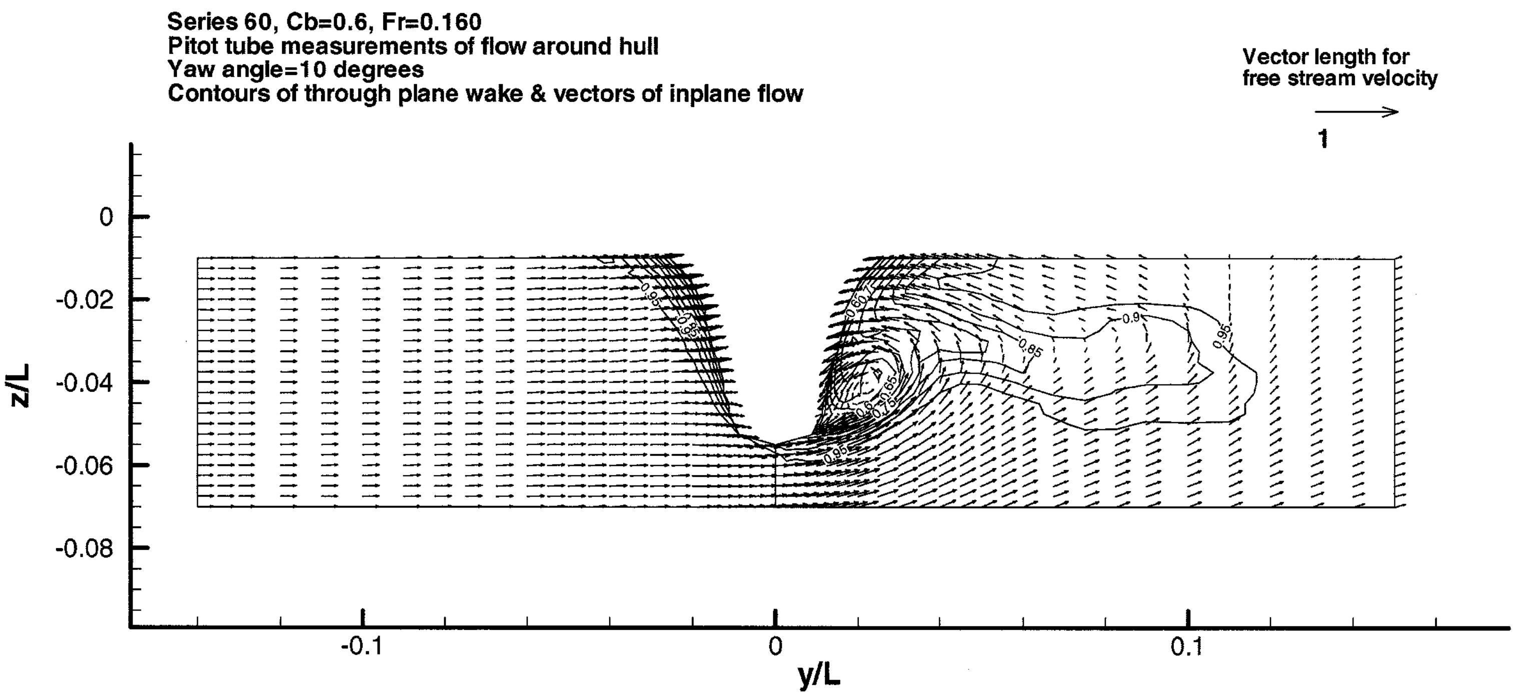

Figure 2-5, Results of pitot tube survey for flow around Series 60, C_B=0.6, section at 90%L

All these figures are for a Froude number of 0.16. The results for Froude number of 0.316 showed similar flow patterns. The Froude number of 0.16 was chosen because it was within the expected Froude number range for escort tugs, and was a close match to the speed used by Di Felice and Mauro (1999) for their experiments, which are discussed below.

2.2.2 LDV Data for Yaw Angle 35 Degrees

Di Felice & Mauro (1999) measured the flow on the downstream side of a double model of a Series 60 C_B=0.6 hull at a scale of 1:100 in a large cavitation tunnel using Laser Doppler Velocimetry (LDV). In this case, the model hull was symmetrical about the design waterline and the free surface effects were ignored. The yaw angle used was 35 degrees, which is within the expected range of operating yaw angles for an escort tug. The Froude number used for these experiments was 0.2, although the free surface was not considered. The flow speed for these experiments was 0.692 m/s.

The LDV used a two-component backscatter method, with estimated velocity resolutions within +/-1%. The flow was seeded with titanium dioxide particles, with a diameter of 1 μm. Measurements were made at two sections, 0.5*L* and 0.9*L*. The data density was 600 points for the first section and 800 points for the second. The measurements were made in the axis system of the tunnel, rather than normal to the centerline of the model. The resulting measurement planes were not at a constant location in ship axes, which was the convention used by Toda et al. (1992) and Longo and Stern (1996, 2002). They were

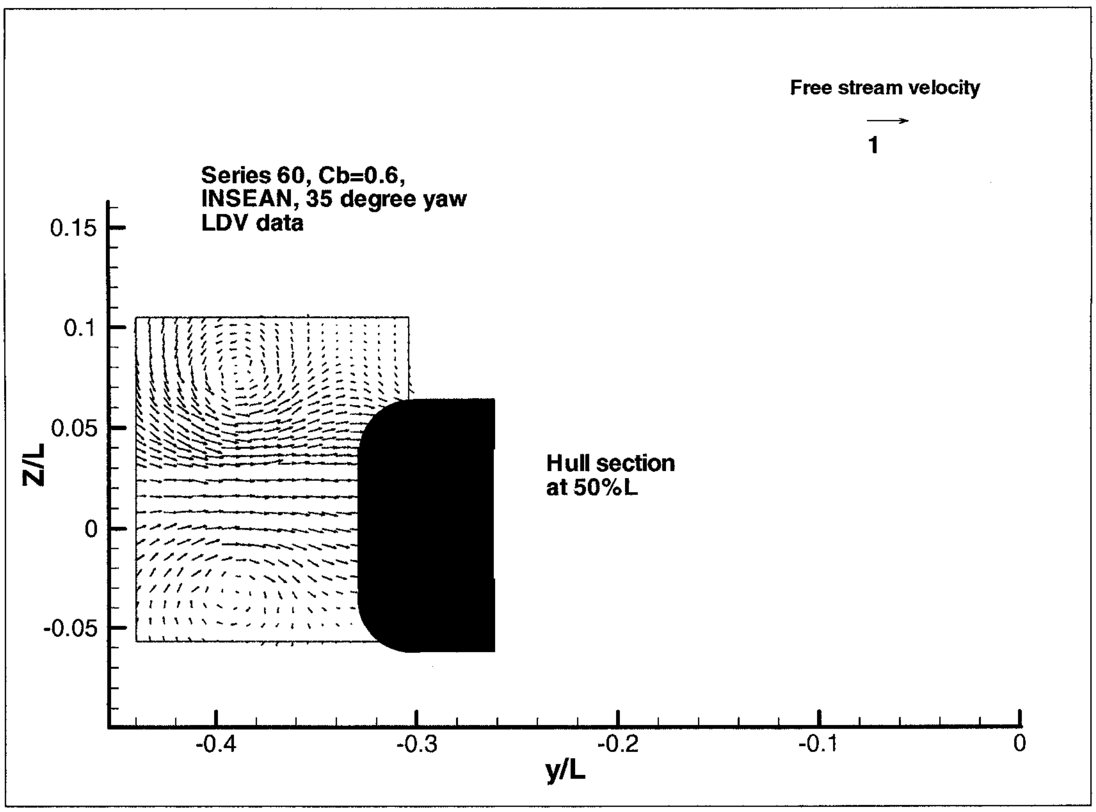

Figure 2-7, Flow vectors measured at 50%*L*, 35 degrees of yaw

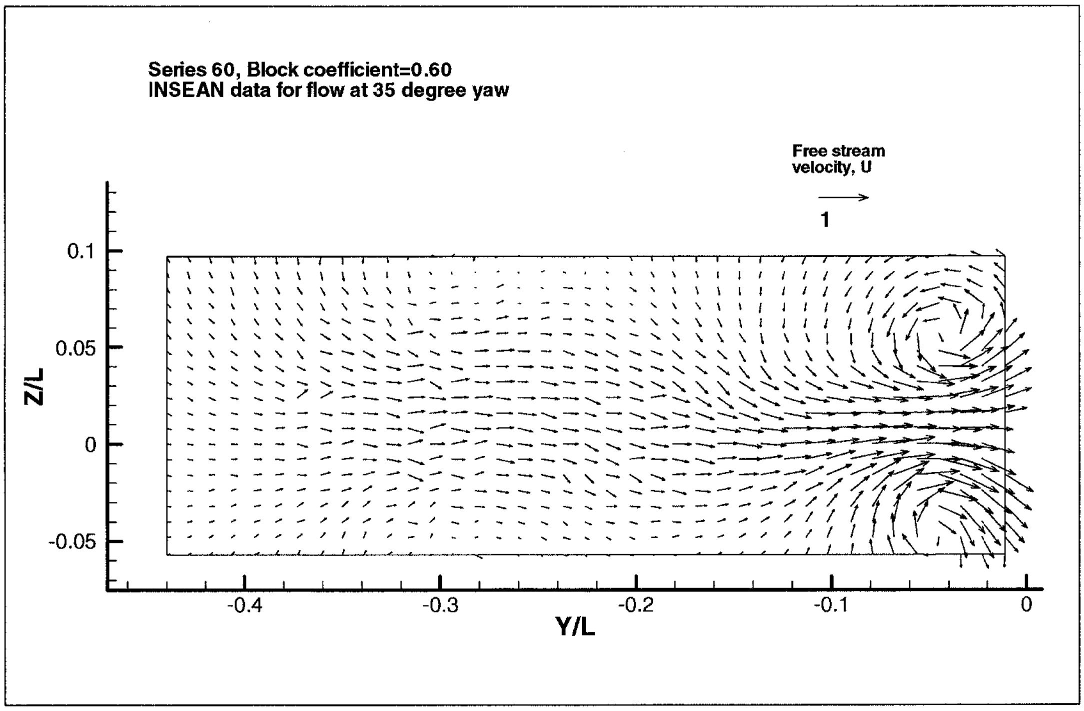

Figure 2-8, Flow vectors measured at 90%*L*, 35 degrees of yaw normal to the direction of the undisturbed flow, rather than normal to the centreline of the ship. This was accepted in order to use the mechanized system for locating the measurement point within the flow, which was fixed in an axis system with the y and z-axes normal to the centerline of the cavitation tunnel. Also, the origin for the system was at the aft perpendicular for the model.

The data from the two yaw angles were obtained in two different axis systems. Each system was chosen for valid reasons based on the nature of the experiments and the facility in which the experiments were carried out. Longo and Stern chose a ship based axis system for measurements in a towing tank. In this system, all measurements were made relative to an axis based on ship coordinates. The three orthogonal axes were defined relative to the centreline of the ship and undisturbed flow crosses the measurement plane at an angle. Di Felice and Mauro chose a measurement axis system based on the flow direction, since they did their experiments in a cavitation tunnel with the measurement system fixed in a direction normal to the centreline of the tunnel. The resulting measurement plane was normal to the undisturbed flow direction. The two axis systems are illustrated for the Series 60 hull at 50%L and 90%L for 35 degrees of yaw in Figure 2-6.

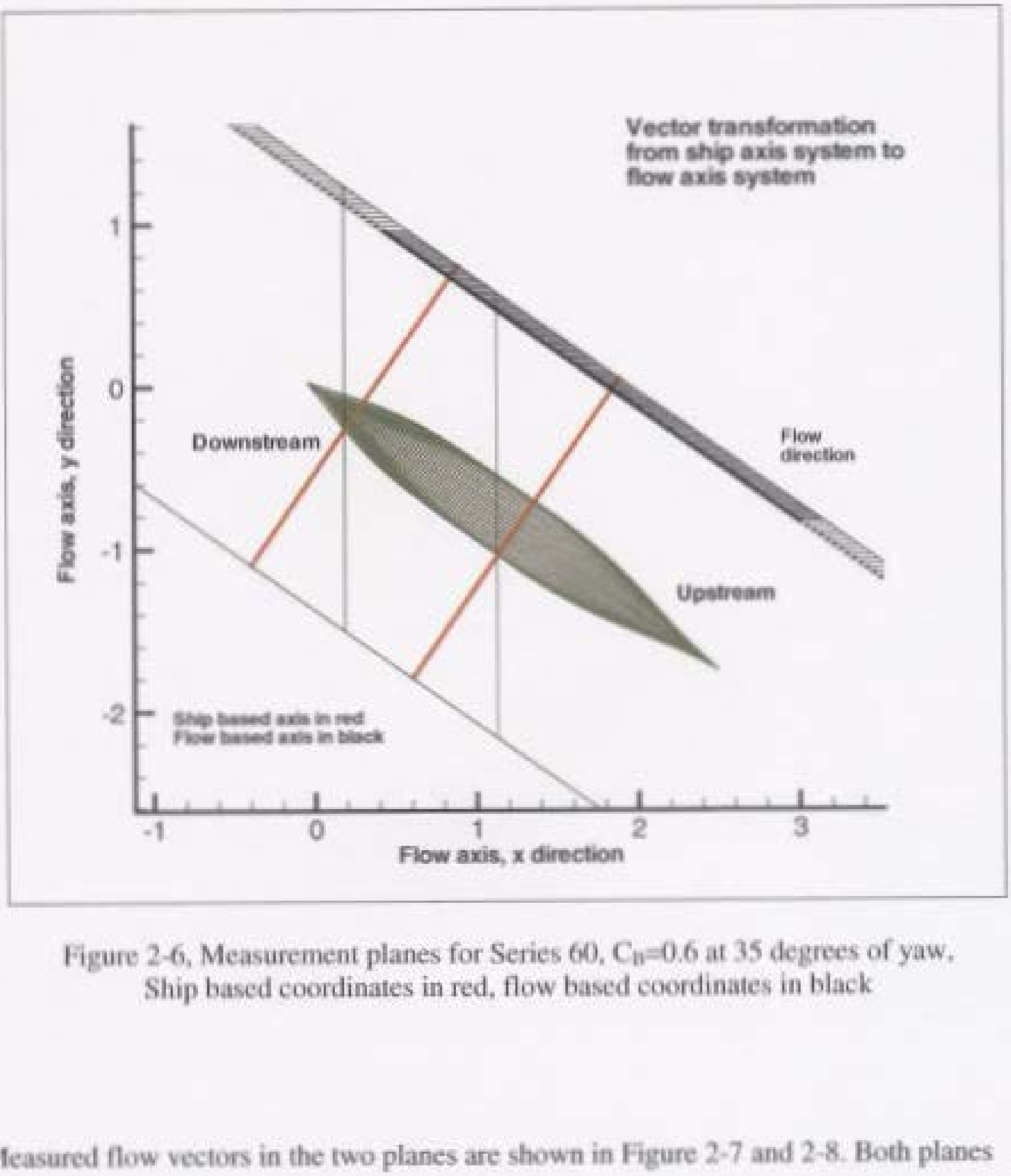

Figure 2-6, Measurement planes for Series 60, C_B=0.6 at 35 degrees of yaw. Ship based coordinates in red, flow based coordinates in black

Measured flow vectors in the two planes are shown in Figure 2-7 and 2-8. Both planes are on the downstream side of the model. The geometric locations were non-dimensionalized by ship length and the mean flow speeds were non-dimensionalized by the speed of the undisturbed flow.

Since the model was symmetrical about the waterline, the results shown in Figures 2-7 and 2-8 should be symmetrical about the *z/L* value of zero, and this is the case, within an allowance for scatter in the results of the experiments (although it looks as though the model may have had a small pitch angle, since the two vortices in Figure 2-7 are not at the same *z/L* location).

Based on the geometry of the experiment, the maximum beam of the hull at 50%*L* was at a value of *y/L* approximately -0.34 and the maximum draft was at *z/L* of +/-0.059. Figure 2-7 shows the approximate locations of the maximum beam and maximum draft within the measurement coordinate system. Note that the origin used in these experiments was at the aft perpendicular and fixed in the axis of the cavitation tunnel, rather than the ship.

Results of the experiments were presented by Di Felice and Mauro (1999) as contours of cross flow velocities, vertical and transversal component standard deviation, Reynolds stresses, vorticity and vertical and transverse component skewness for the downstream side of the hull. The results showed distinct vortices at each plane. Di Felice and Mauro state that the advantage of the LDV method was the ability to measure quantities such as turbulence intensity and Reynolds stresses, as well as detailed measurements of the flow in the cross planes. All these results combined to give information on viscous and turbulent aspects of detached flow generated by the yawed hull.

The data from the experiments was faired by assuming that the lower portion of the measurements was a mirror of the upper. The *z/L* value used for folding the data was not the same for each case. For 50%L the fold was at z/L=0.016, and for 90%L, the fold was at z/L=0.008. These values were chosen to make the centre of the observed vortex symmetrical about the nominal waterline of the model. Average values for the vectors were used, based on the measured values for the upper and lower sections of the hull. Measured data points that were inside the model geometry or very close to the surface of the hull were removed before the results were compared to the CFD predictions.

2.3 MESHING STRATEGIES FOR HULLS WITH YAW

2.3.1 Previous CFD Solutions for Flow Around Series 60 C_B=0.6 Hull

The experiment data for the Series 60 C_B=0.6 hull with a yaw angle of 10 degrees were compared with numerical predictions for the same conditions by Alessandri and Delhommeau (1996), Cura Hochbaum (1996), Campana et al. (1998) and Tahara et al. (2002). All of the methods solve the RANS equations for turbulent flow with a free surface but each author used a different turbulence model. In each case, the computational grid conformed to the body surface and the free surface, using hexahedral grid elements. Predictions were made for Froude numbers of zero (no free surface) and 0.316. All of the authors claim that their method captured the essential features of the flow, such as the asymmetric wave field close to the hull, mean flow fields dominated by strong cross flow effects and asymmetric vorticity distributions along the hull. However, in all cases the agreement was discussed subjectively, without putting any numerical values on the level of accuracy.

The use of hexahedral elements in the computational grid is widely accepted for CFD calculations of flow around ships. One exception to that is the code *FEFLO* (Yang and Löhner, (1998), Löhner et al., (1999)), which only uses a tetrahedral mesh. It was discussions with Professors Löhner and Yang during a visit to St. John's in September 2005 that initiated the consideration of a fully tetrahedral mesh as a suitable solution for a ship hull with a yaw angle.

2.3.2 Mesh Development

In practical situations, high yaw angles for ships only occur at low Froude numbers, where wave making generally has a small effect. At high speeds and high yaw angles, the side force components are large relative to the forward force components and act to slow down the ship. The large forces also generate large heeling and yawing moments. As a result, it may be possible to ignore the free surface for ships with large yaw angles, since practical applications will result in a Froude number based on ship length of under 0.2.

The results of the experiments from Di Felice and Mauro (1999) did not consider a free surface. Results of the flow measurements at 10 degrees of yaw were available for two Froude numbers (Fr=0.16 and 0.32), but for this study, only the lower one was considered. To simplify the mesh developed for this study the free surface was ignored. This was primarily because the main objective of this study was to evaluate the effectiveness of the different mesh strategies, at low Froude numbers, and so ignoring the free surface effects should only have a small effect on the results.

Each mesh strategy was subject to a certain amount of trial and error to obtain acceptable results, which has not been described here. For the tetrahedral mesh this included experimentation with cell size and distances between the inner and outer mesh. For the hexahedral mesh it included a sensitivity study (focusing on the thickness of the elements close to the hull). The selection of the final dimensions of the meshes used was based on a subjective comparison of the forces and flow patterns predicted by the CFD program. The results of a mesh sensitivity study (described in Appendix 1) showed that the predicted forces in the x and y directions were not significantly affected by the number of elements in the mesh.

a) Tetrahedral Mesh for Series 60 C_B=0.6

A file describing the hull surface for the Series 60 C_B=0.6 had been previously used at IOT for construction of a 1:20 scale model. This file was used as the starting point for generating the mesh within *GAMBIT*. This definition of the hull had the origin at the aft perpendicular, and was dimensioned in metres for the full-scale ship. The original hull surfaces were trimmed to the static waterline prior to meshing. The surfaces were then imported into *GAMBIT* as virtual surfaces. Small edges were removed and any edges of adjoining surfaces that did not match were connected. Also some surfaces defined in the original geometry were merged to make the meshing easier.

The next step was to create the domain boundaries and any additional surfaces required for constructing the mesh. For the tetrahedral mesh, three basic volumes were used within the overall geometry. The smallest volume was close to the hull and contained the smallest elements. These were elements with a nominal dimension of 0.2 metre within the hull surface. Two additional volumes were defined. The outer volume included the domain boundaries, and this was meshed with elements with a nominal dimension of 10 metres at the outer boundary, but reduced in size closer to the hull. A third volume between the inner volume and the outer volume was required to provide a transition region between the two. The geometry of each region is given in Table 2-2. The total number of elements within the mesh was 1,759,560. The mesh was nominally symmetrical about the centreline.

Table 2-2, Summary of geometry, tetrahedral mesh

Volume	Element size, m	*X*, min, m	*X*, max, m	*Y*, min, m	*Y*, max, m	*Z*, min, m	*Z*, max, m
Inner	0.2	-5.0	130.0	-9.0	9.0	-0.498	6.502
Intermediate	Transition	-80.0	200.0	-20.0	20.0	-5.498	6.502
Outer	10	-200.0	200.0	-60.0	60.0	-23.498	6.502

An overview of the complete mesh is shown in Figure 2-9. Key sections along the hull are shown in Figure 2-10, for the region close to the hull. This is the region in which measurements were made during the experiments. The mesh shown has been converted to the same coordinates used in the experiments at 10 degrees of yaw (Longo and Stern, 1996).

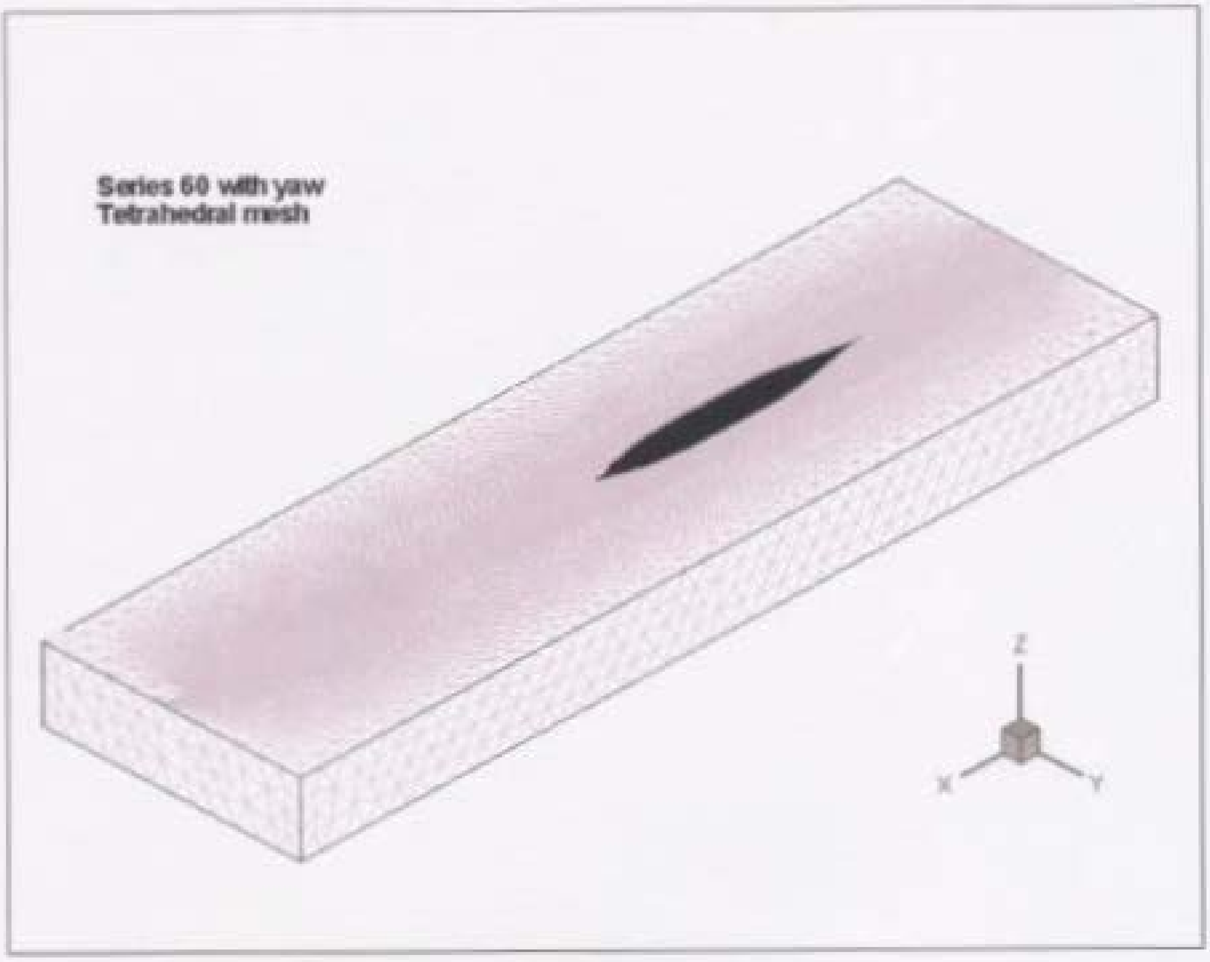

Figure 2-9. Overview of tetrahedral mesh, origin at bow, x positive towards stern

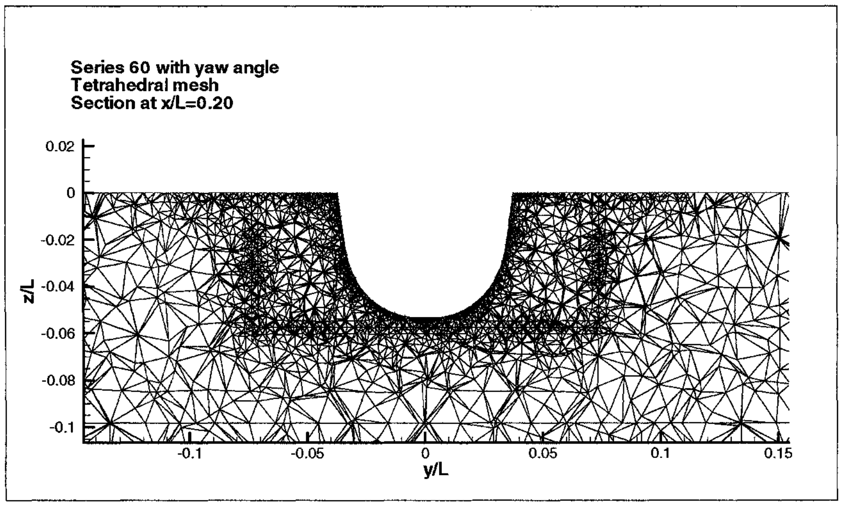

a)

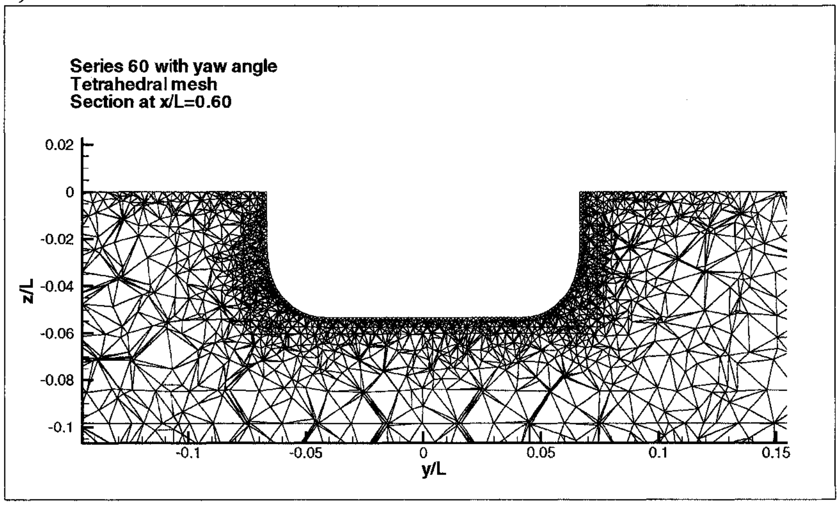

b)

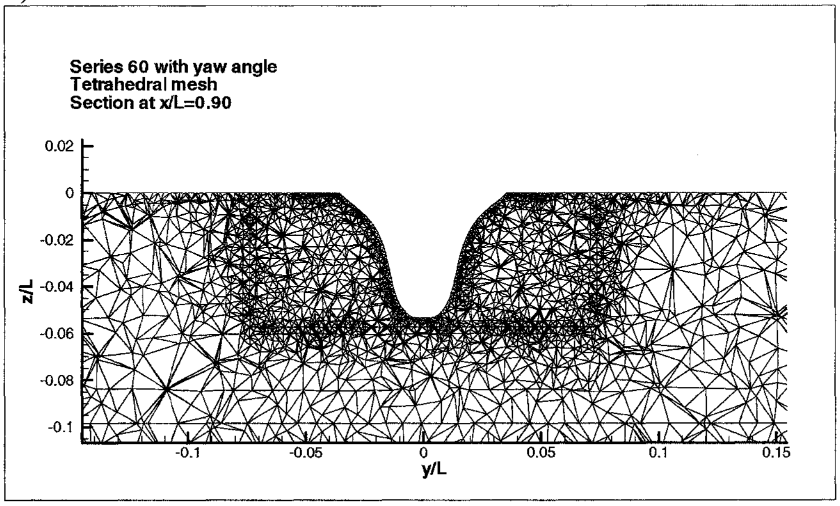

c)

Figure 2-10, Tetrahedral mesh at three representative sections
a) 20%L, b) 60%L, c) 90%L

b) Hexahedral Mesh for Series 60 C_B=0.6

The same surface file was used to create the hexahedral mesh as was used for the tetrahedral mesh. In this case the additional step of creating new surfaces so that the hull could be defined completely in four-sided elements was required. This was done within *Gambit*.

Again the mesh was divided into two regions. One region was close to the hull surface, and one was sufficiently far from the hull surface, that flow conditions were not changing significantly. The hull was defined using 16 cells from the centreline to the waterline, and this had to be kept constant along the whole length of the hull. This required a much more elaborate system of construction planes along the length of the hull, especially close to the bow and the stern.

Once the inner mesh was successfully defined, the cells in the *y-z* plane were extruded to the inlet and outlet boundaries. The mesh was symmetrical about the centreline of the ship.

A summary of the mesh geometry is given in Table 2-3. The total number of elements within the mesh was 423,464, which was less than one quarter of the number used for the tetrahedral mesh.

Table 2-3, Summary of geometry, tetrahedral mesh

Volume	X, min, m	X, max, m	Y, min, m	Y, max, m	Z, min, m	Z, max, m
Inner	-2.86	123.00	-15.0	15.0	-5.498	6.502
Outer	-127.86	185.50	-45.0	45.0	-23.498	6.502

An overview of the complete hexahedral mesh is shown in Figure 2-11. Key sections along the hull are shown in Figure 2-12, for the region close to the hull, over which measurements were made during the experiments. The mesh shown has been converted to the same coordinates used in the experiments at 10 degrees of yaw described by Longo and Stern (1996, 2002).

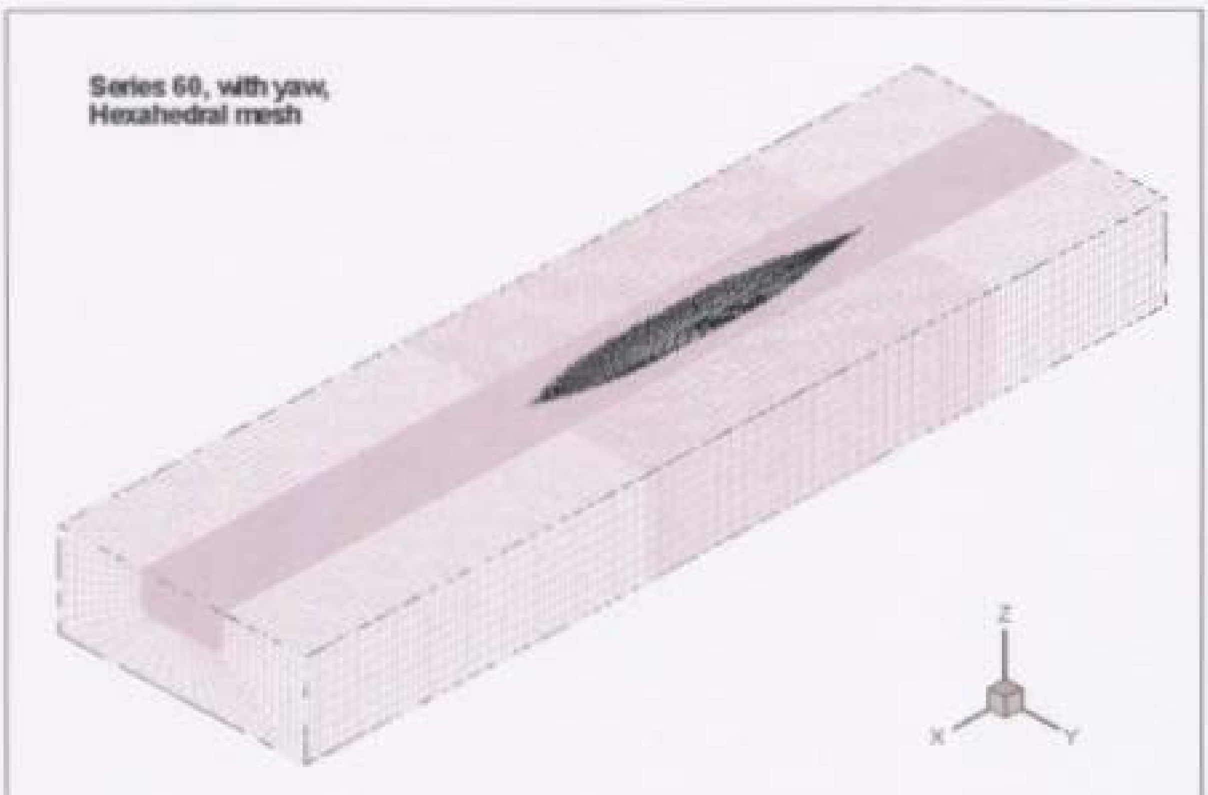

Figure 2-11, Overview of hexahedral mesh, origin at bow, x positive towards stern

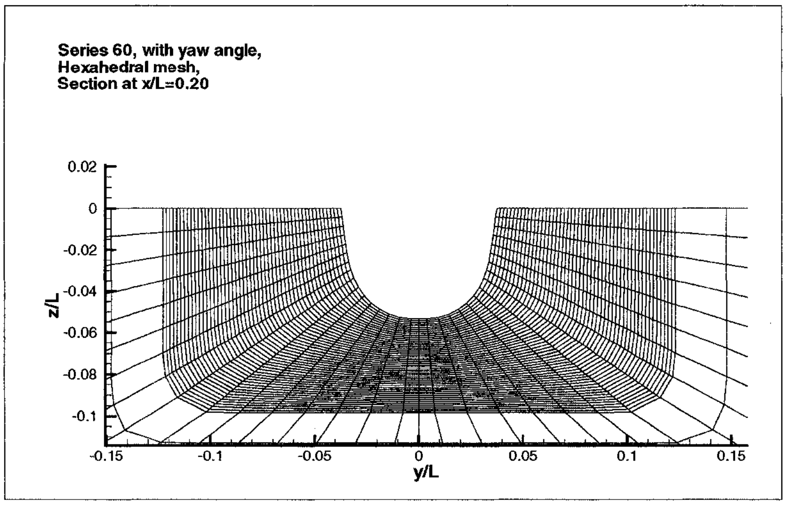

a)

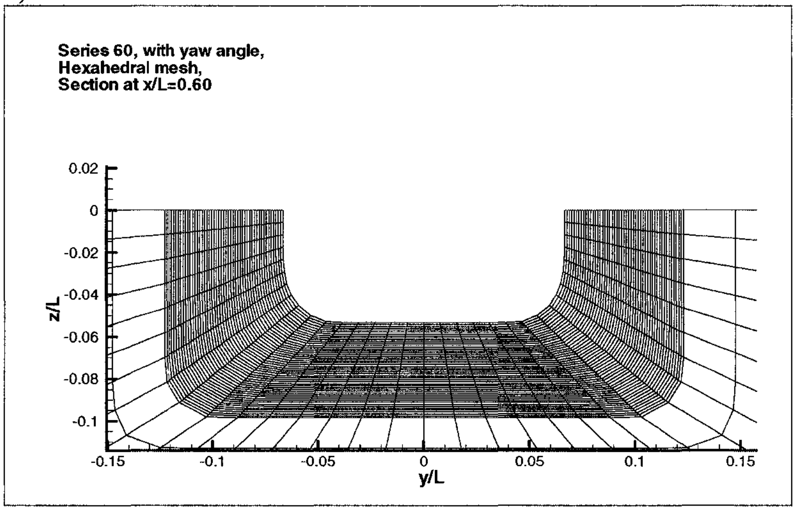

b)

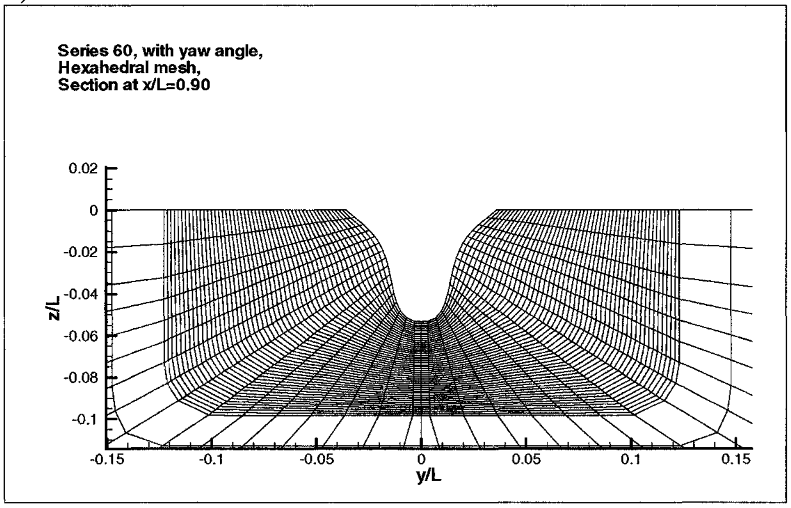

c)

Figure 2-12, Hexahedral mesh at three representative sections
a) 20% L, b) 60% L, c) 90% L

2.3.3 CFD Solutions Obtained Using *Fluent*

The upstream end and upstream side of the domain were defined as velocity inlets and the downstream end and downstream side were defined as pressure outlets. The hull was defined as a no-slip wall, and the upper and lower surfaces were defined as walls with zero shear force.

For the yaw angle of 10 degrees, the mesh coordinates were transformed within *Fluent*. The origin was move to the fore perpendicular, and the x direction reversed so that it was positive towards the stern, and the y direction was also reversed. All values for the mesh were scaled down to represent a model at a scale of 1:40 and a flow speed of 0.875 m/s. Planes within the solutions at constant values of x/L (0.2, 0.6 and 0.9) were extracted for comparison with the results of the experiments. For the yaw angle of 35 degrees, the original coordinate system of the mesh was used, but additional planes were added to intersect the hull, on the downstream side at 50%L and 90%L, which were normal to the undisturbed flow direction.

Predictions of the flow were obtained using *Fluent*. Boundary conditions, turbulence models and solution parameters for both the tetrahedral and hexahedral meshes were the same. Uniform flow entered the domain through a velocity inlet on the upstream boundaries and exited through a pressure outlet on the downstream boundaries. Yaw angle was changed by varying the direction of the flow vector at the boundary using a cosine component for flow along the centreline and a sine component for flow normal to the centreline on the inlet and outlet.

The selection of the turbulence model was based on discussions with experienced users of *Fluent* and other CFD codes (Rhee (2005), Turnock (2006)). The turbulence model used within *Fluent* was the standard κ–ω model with shear force corrections, and the default parameters given in Table 2-4. This is an empirical turbulence model, based on model transport equations for the turbulence kinetic energy (κ) and the specific dissipation rate (ω). Turbulence intensity and turbulent viscosity ratios at the boundaries were set at 1% and 1 respectively. The flow was solved for the steady state case. The convergence limit was set to 10^{-3} (default values within *Fluent*) for all parameters. All solutions converged within these limits. Flow speeds were non-dimensionalized using the free stream flow speed for presentation of the results.

Table 2-4, Parameters for κ–ω turbulence model

α_∞^*	1.0
α_∞	0.52
α_0	0.111
β_∞^*	0.09
β_i	0.072
R_β	8
ζ^*	1.5
M_{t0}	0.25
TKE Prandl number	2
SDR Prandl number	2

For the 10 degree yaw case, results of the tetrahedral mesh are shown in Figures 2-13 to 2-15, and for the hexahedral mesh in Figures 2-16 to 2-18. These predictions are for the same flow conditions as the experiments of Longo and Stern (1996, 2002) shown in Figures 2-3 to 2-5.

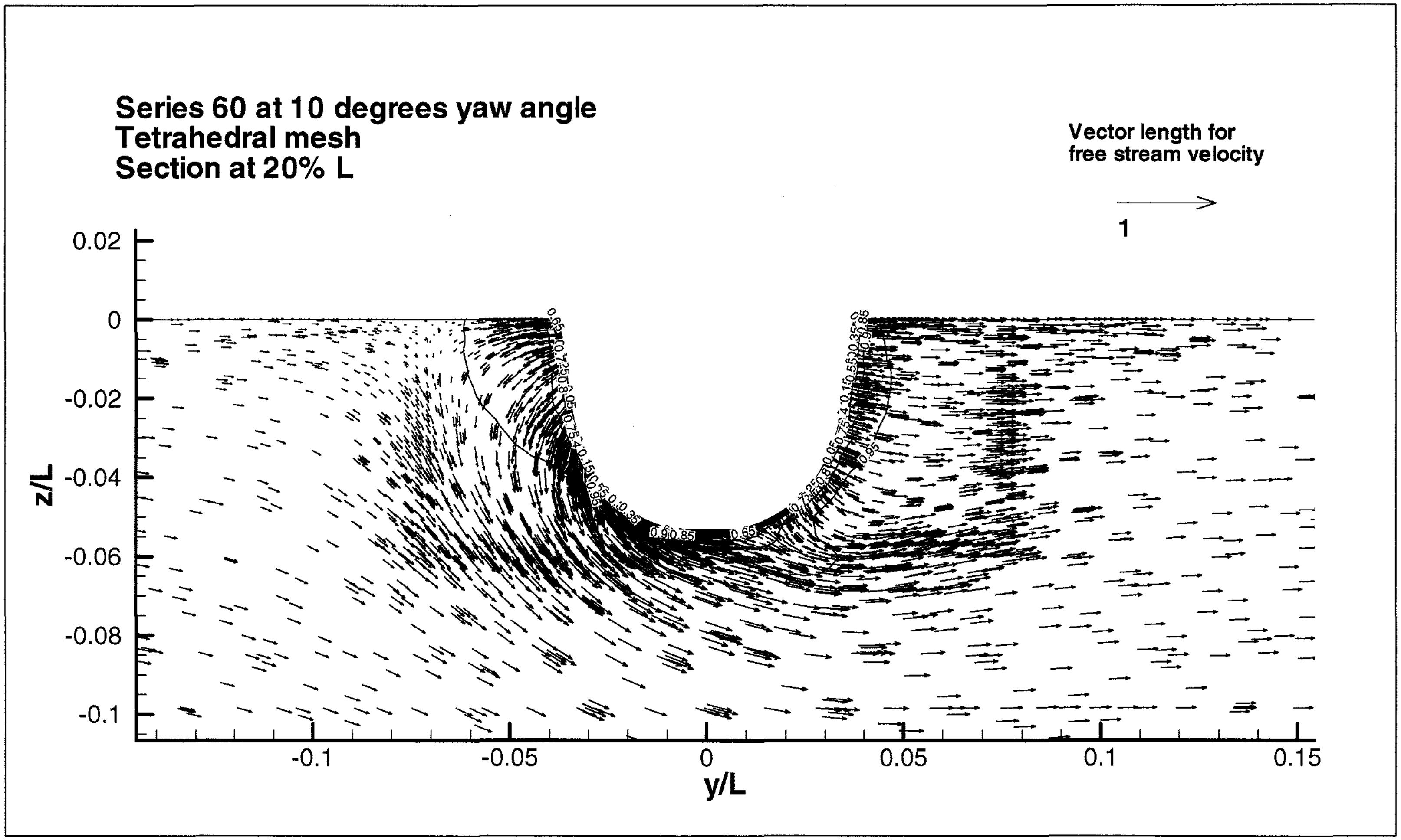

Figure 2-13, Tetrahedral mesh, Yaw angle 10 degrees, CFD predictions of flow patterns at 20% *L*

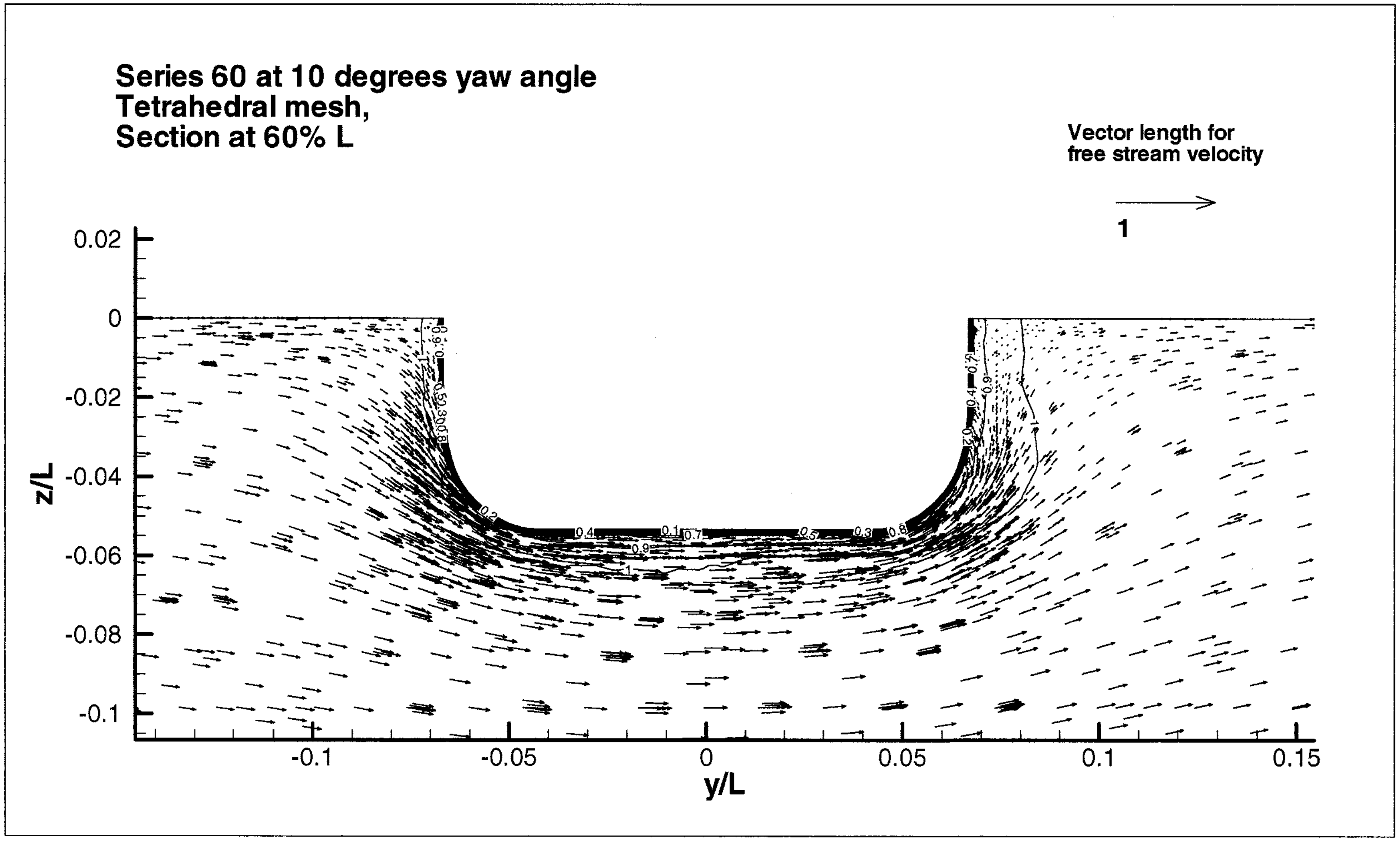

Figure 2-14, Tetrahedral mesh, Yaw angle 10 degrees, CFD predictions of flow patterns at 60% *L*

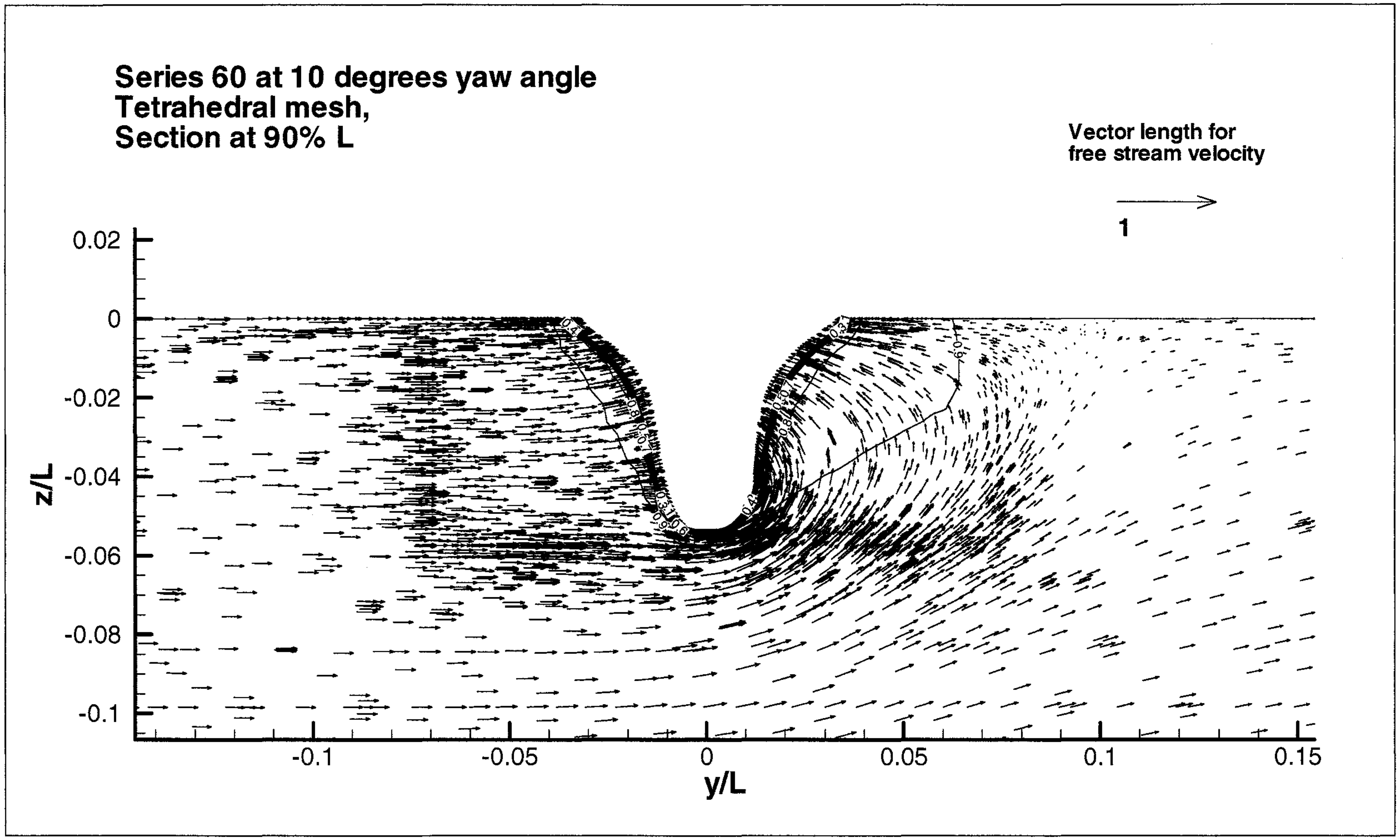

Figure 2-15, Tetrahedral mesh, Yaw angle 10 degrees, CFD predictions of flow patterns at 90% *L*

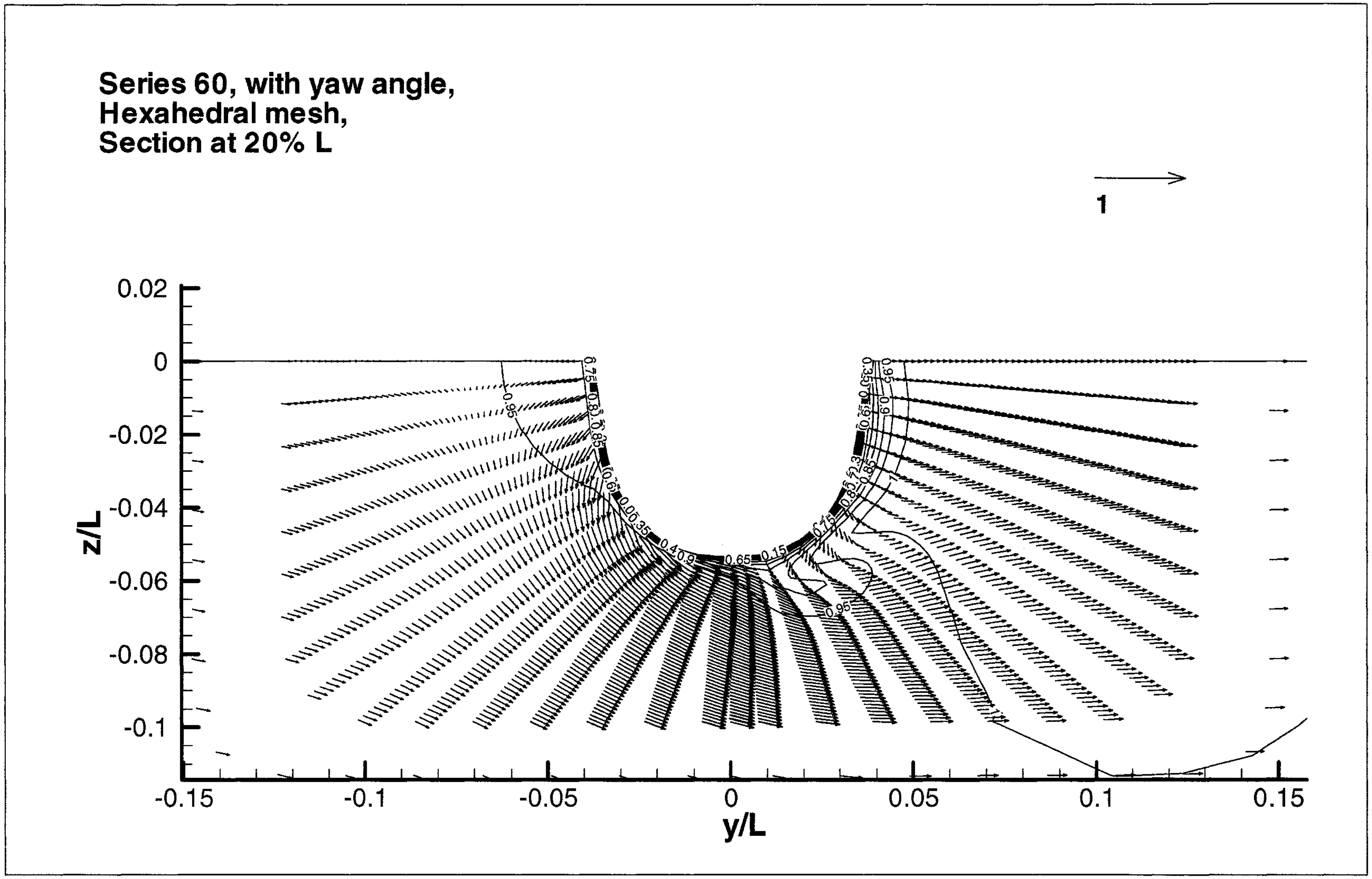

Figure 2-16, Hexahedral mesh, Yaw angle 10 degrees, CFD predictions of flow patterns at 20% L

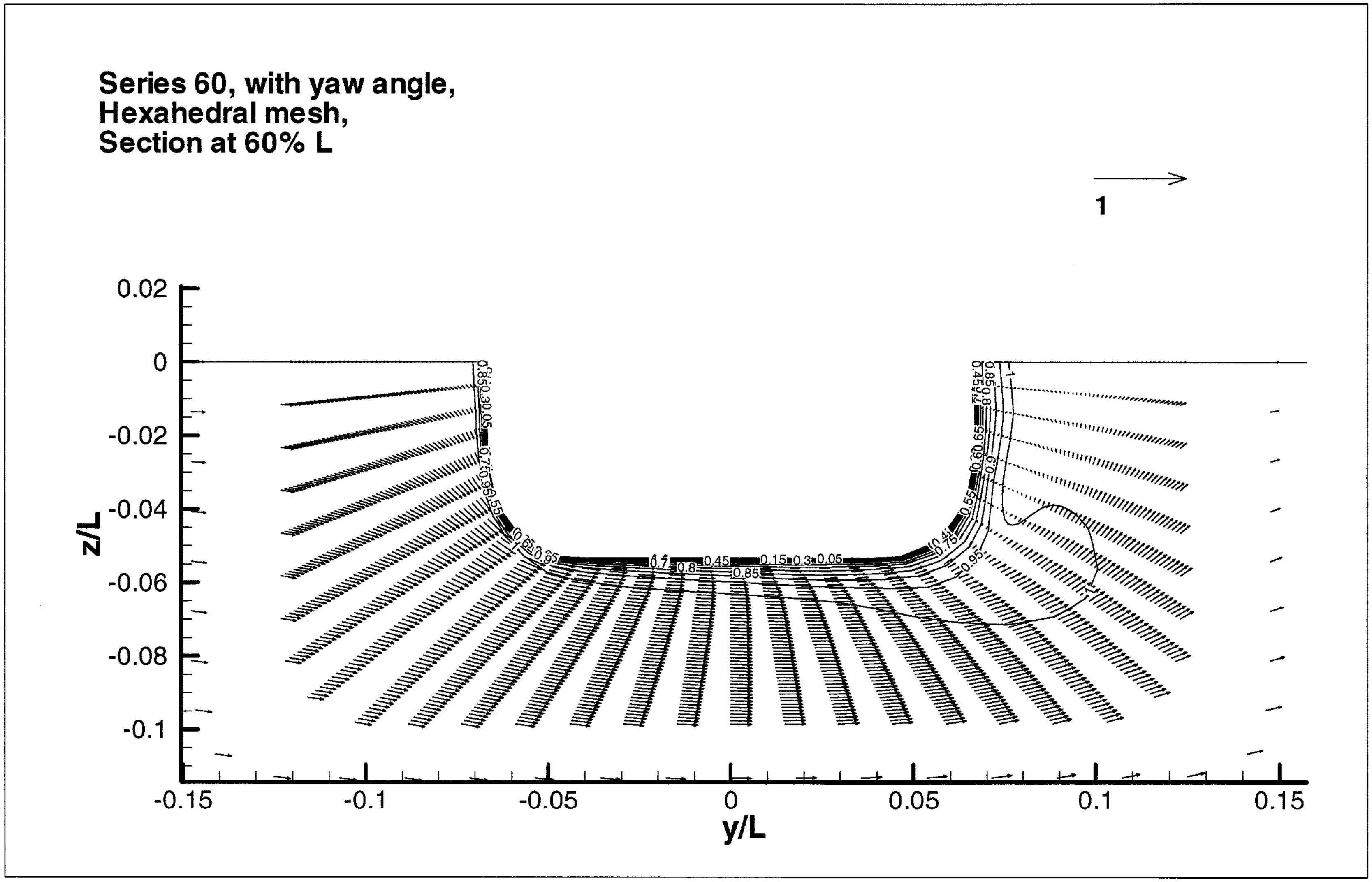

Figure 2-17, Hexahedral mesh, Yaw angle 10 degrees, CFD predictions of flow patterns at 60% *L*

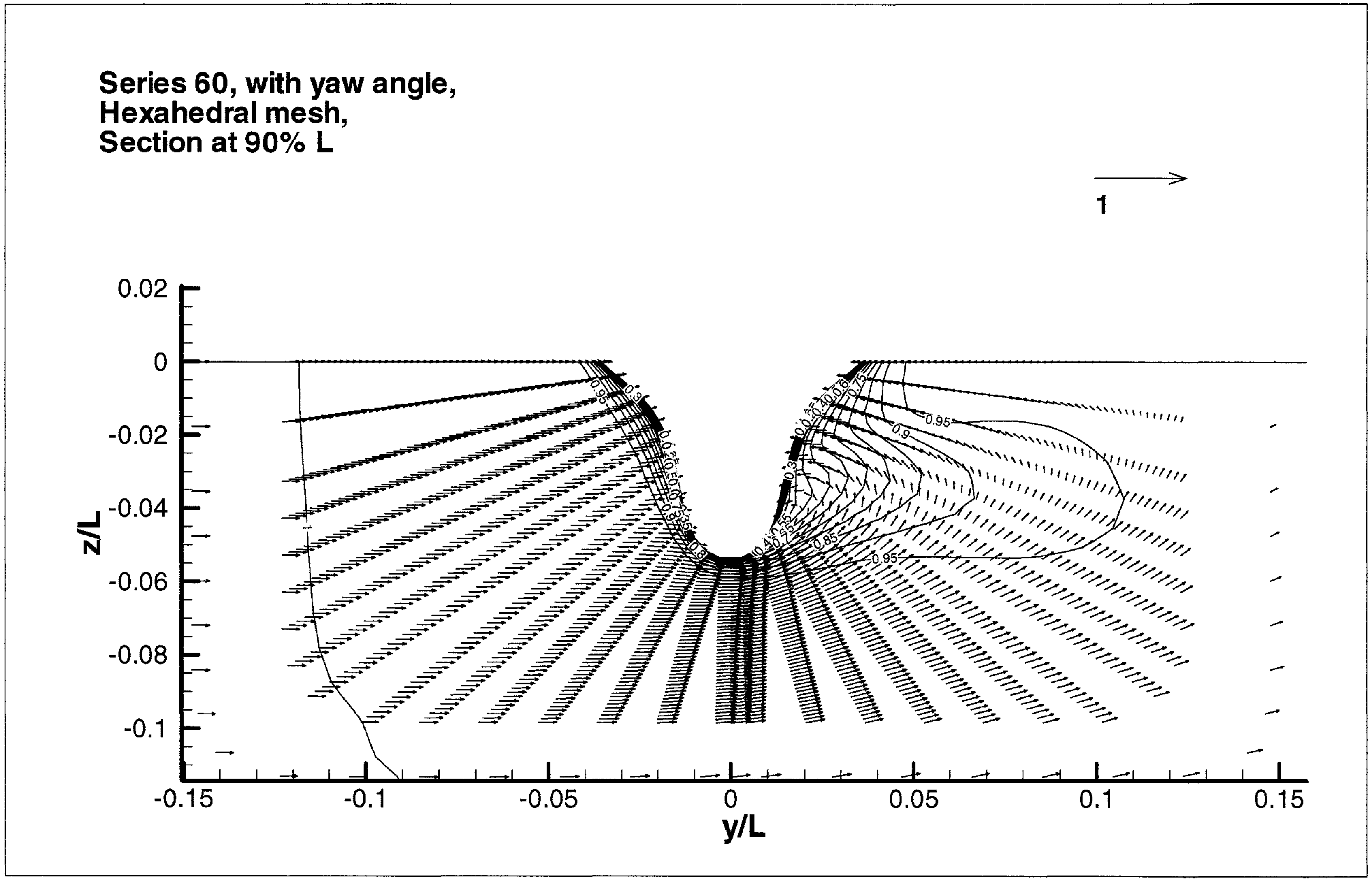

Figure 2-18, Hexahedral mesh, Yaw angle 10 degrees, CFD predictions of flow patterns at 90% *L*

Additional planes were created within the CFD solution for comparing the CFD predictions with model experiments at 35 degrees of yaw, based on the measurement planes used in the experiments. The velocity components in these planes were given by *Fluent* in the original (ship-based) coordinate axis system. The results of the CFD simulations required some manipulation before they were comparable with the measurements made in the experiments. For the experiments at 35 degrees yaw, the origin was at the aft perpendicular of the model, with x direction positive towards the bow, and the flow components were in the negative x and y directions. The flow vectors and associated grid points taken from the CFD solution within the measurement planes were transformed into an in-plane and through-plane coordinate system using the following transformations;

$$x_f = (x_s \text{Cos}\,\theta + y_s \text{Sin}\,\theta)$$
$$y_f = (-x_s \text{Sin}\,\theta + y_s \text{Cos}\,\theta)$$

where;

x_f and y_f are in the flow based coordinates
x_s and y_s are in the ship based coordinates
θ is the angle between the flow direction and the ship based coordinates.

Since the transformation about the vertical axis was purely rotation, the third axis (z in the experiment notation) was unchanged.

The predicted flow patterns in the flow based axis system are shown in Figures 2-19 and 2-20 for the tetrahedral mesh and Figures 2-21 and 2-22 for the hexahedral mesh. These predictions can be compared to the results of the experiments given by Di Felice and Mauro (1999), shown in Figures 2-7 and 2-8.

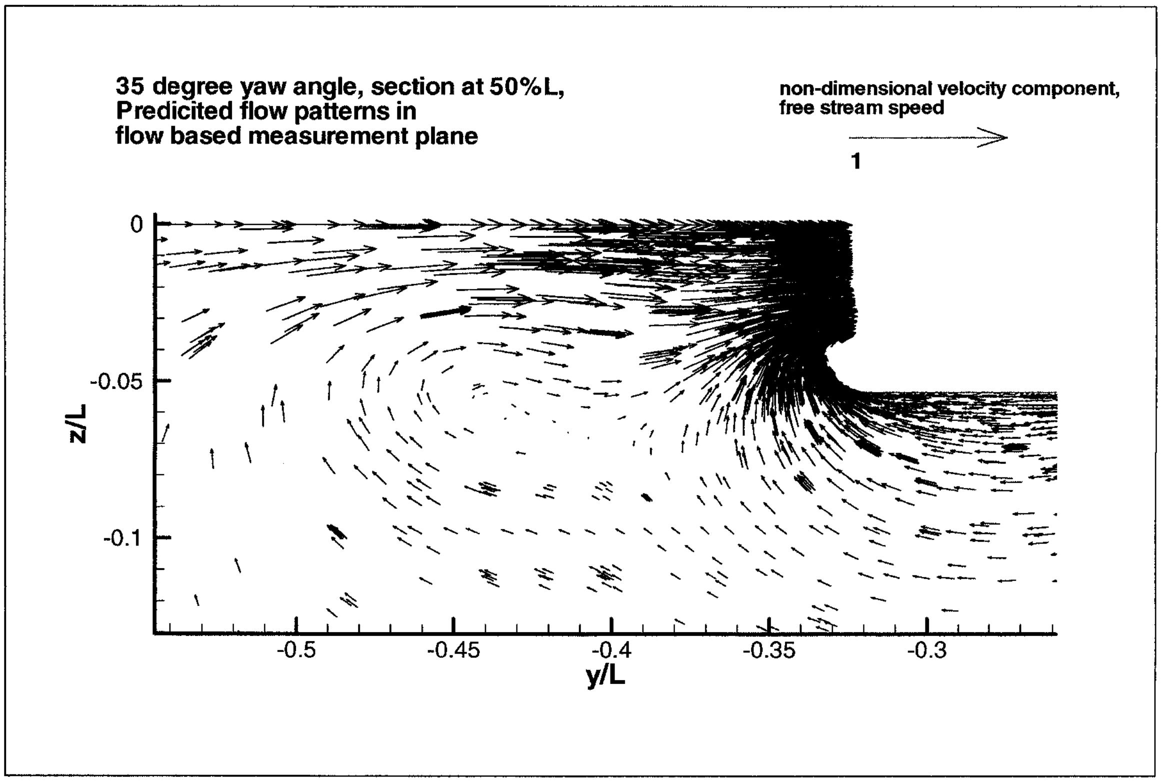

Figure 2-19, Tetrahedral mesh, Yaw angle 35 degrees, CFD predictions of flow patterns at 50% *L*

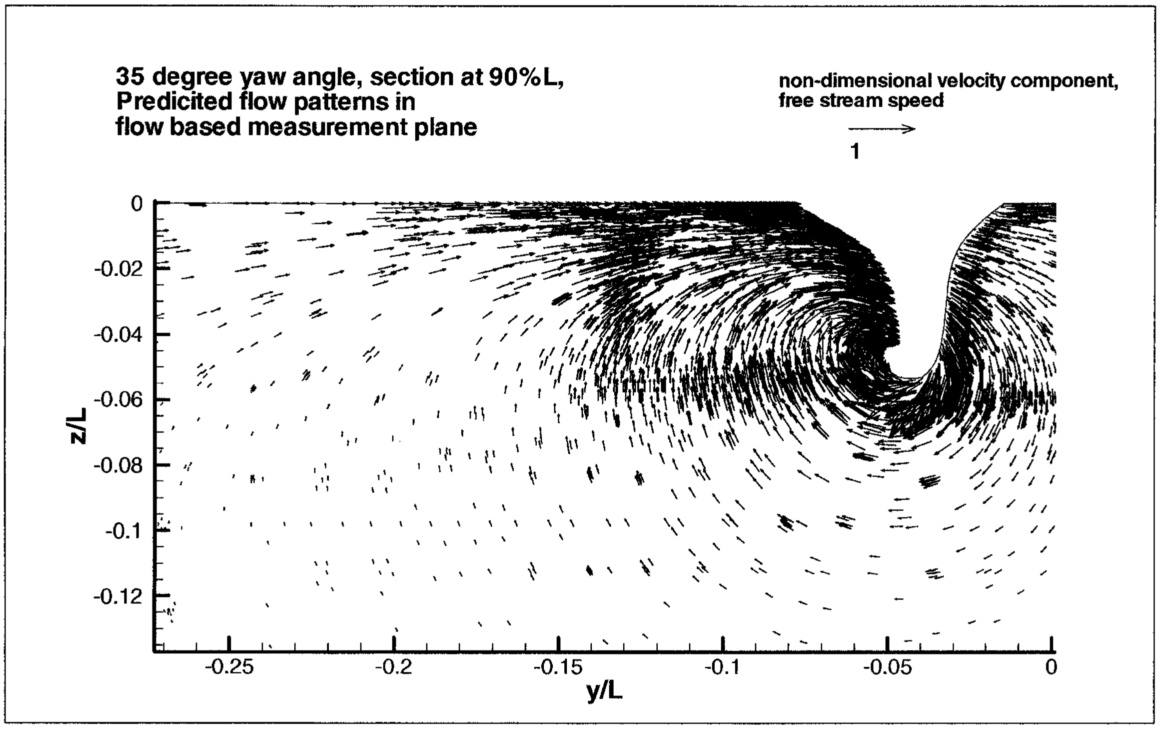

Figure 2-20, Tetrahedral mesh, Yaw angle 35 degrees, CFD predictions of flow patterns at 90% *L*

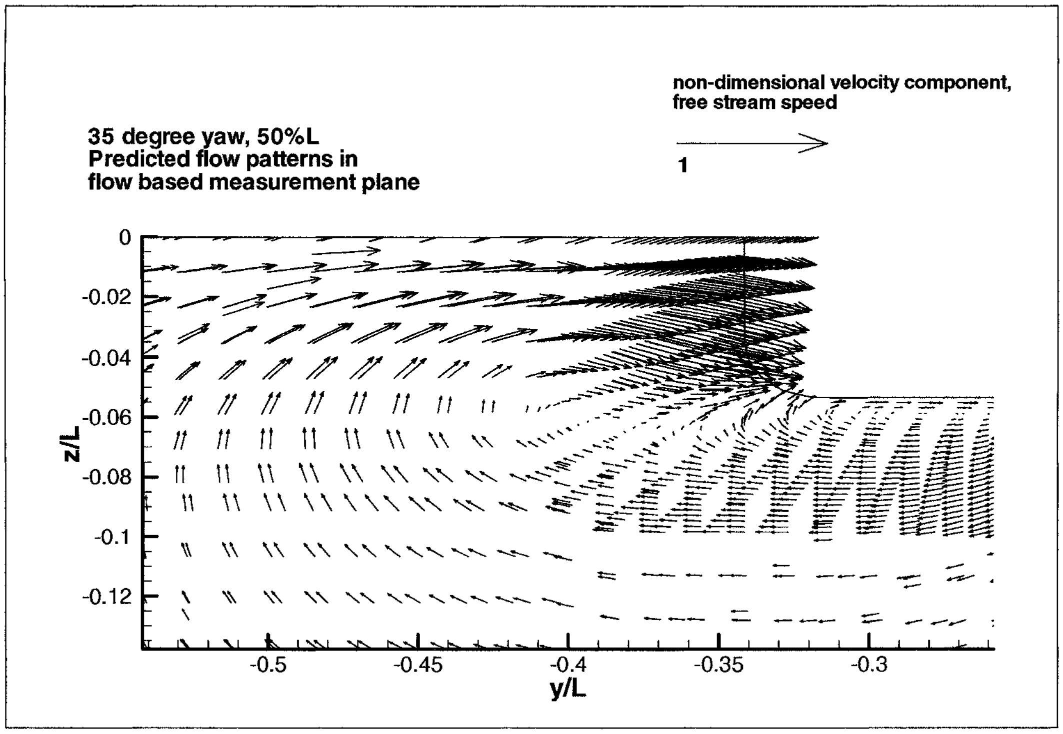

Figure 2-21, Hexahedral mesh, Yaw angle 35 degrees, CFD predictions of flow patterns at 50% *L*

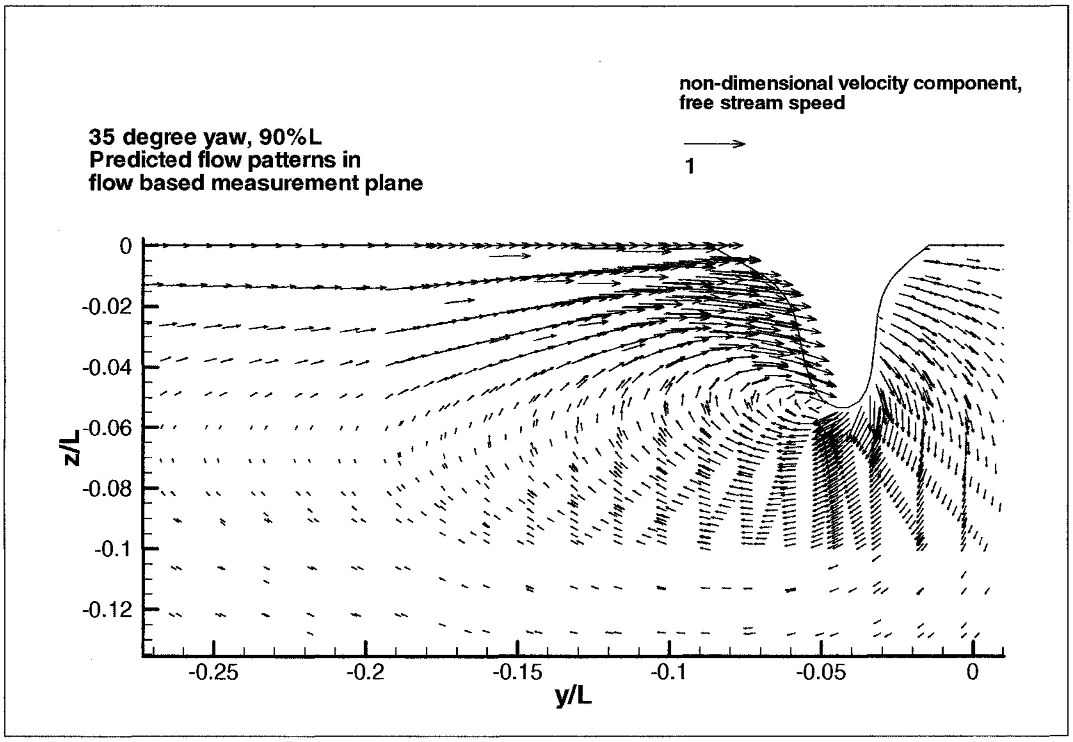

Figure 2-22, Hexahedral mesh, Yaw angle 35 degrees, CFD predictions of flow patterns at 90% *L*

2.3.4 Discussion of Observed Flow Patterns

The three sections around the hull chosen for comparison between experiment results and CFD predictions were at x/L=0.2, 0.6 and 0.9. These represented three distinct regions within the flow. These may be broadly categorized as an entry region, in which the flow is accelerating around the hull, a midsection region, where the flow is at the maximum distortion from the free stream, and a stern region, where the flow is dominated by the wake of the hull.

Based on the results of the experiments some key features of flow patterns around a Series 60 hull with a yaw angle were observed and it is important that the CFD simulations capture these features. These observations are summarized in Table 2-5.

Table 2-5, Summary of observed flow patterns for experiments and CFD predictions

Yaw angle, deg.	Flow feature	Figure, Experiment	Figure, Tetrahedral mesh	Figure, Hexahedral mesh
10	Closed contour of *u* velocity component that moves from the centreline towards the downstream side of the hull as flow moves further aft along hull	2-3, 2-4, 2-5	2-13, 2-14, 2-15	2-16, 2-17, 2-18
10	Strong downward flow component on upstream side of hull, up to 60%L	2-3, 2-4	2-13, 2-14	2-16, 2-17
10	Strong upward flow component on downstream side of hull from 60%L to stern	2-4, 2-5	2-14, 2-15	2-17, 2-18
10	Strong circulating flow component on down stream side at 90%L	2-5	2-15	2-18
35	Strong circulating flow on downstream side of the hull at 50%L, which was not observed at 10 degrees	2-7	2-19	2-21
35	Strong circulating flow on downstream side of hull at 90%L	2-8	2-20	2-22

At 10 degrees yaw, both meshes capture the in-plane velocity components well, with the exception of the local region close to the vortex observed at each section. Neither of the meshes gives adequate representation of the flow around the vortex core. The hexahedral mesh however, appears to do a better job of predicting the through-plane velocity component. The contours of u for this case show greater resemblance to the experiment values along the length of the hull.

At 35 degrees of yaw, the experiment data is sparser, since only two sections were measured, and only in two dimensions. The experiment results show a strong flow towards the hull at the waterline, and a well-developed vortex shed from the keel. Both CFD predictions show these characteristics, although the flow around the vortex core is less circular than the flow observed in the experiments. Although there are some obvious local deficiencies in the flow patterns when compared to the experiments, the results of the CFD predictions capture the essential features of the flow around a hull with a yaw angle.

2.4 DEVELOPMENT OF A NUMERICAL EVALUATION METHOD FOR COMPARING FLOW PATTERNS FROM CFD PREDICTIONS WITH EXPERIMENTS

A detailed comparison of a CFD simulation with physical measurements of the same flow condition is an important step in assessing its accuracy. The methods used to make the comparison depend on the overall objectives required from the simulations. In many engineering studies, accurate predictions of the forces and moments resulting from the fluid flow around an object are a sufficient measure of the accuracy of the simulations. If the results of the CFD simulations are within the uncertainty of the experiments, then the predictions have been made with sufficient accuracy. This assessment approach is attractive since it is based on a single quantity that is significant to many engineering solutions. It is however only a partial understanding of the accuracy of the CFD prediction. A full validation includes comparing the flow patterns as well as the resulting forces.

The discussion above on the comparison between the experiment results and the CFD predictions is subjective. In order to make meaningful evaluations, a structured numerical approach is required. This section outlines the development of a method that can be used for making comparisons between experiment results and the different CFD meshes, in order to determine the most effective meshing strategy.

Flow measurements for the Series 60 hull were two-dimensional LDV measurements of in-plane flow components at a yaw angle of 35 degrees and three-dimensional velocity components measured with Pitot tubes at a yaw angle of 10 degrees. Since the most generally accepted way to present the results of flow around a hull with yaw is as vectors of in-plane velocity combined with contours of through-plane velocity, this was used as the basis of the comparison, but it was recognized that three velocity components might not be available in every case. The steps in the evaluation process are described below, and where necessary they are graphically illustrated using experiment data for the Series 60 hull, from the section at x/L=0.9 at 10 degrees of yaw and CFD predictions for the hexahedral mesh for the same condition.

2.4.1 Preliminary Processing

The first step in the preliminary processing is to make the velocity components non-dimensional, by dividing by the free stream velocity. This makes all analysis relative to the free stream flow values of 1.0, and as a result interpretation of the comparisons is easier, since the results are dimensionless. Also, for PIV or LDV measurements it is necessary to remove any flow measurements at spatial coordinates inside the geometry of the hull. These data points are usually caused by reflections from the surface of the model.

2.4.2 Grid for Comparison of Data

A grid must be developed which is common to the experiment results and the CFD predictions. A typical experiment grid will contain far fewer points than a CFD grid, and as a result is the most likely candidate for the grid used for the evaluation, but it is possible that the experiment grid is larger than required for the comparison, or that the original spacing was not optimum.

The development of the evaluation grid can be an iterative process. If the experiment grid is very large, then there may be areas where flow measurements are close to the free stream conditions. In these cases, agreement between the experiment results and the CFD simulations should be easy to obtain, and this will bias the overall error comparison, by including a large number of points with small errors. The selection of the region for comparison is subjective, and the most appropriate area depends on the specific flow conditions being investigated. An example of a comparison grid is shown in Figure 2-23. In this case the grid has been reduced from the complete experiment grid, because the errors on the upstream side of the hull were very small.

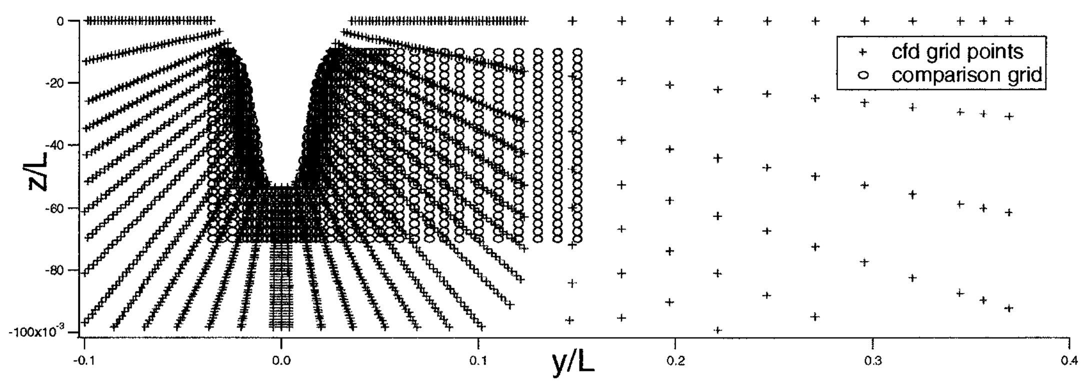

Figure 2-23, Comparison of CFD grid points with comparison grid

2.4.3 Interpolate CFD and Experiment Results on Common Grid

The three experimentally obtained velocity components in the orthogonal x, y, z planes were referred to as u_{expt}, v_{expt} and w_{expt}. The magnitude and direction of the in-plane velocity vectors were obtained by combining the v and w components.

$$|V|_{expt} = \sqrt{v_{expt}^2 + w_{expt}^2}$$
$$\theta_{expt} = \tan^{-1}\left(\frac{w_{expt}}{v_{expt}}\right)$$

Individual velocity components from the CFD solutions were plotted as contours over the complete fluid domain at the section used for comparison. The contours of single velocity component were interpolated at the points of the grid used for comparison. The resulting velocity components were u_{cfd}, v_{cfd} and w_{cfd}. Vectors of in-plane flow were calculated from the combination of v and w components.

$$|V|_{cfd} = \sqrt{v_{cfd}^2 + w_{cfd}^2}$$
$$\theta_{cfd} = \tan^{-1}\left(\frac{w_{cfd}}{v_{cfd}}\right)$$

An example of the comparison between the experiment values and the CFD predictions, plotted on the same grid is shown in Figure 2-24. This is for the same grid shown in Figure 2-23.

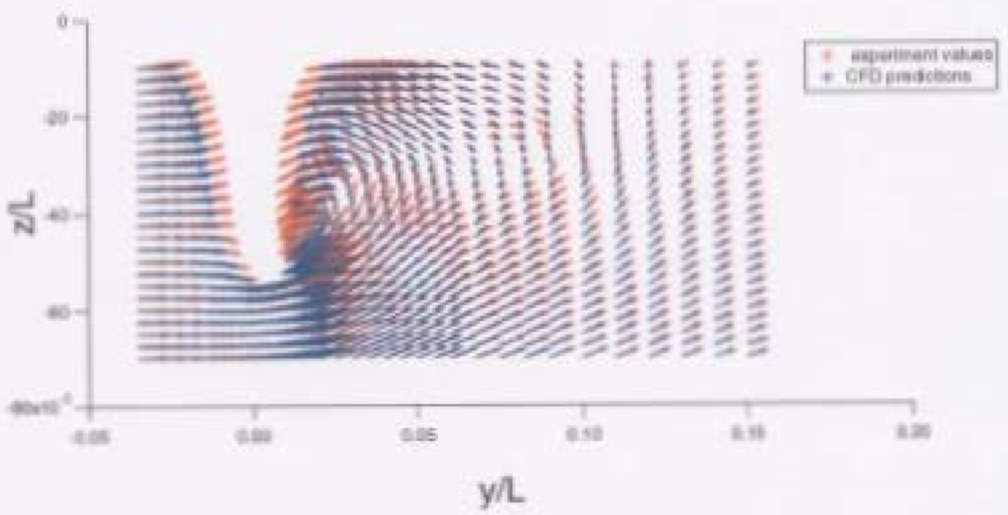

Figure 2-24, Comparison of in-plane vectors on common grid

An effective graphical method of presenting the error within the plane of the measurement was to subtract these two vectors.

$$\overline{V_{error}} = \overline{V_{expt}} - \overline{V_{cfd}}$$

This can then be graphed over the comparison grid. When the difference between these vectors was small, the CFD prediction was a good match to the experiment results, and when the difference was large, the CFD results were a poor fit. An example is shown in Figure 2-25.

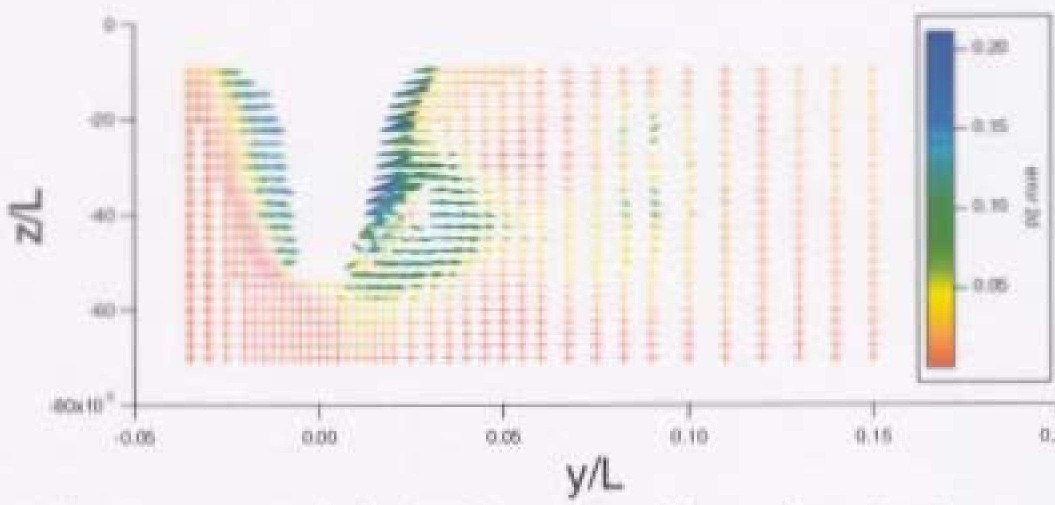

Figure 2-25, Error vectors for in-plane flow, coloured by two-dimensional error magnitude

The errors in magnitude and direction are both shown in this figure. The length of the arrow gives the magnitude of the error, with a small arrow corresponding to a small magnitude. If the arrow is pointing horizontally, from left to right, then there is an error in magnitude but no error in direction. As the arrow rotates away from this position, it indicates an increasing error in direction. Colour is used to put a numerical scale on the value of the magnitude of the error. Figure 2-25 shows that the largest errors occur very close to the hull surface and within the vortex on the downstream side of the hull.

The following parameters were also used as part of the numerical evaluation of the difference between the experiment values and the CFD predictions

$$Error_u = u_{\mathrm{expt}} - u_{cfd}$$
$$Error_v = v_{\mathrm{expt}} - v_{cfd}$$
$$Error_w = w_{\mathrm{expt}} - w_{cfd}$$

These parameters gave information on any bias in the flow components between the experiments and the CFD predictions. If the error was negative, then the CFD prediction was over estimating the flow speed, and if it was positive, it was under estimating. The numerical values of the mean, the standard deviation, the minimum and maximum of these components gave additional insight into the level of the match. A perfect match would have all four values as zero. This is not likely, and so the actual values of these parameters can be used to compare the different results. The better match between experiments and CFD predictions for two different grids would have the smallest mean, the smallest standard deviation, the highest minimum value and the lowest maximum value of the error components. A histogram of the velocity components can also help in interpreting the results. A histogram of the distribution of the error in the u velocity component is given in Figure 2-26.

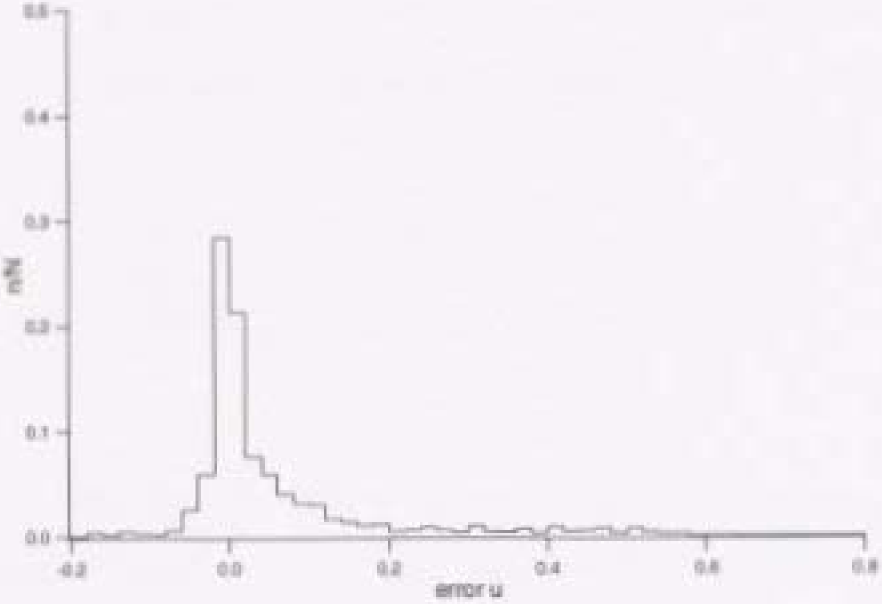

Figure 2-26, Histogram of error in u velocity component

Also, plotting the grid values, coloured by the error in each velocity component, can show the distribution of the error in a single velocity component over the comparison mesh. An example of this for the through-plane velocity is shown in Figure 2-27.

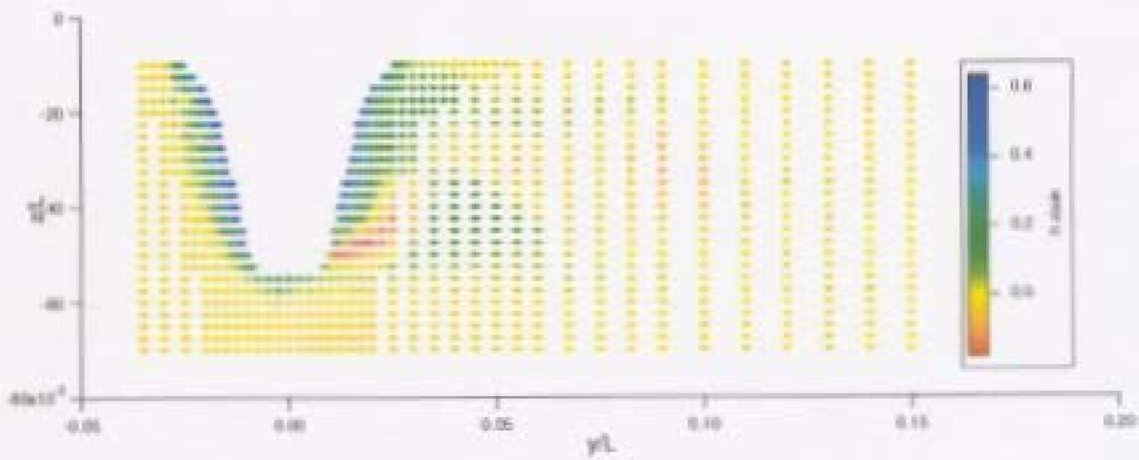

Figure 2-27, Spatial distribution of error in through-plane velocity

Two additional values were calculated as indications of the magnitude of the error between the experiment results and the CFD predictions.

$$Error_{2D} = \sqrt{Error_v^2 + Error_w^2}$$

$$Error_{3D} = \sqrt{Error_u^2 + Error_v^2 + Error_w^2}$$

These were found to be useful in comparing the magnitude of the error in the combined velocity components, which was not available from the individual velocity components. For example, using $Error_{2D}$ to colour the presentation of the error vector results puts a numerical scale on the magnitude of the error and enhanced the presentation of the results. Also, histograms of these parameters were found to be helpful in comparing the results from different meshes. An example of a histogram of the error of the in-flow velocity components ($Error_{2D}$) is given in Figure 2-28. The numerical values obtained from the comparisons can be presented in a table, such as Table 2-6.

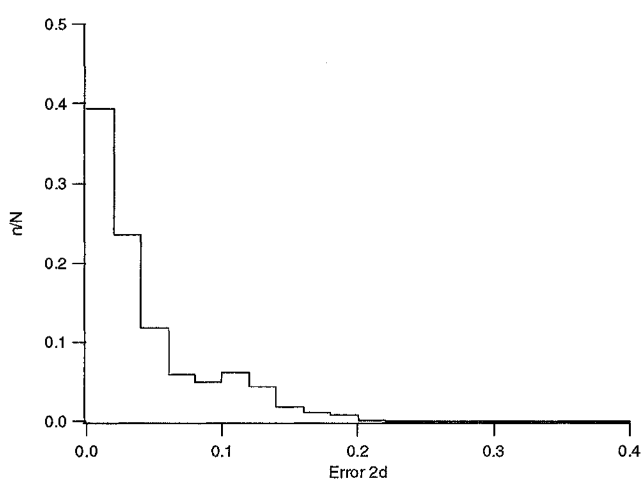

Figure 2-28, Histogram of error for in-plane velocity ($Error_{2d}$)

Table 2-6, Example of numerical values used for error analysis

Hexahedral mesh Section at 90%L					
	Average	Standard Deviation	Minimum	Maximum	Range
In-plane velocities					
$Error_v$ (transverse component)	0.005	0.052	-0.187	0.149	0.336
$Error_w$ (vertical component)	-0.001	0.033	-0.162	0.127	0.289
$Error_{2D}$	0.044	0.043	0.001	0.211	0.210
Through plane velocity					
$Error_u$ (longitudinal component)	0.056	0.127	-0.175	0.638	0.812
$Error_{3D}$	0.091	0.122	0.004	0.655	0.650

The numerical analysis and visualization of the error between the experimental values and the CFD predictions was carried out using *Igor* (Wavemetrics Inc., 2005). This is a general-purpose computer program for data analysis and presentation.

The method presented was based on comparing measured and predicted three-dimensional velocity components at a common plane within the fluid. This type of planar arrangement of the experiment data is typical of several types of experiments. PIV measurements naturally lead to this approach, where the measurement window within the fluid is a plane created by the laser sheet. LDV measurements are typically carried out in one plane, which has some relevance to the geometry of the problem. Pitot tube measurements, such as those used for wake surveys of ship models are also carried out in a similar way, although there is no need to limit measurements to points in a plane. The comparison method could be expanded to a volume comparison, but it would need several closely spaced planes of experiment data in order to make the comparison meaningful. It was assumed that if the planes were well separated (where small changes in the flow at one plane would have negligible changes in the flow at the downstream planes), then it was more meaningful to keep the comparisons to the separate planes.

2.5 ANALYSIS OF CFD PREDICTIONS USING TETRAHEDRAL AND HEXAHEDRAL MESHES FOR SERIES 60 HULL WITH YAW ANGLES OF 10 DEGREES AND 35 DEGREES

2.5.1 Yaw angle 10 degrees

The forces from the CFD predictions are compared with the measured values, expressed as non-dimensional coefficients, in Table 2-7. The force coefficients were defined as

$$Ct = \frac{F_x}{0.5\rho A V^2} \qquad Cs = \frac{F_y}{0.5\rho A V^2} \qquad Cst = \sqrt{Cs^2 + Ct^2}$$

where F_x is the force component along the centreline of the hull (positive towards the stern), F_y is the force component normal to the centreline of the hull (positive to starboard), A is the wetted surface area of the hull, ρ is the density of the fluid, and V is the speed of the flow.

On the basis of force predictions alone, the tetrahedral mesh is the most accurate, and the total force given by the CFD prediction is within 5 percent of the value measured in the experiments. The hexahedral mesh has a force prediction within 14 percent of the value measured in the experiments.

Table 2-7, Summary of Forces from CFD predictions and model experiments, yaw angle 10 degrees

Mesh	Number of Iterations	*Fx, N*	*Fy, N*	$Ct*10^{-3}$	$Cs*10^{-3}$	$Cst*10^{-3}$
CFD, Tetrahedral	176	4.508	13.56	$7.471*10^{-3}$	$22.474*10^{-3}$	$23.683*10^{-3}$
CFD, Hexahedral	116	3.404	15.18	$5.642*10^{-3}$	$25.152*10^{-3}$	$25.777*10^{-3}$
Model experiments				$5.35*10^{-3}$	$22.0*10^{-3}$	$22.641*10^{-3}$

The evaluation method described above was used to compare the flow patterns predicted by the CFD simulations from the two different meshes against the results of the experiments. For the yaw angle of 10 degrees, the sections used for the comparison were 20% *L*, 60% *L* and 90% *L*. A preliminary analysis was carried out using the complete experiment grid as the basis for comparison. This analysis showed that at all sections on the upstream side of the hull, far from the model, the agreement between the CFD predictions and the experiments was very good (within 2% of the free stream flow on $Error_{2d}$). Similar agreement was found on the far downstream side of the model at sections of 20% *L and* 60% *L*. As a result the width of the experiment grid was reduced, so that areas far upstream and downstream, where the agreement was within 2% were not considered, and the comparison was based on a reduced experiment grid focusing on flow close to the hull.

The in-plane error vectors and the through plane error for the three sections are shown in Figures 2-29 to 2-34, and summarized in Table 2-8.

At 20% *L*, the largest errors in predictions of in-plane flow for both meshes are seen around the core of the vortex, located at approximately *y/L* of 0.03 and *z/L* of -0.06.

Outside of this region, the largest errors in the hexahedral mesh are close to the hull on both sides. This region is within the boundary layer measured in the experiments. Comparing the numerical values from Table 2-8, shows that the mean in-plane error magnitude is almost the same for both meshes, but the tetrahedral mesh has a slightly smaller standard deviation than the hexahedral mesh for the in-plane flow components. The hexahedral mesh has a lower error when the through plane flow components are introduced.

At 60% *L*, the largest errors are again observed around the vortex on the downstream bilge radius. The hexahedral mesh predicts the flow better in the very localized region between the vortex core and the hull but the overall average values of the in-plane error for the two meshes are almost identical, although the hexahedral mesh has a lower standard deviation. When the through-plane flow is considered, the tetrahedral mesh is more accurate than the hexahedral mesh.

At 90% *L*, the evaluation of the two meshes, based on the comparison of the two CFD predictions against the experiments is more complex. The hexahedral mesh shows a better agreement with the experiment results than the tetrahedral mesh for the in-plane flow vectors, especially on the downstream side of the hull close to the waterline. For the two-dimensional comparison, the mean, standard deviation and range are all lower for the hexahedral mesh than for the tetrahedral mesh. Based on a subjective comparison of the through plane contours of velocity (Figure 2-15 for the tetrahedral mesh and Figure 2-18 for the hexahedral mesh) it looks as though the hexahedral mesh is a better predictor of the flow, since the contours on the downstream side look more like those observed in the experiments. Numerically however, when the whole comparison region was considered, the mean error in the tetrahedral mesh was lower. The only factor that is better for the hexahedral mesh was that the range, between the maximum and minimum error was reduced.

Overall, both meshes give average in plane error magnitudes of less than 5% of the free stream velocity, with the exception of the tetrahedral mesh at *x/L* of 0.9, where the value is less than 7%. Maximum error magnitudes for the in-plane components are between 21% and 32.5% of the free stream values, and these typically occur around the vortex core, or close to the hull, within the boundary layer for the model experiments.

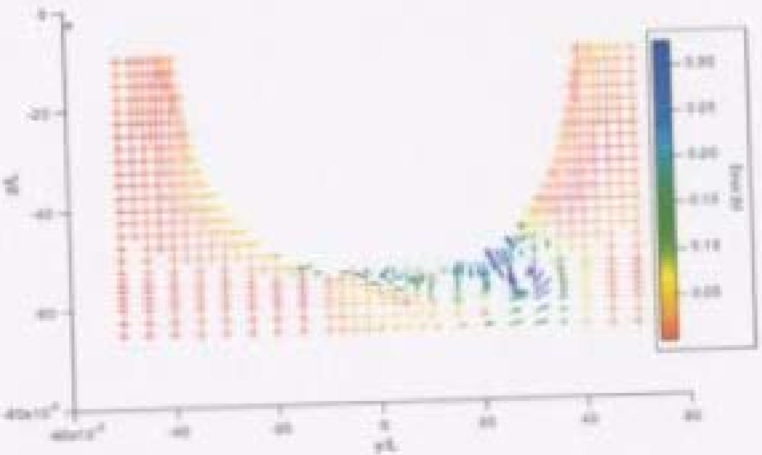

a) In-plane error

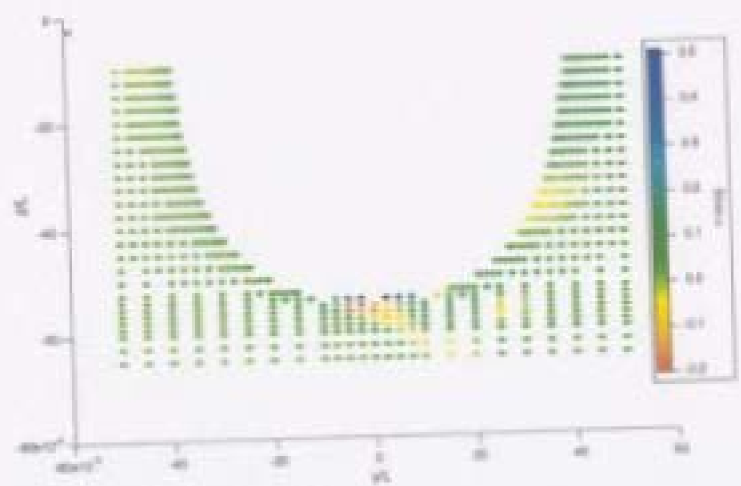

b) Through plane error
Figure 2-29, Error map, section at 20%L, Tetrahedral mesh

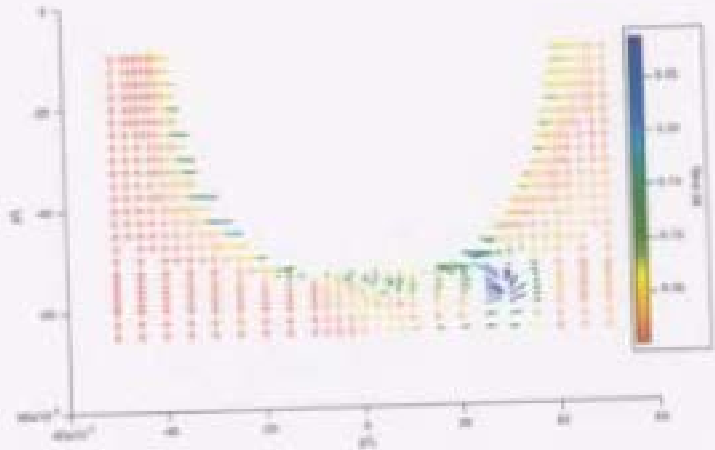

a) In-plane error

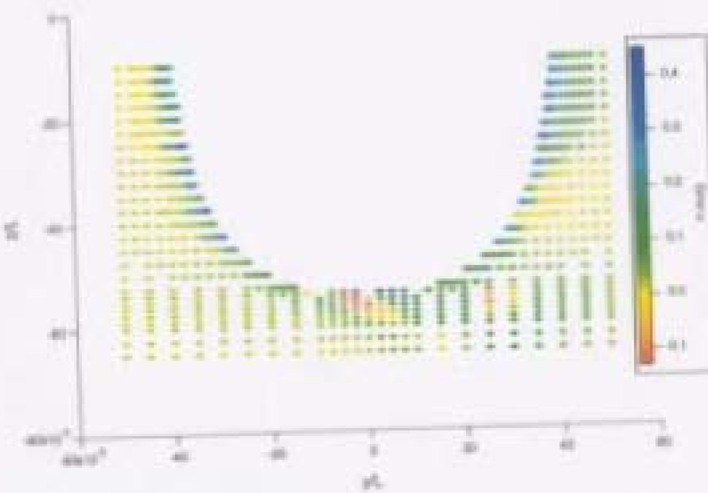

b) Through plane error
Figure 2-30, Error map, section at 20%L, Hexahedral mesh

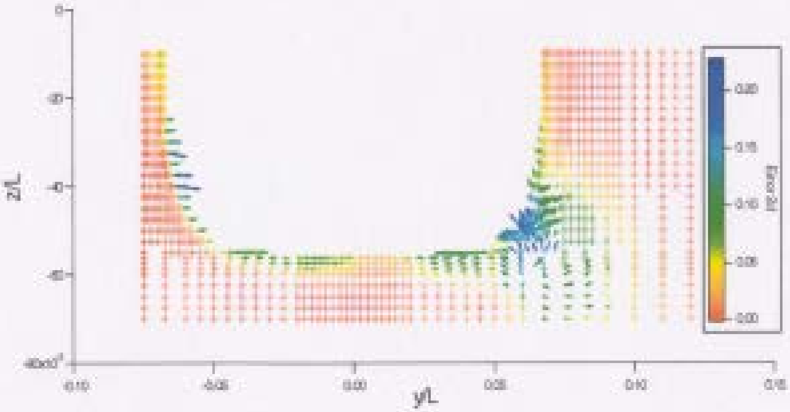

a) In-plane error

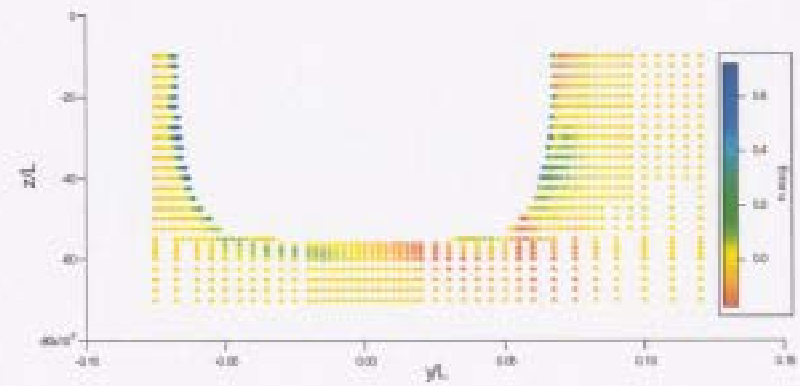

b) Through plane error
Figure 2-31, Error map, section at 60%L, Tetrahedral mesh

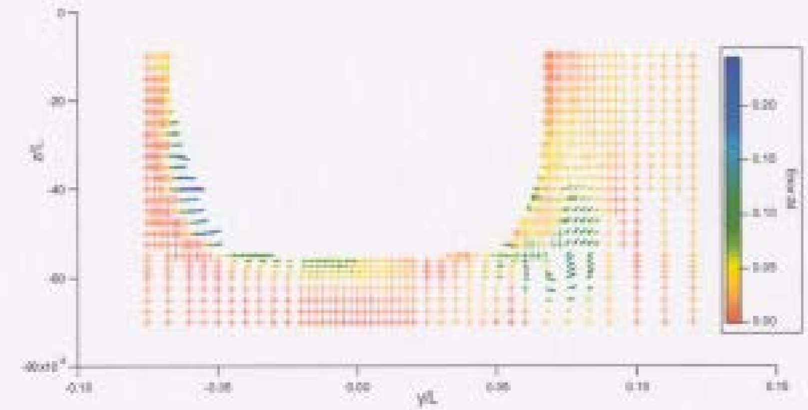

a) In-plane error

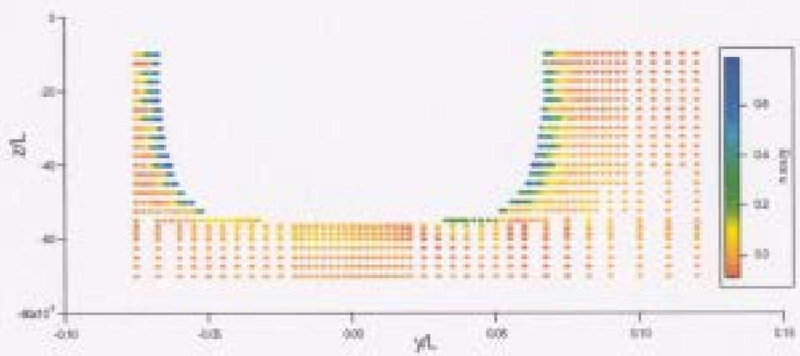

b) Through plane error
Figure 2-32, Error map, section at 60%L, Hexahedral mesh

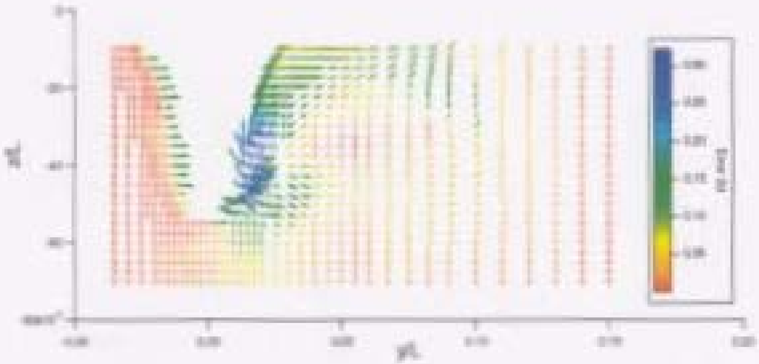

a) In-plane error

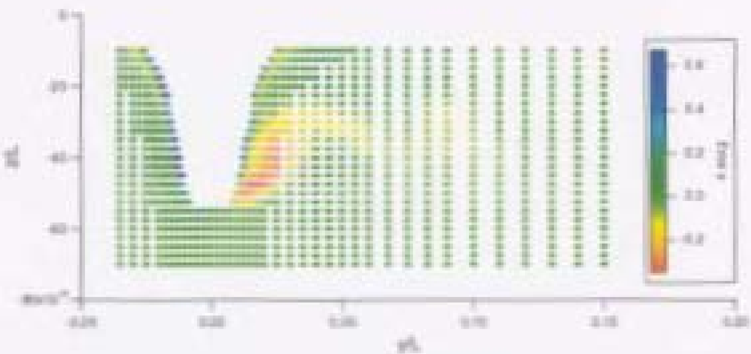

b) Through plane error
Figure 2-33, Error map, section at 90%*L*, Tetrahedral mesh

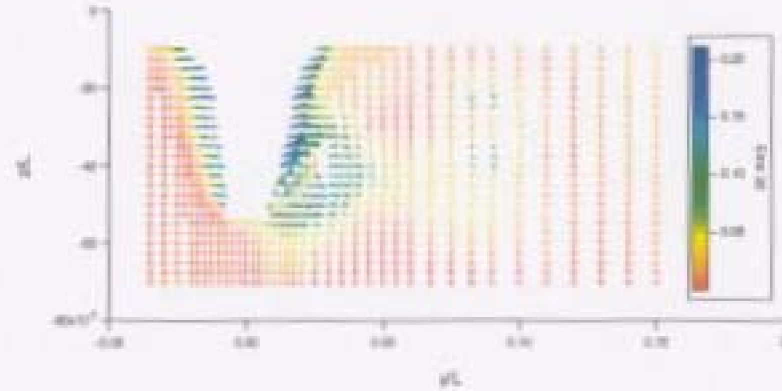

a) In-plane error

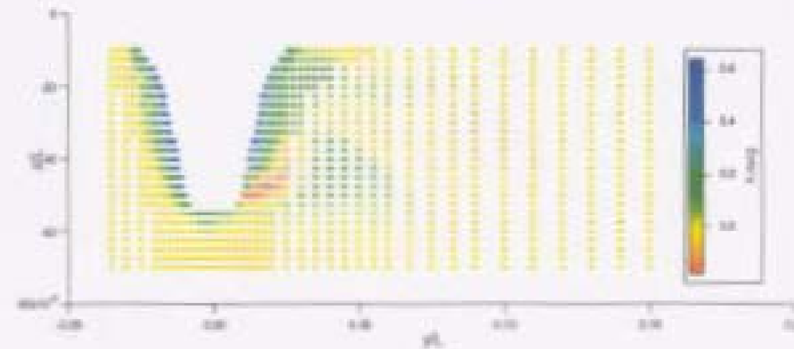

b) Through plane error
Figure 2-34, Error map, section at 90%*L*, Hexahedral mesh

Table 2-8, Comparison data for tetrahedral and hexahedral meshes, Series 60 C_B=0.6 at 10 degrees of yaw

Tetrahedral mesh
Section at 20%L

	Average	Standard Deviation	Minimum	Maximum	Range
In-plane					
$Error_v$ (transverse component)	0.003	0.051	-0.277	0.206	0.483
$Error_w$ (vertical component)	-0.009	0.046	-0.243	0.285	0.528
$Error_{2d}$	0.050	0.048	0.002	0.287	0.285
Through plane					
$Error_u$ (longitudinal component)	0.066	0.091	-0.129	0.451	0.580
$Error_{3d}$	0.093	0.094	0.007	0.495	0.487

Tetrahedral mesh
Section at 60%L

	Average	Standard Deviation	Minimum	Maximum	Range
In-plane					
$Error_v$ (transverse component)	-0.010	0.038	-0.140	0.136	0.276
$Error_w$ (vertical component)	-0.005	0.039	-0.182	0.102	0.284
$Error_{2d}$	0.038	0.041	0.001	0.227	0.227
Through plane					
$Error_u$ (longitudinal component)	0.025	0.106	-0.164	0.718	0.881
$Error_{3d}$	0.074	0.098	0.002	0.753	0.751

Tetrahedral mesh
Section at 90%L

	Average	Standard Deviation	Minimum	Maximum	Range
In-plane					
$Error_v$ (transverse component)	-0.007	0.057	-0.177	0.148	0.324
$Error_w$ (vertical component)	-0.024	0.071	-0.317	0.082	0.400
$Error_{2d}$	0.069	0.064	0.002	0.320	0.318
Through plane					
$Error_u$ (longitudinal component)	0.006	0.113	-0.341	0.670	1.011
$Error_{3d}$	0.102	0.106	0.006	0.683	0.677

Hexahedral mesh
Section at 20%L

	Average	Standard Deviation	Minimum	Maximum	Range
In-plane					
$Error_v$ (transverse component)	-0.008	0.057	-0.301	0.170	0.471
$Error_w$ (vertical component)	-0.011	0.047	-0.272	0.293	0.565
$Error_{2d}$	0.047	0.058	0.001	0.325	0.323
Through plane					
$Error_u$ (longitudinal component)	0.033	0.055	-0.199	0.509	0.708
$Error_{3d}$	0.069	0.070	0.006	0.521	0.515

Hexahedral mesh
Section at 60%L

	Average	Standard Deviation	Minimum	Maximum	Range
In-plane					
$Error_v$ (transverse component)	0.012	0.032	-0.083	0.192	0.275
$Error_w$ (vertical component)	0.007	0.034	-0.194	0.134	0.328
$Error_{2d}$	0.039	0.029	0.000	0.244	0.244
Through plane					
$Error_u$ (longitudinal component)	0.090	0.173	-0.082	0.785	0.866
$Error_{3d}$	0.123	0.160	0.004	0.822	0.818

Hexahedral mesh
Section at 90%L

	Average	Standard Deviation	Minimum	Maximum	Range
In-plane					
$Error_v$ (transverse component)	0.005	0.052	-0.187	0.149	0.336
$Error_w$ (vertical component)	-0.001	0.033	-0.162	0.127	0.289
$Error_{2d}$	0.044	0.043	0.001	0.211	0.210
Through plane					
$Error_u$ (longitudinal component)	0.056	0.127	-0.175	0.638	0.812
$Error_{3d}$	0.091	0.122	0.004	0.655	0.650

2.5.2 Yaw Angle 35 degrees

The forces resulting from the CFD predictions are compared in Table 2-9. No measured force data was available for this yaw angle. In this condition there was a very large difference in the predicted forces, but since there were no experiment values to compare with the predictions, there is no indication of which method is the most accurate.

Table 2-9, Summary of Forces from CFD predictions, yaw angle 35 degrees

Mesh	Number of Iterations	*Fx, N*	*Fy, N*	*Ct*	$Cs*10^{-3}$	$Cst*10^{-3}$
CFD, Tetrahedral	190	-3.665	-71.29	$6.074*10^{-3}$	$118.2*10^{-3}$	$118.4*10^{-3}$
CFD, Hexahedral	176	-2.660	-100.6	$4.409*10^{-3}$	$166.7*10^{-3}$	$166.8*10^{-3}$

At 35 degrees of yaw, flow patterns were measured at two sections, over a smaller region of flow. These sections were at *x/L* of 0.5 and 0.9. The only change to the experiment grid to make it into the comparison grid was to remove the points that were inside or very close to the surface of the hull. Also, since only in-plane vectors were measured in the experiments, the comparison with the CFD predictions was limited to the in-plane flow values only. The comparisons of the experiment results and CFD predictions are shown in Figures 2-35 to 2-38 and Table 2-10.

Overall, the CFD predictions for the yaw angle of 35 degrees show more error, when compared to the experiment values than for 10-degree yaw case. At 35 degrees, the average error magnitude was between 10 and 25% of the free stream velocity, with maximum error being as high as 65%. At *x/L* of 0.5, this larger error was mostly created by the inability of either CFD mesh to match the shape of the vortex measured in the experiments. The measured vortex was approximately circular, but in each case the predicted vortex was elongated in the y/L direction, relative to the z/L direction. At the aft section, both meshes do a better job of predicting the direction of the flow, although the magnitude of the error is still relatively high, compared to the values for a yaw angle of 10 degrees.

Based on the average error values, the flow at the aft section was predicted more accurately by both meshes than the mid section, but the maximum error was higher at the aft section. At x/L=0.5, the hexahedral mesh was slightly more accurate, than the tetrahedral mesh, but at the aft section, the situation was reversed.

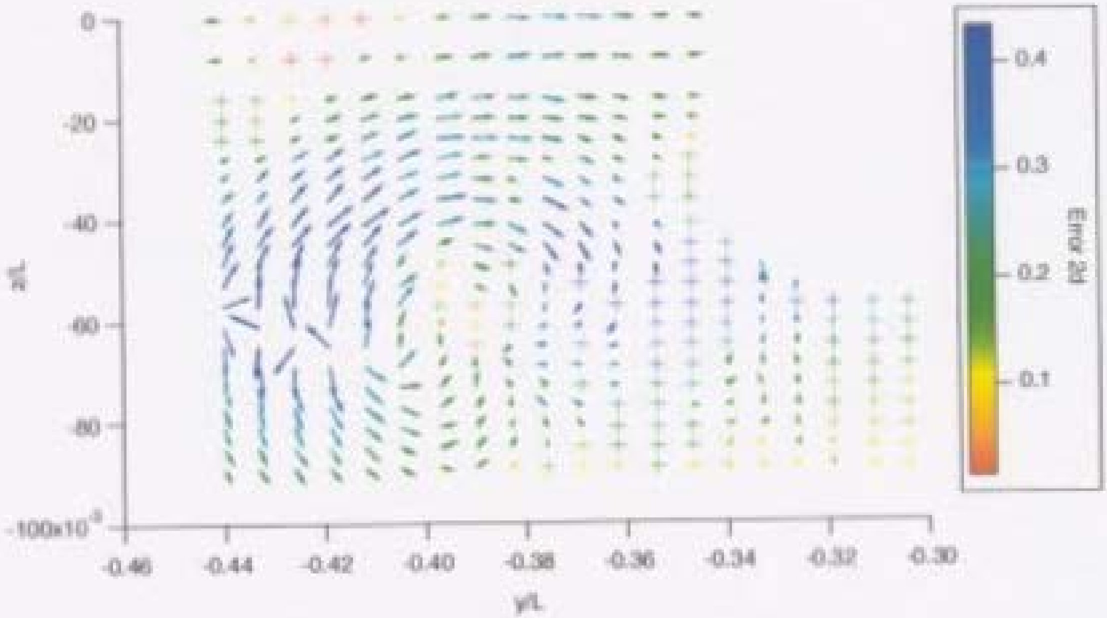

Figure 2-35, Section at 50%L, Tetrahedral mesh, in-plane error

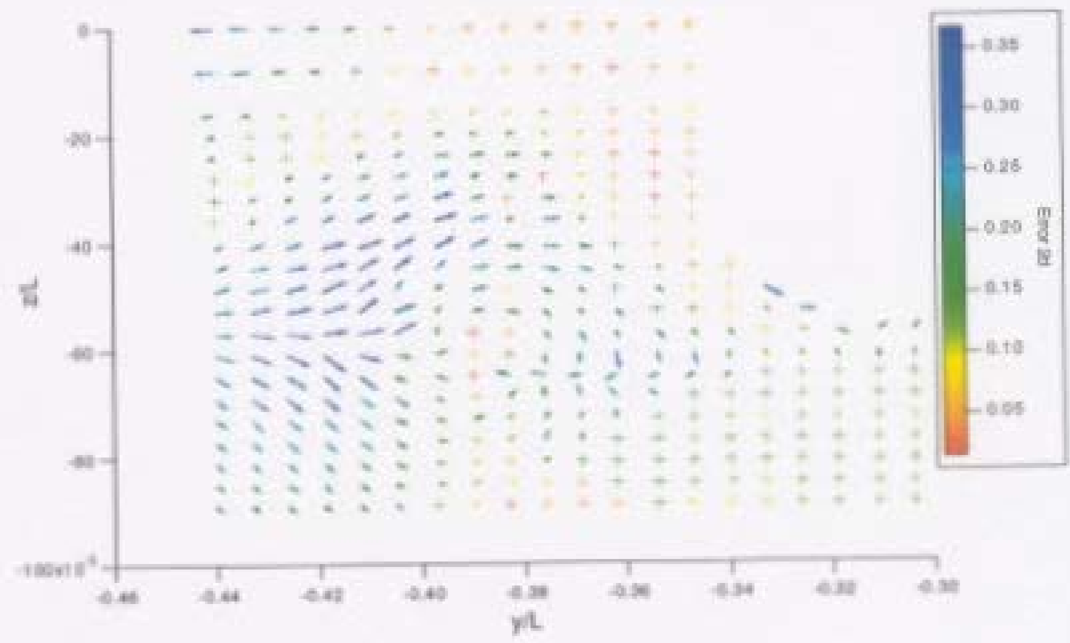

Figure 2-36, Section at 50%L, Hexahedral mesh, in-plane error

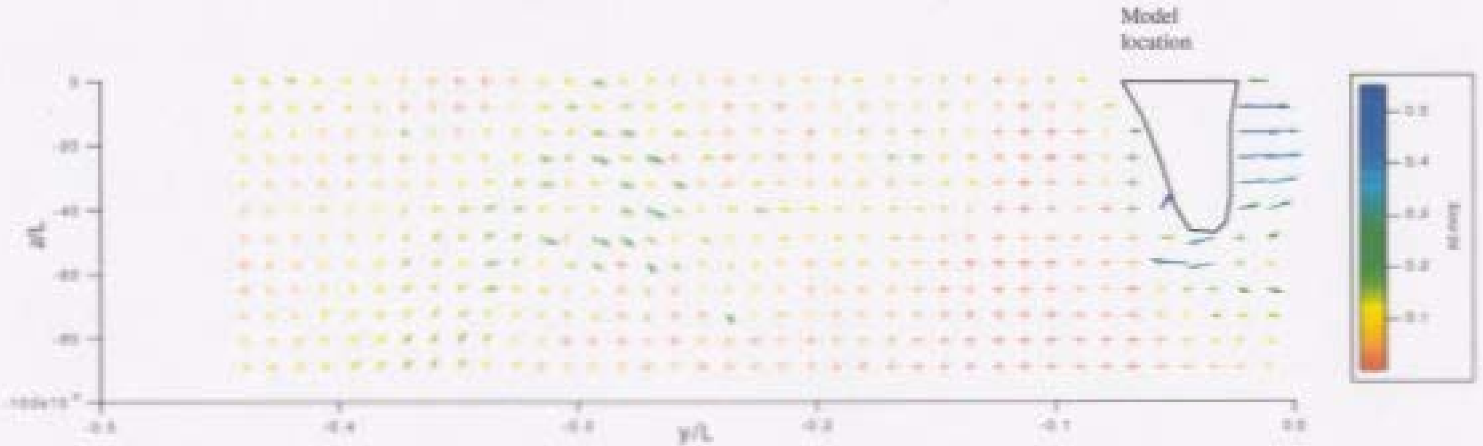

Figure 2-37, Section at 90%*L*, Tetrahedral mesh, in-plane error

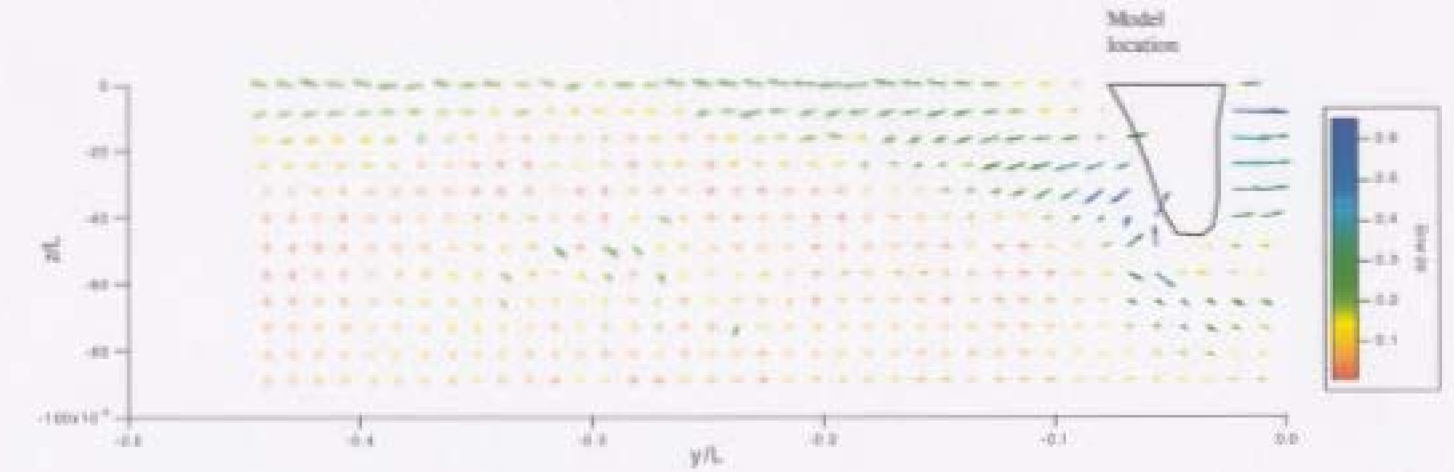

Figure 2-38, Section at 90%*L*, Hexahedral mesh, in-plane error

Table 2-10, Comparison data for tetrahedral and hexahedral meshes, Series 60 C_B=0.6 at 35 degrees of yaw

Tetrahedral mesh
Section at 50%L

	Average	Standard Deviation	Minimum	Maximum	Range
In-plane					
$Error_v$ (transverse component)	0.091	0.118	-0.210	0.336	0.546
$Error_w$ (vertical component)	0.013	0.209	-0.386	0.388	0.774
$Error_{2d}$	0.241	0.088	0.163	0.432	0.269

Hexahedral mesh
Section at 50%L

	Average	Standard Deviation	Minimum	Maximum	Range
In-plane					
$Error_v$ (transverse component)	0.053	0.096	-0.288	0.292	0.580
$Error_w$ (vertical component)	0.049	0.135	-0.265	0.305	0.570
$Error_{2d}$	0.164	0.077	0.016	0.366	0.351

Tetrahedral mesh
Section at 90%L

	Average	Standard Deviation	Minimum	Maximum	Range
In-plane					
$Error_v$ (transverse component)	0.036	0.088	-0.229	0.537	0.765
$Error_w$ (vertical component)	0.026	0.073	-0.169	0.513	0.682
$Error_{2d}$	0.102	0.069	0.004	0.548	0.544

Hexahedral mesh
Section at 90%L

	Average	Standard Deviation	Minimum	Maximum	Range
In-plane					
$Error_v$ (transverse component)	-0.023	0.138	-0.407	0.628	1.036
$Error_w$ (vertical component)	0.037	0.093	-0.199	0.617	0.816
$Error_{2d}$	0.142	0.096	0.010	0.647	0.637

2.5.3 Improvements to CFD Mesh

The main focus of this research described in the Chapter was to investigate the effect of two different meshing strategies on the resulting forces and flow patterns for a hull with a yaw angle. This required the development and testing of numerical techniques for comparing the resulting flow patterns against the results of experiments. Generating the meshes was a necessary step in learning the details of the mesh generation program and the CFD solver but the objective of this research was not to develop fully accurate CFD predictions of flow around a Series 60 hull. Provided that the flow patterns were generally in agreement with the observed values, and that the meshes were at the point where further refinement had little effect on forces or flow patterns, then the results were considered adequate for the purposes of the comparison. A more rigorous approach would be to use the analysis methods developed here to evaluate systematically varied mesh geometries, where the effect of the number of elements and the proximity of the boundary to the ship was studied in detail.

Some refinements to the mesh may improve the accuracy of the results. Both the tetrahedral and hexahedral meshes were symmetrical about the ship centreline. Although it was not reported here, the zero yaw angle case was part of the initial study. The same mesh was used for yaw angles of zero, 10 degrees and 35 degrees. The flow direction was varied by changing the vector direction at the domain boundary rather than rotating the hull within the domain. This resulted in the grid being fixed in relation to the geometry of the hull and not the flow conditions. One possible refinement would be to make the mesh asymmetric, so that the mesh was finer on the downstream side of the hull and in the region of the vortex generated under the hull. A further improvement would be to make the boundaries of the mesh the same as the physical boundaries of the experiment facility. Finally, using more elements at the hull surface would refine the hexahedral mesh.

For the 10 degree yaw angle case, the velocity measurements stopped below the free surface (z/L=-0.1) and for the 35 degree yaw angle, there was no free surface, so measured flow patterns close to the free surface were not available. Omitting the free surface will have some effect on the predicted forces and flow patterns, even at Froude numbers of 0.2 or lower. Extending the CFD predictions to include the free surface and comparing the results for the case at zero Froude number is the most obvious recommendation.

2.6 CONCLUSIONS

An evaluation method, based on numerical and graphical methods, has been developed that allowed comparisons to be made between experimental measurements of fluid velocity and predictions of the same flow conditions made using CFD. The method required the definition of an area over which the evaluation was to be made, and a grid of comparison points within this area. The user must decide on the most appropriate measurement area and grid pattern. Both of these choices will be specific for the flow patterns being studied.

Experiment values and CFD predictions were interpolated on these common grid points and numerical and graphical comparisons of the flow vectors were made. The most accurate prediction will have the smallest values for the mean error between experiments and predictions, small magnitudes for the error between the vectors and a small standard deviation of the individual velocity components. The graphical presentation shows the error in magnitude and direction between the predicted and measured vectors. The accuracy of the CFD predictions over the complete comparison area can be seen and related to the geometry of the object or key features within the flow, such as a vortex or a boundary layer.

Two CFD meshes were created for the Series 60 C_B=0.6 hull, one using tetrahedral elements and one using hexahedral elements. On the basis of the numerical evaluation of the flow patterns no mesh had a consistent advantage over the other for all flow conditions, if the hull was at an angle of attack to the flow. Both meshes gave more accurate predictions of flow patterns for a yaw angle of 10 degrees than for 35 degrees. If the predicted forces were included in the comparison, then at 10 degrees of yaw, the tetrahedral mesh was the most accurate. At 35 degrees yaw, the comparison can only be based on the flow patterns, and there was no clear evidence of one method being superior to the other.

Other factors, such as the time and level of skill required to create the mesh and the computational time required to come to a solution within the set tolerances can be considered in evaluating the mesh strategy. The tetrahedral mesh required a lower level of skill to create than the hexahedral mesh, although it took longer to solve a single iteration within the solution. The number of elements for the tetrahedral mesh was more than four times that of the hexahedral mesh, which was the biggest factor in determining the solution time. Even with the higher number of elements a solution for a single yaw angle and flow speed combination could be obtained overnight from the tetrahedral mesh using a PC workstation[1].

Based on the Series 60 hull form, for a yaw angle of 10 degrees or higher, the tetrahedral mesh was a viable strategy for meshing CFD solutions, if predicting the resulting forces and flow pattern was the primary objective. Flow patterns predicted with this mesh were just as accurate as the more commonly used hexahedral mesh. The Series 60 hull form is not designed for operation at high yaw angles so some of its design features may result in exaggerated flow conditions, and the conclusions obtained from this Chapter should be checked against a hull form expected to operate in 'off design' conditions. An escort tug was selected as a typical example of a hull expected to operate at a high yaw angle.

A review of the literature found there was published force data for the typical range of operating speeds and yaw angles for an escort tug (Hutchison et al. (1993), Allan et al. (2000), Allan and Molyneux (2004)), but there was no measured flow data available. An important step in the research was to obtain flow measurements around an escort tug hull, which could be used to compare with CFD predictions. The commissioning of a PIV system to obtain these measurements is described in Chapter 3 and the results of the experiments are given in Chapter 4.

[1] 2.80 GHz processor with 2.00 GB RAM

CHAPTER 3

DESCRIPTION OF THE STEREOSCOPIC PARTICLE IMAGE VELOCIMETRY SYSTEM USED BY MEMORIAL UNIVERSITY OF NEWFOUNDLAND

3.1 INTRODUCTION

Particle Image Velocimetry (PIV) is an important technique for measuring velocities within a fluid. The flow through an illuminated plane (or volume) is seeded with small, reflective particles and a sequence of digital photographs is taken. By timing the intervals between photographs to ensure that the same particles are within the measurement space for each exposure, flow vectors can be calculated, once the measurement space has been calibrated. To calculate the velocity vectors, the total image is divided into smaller interrogation windows. The average particle movement within each interrogation window between two successive exposures is calculated. Velocity is determined by dividing the distance moved by the time interval between exposures. In its simplest form, the technique is applied in two dimensions using a single camera, but by using stereo photography, it can be extended to three dimensions. The main advantage of PIV over other measurement methods is that it can determine fluid velocity at all locations within the measurement plane simultaneously instead of having to make separate measurements at a series of different point locations. This is an important feature for analyzing unsteady flow.

The fundamental assumption in PIV analysis is that the calculated flow vectors follow a linear path based on the average seed particle displacement within a small area of the fluid. If there is a high degree of curvature to the flow, relative to the size of the interrogation window, the calculated particle traces will not match the real flow conditions. The PIV method will have difficulty in producing accurate results when there are large variations in the flow speed across the measurement area. In this situation, it is hard to determine the optimum time interval between the exposures. PIV analysis will be most accurate when using small interrogation windows and will be inaccurate for flow conditions where circulation occurs within an interrogation window.

The PIV system at Memorial University of Newfoundland was manufactured by LaVision GmbH of Goettingen, Germany and was purchased from LaVision Inc. of Ypsilanti, MI, USA. The system consisted of four main elements:

- Two Charge Coupled Device (CCD) cameras
- Twin-head Nd:YAG[1] laser and controller
- Computer for timing of laser and cameras and data acquisition

A photograph of the complete system, assembled in air, is shown in Figure 3-1.

[1] Neodium doped:Yttrium Aluminium Garnet

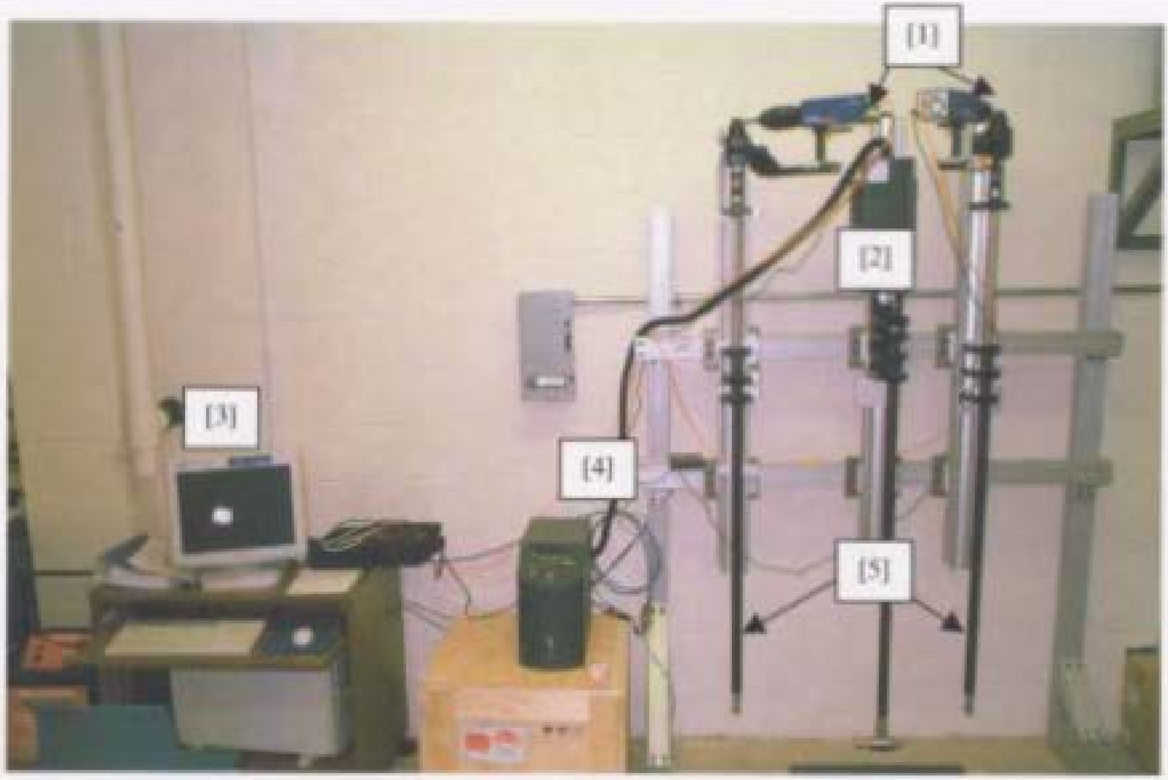

Figure 3-1, PIV System, view of complete system showing CCD cameras [1], laser head [2], computer [3], laser controller [4] and borescopes [5].

This PIV system was designed for the unique requirements of a ship model towing tank, where the operating fluid was water with a free surface. The unique features of this PIV system were the two borescopes. The cameras were mounted in air at the top of a borescope, which provided the capability for obtaining the underwater views. The advantage of this arrangement was that delicate cameras were kept well above the water surface, removing the need for expensive watertight housings. A similar arrangement was provided for the laser, but this was a plain tube, without the optics of a borescope.

There was some initial concern that the small aperture of the borescopes and the lenses inside the borescopes would result in the loss of too much laser energy and as a result photographs of the particles would be too dark. This was found not to be the case, provided that the underwater optics were cleaned daily.

Detailed descriptions of the component parts and analysis methods are given below (LaVision, 2005), together with a discussion on factors within the experiment and analysis procedures that affect the uncertainty of the results. Xu et al (2005) gave an overview description of the PIV system together with the results of some preliminary experiments.

3.2 SYSTEM COMPONENTS

3.2.1 Laser and Light Sheet Optics

The laser system used was a Solo 120 model supplied by New Wave Inc. This system consisted of a pair of Nd:YAG lasers with maximum energy output of 120 mJ/pulse and a maximum pulse repetition rate of 15 Hz. The pulsed laser beams were directed downwards through a stainless steel tube to a waterproof housing containing the light sheet optics. The light sheet optics consisted of a 45 degree mirror to turn the beam from vertical to horizontal and a fixed focal length cylindrical lens which controlled the divergence angle of the light sheet (lenses for 15° and 22.5° divergence angles were available). A second 45° mirror could be used to change the direction of the laser beam. With the second mirror removed, the laser shone directly out of the rear of the optical housing. With the second mirror in place, the beam was turned normal to the housing. Rotating the complete unit changed the direction of the beam.

At the top of the tube were two telescopic lenses with infinitely adjustable focal lengths (between 400 mm and 2500 mm in water). These lenses were used to adjust the diameter of the laser beam, which in turn affected the thickness of the light sheet. These lenses were adjusted with the system assembled. The downstream side of the light sheet housing and connecting tube was fitted with a faired trailing edge to minimize wake turbulence.

3.2.2 Charged Couple Device Camera & Borescopes

Two identical Imager Intense™ cameras were used in the PIV system. Each camera had an adapter so that it could be used with standard Nikon C-mount or F-mount lenses. Specifications for the cameras are given in Table 3-1.

There was serial data transfer between the camera and the PCI-Interface-Board. A Programmable Time Unit (PTU) controlled the triggering of the camera and the synchronization with the laser. The exposure time of the camera, the laser power, and the interval between the two laser pulses were also adjusted by the PTU.

Table 3-1, Imager Intense Camera System Specification

Parameter	**Specification**
Resolution (pixels)	1376*1040
Dynamic Range, Digitization	12 bits
Cooling	2-stage thermo electric
Quantum Efficiency	65% at 500 nm
Readout noise	4e
Readout Rate	16 MHz
Data Rate (Vector Fields/sec)	5Hz
Capture Sequence Capacity to RAM	2GB
Capture Sequence Duration to RAM	34 sec
Camera Interface	High Speed Serial, PCI bus

The borescopes used in conjunction with the cameras were 1.9 m long. The collection cone angle of each borescope with no other optical devices was 35° (in air). At the lower end of each borescope was a prism, with a nominal collection angle of 20° (in air). In water the collection angle was reduced to 16° in width and 12° in height. The nominal viewing angle of each prism was normal to the borescope body but it could be changed within +/- 15° by adjusting the angle of the prism. Each borescope was fitted with a tapered fairing to minimize wake. Rotating the borescope about its centerline set the viewing direction.

3.2.3 Optimum Arrangement of CCD Cameras and Laser Light Sheet

The arrangement of the PIV system with the least optical distortion will occur when the cameras are symmetrical about the light sheet as shown in Figure 3-1 since this arrangement has the same distortion for the field of view of each camera. It is also relatively easy to maximize the overlap of the field of view for each camera to ensure the largest possible measurement space.

The optimum arrangement cannot always be obtained in practice. An alternative arrangement would be to have the two cameras located on the same side of the light sheet. In this case, the field of view common to both cameras can be maximized, but the distortion is no longer symmetrical, and so spatial resolution is compromised slightly.

In two-dimensional PIV systems, the laser light sheet should be aligned with the strongest flow component and the camera image plane should be parallel to the light sheet. In practice this cannot always be achieved and the camera may be at some angle to the light sheet. In this situation the depth of field becomes reduced, and only the centre of the image will be in focus.

This can be corrected by satisfying the Scheimpflug criterion, which requires the object plane, the lens and the image plane to intersect on a common axis. In practice, the lens rotates relative to the image plane. The result is a constant depth of field over the complete image, but the image has increased perspective distortion. The Memorial PIV system cannot use the Scheimpflug criterion, because the lenses are directly fitted to the ends of the borescopes and rotating the lenses in this situation is not practical.

3.2.4 Calibration.

Image distortion correction is an essential part of stereo PIV analysis because the image plane of the two cameras will always be at an angle to the object plane. In order to correct for the distortion between the two images a calibration procedure must be carried out. For stereoscopic PIV this requires two planes, parallel to each other and a known distance apart, with marks at known locations on a grid that covers the complete field of view of each camera.

3D-PIV measurements require two different viewing angles of the same measurement space. The projected images of the 2-dimensional vectors on each plane are combined to give 3-dimensional vectors. Since the arrangement of both cameras is fixed it is possible to calculate three velocity components from the two projections, by calibrating the measurement space against a matrix of points with known spacing in three dimensions.

The mapping function used for image distortion correction in the DaVis FlowMaster software (LaVision 2005) is a third order two-dimensional polynomial function to map x_1 and y_1 in pixel coordinates within the image plane for camera one (including distortion) to corrected coordinates x and y in the object plane without distortion. The mapping function (for camera one at one z location) is of the form:

$$\begin{pmatrix} x_1 \\ y_1 \end{pmatrix} = \vec{f}\begin{pmatrix} x \\ y \end{pmatrix} = \begin{pmatrix} x + dx_1(x,y) \\ y + dy_1(x,y) \end{pmatrix}$$

With the normalized coordinates

$$s = \frac{2(x - x_0)}{nx}$$

$$t = \frac{2(y - y_0)}{ny}$$

defined by image size nx, ny (in pixels) with the origin (x_0, y_0) at the midpoint of the image. The values of dx_1 and dy_1 are given by

$$\begin{pmatrix} dx_1 \\ dy_1 \end{pmatrix} = \begin{pmatrix} a_0 + a_1 s + a_2 s^2 + a_3 s^3 + a_4 t + a_5 t^2 + a_6 t^3 + a_7 st + a_8 s^2 t + a_9 st^2 \\ b_0 + b_1 s + b_2 s^2 + b_3 s^3 + b_4 t + b_5 t^2 + b_6 t^3 + b_7 st + b_8 s^2 t + b_9 st^2 \end{pmatrix}$$

An additional set of coefficients can be obtained for camera one at the second z location and two sets of coefficients for camera two at the same two z locations as camera one, for a total of four mapping functions. The calculation of the mapping functions requires at least 40 common grid points being visible in both camera images. For stereo PIV, the image distortion correction is applied to the particle images for each camera. The two-dimensional vectors are calculated for each camera plane, using the correlation function and then finally the three-dimensional vectors are calculated.

The mapping functions are determined empirically using stereo images of a specially manufactured plate. The plate was machined so that each face is stepped with two parallel planes. Each plane has a matrix of white markers, evenly spaced at 22.5 mm. The thickness of the plate is 9mm and the step between the rows of dots on the plate is 2 mm. The advantage of this approach is that two parallel planes are accurately defined relative to each other. It is critically important that the calibration plate is located within the laser sheet and parallel to it, even though the calibration is carried out using visible light. Any rotation between the laser and the calibration plate will reduce the accuracy, since the vectors will be calculated in the reference frame of the calibration plate, not the frame of the light sheet.

For evaluation of the accuracy of the mapping function, the DaVis software calculates the size of the average deviation between the calculated position of the marks and the actual positions. The software manual (LaVision GmbH, 2005) states that a good calibration is considered to have an average error in the mapping function of less than 0.5 pixels and recommends that experiments should not be carried out if the average deviation is more than 2.0 pixels. The dialogue box also gives the dimensions of the 3-D image (in pixels), a chi squared statistic for the x and y directions, the number of marks used for calculating the mapping function and the average peak ratio (intensity) of the marks. The size of the image common to both cameras is greatest when the reference point is at the same pixel coordinate in both views, and the cameras are symmetrically located about the image plane.

3.2.5 Data Collection and Image Processing

Data collection and image processing can be carried out with DaVis 7.1 software, supplied by LaVision Inc (LaVision 2005). This is a comprehensive software package that allows the user to manage all the optical aspects of carrying out a PIV experiment and analyzing the results.

Camera exposure times, the time between laser pulses and the number of frames used by the cameras can all be set by the user, depending on the nature of the experiment. For stereo images, four exposures are required to produce results. The four views are one from each camera at time t and one from each camera at $t+\delta t$. A series of frames can be taken, which depended on the nature of the experiment.

The basis data product from each CCD camera is a pair of images of particles within the flow, separated by a time interval, δt. Each image represents a 2-dimensional projection of the seed particles within the illuminated plane. The first step is to analyze each image pair in the image plane of the camera. The total CCD image is divided into square interrogation windows (i.e. 128 x 128 pixels). A cross-correlation procedure is carried out to determine the correlation between pixel images in the first frame and the second frame.

The correlation function for one camera is of the form:

$$C(dx,dy) = \sum_{x=0,y=0}^{x<n,y<n} I_1(x,y)I_2(x+dx,y+dy), \frac{-n}{2} < dx,dy < \frac{n}{2}$$

I_1 and I_2 are the image intensities (grey scale) of the first and second interrogation windows, and the 2-dimensional array C gives the correlation strength for all integer pixel displacements (dx, dy) between the two interrogation windows. The size of the window is n x n pixels. This is also usually the size of the correlation plane, so that the maximum displacement calculated is $\pm n/2$. If a single pass analysis procedure is used, the interrogation windows have the same pixel coordinates in each frame.

The peak of the correlation function gives the most likely mean value of particle movement within the interrogation window (dx,dy). The position of the correlation peak can be identified to sub-pixel accuracy and the expected accuracy is between 0.1 and 0.5 pixels (LaVision GmbH, 2005). Individual peaks are determined from a three point Gaussian function. The actual resolution depends on the image quality, which is influenced by particle size, particle density and contrast. The correlation procedure is repeated for each interrogation window and for each camera, resulting in two sets of vectors (Vx_1, Vy_1) for camera 1 and (Vx_2, Vy_2) for camera 2.

Particles are excluded from the calculation if they flow out of the measurement space of either camera during the time interval δt. The particles can move out of the in-plane interrogation window, or if the flow is three-dimensional, they can flow out through the plane of the light sheet. The value of δt to minimize the loss of seed particles from within the laser sheet depends on the local flow velocity components for the experiment and must be adjusted accordingly. The reliability of vector calculations will be increased considerably by aligning the laser so that the weakest flow component is through the plane of the laser.

The required vector is (*Vx, Vy, Vz*) relative to the plane of the light sheet. The set of equations determined from the two cameras is over specified in that there are four variables available to solve for three unknown quantities. This feature can be used to improve the accuracy of the PIV measurement by providing an additional check on vector accuracy. The linear equation system is solved by the normal equation and the remaindered degree of freedom error should be small (<3 pixels), which provides a criterion for removing spurious vectors.

The size of the interrogation window must be decided a priori or by trial and error. If trial and error is used, the interrogation window sizes used in the analysis are reduced until there is no significant change in the calculated flow patterns.

The basic image analysis procedure described above can be refined to increase the signal to noise ratio. Initially, the division of the pixel image of the seed particles into interrogation windows was based on the geometry of the window and not the flow pattern. Particles close to the downstream edge of an interrogation window at the first exposure may have moved out of that window in the second exposure, and new particles will have flowed in. As a result, the number of particles common to both views is reduced.

Using one of the following techniques can increase the number of particles included in the analysis:

- Overlap windows: The second interrogation window includes an overlap with neighbouring windows, based on a fixed fraction of the original grid.
- Adaptive Multiple passes
    - Fixed window size: Uses vectors calculated in first iteration to move the second interrogation window off the initial grid.
    - Reduced window size: For the second iteration, the window size is half the initial size, and the shift relative to the original window is calculated based on the mean vector calculated in the first pass.

The origin for starting the analysis of the PIV images is the top left-hand corner of the CCD image. If a fixed window size is used, there may be parts of the image that are not processed (bottom and right side) if the full image dimension is not an integer number of interrogation windows.

Once the flow vectors have been computed for an equidistant grid, further processing can be carried out to improve the quality of the image by removing spurious vectors. These include:

1. Allowable vector range

The calculated vectors are filtered on the basis of allowable ranges (in pixel or m/s). The range is specified based on a mean value, with upper and lower limits (which are the same).

2. Peak ratio

The peak ratio factor Q, compares the magnitudes of the highest peak in the correlation coefficient matrix relative to the noise and the second highest peak relative to the noise, based on the function

$$Q = \frac{P_1 - \min}{P_2 - \min}$$

where P_1 is the highest value in the correlation matrix, P_2 is the second highest peak, and min is the lowest value. For Q=1.5 or higher, the main peak is well defined and probably represents a valid vector. Peak ratios close to 1.0 most likely represent invalid vectors and should be removed.

3. Median filter

In this case, the analysis is based on a three by three grid of interrogation windows, and the vector in the centre square is compared to the values in the other eight squares. The centre vector is rejected if it is outside the range given by the median vector of the eight neighbours, plus or minus a deviation based on a multiple of the RMS of the neighbouring vectors. Another criterion for filtering includes removing the vector if there are less than a set number of neighbouring cells with calculated vectors.

In some cases, the background to the particle image may not be a constant intensity. This is most likely to occur in regions of the image close to the solid boundary of a model, where the laser light is reflected. To improve particle images in these situations, a filter, similar to a high pass filter, can be used. The aim is to make the background more uniform and increase the contrast between the particles and the background. To obtain this condition, a scale parameter is used, which must be at least twice the mean particle diameter in pixels. An alternative is to subtract a constant value. The disadvantage of this technique is that some information is being removed from the image, and the user must be sure that the information being removed is less important than the information being retained.

Once the most suitable analysis procedure has been developed for a particular experiment, based on a single frame using interactive methods, the image processing and vector analysis can then be carried out for all frames in a sequence using batch processing. For steady flows, sets of vectors can be combined to provide an average vector map over a period of time.

The results can be visualized in a variety of ways. Particle images and calculated vectors can be viewed as movies, so that particle movement and calculated vectors can be inspected. Vector maps of the flow can be plotted, and summary statistics of the images (particles or vectors) can be calculated.

3.2.6 Effect of Seeding on Accuracy of PIV Measurements

Successful seeding of the flow is a key factor in obtaining reliable results from PIV experiments. The seed particles should be neutrally buoyant in the test fluid, so that there are no velocity components occurring due to gravity or buoyancy forces. Also, the particles should be small in relation to the flow patterns, so that the particles follow the local movement of the fluid, not the motion due to average fluid forces acting on the particle.

It is desirable to have particle diameters viewed at the CCD between two and three pixels. The DaVis software uses a three-point Gaussian peak approximation on the measured intensities to identify the centre of a seed particle to sub-pixel accuracy. If the image size is less than one pixel, there is a tendency for the calculated vectors to be integer numbers of pixels and resolution of the vector field is compromised.

The accuracy of the vector calculation within a given interrogation window increases with the number of particle image pairs included in the correlation calculation. In practice three or four particle image pairs in each interrogation window are sufficient for accurate definition of the correlation peak. Increasing seed density allows the size of the interrogation window to be reduced, with the result that the spatial resolution of the flow can be increased. The upper limit of seeding concentration is that there must be a clear contrast between particles and the background

The final factor to consider in determining the accuracy of PIV measurements is the number of images of the same nominal flow condition. The accuracy of steady flow conditions can be improved if the vectors are based on the average value from multiple image pairs. The number of frames used to determine this will depend on factors such as the degree of spatial resolution required and the length of time available for the experiment.

3.3 PREVIOUS APPROACHES TO ESTIMATING UNCERTAINTY IN STEREOSCOPIC PIV EXPERIMENTS

Uncertainty in stereoscopic PIV systems has been discussed in the literature, but the focus has been on the accuracy of the mapping function and the vector reconstruction. The theoretical errors in the vector reconstruction from stereo images have been determined (Lawson and Wu, 1997a). The uncertainty in translational systems (with no Scheimpflug correction) and rotational systems (with Scheimpflug correction) were determined. The focus of the analysis was on determining the relative error between the in-plane vectors (x, y) and the through plane vectors (z) and results were presented in the form of an error ratio, rather than an absolute value. The objective was to determine the arrangement of the PIV system with the minimum uncertainty in the z direction, relative to the x-y plane.

To carry out this analysis Lawson and Wu (1997a) assumed that the uncertainty in the vectors determined at the object plane (x, y, z) was represented by an RMS value and that this value was equal in each direction. Then, by considering the geometry (distances between cameras and viewing angles) and the magnification of the PIV system, the error ratio (uncertainty) based on the geometric reconstruction was calculated. The error ratio was mapped over the complete object plane.

Lawson and Wu's analysis showed that at the centre of the lens, the two systems produced very similar ratios, but as the distance off the centre was increased, the error ratios for the rotational system were up to 40% lower than the for the translational system. This analysis did not consider any errors due to distortion correction.

The same authors carried out an uncertainty analysis of a complete stereoscopic PIV system in another paper (Lawson and Wu (1997b)). This was an experimental approach to uncertainty analysis, starting with determination of the 3-D mapping function, using a calibration plate. A test PIV specimen was constructed by suspending seed particles in epoxy resin. The advantage of this approach was that it used real seed particles, but fixed them relative to each other. When the block was moved all particles were moved a constant distance and the resulting vectors calculated by the PIV software should be constant across the whole field of view for each camera. The test specimens were illuminated using laser light, and images collected. The specimen was then moved known distances (δx, δy, δz) and the distances calculated by the PIV system were compared to the known distances. Different viewing angles between 10 and 45 degrees were evaluated, but the cameras were always on the same side of the light sheet, and at the same viewing angle relative to the light sheet.

Lawson and Wu (1997b) concluded that optimum performance will be obtained by using viewing angles between 20 and 30 degrees for camera *f* numbers of *f*16 and higher. The uncertainty analysis for uniform flow gives RMS errors of 1-2% for the in-plane flows and 3-4% for the through plane flow. These values were for cases where particle movement was restricted to between 15% and 30% of the interrogation window dimension. Below this displacement range, the system did not have enough resolution.

Other researchers have used variations on the basic approach taken by Lawson and Wu. Soloff et al (1997) investigated the robustness of a 3-dimensional mapping function for stereoscopic PIV analysis. They used an aluminium calibration plate with a 9 by 9 grid of holes, 0.5mm diameter at 27mm intervals. The plate was lit from behind. The calibration procedure was to take images of the plate at three z locations of 0, +/-0.5 +/-0.005mm. This gave rms errors in the mapping function of 1.1 pixels for camera 1 and 1.2 pixels for camera 2. This translated to 0.045mm and 0.051 mm respectively.

After the calibration, images of the plate were taken with each camera, and then the plate was moved small but known distances in y and z directions, and images of the plate at the new location were taken. Cross correlation was used to analyze the image pairs from each camera. The two-dimensional vector fields for each camera were filtered and then stereoscopically combined to obtain the three-dimensional vectors (x, y, z) calculated from the PIV software.

The errors between the calculated vectors and the known movement of the calibration plate (in each direction) were plotted as contours of error against the x and y coordinates for the measurement space. The results were contours of error, spatially distributed over the measurement area.

The estimated error (based on the highest contour shown, which looks to be about 95% of all measurements) for each axis was

x	+/-0.0050 mm
y	+/-0.0036 mm
z	+/-0.0200 mm

Resulting errors were not evenly distributed over the measurement space, and it would have been useful to see an overall statistical distribution of the errors. The error in the results was the same order of magnitude as the error calculated from the mapping function for each camera during the calibration, so in this case the mapping function is the primary source of the error.

Calcagno et al. (2002) discussed the uncertainty of a stereoscopic PIV system designed to measure flow in the wake of a model propeller behind a ship. The facility used for conducting these experiments was a cavitation tunnel. An underwater camera was aligned directly behind model to measure flow in the plane of the propeller. The second camera, mounted outside the cavitation tunnel had a viewing angle between 36 and 40 degrees off the centreline of the model.

For the camera looking directly at the in-plane vectors, the mapping function had an estimated particle resolution within 0.1 pixels (4 cm/s for the flow conditions considered). This view was treated as a two dimensional view, with minimal distortion. Error in the through plane measurements was thought to come from the stereo reconstruction (mapping function). This was analyzed using a target consisting of a 'typical' PIV image, which was moved a known distance (1mm) along the normal axis. The calculated uncertainties were under 2.5% in the 'in-plane' displacements and under 3% in the through plane displacements. The authors discuss the fact that the errors may be optimistic, since they were obtained from a bench test, without the model or the rotating propeller.

3.4 UNCERTAINTY ESTIMATES FOR MEMORIAL UNIVERSITY'S PIV SYSTEM

A detailed uncertainty analysis for the PIV measurement geometry, such as the one described by Lawson and Wu (1997b) was not carried out for the PIV system. The facility schedule did not allow enough time to carry this out in situ. The uncertainty was estimated from the combination of the errors in the mapping function reported by the DaVis 7.1 software, and some special experiments to measure undisturbed flow.

Preliminary experiments to measure flow patterns around a ship model in a towing tank (Molyneux & Xu (2005)) showed that it was necessary to have a seeding system to inject the seed particles into the flow. Without a seeding system, there was insufficient particle concentration to obtain consistent measurements. One of the main concerns with this approach was the effect of the seeding system on the flow. Some experiments were designed to determine this effect, and these were combined with the uncertainty analysis.

The PIV measurements to study the flow patterns created by the seeding rake were carried out in the Ice Tank of the National Research Council's Institute for Ocean Technology. The ice tank is 80 m long, 12 m wide and 3 m deep. The tank is equipped with a large towing carriage, which is fitted with an adjustable test frame. The whole frame can be adjusted vertically and the as two longitudinal beams that can be moved independently. Each beam has a measurement scale relative to the centreline of the carriage, so the exact position of the beam is known. The PIV equipment was fitted to the beam on the south side of the carriage.

A temporary frame for the PIV system was built around the test beam, using extruded aluminium sections. The laser was oriented normal to the direction of motion, so that the measurement plane was across the direction of motion for the undisturbed flow. The borescopes for the CCD cameras were mounted symmetrically, approximately 650mm either side of the laser sheet. Camera 1 was at the forward end of the carriage, and Camera 2 was at the aft end. The centre of the measurement window was approximately 950 mm away from the underwater optical unit for the laser. The PIV system is shown fitted to the towing carriage in Figure 3-2.

Figure 3-2, PIV system fitted to towing carriage

In-situ calibration of the measurement space was carried out prior to testing. A Type 30 calibration plate, supplied by LaVision GmbH, was used. The plate was 300mm by 300 mm square. The plate was suspended within the laser plane. The views from each camera were checked to ensure that the field of view was approximately the same. The calibration was carried out using visible light, following the procedures described in the DaVis 7.1 software (LaVision, 2005).

The image taken from Cameras 1 and 2 during the calibration, together with the calculated mapping functions are shown in Figures 3-3 and 3-4. The combined image, after correction for the distortion is shown in Figure 3-5. This image is the calculated view normal to the plane of the calibration plate, whereas the raw images from the cameras include the perspective distortion.

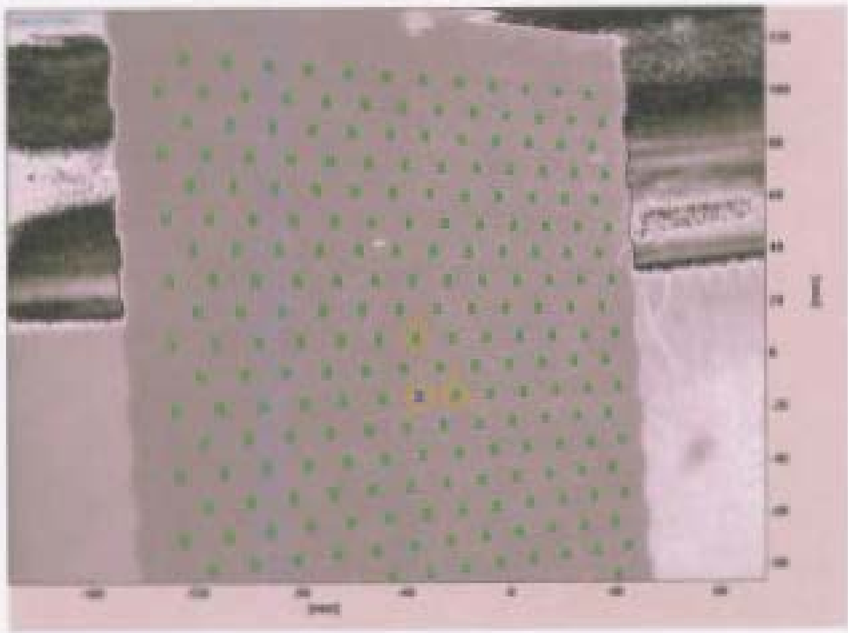

Figure 3-3, Image from Camera 1 showing points used in calculating mapping function

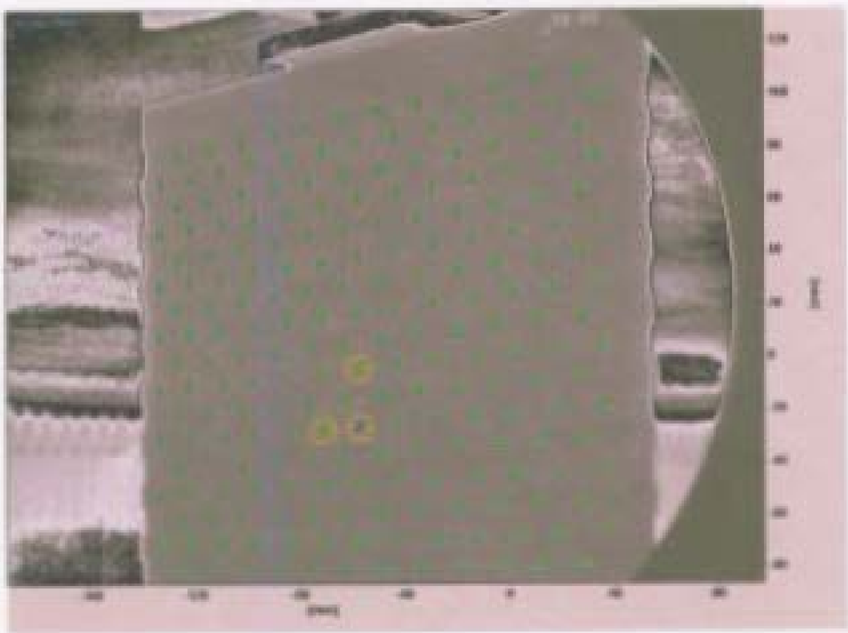

Figure 3-4, Image from Camera 2 showing points used in calculating mapping function

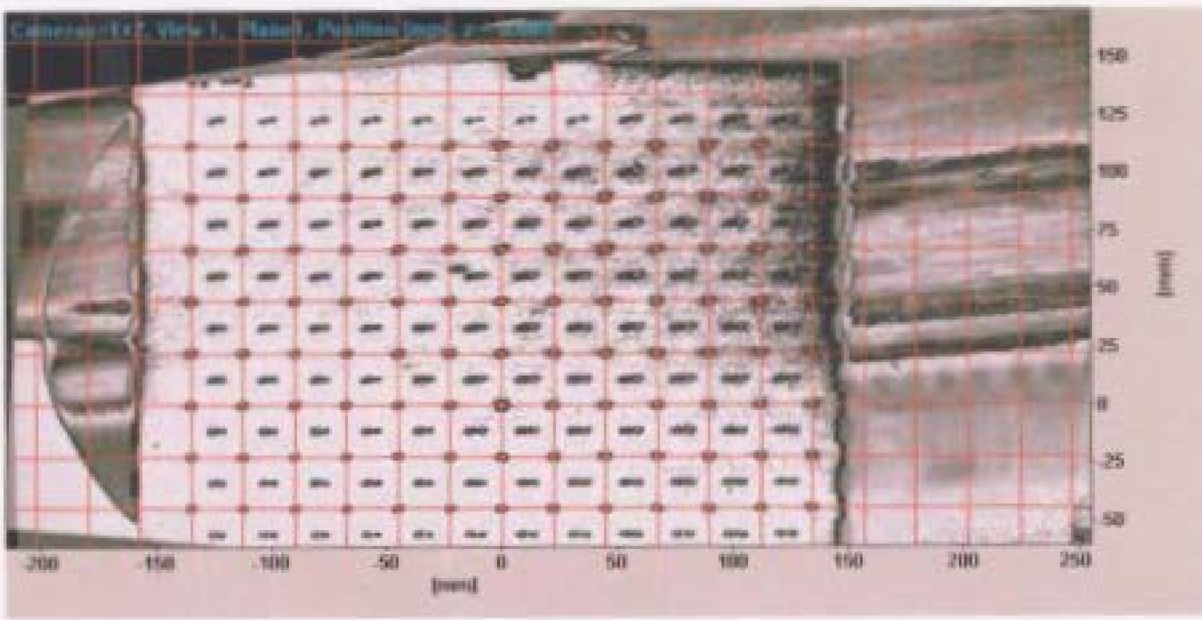

Figure 3-5, Corrected image, showing extrapolation over full image

A summary of the fit of the mapping function to the known distance between the points on the calibration plate is given in Table 3-2. The final corrected image had the dimensions given in Table 3-3.

Table 3-2, Fit to mapping functions

	Camera 1	Camera 2
RMS deviation, pixel	0.141390	0.173760

Table 3-3, Final image size, corrected image

	pixel	mm	Pixel/mm
X dimension	2250	463.811	4.851
Y dimension	1110	333.995	3.323
Average			4.087

Table 3-4, 95% Confidence Intervals for calculated speeds, based on uncertainty in mapping function

δt, microsec	δt, sec	95% CI, mm	95% CI, m/s
500	0.0005	0.083325	0.166649
700	0.0007	0.083325	0.119035
800	0.0008	0.083325	0.104156
1000	0.001	0.083325	0.083325

Assuming that the residuals in the polynomial fit to the mapping function follow a normal distribution, then the confidence intervals for the calculated speeds can be calculated for different laser timing intervals. The resulting calculations are given in Table 3-4, for the range of time intervals between first and second exposures, used in the free stream experiments.

The calculated uncertainties are relatively high compared to the published uncertainty analyses discussed above. The calculated RMS deviation of the mapping function, in pixels, is very good when compared to the previously published results (Soloff et al, 1997), which determines RMS errors to within 1 to 1.1 pixels. Soloff's results however translated into much smaller spatial errors of 0.05mm, since the measurement area was much smaller.

Smaller measurement areas are more common in previously published PIV research on ship models. A study of ship wake using PIV in a large circulating water tunnel (Di Felice and De Gregorio, 2000) used a measurement window of 18,000 mm^2. Gui et al (2001) presented wake data for a ship model using a measurement window of 5,625 mm^2.

Calcagno et al (2002) used the largest measurement area of 50,000 mm^2 for measuring the downstream wake in the race of a working propeller behind a ship model. This large window size captured all the important features of the flow in a single window. The measurement window for the MUN PIV system used in this study was 155,000 mm^2, which is over three times the size of the next largest. Test particle images showed that the average particle diameter was between 2 and 3 pixels, so data collected using the large window should not be subject to bias caused by peak locking. Since the flow conditions were expected to be unsteady, the largest possible measurement window was desirable.

Table 3-4 gives the effect of the time between the laser pulses on the uncertainty in the resulting speed measurement. When the PIV measurement plane is oriented across the flow, it is necessary to use short time intervals between the laser pulses, otherwise particles have moved through the laser sheet, and no data is obtained. With this orientation, it is necessary to accept higher uncertainty than for an orientation along the flow, where there is more possibility for variation in the timing of the pulses.

The analysis described here makes no allowance for the errors in separate velocity components. The more detailed analysis of stereo PIV carried out by other researchers suggests that the through plane measurements are generally less accurate than the in-plane measurements.

3.5 SEEDING DELIVERY SYSTEM

Seeding the flow is an essential element of PIV measurements. If the PIV system is stationary and the fluid is stationary, then it is only necessary to seed the volume of fluid close to the laser sheet. This option is feasible for a stationary PIV system in a towing tank, where the ship model passes through the measurement volume. The movement of the model ship through the seeded fluid will cause a disturbance and the movement of the seed particles can be observed. The disadvantage of this system is that very little data is obtained at a specific location on the hull, since only one set of frames is obtained for each run down the tank.

If the fluid is moving relative to the PIV system then one option is for the complete volume of the fluid to be seeded. This option is feasible for a circulating water tunnel, where particles can be kept in circulation by the moving fluid. This is not a practical option in a towing tank, which has a very large volume of stationary fluid. Eventually almost all of the seed particles will either sink to the bottom or float to the top requiring the fluid to be re-seeded after a certain period of time.

A practical alternative is to introduce particles to the flow so that seeding is present only in the measurement volume for the duration of the measurements. This should allow for a controlled use of the seeding particles, and should provide high quality PIV images, since the seeding density is correct for the volume of fluid being studied, and the parts of the flow that are of no interest to the study are ignored. The disadvantage of this approach is that the seeding delivery system may affect the momentum of the seeding particles, which will influence the results.

3.5.1 Proto-type Seeding Delivery System

Since there was very limited experience at Memorial University with seeding systems for PIV, it was decided to make the initial system as cheaply as possible, so that it would be a small expense if it had to be scrapped completely. A sketch of the initial concept is shown in Figure 3-6.

The prototype system was constructed from readily available plumbing parts and included:

- Holding tank and drain (plastic laundry tub)
- Dishwasher connectors and pipes
- Tap to control flow rate
- Seeding rake made from 22.2 mm ($^7/_8$ inches) diameter copper pipe and plumbing connectors

The system used hydrostatic pressure to deliver the seeded flow from the holding tank to the measurement volume. Adjusting the height of the holding tank, relative to the water level, controlled the static head and a tap was used to control flow rate. Water in the holding tank was taken from the local mains supply. The seeding particles were added and the mixture was stirred prior to carrying out an experiment, to keep the seeding evenly distributed.

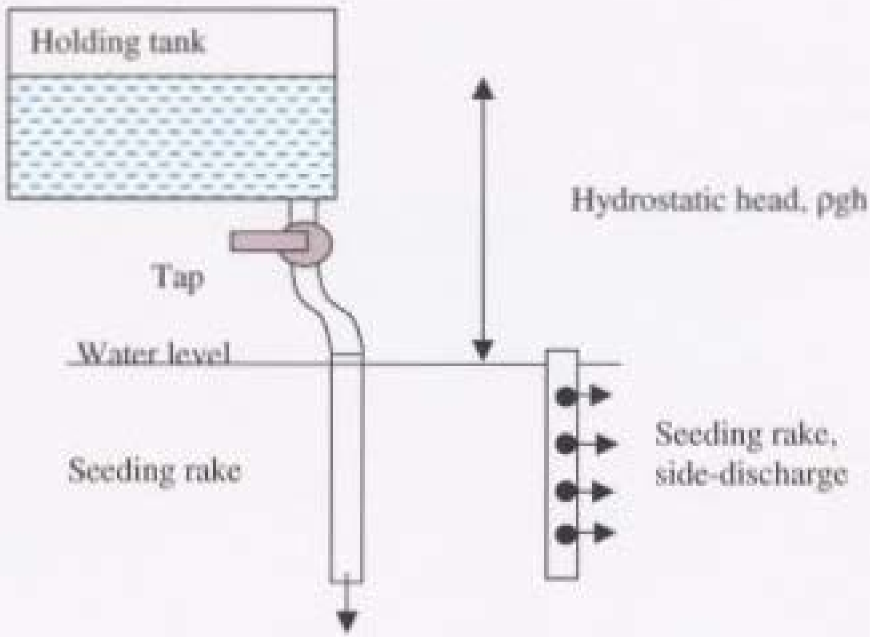

Figure 3-6, Concept sketch for seeding delivery systems

Two arrangements of discharge holes were evaluated. The end-discharge system was intended to seed the flow upstream and above the area of interest for the flow measurements, as shown in Figure 3-7a). Since the rake was nominally above the measurement area, the disturbance to the flow caused by the rake over the measurement area was minimized. The side-discharge system was also placed upstream of the required measurement area but the seeded fluid was discharged from the downstream side of the pipe, as shown in Figure 3-7b). The potential disadvantage of this approach was that the rake was close to the path of fluid entering the measurement area, and the wake of the seeding rake may effect the measurements.

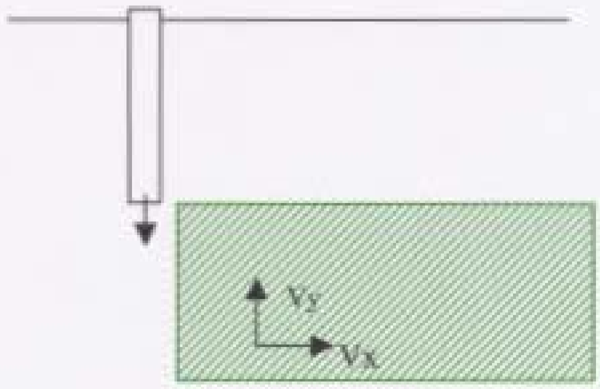

Figure 3-7a) Measurement area for end discharge rake and velocity components

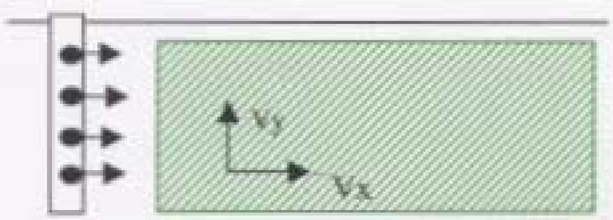

Figure 3-7b) Measurement area for side discharge rake and velocity components

Two versions of the side-discharge seeding rake were made. The first version had holes 6.35 mm ($^1/_4$ inches) diameter drilled at 41.3 mm ($1^5/_8$ inches) spacing and the second version had holes 1.58 mm ($^1/_{16}$ inches) diameter drilled at 19.1 mm ($^3/_4$ inches) spacing. The version with small holes worked well at zero velocity, but did not deliver sufficient seeding particles at the forward speeds required for ship model work (0.1m/s and above). The seeding rakes are shown in Figure 3-8.

Figure 3-8, Prototype seeding rakes (rake with large diameter holes on right)

3.5.2 Seeding Particles

The seeding particles used for all the experiments were hollow, silver coated spheres (SH400S33) supplied by Potters Industries of Valley Forge PA, USA. Preliminary experiments on different types of seeding powder (Molyneux & Xu, 2005) indicated, that although these were the most expensive in terms of unit price, the image quality and the ability of the particles to stay suspended for the longest time make them the most viable technical solution. A significant advantage of the silver coating was that it was highly reflective to laser light and the particles appeared bigger than actual size when viewed in the CCD camera. The particle specifications are given in Table 3-5 (Potters Industries, 2005).

No formal method for ensuring constant seeding concentration was developed for these experiments. The holding tank was filled to approximately the same level each time and seeding particles were added by scoops with a small spoon. Visually, the mixture was opaque and cloudy grey in colour. The analysis software was tolerant to a range of particle concentrations within the required minimum of three or four vector pairs per interrogation window and the practical maximum of sufficient contrast between particles and background. As a result, it was not critical to keep seeding concentration tightly controlled.

Table 3-5, Seeding particle specifications

Particle composition	Silver coated glass
Shape	Spherical
%Ag metal	33
Ten percentile, particle diameter, microns	8
Ninety percentile, particle diameter, microns	20
Mean particle diameter, microns	14
True density, g/cc	1.7

3.5.3 Experiments with Proto-type Seeding Delivery System

Experiments with the prototype seeding system were carried out in the Ocean Engineering Research Centre towing tank (Molyneux and Xu, 2005). The measurement plane for these preliminary experiments was to have the laser parallel to the direction of motion for the carriage, so that the strongest flow direction was in the plane of the measurement. Data was collected and analyzed using DaVis 6.2.3, which was the software originally supplied with the PIV system in January 2004. DaVis 7.1 was not available at the time the preliminary experiments were carried out.

Measurements of flow vectors for carriage speeds of 0.10, 0.30, 0.50, 0.75 and 1.00 m/s were made using the PIV system. Some experiments were carried out with particles introduced to the flow using the seeding systems described above and some were carried out using only particles left in the fluid from previous runs. When the seeding system was used, it was located upstream of the measurement area, just out of the field of view for the cameras. For the side discharge version, the rake extended across the depth of the field of view. For the end discharge version, the bottom of the rake was ahead and just above the field of view. A summary of the experiment conditions is given in Table 3-6 and calculated mean speeds over the complete vector field are given in Table 3-7. *Vx* was defined as flow parallel to the direction of motion of the towing carriage, *Vy* was the vertical flow component and *Vz* was the through plane flow, based on a right-handed coordinate system.

An effective wake fraction for the seeding system was defined as *(Vc-Vx)/Vc*, (where *Vc* was the speed of the carriage) and the calculated values for each experiment are given in Table 3-7. These results showed that the smallest wake was for Test_24, which was made with the residual seeding left in the tank from previous runs. This case showed no measurable difference between the flow speed and the carriage speed.

Table 3-6, Summary of experiments carried out in steady flow

File	δt (μs)	Seeding	Laser power	Carriage speed
Test_05	5000	Rake, side holes	50%	0.1 m/s
Test_06	3000	Rake, side holes	50%	0.3 m/s
Test_07	2000	Rake, side holes	50%	0.5 m/s
Test_08	3000	Rake, side holes	50%	0.5 m/s
Test_09	1000	Rake, side holes	50%	0.75 m/s
Test_10	1000	Rake, side holes	50%	1.00 m/s
Test_23	300	Rake, end hole	50%	0.75 m/s
Test_24	300	Residual	50%	0.75 m/s

Table 3-7, Summary of PIV flow measurements, prototype seeding system

File	Carriage Speed, m/s	Mean value calculated from PIV, m/s					
	Vc	Vx	Vy	Vz	|V|	Rms (V)	Wake fraction
Test_05	-0.1	-0.114	0.01	0.008	0.122	0.031	-0.14
Test_06	-0.3	-0.148	0.013	0.037	0.174	0.056	0.507
Test_07	-0.5	-0.244	0.015	0.064	0.299	0.01	0.512
Test_08	-0.5	-0.198	0.02	0.062	0.278	0.166	0.604
Test_09	-0.75	-0.349	0.019	0.107	0.416	0.135	0.535
Test_10	-1	-0.753	-0.008	0.664	1.194	0.471	0.247
Test_23	-0.75	-0.532	0.054	-0.046	0.563	0.082	0.291
Test_24	-0.75	-0.75	0.031	-0.223	0.84	0.184	0

In all other cases, the flow was affected by the presence of the seeding system. For the side-discharge seeding system, at the lowest speed (Test_05), the calculated velocity was within 14% of the free stream speed, but in all other cases the effective wake fraction was between 25% and 50%. There was a significant reduction in the wake between the side discharge version (Test_09) and the end discharge version (Test_23), but even the end discharge version has a significant effect on the flow.

Neither of the systems used gave consistently even particle distribution. The side discharge system resulted in periodic waves of particles across the field of view, shown in Figure 3-9, whereas the end discharge system resulted in periodic clouds of particles, shown in Figure 3-10. The periodic waves were possibly caused by vortices shed off the rake, whereas the periodic clouds were probably caused by the mixing of the jet from the rake with the undisturbed flow. The end discharge system also resulted in air bubbles appearing in the field of view, which can be seen at the top of Figure 3-10.

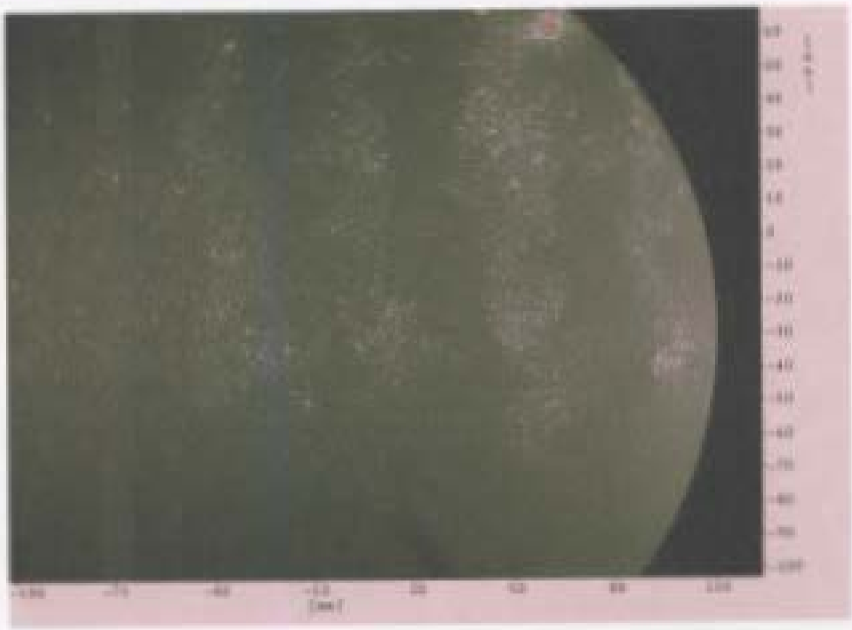

Figure 3-9, Seeding particles from side discharge rake at 0.75 m/s, showing periodic waves of particles

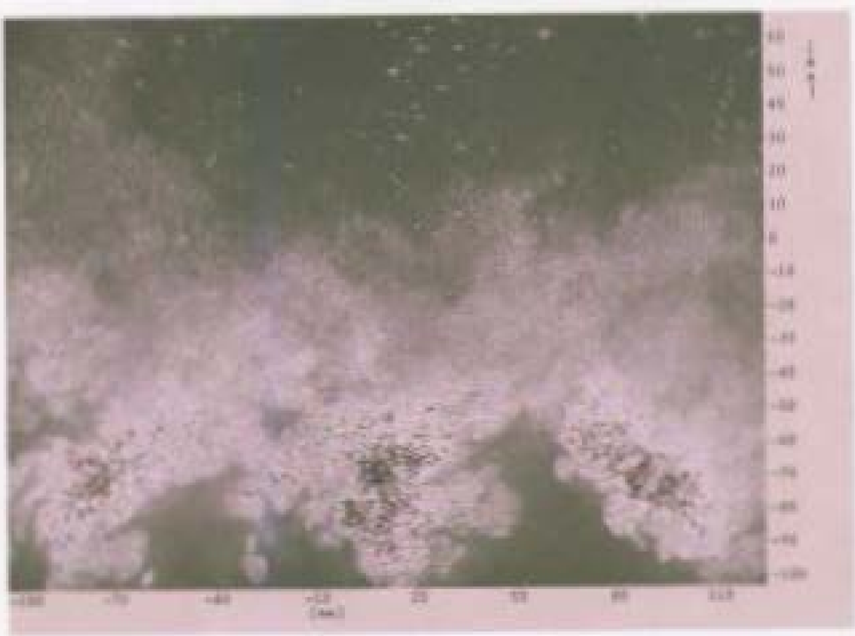

Figure 3-10, Seeding particles from end discharge rake at 0.75 m/s, showing periodic clouds of particles

3.5.4 Seeding Rake Design Improvements

The prototype seeding rake, with side discharge was used for a set of preliminary experiments to measure the flow around an escort tug with a yaw angle (Molyneux and Xu, 2005). These experiments showed that a seeding rake was necessary for measuring flow around a hull with a yaw angle; otherwise there was insufficient seeding concentration in the measurement area, especially on the downstream side of the hull. During the preliminary experiments with the ship model, it was also found that for a measurement plane orientation across the direction of motion of the carriage, a single discharge pipe gave a narrow band of particles that did not extend across the whole field of view of the cameras. The preliminary experiments had also shown that it was unlikely that one seeding system would be suitable for all measurement locations.

A second generation of seeding system was required, which had improved performance relative to the prototype system. The key features required were an even distribution of particles, and a reduced wake. The revised seeding rakes were constructed from smaller diameter pipe (to reduce the wake) and multiple fingers to extend the width of the particle clouds. Two rakes were made with vertical fingers, one with three fingers and a maximum dimension of 300 mm across the flow and one with five fingers and a maximum dimension of 500 mm across the flow. A second orientation was used with three fingers oriented horizontally, with a maximum dimension of 300 mm across the flow. This orientation was designed for measuring flow under the hull. These rakes are shown in Figures 3-11 to 3-13.

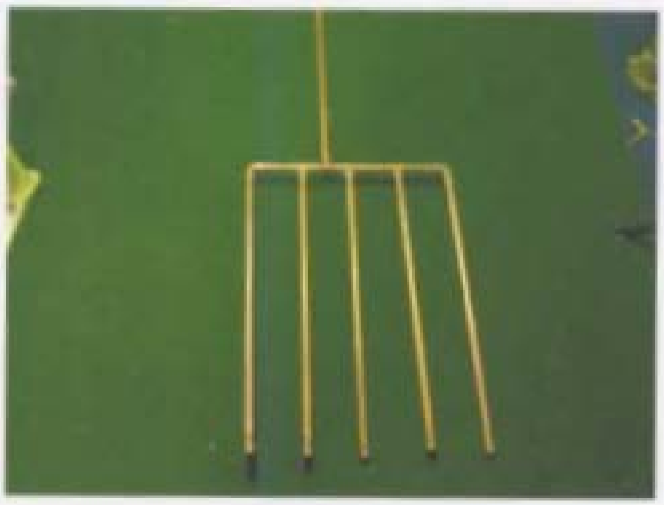

Figure 3-11, Five-fingered vertical seeding rake

Figure 3-12, Three-fingered vertical seeding rake

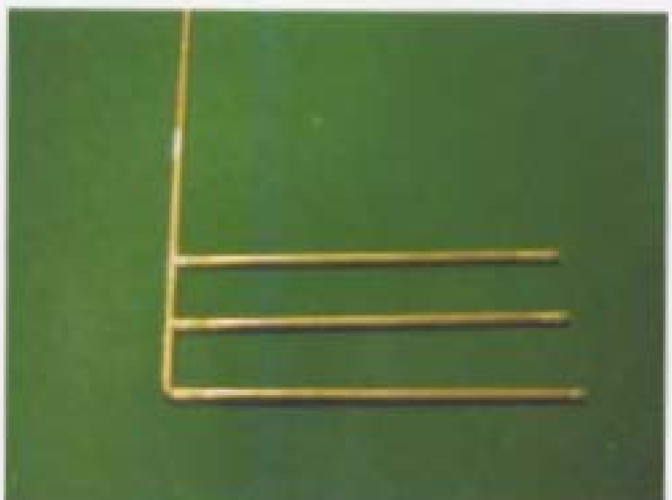

Figure 3-13, Three-fingered horizontal seeding rake

All of the rakes were made from copper pipe, with an inside diameter of 12mm. The smaller diameter, relative to the prototype system was used in an attempt to reduce the overall wake of the rake. Each finger had two rows of holes (3 mm diameter on 25 mm spacing). Seeded fluid was injected normal to the direction of motion of the rake.

3.5.5 Analysis of Wake Behind Seeding Rake

The wake of the five-fingered rake was determined from experiments in the ice tank at NRC's Institute for Ocean Technology. Two speeds were investigated, 0.5 m/s and 1.0 m/s, which were set from a computer file specified the acceleration rate, the steady speed and the deceleration rate. One file was created for each speed, and only these files were used to control the carriage during the experiments. The steady speed part of the profile was checked against an independent sensor for five runs at each speed. The comparison between the set speed and the independently verified speed is given in Table 3-8.

Table 3-8, Results of experiments to check carriage speed

Nominal value (m/s)			*Vc* m/s		Segment Time sec	Number Samples N
	T1	T2	Mean	Std. Devn.		
0.50	19.28	71.58	0.49971	0.000673	52.3	2615
0.50	24.62	85.42	0.49957	0.000606	60.8	3040
0.50	31.94	90.06	0.49951	0.000556	58.12	2906
0.50	14.78	84.42	0.49962	0.000634	69.64	3482
0.50	14.82	91.94	0.49973	0.000572	77.12	3856
Average value			**0.49963**			
1.00	24.28	55.86	0.99916	0.000759	31.58	1579
1.00	26.22	57.8	0.99919	0.000749	31.58	1579
1.00	23.48	58.3	0.99942	0.000776	34.82	1741
1.00	21.48	57.04	0.99931	0.000751	35.56	1778
1.00	32.82	74.18	0.99952	0.000808	41.36	2068
Average value			**0.99932**			

The five-fingered seeding rake was used, since it had the largest effective area, which covered the whole of the measurement window of the PIV system. It was fixed with its fingers across the direction of the undisturbed flow and parallel to the laser plane directed across the direction of motion for the carriage. The rake position was moved over the maximum distance that was practically obtainable. Three locations for the rake, with distances of 720 mm, 1400 mm and 3600 mm ahead of the laser sheet. A sketch of the orientation of the seeding rake, the laser sheet and the direction of motion of the fluid is given in Figure 3-14.

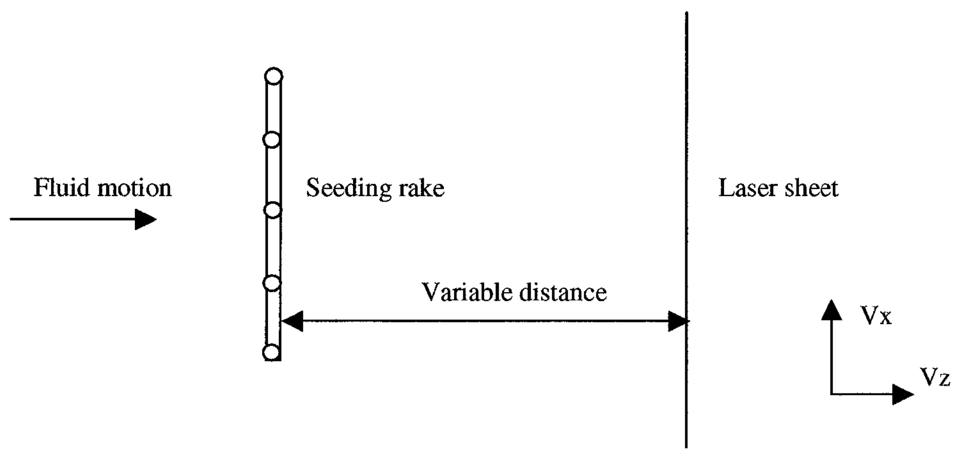

Figure 3-14, Orientation of seeding rake and laser sheet, and velocity components

For these experiments, the coordinate system was different from that used with the preliminary seeding system, due to the re-orientation of the laser sheet. *Vx* was defined as flow parallel to the laser sheet, *Vy* was the vertical flow component (positive towards the free surface) and *Vz* was the through the laser plane flow, based on a right-handed coordinate system. *Vc* was the speed of the carriage (assumed to be the same as the undisturbed flow).

For the case with no ship model present, it was possible to pre-seed the fluid and remove the rake during data collection. These experiments were used to confirm the accuracy of the PIV system. In this situation, seeding was carried out when the carriage was going in reverse towards its home point and then removing the rake for the PIV measurements, made with the carriage going forwards.

In all the experiments, determining the optimum time interval between laser exposures required a certain amount of trial and error to obtain flow vectors over the maximum area within the field of view.

The time between individual runs was approximately five minutes, although in some cases it was as low as three and in others it was as high as ten. It was not necessary to let all the particles settle out of the fluid but it was important that the disturbances caused by the passage of the rake had died out, before a new data collection run was started.

All data for this series of experiments was collected and analyzed using DaVis 7.1 (LaVision (2005)), an upgraded version of the software used for the experiments with the prototype rakes. The average and RMS deviation were calculated from the 50 pairs of PIV frames, using the time averaging function average function within DaVis 7.1. This function has a threshold value for the minimum number of time steps with a vector at a given interrogation window before the average and RMS values are calculated. For all data sets used in the wake analysis the threshold value was set at 7. Varying this parameter from 5 to 50 produced variations of the mean value of the vector modulus of less than 1.5%. The value of 7 was found to be a reasonable compromise to remove values based on very small numbers of points, without removing significant amounts of information.

The calculated vector components with and without the seeding rake are given in Tables 3-9 and 3-10 for speeds of 0.5 m/s and 1.0 m/s respectively. Included in these tables are the results of the experiments with no seeding system. In all cases it can be seen that the x and y components of the flow (within the measurement plane) are effectively zero, compared to the z velocity component (through the measurement plane).

The results show that at 0.5 m/s the location of the rake has little effect on the measured mean flow. The mean flow was between 10% and 12% lower than the nominal free stream case. The RMS deviation of the flow did not change with the location. At 1 m/s, the average wake fraction based on the three measurement locations was 15% of the free stream flow. There was more variation in the results than at 0.5 m/s, which may have been due to more turbulence in the flow. At 1 m/s, it was noticeable that the RMS deviation of the velocity decreased as the distance from the rake increased, whereas for 0.5 m/s it was approximately constant. In both cases where the seeding rake was removed, the free stream speed calculated by the PIV system was the same as the set speed (within 95% Confidence Interval).

Table 3-9, Results from experiments at nominal speed of 0.5 m/s

Rake at 720 mm away from laser				δt, μs
Cam_Date=060201_Time=095416				1000
	min	max	mean	rms
Vx	-0.10506	0.15533	0.00203	0.02156
Vy	0.08426	-0.09290	-0.00246	0.01382
Vz	0.34589	0.55785	0.43743	0.02119
/V/	0.34935	0.57509	0.43818	0.02132
Vc			0.49963	
Wake fraction			0.124498	

Rake @ 1400mm away from laser				δt, μs
Cam_Date=060131_Time=161447				500
	min	max	mean	rms
Vx	-0.22546	0.29304	0.00536	0.03306
Vy	0.26403	-0.23092	-0.00643	0.02351
Vz	0.21475	0.63912	0.43851	0.02723
/V/	0.23608	0.69629	0.44036	0.02890
Vc			0.49963	
Wake fraction			0.122329	

Rake at 3600 mm away from laser				δt, μs
Cam_Date=060201_Time=103347				1000
	min	max	mean	rms
Vx	-0.14252	0.11699	-0.00139	0.01977
Vy	0.13939	-0.13122	-0.00145	0.01467
Vz	0.36573	0.55456	0.45032	0.01851
/V/	0.36672	0.55622	0.45097	0.01912
Vc			0.49963	
Wake fraction			0.098695	

No seeding rake				δt, μs
Cam_Date=060201_Time=104950				500
	min	max	mean	rms
Vx	-0.17004	0.28746	0.01635	0.02688
Vy	0.20805	-0.15970	-0.00591	0.02486
Vz	0.24920	0.67043	0.50790	0.02547
/V/	0.38104	0.68193	0.50951	0.02545
Vc			0.49963	
Wake fraction			-0.01655	

Table 3-10, Results from experiments at nominal speed of 1.0 m/s

Rake at 720 mm away from laser				δt, μs
Cam_Date=060201_Time=100604				500
	min	max	mean	rms
Vx	-0.35342	0.36902	0.01803	0.05916
Vy	0.26067	0.24988	-0.01902	0.03675
Vz	0.61718	1.30182	0.87445	0.07062
/V/	0.64439	1.30560	0.87747	0.07233
Vc			0.99932	
Wake fraction			0.124955	

Rake @ 1400mm away from laser				δt, μs
Cam_Date=060131_Time=163013				700
	min	max	mean	rms
Vx	-0.20548	0.21266	-0.00401	0.03873
Vy	0.12146	-0.16017	-0.00924	0.02317
Vz	0.69619	0.96175	0.81102	0.04233
/V/	0.69984	0.98357	0.81232	0.04281
Vc			0.99932	
Wake fraction			0.188427	

Rake at 3600 mm away from laser				δt, μs
Cam_Date=060201_Time=104155				700
	min	max	mean	rms
Vx	-0.20670	0.23962	0.01007	0.03318
Vy	0.13346	-0.11231	-0.00091	0.02102
Vz	0.72836	1.02592	0.85856	0.03355
/V/	0.75712	1.03112	0.85950	0.03396
Vc			0.99932	
Wake fraction			0.140855	

No seeding rake				δt, μs
Cam_Date=060201_Time=105457				500
	min	max	mean	rms
Vx	-0.16372	0.25600	0.00659	0.03708
Vy	0.20408	-0.18448	-0.01302	0.02740
Vz	0.88357	1.20391	0.98504	0.04024
/V/	0.84217	1.20609	0.98622	0.04045
Vc			0.99932	
Wake fraction			0.014289	

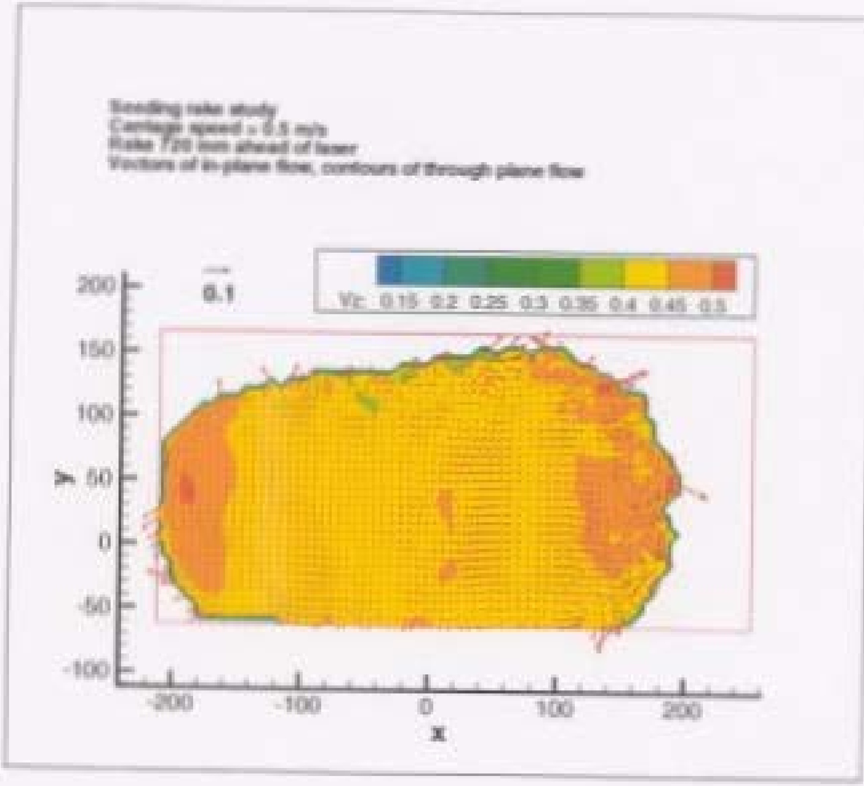

Figure 3-15, Calculated mean flow patterns for 0.5 m/s, rake at 720 mm ahead of laser

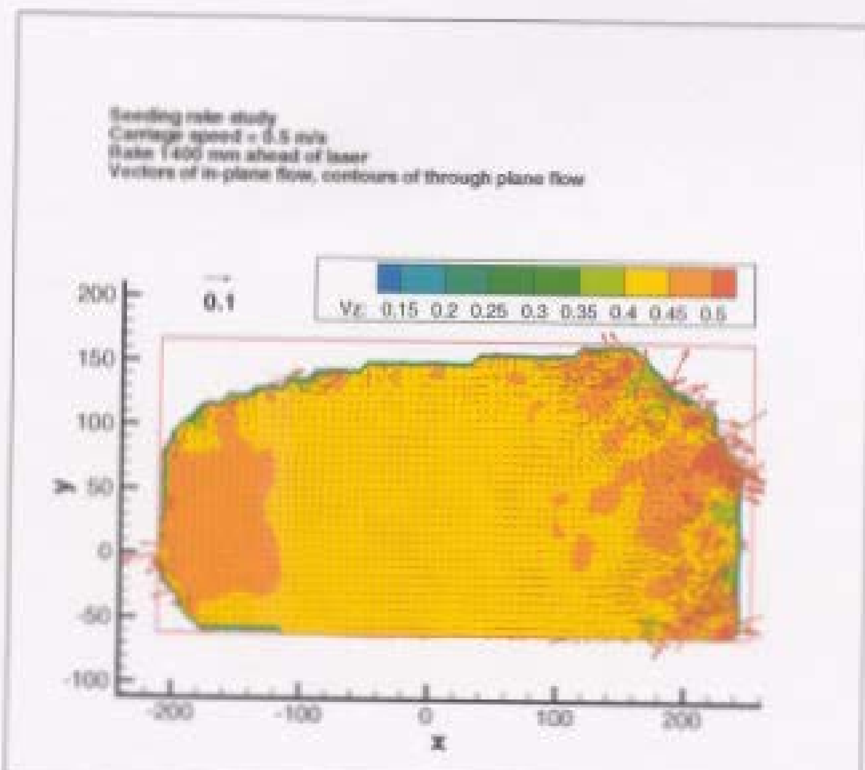

Figure 3-16, Calculated mean flow patterns for 0.5 m/s, rake at 1400 mm ahead of laser

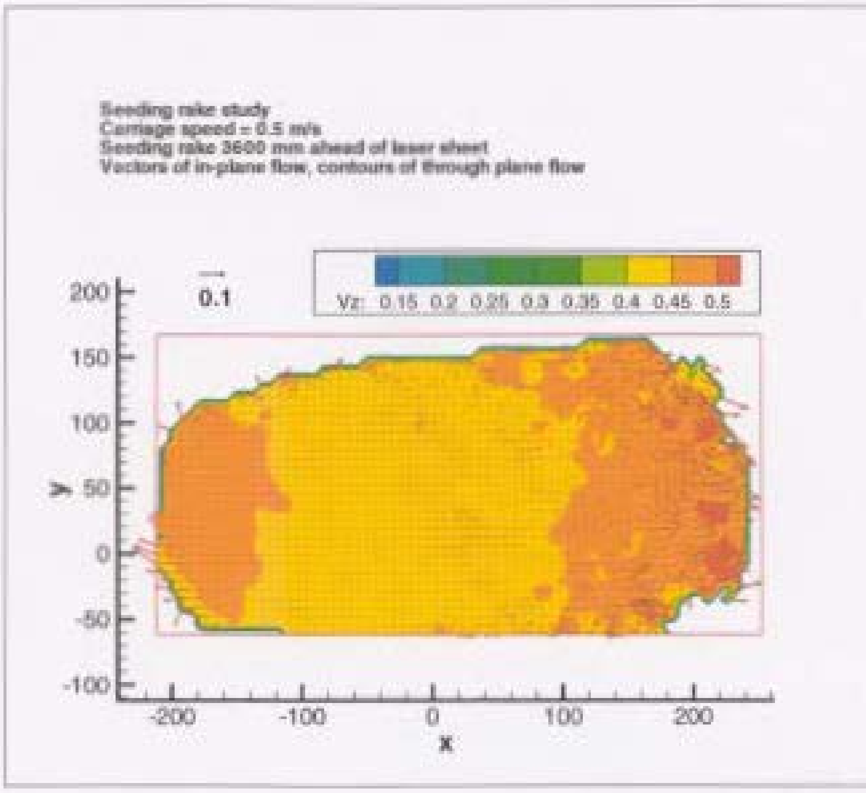

Figure 3-17, Calculated mean flow patterns for 0.5 m/s, rake at 3600 mm ahead of laser

Close to the seeding rake, the wake from the individual fingers could be seen as vertical bands within the in-plane plane velocity vectors. This pattern dissipated as the distance from the rake increased. This is illustrated in Figures 3-15 to 3-17, which show flow measurements for 0.5 m/s, for the seeding rake at distances of 720 mm 1400mm and 3600 mm from the laser sheet.

The case with no seeding rake is shown in Figure 3-18. When the seeding rake was removed, the number of individual vectors used to calculate the mean flow pattern was smaller than for the cases with active seeding. This highlights that even for very steady flow, the seeding rake provides uniform seeding concentration, but the average flow speed behind the rake is 12 to 15% lower than the nominal free stream case. It is hoped that by having a seeding rake that extends beyond the measurement region of the PIV system, that all the flow through the measurement window will be slowed by a uniform amount. Flow patterns around an object, such as a ship model with different geometries, should be comparable, if the same seeding rake and approximate location are used for both sets of experiments.

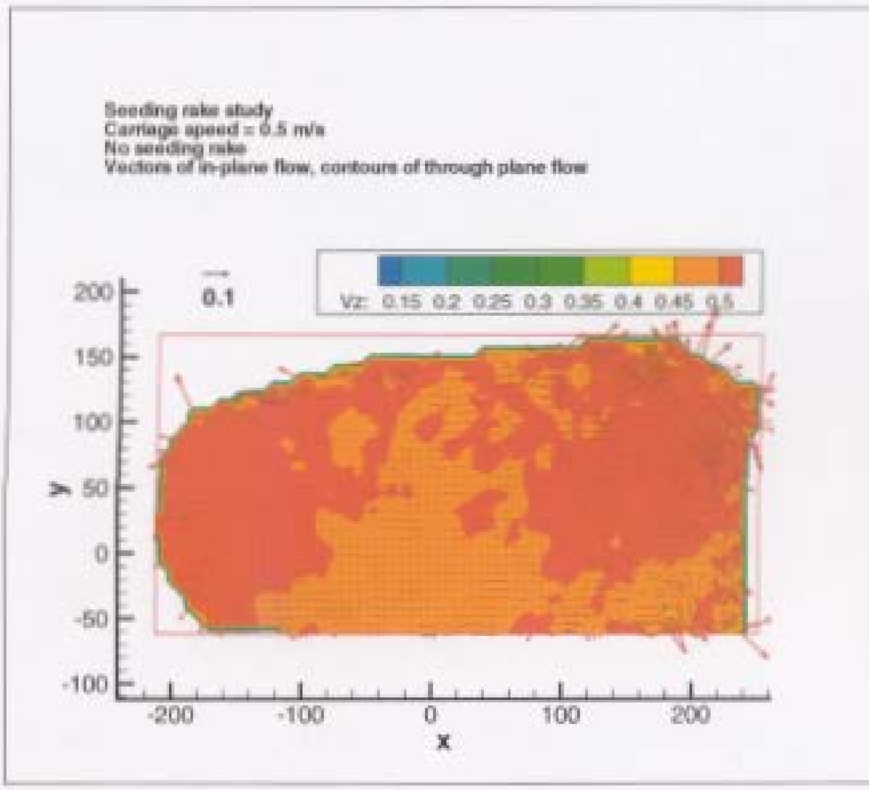

Figure 3-18, Calculated mean flow patterns for 0.5 m/s, no seeding rake

The new seeding rake creates a more even distribution of particles than the prototypes. Figure 3-19 shows a particle image taken at 0.5 m/s with the laser 1400mm behind the seeding rake. This figure does not show the periodic waves of particles shown in Figure 3-7 or the clouds of particles shown in Figure 3-8. The calculated flow patterns for the particles shown in Figure 3-19 are given in Figure 3-16.

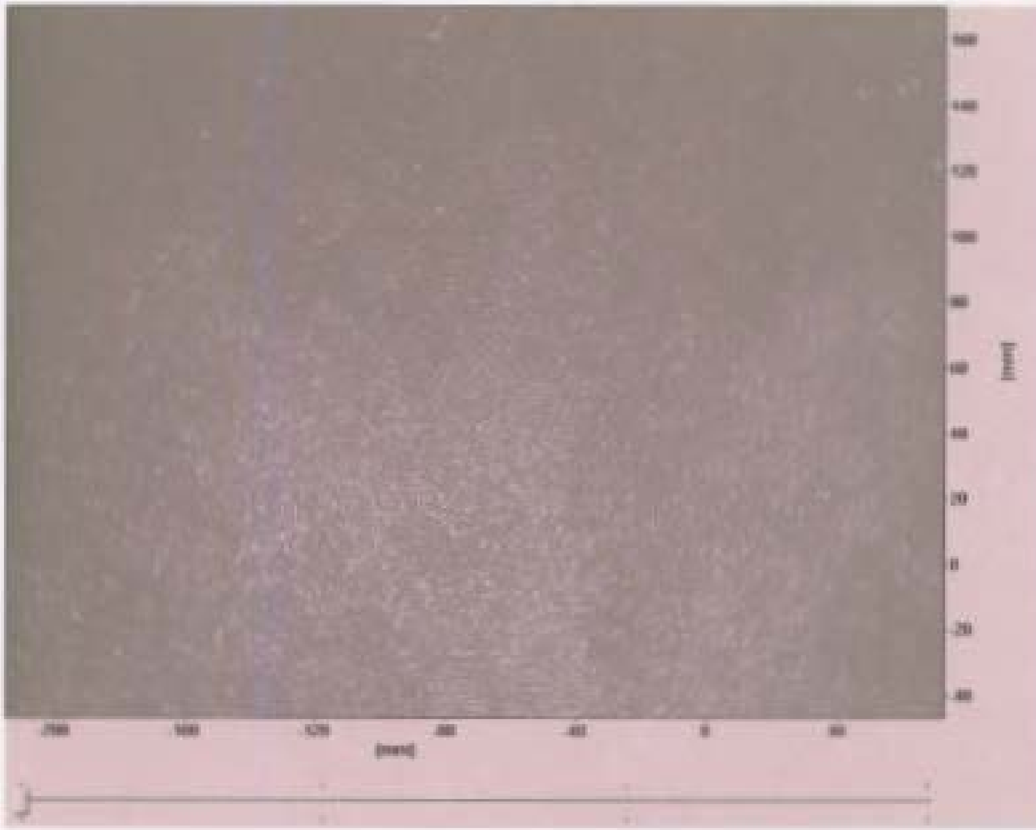

Figure 3-19, Particle distribution behind the seeding rake, 0.5 m/s

It might be possible to improve the design of the seeding rake, by reducing the level of the wake. The cylindrical sections used had the advantages of being cheap and readily available, but had a relatively high drag coefficient. Further work could be done in the development of seeding rakes with lower wakes, such as using airfoil shapes rather than cylinders. It is unlikely that the wake from this type of system can be removed completely, but a lower value that the current of 12-15% is probably achievable. If the wake could be reduced to 5%, it would be a significant improvement over the current system.

3.6 CONCLUSIONS

A preliminary study (Molyneux and Xu (2005)) had shown that it was necessary to use a seeding rake when carrying out experiments using PIV to measure the flow vectors around a ship model in a towing tank. Without active seeding of the flow, it was not possible to make consistent measurements of flow velocity, especially on the downstream side of the hull, because the seed particle concentration was too low. The rake was needed to deliver seeding particles into the flow, and maintain the minimum concentration required for accurate measurements. Ideally the rake should have no effect on the flow, but this is impossible. The next best option is to have minimum disturbance to the flow, and to have that disturbance distributed uniformly across the measurement window of the PIV system.

The rakes used for these experiments create a uniform disturbance across the measurement area, but reduced the mean flow speed by 12 to 15%, depending on the flow speed. The location of the rake relative to the measurement area has little effect on the measured mean speed, but the particle concentration decreases as the distance is increased. Since the area of the rake is large, in relation to the measurement area, it should affect all of the flow being studied. As a result, if the same rake and relative location are used, then flow patterns measured for different geometric arrangements of a ship model should be comparable, but with a similar bias to the results, caused by the presence of the seeding rake.

The estimated uncertainty for the PIV velocity analysis is higher than the range discussed by other researchers, and is expected to be between 8% and 16%. The 8% values of uncertainty are estimated for a flow speed of 1.0 m/s with laser pulse times of 1000 μs. The 16% value of uncertainty was estimated for a flow speed of 0.5 m/s, with a laser pulse time of 500 μs.

Using a smaller measurement area, with less magnification, would lower the uncertainty. Another way of lowering the uncertainty would be to increase the time between the laser pulses. The nature of the expected flow patterns for the escort tug required the relatively high uncertainty to be accepted for two main reasons. The first was the desire for a large measurement area to maximize the data collected in unsteady flow conditions from a single field of view. The second requirement was for the measurement plane across the strongest flow direction, since this is the primary plane of interest for many flow measurements around a ship hull (e.g. a wake survey through the propeller plane). This required relatively short laser pulse times to ensure the same particles are within the measurement space for both image pairs.

The design of the rake should be improved so that it has a lower wake. It is unlikely that the wake will be removed completely, but a wake of 5% would be a significant improvement over to the currently achieved value of 12-15%.

CHAPTER 4

PARTICLE IMAGE VELOCIMETRY MEASUREMENTS OF FLOW AROUND AN ESCORT TUG MODEL WITH A YAW ANGLE OF 45 DEGREES

4.1 INTRODUCTION

Experimental measurements of flow velocity around a Series 60 C_B=0.6 hull at two different yaw angles were compared to CFD predictions for the same flow conditions in Chapter 2. The CFD predictions were made using both tetrahedral and hexahedral meshes. The main conclusion was that for this type of hull with a yaw angle, the meshing strategy had little effect on the accuracy of the predicted flow patterns for yaw angles of 10 degrees and 35 degrees. At 10 degrees of yaw, the tetrahedral mesh gave more accurate predictions of the measured forces, but no force data was available at 35 degrees yaw.

The Series 60 hull form was not designed for operation at large yaw angles and although the CFD predictions of the in-plane flow velocities were accurate to within 7 per cent at 10 degrees yaw and 24 percent at 35 degrees yaw, there may be some features of the flow that were exaggerated because of the shape of the hull.

An escort tug must operate at large yaw angles to generate the forces needed to stop a loaded oil tanker, in an emergency. An example of this type of hull is shown in Figures 4-1and 4-2. This hull was a preliminary design for a tractor tug, developed by Robert Allan Ltd. of Vancouver, B. C (Allan et al. 2000). The 1:18 scale model was tested (Molyneux, 2003) at the NRC Institute for Ocean Technology (IOT). The focus of this experiment program was to obtain lift and drag forces for the hull in combination with different appendages. The range of ship speeds was from 4 to 12 knots (with model speeds based on Froude scaling). Yaw angle was varied between zero and 105 degrees but no measurements of the flow velocities had been made.

Obtaining detailed flow measurements around this type of hull at a large yaw angle is an essential step in establishing the reliability of CFD predictions in these flow conditions. This chapter describes experiments carried out to measure the flow patterns around a scale model of an escort tug using Particle Image Velocimetry (PIV) and presents the results. Some discussion on the results is given and recommendations are made for improvements to the experiment techniques. The PIV system that was used has been described in Chapter 3. The results of these experiments will be used to compare with CFD predictions for the same flow conditions. These comparisons will be described in Chapter 5.

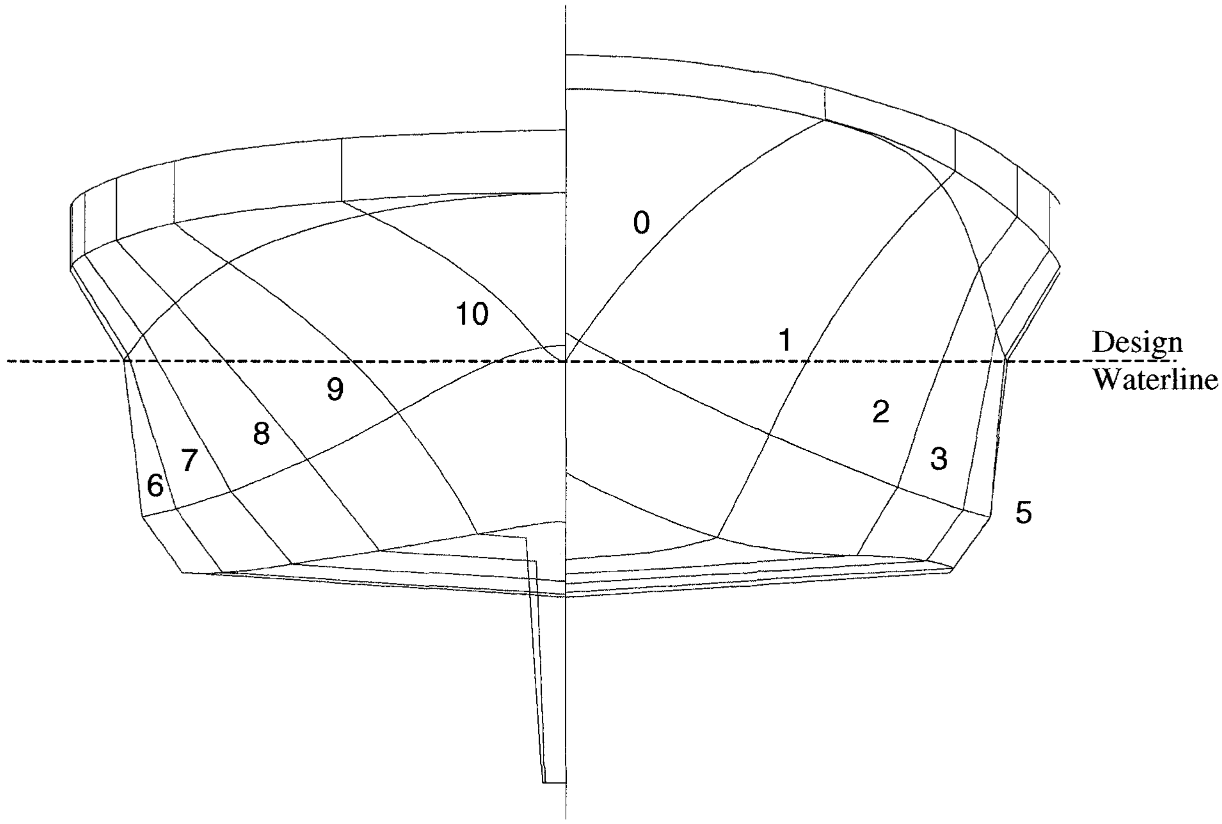

Figure 4-1, Body plan for tug model, used in PIV experiments.

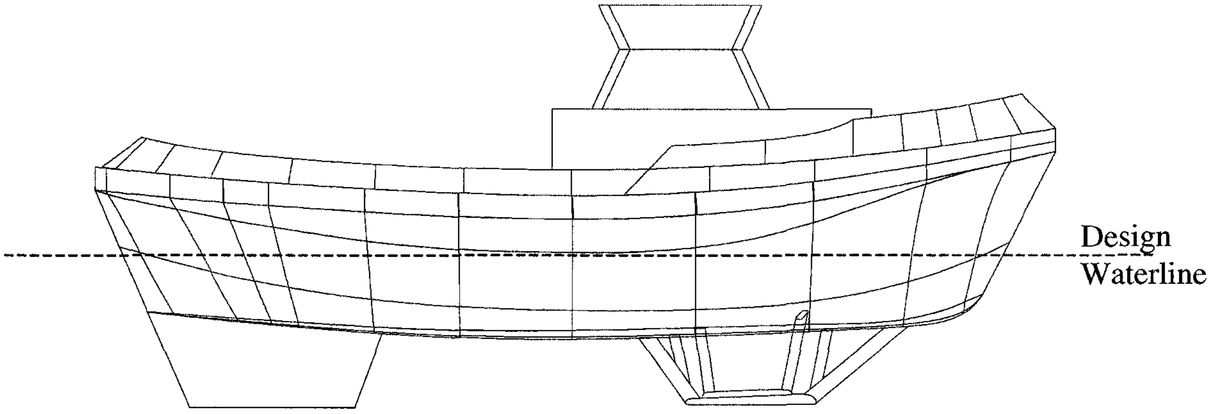

Figure 4-2, Profile view of tug, with fin and propulsion cage

4.2 DESCRIPTION OF SHIP MODEL

The hull chosen for the flow measurements was a concept for a tractor tug developed by Robert Allan Ltd. of Vancouver, B. C (Allan et al., 2000). The 1:18 scale model was previously tested at the NRC Institute for Ocean Technology (IOT), when force measurements were made for a range of yaw angles from zero to 105 degrees (Molyneux, 2003). Some preliminary experiments were carried out in the towing tank at Memorial University, to develop the techniques necessary for obtaining reliable results from PIV measurements for a hull with a yaw angle in a towing tank. These initial attempts which were carried out prior to the experiments described in this chapter, have been described elsewhere (Molyneux & Xu, 2005).

A summary of the tug model geometry is given in Table 4-1. For this series of experiments the model was always moving with the fin (when fitted) going forwards (although the ship is actually going astern based on conventional definitions of bow and stern).

Table 4-1, Summary of model particulars

Length, waterline, m	2.122
Beam, waterline, m	0.789
Draft, hull, m	0.211
Daft, maximum, m	0.471
Displacement, kg	213.3
Nominal scale	1:18

To reduce the corruption of recorded images by reflected laser light, the hull was painted matt black. Contrasting targets, made from narrow yellow strips of tape were placed at key locations on the model. These were used to align the laser beam, to ensure that it was at the required position relative to the model.

For the PIV experiments no bulwarks or deckhouses were fitted, although they are shown in the figure. The propulsion cage was also removed, so that the fin was the only appendage. Some experiments were also carried out with the fin removed.

4.3 PROGRAM OF EXPERIMENTS

4. 3.1 Test Conditions

The yaw angles and speeds for which PIV measurements were made are summarized in Table 4-2. The mean yaw angle for escort tug operation is 45 degrees. Two speeds were chosen to cover the expected range of operation for the ship.

Table 4-2, Yaw angles and speeds tested

Yaw angle, degrees	Model speed, m/s	Ship speed, knots
45	0.5	4.12
45	1.0	8.24

Preliminary CFD simulations (Molyneux, 2005) had shown that the fin should have a very large effect on the flow patterns on the underside of the hull and on the downstream side. To confirm this effect, some experiments were carried out with the fin fitted and with the fin removed. The CFD predictions also indicated that the fin had a very small effect on the upstream side and so experiments for that location were only carried out with the fin removed.

The measurement plane locations and the appendage configurations are given in Table 4-3.

Table 4-3, Summary of measurement plane locations

Measurement location	Yaw angle, degrees	Appendages	Speed, m/s
Midships, upstream side	+45	Fin off	0.5, 1.0
Midships, downstream side	-45	Fin off	0.5, 1.0
Midships, downstream side	-45	Fin on	0.5, 1.0

4.3.2 Installation of Model and PIV System in IOT's Ice Tank

The preliminary CFD simulations (Molyneux, 2005) had shown that the effect of the fin was most visible on the flow patterns under the hull, on the downstream side of the centreline. This region of the flow should contain a large vortex formed by the fin. In order to visualize this large vortex, the laser plane for the PIV system needed to be oriented across the direction of the undisturbed flow. The laser sheet was oriented across the tank, normal to the direction of motion of the towing carriage. A flow-based coordinate system was chosen, since this would eliminate the need to re-orient the laser plane if the yaw angle of the tug was changed.

The preliminary CFD simulations (Molyneux, 2005) also predicted that more than one measurement window from the PIV system would be required to fully observe the flow patterns caused by the fin. The disturbance to the flow by the fin was expected to cover an area of approximately 1.0m by 0.5m on the downstream side of the hull. A typical measurement window for the PIV system was 0.3m square. If the PIV system had to be moved to obtain this range of measurement, there was the potential requirement to recalibrate the system each time it was moved. It was important not to waste facility time, which was limited, and so the test set-up was designed to allow the laser to remain fixed in one location. Movement of the measurement window relative to the model was obtained by moving the model or by moving the complete PIV system as a unit.

The sign convention for the model geometry (used for the CFD simulations) was a right-handed system, with the origin at the leading edge of the static waterline (the end of the hull with the fin), x positive from the bow to the stern, and z positive upwards. On this coordinate system, the yaw angle was positive when the bow was turned to port. Note that for the upstream side, the yaw angle was changed to 45 degrees, so that the PIV system did not have to be moved.

Figure 4-3, Location of measurement plane, upstream side of hull

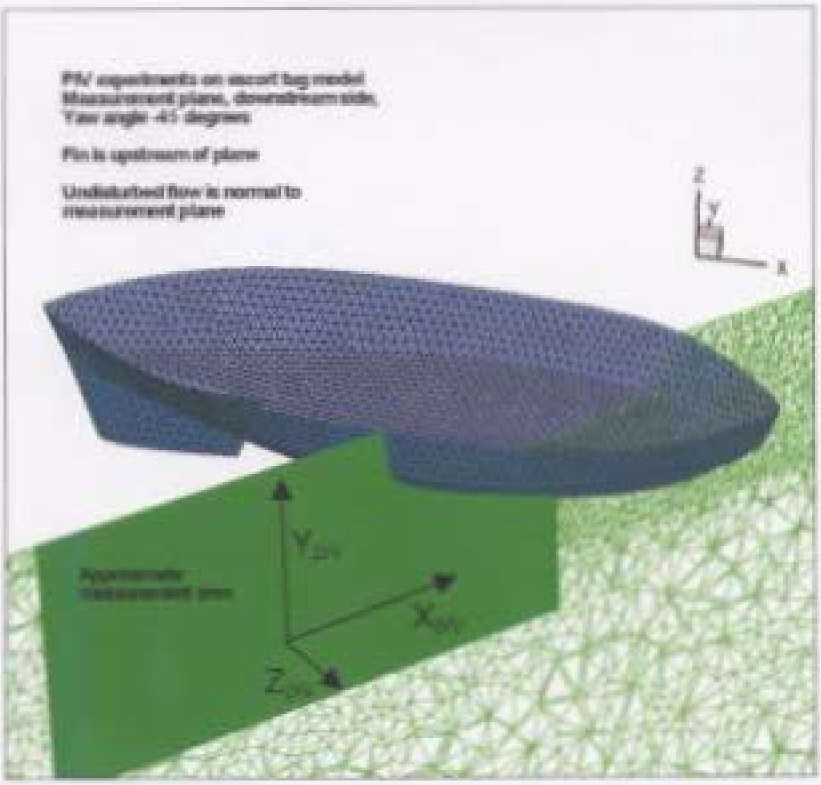

Figure 4-4, Location of measurement plane, downstream side of hull

The results of the PIV experiments given below are presented using a coordinate system, which was based on the measurement plane (LaVision, 2005). In this system, x and y axes were within the measurement plane, and the z axis was through the measurement plane. The measurement planes relative to the model geometry and the coordinate systems are shown in Figure 4-3 for the upstream side and Figure 4-4 for the downstream side. In the PIV coordinate system, undisturbed flow had a z velocity component, equal to the speed of the towing carriage, and the x and y velocity components would be zero.

The PIV measurements were carried out in the Ice Tank of the National Research Council's Institute for Ocean Technology. In the centre of the carriage was a test frame, which was adjustable vertically and had two longitudinal beams that can be moved independently but remain parallel to the centreline of the carriage. This adjustment feature was used to vary the location of the measurement window, relative to the model. Each beam had a scale so that the exact locations of the beam, relative to the centreline of the test frame were known. The PIV equipment was fitted to the beam on the South side of the carriage, and the model was fitted to the beam on the North.

At a given yaw angle and measurement section, the most common movement of the measurement window was in the x-direction of the PIV axis. This was obtained by moving one or other of the test beams. Vertical movement (y-axis in the PIV system) was the next most frequent adjustment, which was made by raising or lowering the borescopes and laser fixed amounts. The model and attachment frame were moved along the test beam until the target at the required section was aligned with the laser sheet. Once this was obtained, the model was clamped in place. Yaw angle was the least frequent adjustment, and this was made using a yaw table, built for earlier model tests on an Autonomous Underwater Vehicle.

A frame for the PIV system was built around one test beam, using extruded aluminium sections. The laser was oriented normal to the direction of motion, so that the measurement plane was across the direction of motion for the undisturbed flow. The borescopes for the CCD cameras were mounted symmetrically, approximately 650mm either side of the laser sheet. Camera 1 was upstream of the laser sheet, and Camera 2 was downstream. The centre of the measurement window was approximately 950 mm away from the under the water optical unit for the laser. At no time during the testing were these positions changed. The minimum separation between the beams of the test frame was 922 mm. The final arrangement of the PIV system on the Ice Tank carriage test beam is shown in Figure 4-5.

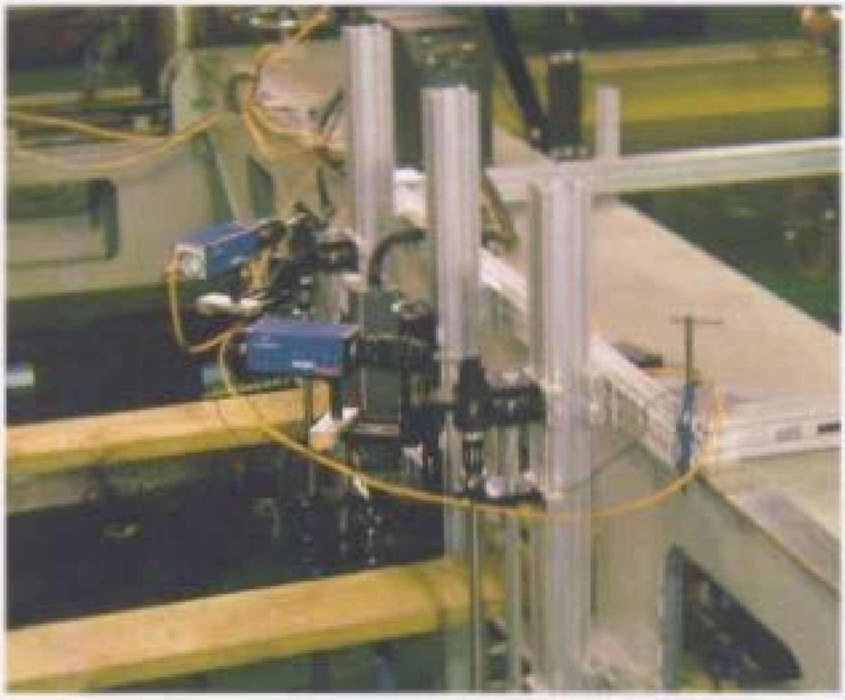

Figure 4-5, PIV system attached to towing carriage in IOT Ice Tank

The model was connected to the carriage by two vertical, cylindrical poles and a yaw table. This yaw table enabled yaw angle to be adjusted from zero to ninety degrees, in five-degree increments. The model hull was rigidly connected to the towing carriage, by bolting the yaw table around the carriage beam. Yaw angle for the model was adjusted using the yaw table. To adjust the position of the model, relative to the laser sheet, the bolts around the beam were slacked off and the model slid forwards or backwards as required until the laser sheet was directed at the correct target on the model. The model and the assembled PIV system are shown in Figure 4-6.

Figure 4-6, Escort tug model and PIV system attached to towing carriage in IOT Ice Tank (model shown at zero yaw angle).

4.3.3 PIV System Calibration, Operation and Maintenance

In-situ calibration of the measurement space was carried out prior to testing using a Type 30 calibration plate, supplied by LaVision GmbH. The plate was suspended from the model using an adjustable support frame. During calibration, the top of the plate was level with the waterline. The plate was adjusted, using the frame, until it was aligned with the laser sheet. Figure 4-7 shows the calibration plate and the laser. The calibration was carried out using visible light, following the procedures required in the DaVis 7.1 software (LaVision, 2005).

Figure 4-7, Calibration plate location for in-situ calibration of measurement space

Although the system was not moved, it was recalibrated once during the middle of the testing. The summary of the fit of the mapping function to the known grid points and the resulting size of the de-warped image is given in Table 4-4. The PIV system, including the expected uncertainties, has been described in Chapter 3.

Table 4-4, Summary of mapping function fit to known grid points

Date	RMS Deviation Camera 1	RMS Deviation Camera 2	De-warped window size, Pixels (x-y)	De-warped window size, mm (x-y)
1st calibration January 13, 2006	0.16625	0.12142	2367 x 1258	525.03 x 273.34
2nd calibration January 20, 2006	0.30769	0.13965	2128 x 1228	438.74 x 249.79

The reference frame for analysis of the images was a right-handed axis system for x, y and z velocity components. The x-y plane was in the plane of the laser sheet, with the x-axis parallel to the water surface. Positive x was from port to starboard on the ship model, and positive y was towards the water surface. The z-axis was positive in the direction of the carriage motion.

On completion of the calibration, the position of the beams was adjusted until the edge of the model at the upper borescope location was clearly visible in the camera images. This position was then used as the reference location. Since more than one view of the flow patterns was required, the relative position of the model and the laser were adjusted from this origin, by moving one or the other of the test beams. Moving the model away from the laser was a negative shift in the x-direction, and moving the laser nearer the model was a positive shift, based on the coordinates used for the PIV measurements.

The same general procedure for the carrying out the experiments was followed throughout the test program. First the model or the laser was adjusted to the required position, by moving one of the test beams. The most appropriate seeding rake was selected and its best location for each experiment was found by trial and error. During these trial runs, the optimum time interval for the exposures was also determined. Once the best seed particle distribution and timing had been determined, images were collected for 50 or 100 successive time intervals for speeds of 0.5 and 1.0 m/s, with at least one repeat run for each condition.

For each data collection run, the sequence of action was to turn on the seeding system as the carriage started to move. PIV image data was collected for 50 or 100 image pairs once the carriage had reached a steady speed. On completion of data collection, the carriage was stopped and returned to its initial position. All runs were made collecting data when the carriage was moving towards the melt pit (from East to West). On completion of all the data collection runs at one location, the beam with the model or the beam with the laser was moved to the new position. A summary of all the experiments, including test dates, measurement locations, number of image pairs used in analysis and the time intervals between the laser pulses, is given in Appendix 2.

Some routine checks were performed throughout the test program. Prior to the start of testing each day, the focus of each camera was checked. This was done by seeding the measurement space when the carriage was stationary and if necessary, adjusting the focus of the borescopes. In order to keep the PIV system optics clean, the borescopes and the laser tube were raised out of the water at the end of each day's testing. The optical parts were then washed with fresh water and lens cleaner to prevent the build-up of dirt.

4.3.4 Seeding

Seeding the flow proved to be the most challenging aspect of carrying out these experiments. The CFD predictions suggested that the most important flow patterns were caused by the fin, and occurred under the hull towards the downstream side. For regions close to the hull, the three-fingered vertical rake was used. A typical installation is shown in Figure 4-8(a). The flow in this region was unsteady, with quite abrupt changes in direction. As a result, locating the seeding rake was largely a matter of trial and error. The final location of the seeding rake for each measurement window had to be far enough upstream that the wake from the rake has stabilized, but close enough that the required concentration of particles was obtained across a large enough part of the measurement window. This position varied depending on the flow conditions and the location of the measurement window relative to the tug.

For locations close to the hull surface, but below the free surface the 3-fingered horizontal rake was used. The shape of this rake allowed it to get well under the model. This rake could be used for seeding from the upstream or downstream side of the model. Upstream seeding was used when the measurement window was under the hull, and close to the centreline of the hull. Downstream seeding was used when the measurement window was on the downstream side of the hull at the deepest locations for the measurement window. A typical location for seeding on the downstream side of the model is shown in Figure 4-8(b).

As the measurement window was moved to be far away from the model, the type of rake chosen was less critical. Any of the rakes could be used for measurements in these regions, and Figure 4-8(c) shows the 3-fingered horizontal rake located for seeding a measurement area well away from the model.

(a), Seeding location close to hull and free surface

(b), Seeding location close to hull but below free surface

(c), Seeding location far from hull

Figure 4-8, Typical locations of seeding rake during experiments

Some representative pictures of the seed particles, at a location close to the model are shown in Figures 4-9(a) and 4-9(b). Figure 4-9(a) shows the view from Camera 1 and Figure 4-9(b) shows the view at the same time from Camera 2. These pictures were obtained from Run 15:29:35[1], recorded on January 18, 2006 and were chosen because they show the degree of overlap of the two fields of view, relative to a section of the model. The bright line in each figure is the laser shining on the hull, and shows the model from the waterline to the corner of the bilge. The seeding rake position was approximately that shown in Figure 4-8(a).

[1] The DaVis software gives each experiment a file name based on the date and the time of day when it was acquired. The experiments in this report are referred to by the time (hh:mm:ss) only. The date of each experiment is given in Appendix 2.

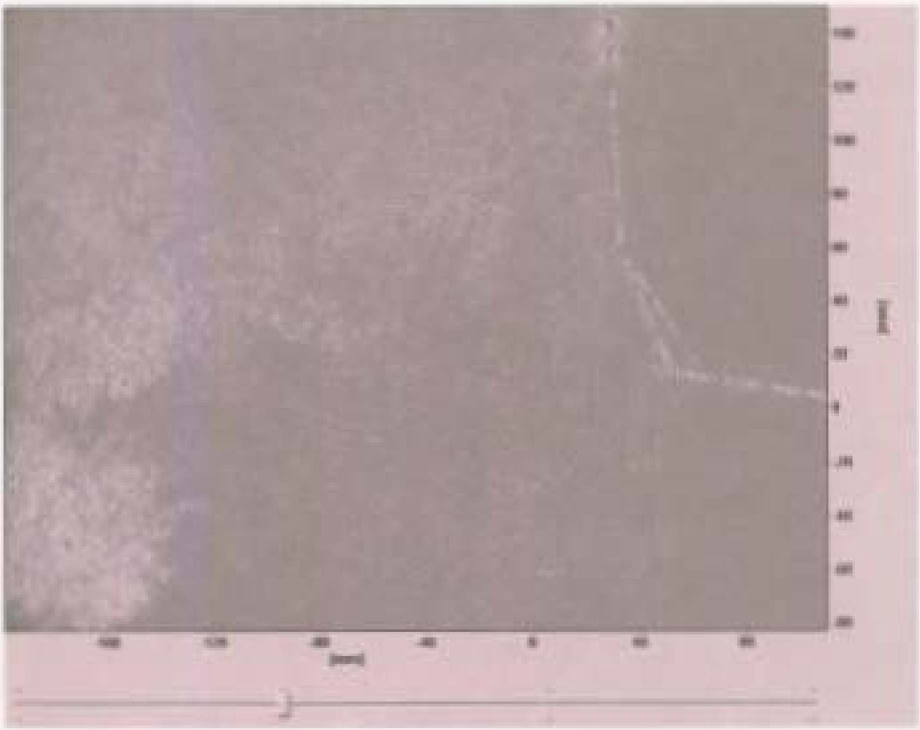

(a), Run 15:29:35 Camera 1

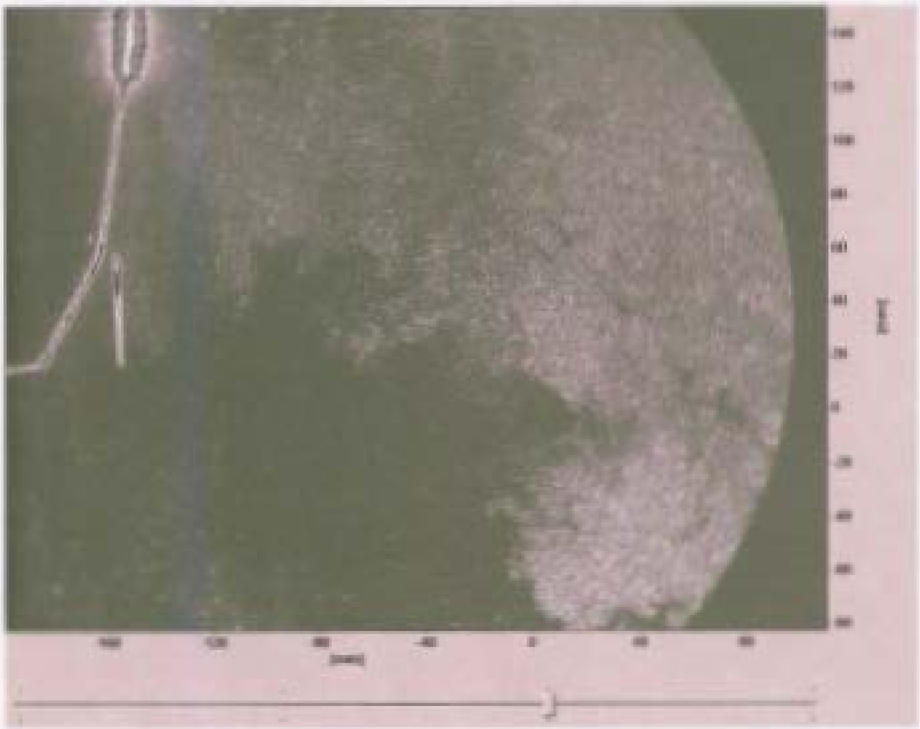

(b), Run 15:29:35 Camera 2
Figure 4-9, Particle images with tug model, flow speed 0.5 m/s

4.4 SINGLE PIV MEASUREMENT WINDOW

4.4.1 Analysis of Experiments

The analysis methods used in the *DaVis* software were described in Chapter 3. Data collection and preliminary analysis of the PIV experiments were carried out using the *DaVis* software package (LaVision, 2005). Complete processing of each data set before moving on to the next experiment was too time consuming. Individual frames were analyzed immediately after the experiment had finished, and selected runs were fully processed when a suitable gap between the experiments occurred, such as lunch breaks, or in the evenings. This preliminary analysis was enough to ensure that the data being collected was sufficiently accurate to be analyzed in more detail on completion of the experiment program.

The final data processing was carried out in batch mode using the procedures described below. These settings were found to give consistent results for all the flow conditions tested. The final values of the settings within the software were determined using the combination of recommendations from LaVision and trial and error during the preliminary analysis.

Pre-processing of each image was carried out prior to calculating the velocity vectors. This consisted of subtracting a sliding background scale, based on 16 neighbouring pixels. When the vectors were calculated, the allowable range in pixels was zero plus or minus 10 for the x and y velocity components (within the measurement plane) and zero plus or minus 20 in the *z* velocity component (through the measurement plane). Vectors outside this range were excluded. Vectors were also excluded if the three-dimensional validation error was greater than 5 pixels. Vector post processing was based on an adaptive multi-pass method, with an initial window size of 64x64 pixels and a final window size of 32x32 pixels. Vectors were smoothed using a median filter with removal and replacement criteria based on two times and three times the RMS values of the eight neighbouring windows respectively. A second pass was made, based on the same allowable vector ranges, after the removal and replacement criteria had been applied once. This analysis gave consistent results through the experiment program, for the range of times between laser sheets used for the flow conditions studied.

Further vector processing was carried out to calculate the mean flow pattern across the complete time history of the measurements for each set of calculated vectors. This was carried out using the vector statistics function within *Davis* 7.1. This function required the specification of a minimum number of frames for which a vector must appear at each interrogation window. This threshold ensured that areas within the flow that were poorly defined were excluded from the analysis.

After some preliminary investigations, 25% of the total number of frames taken was found to be a suitable threshold. Based on trial and error, this level provided an acceptable compromise between data density over the full frame and the standard deviation of the vectors based on small samples. For the majority of the data runs, this value was 25 frames out of a total of 100, but for some of the early runs, this was 12 out of 50. The calculated vectors were exported from the *DaVis* PIV data collection and analysis software as *Tecplot* data files. *Tecplot* was used by for presenting of the results.

4.4.2 Discussion Of Results

The most reliable interpretation of the experiment data should be on the basis of results at a single measurement window, since these required the minimum amount of data processing. Six key locations were identified from the results, where a single measurement window gave vectors that were important to understanding the flow around an escort tug hull with a large yaw angle.

All of the locations chosen for discussion were close to the hull. The results are presented on a grid relative to the complete measurement plane, rather than the grid for a single PIV window, so that the flow patterns can be more easily related to the position of the model and more easily compared from location to location. All the figures show vectors of in-plane velocity (V_x and V_y) and all the cases but one show repeat experiments superimposed on the same grid.

The discussion below is based on a single flow speed of 0.5 m/s, but as can be seen from the combined data sets that will be discussed later, the difference in flow pattern with speed was very small, although the magnitude of the flow velocity vectors changed.

a) Tug Without Fin, Upstream Side, Close to Waterline

Mean flow vectors for the upstream side of the tug (with no fin) between the waterline and the bottom of the hull are presented in Figure 4-10. Two sets of mean in-plane vectors at the same location are presented, and it can be seen that the mean flow vectors were coincident between experiments over almost all of the measurement space. This indicated that the mean flow measured in two separate data collection runs was stable over the measurement space.

Figure 4-10 shows that the flow vectors were generally directed away from the hull surface and downwards (in negative x and y directions) with little change in velocity magnitude. A region with rapidly changing flow direction is where the flow is starting to separate from the hull in the bottom right hand corner of the measurement window.

At this window location, it was found to be very difficult to get seed particles into the region just below the waterline and very close to the hull. The z-velocity in this region is low. Seeding particles introduced to the flow sufficiently far upstream of the measurement window to avoid unsteady flow caused by the rake did not reach the measurement window. This accounts for the absence of vectors in that region.

The three-fingered vertical rake was used for this location.

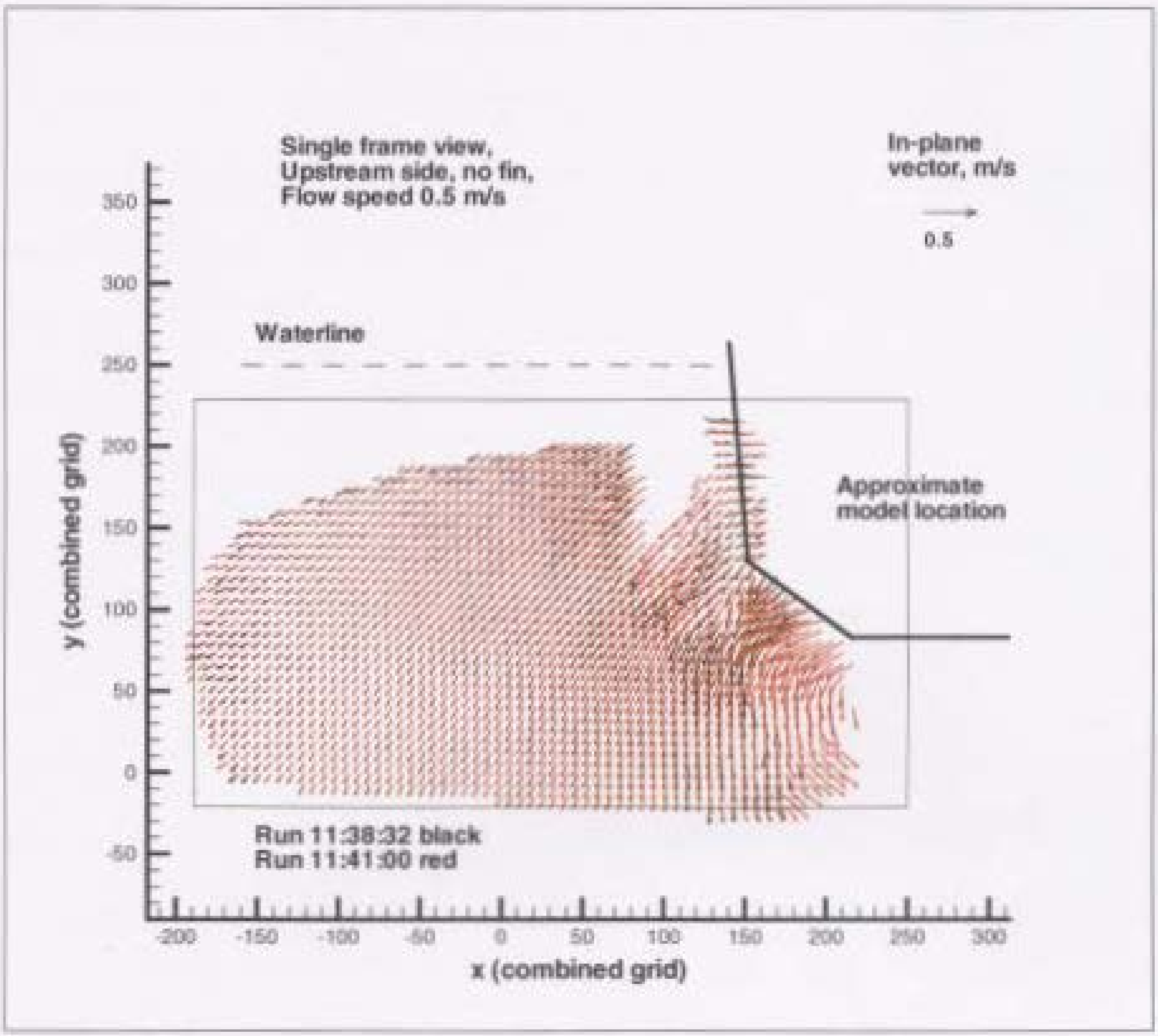

Figure 4-10, Mean in-plane flow vectors, upstream side of hull without fin, bilge to waterline, flow speed 0.5 m/s

b) Tug Without Fin, Upstream Side, Under Hull

Figure 4-11 shows another region of the flow for the same conditions as Figure 4-10. The area of flow shown in Figure 4-11 is under the hull on the upstream side. This figure shows four distinct flow directions in different parts of the measurement window. The first region is at the far left hand side where the flow is vertically downwards. The second region consists of a narrow band of fluid (approximately 50 mm thick) close to the hull, where the fluid was flowing towards the upstream bilge corner. The third region is immediately below the band of upstream flow. In this region the flow is rapidly changing speed and direction. Over the rest of the flow measurement window the flow direction is from top left to bottom right.

This figure reinforces the observation made in Figure 4-10 that the flow is separating off the upstream bilge corner. Figure 4-11 shows areas of rapidly changing flow speed and direction and it is likely that a vortex was formed under the hull, although the circulation pattern is incomplete, and likely extends beyond this measurement window.

Figure 4-11 shows two sets of measurements superimposed, and as in Figure 4-10 there is very good overlap of the calculated flow vectors. To obtain this PIV result, the three-fingered horizontal seeding rake was positioned under the model.

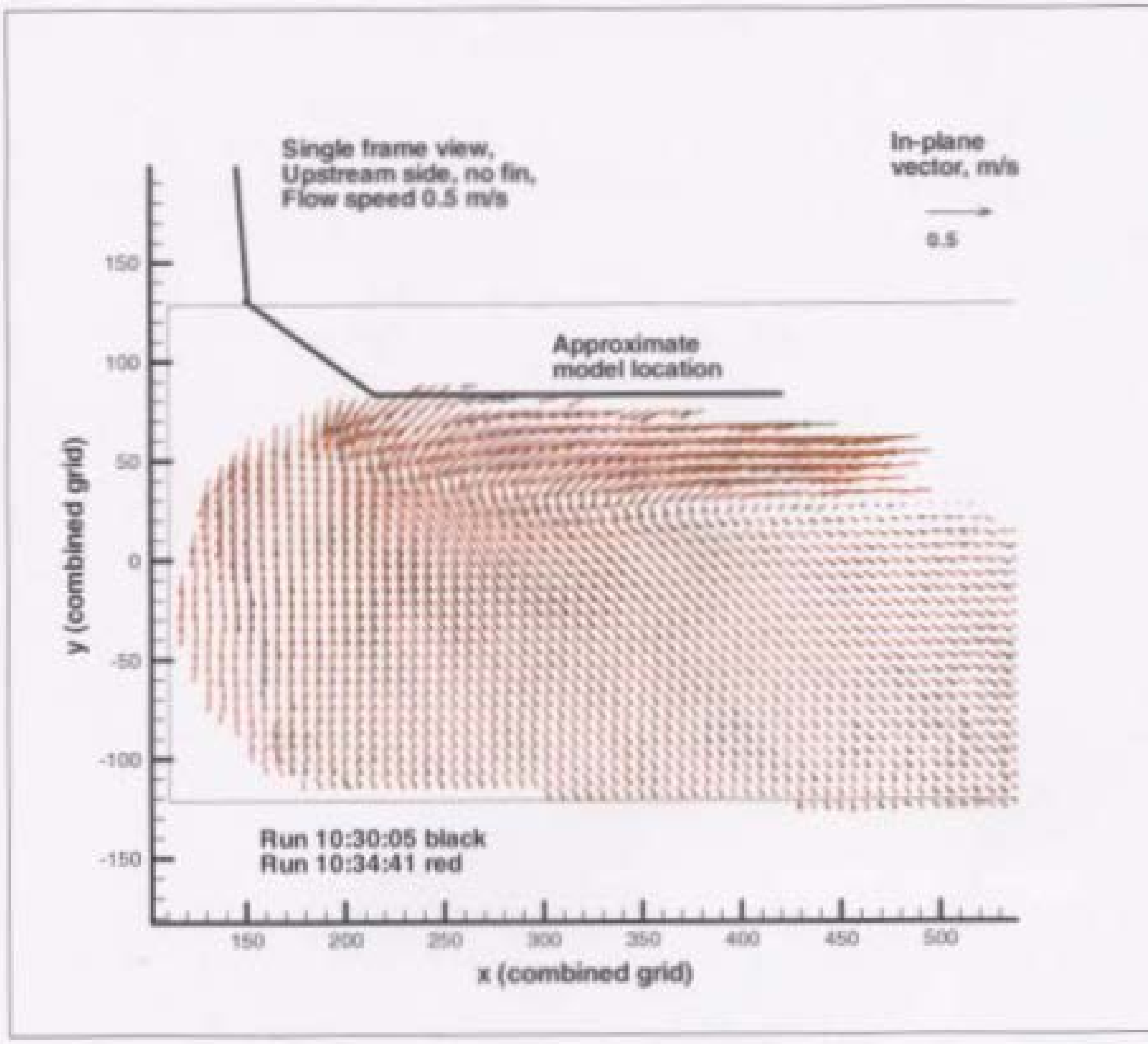

Figure 4-11, Mean in-plane flow vectors, upstream side of hull without fin, under hull, flow speed 0.5 m/s

c) Tug Without Fin, Downstream Side, Close to Waterline

Figure 4-12 shows the flow vectors on the downstream side of the hull, with no fin, from the bilge to the waterline. This figure shows the development of a vortex close to the downstream side of the hull, caused by the flow separating off the corner of the bilge. The rest of the figure shows a strong upward flow component in the lower right hand corner and a horizontal flow component entering the window from the far left hand side.

Seeding in this situation proved to be extremely challenging when only one rake was used. For the view given in Figure 4-12, the 3-fingered vertical seeding rake was situated close to the waterline. This arrangement resulted in the absence of vectors in the lower right hand corner, which would have completed the definition of the flow around the core of the vortex.

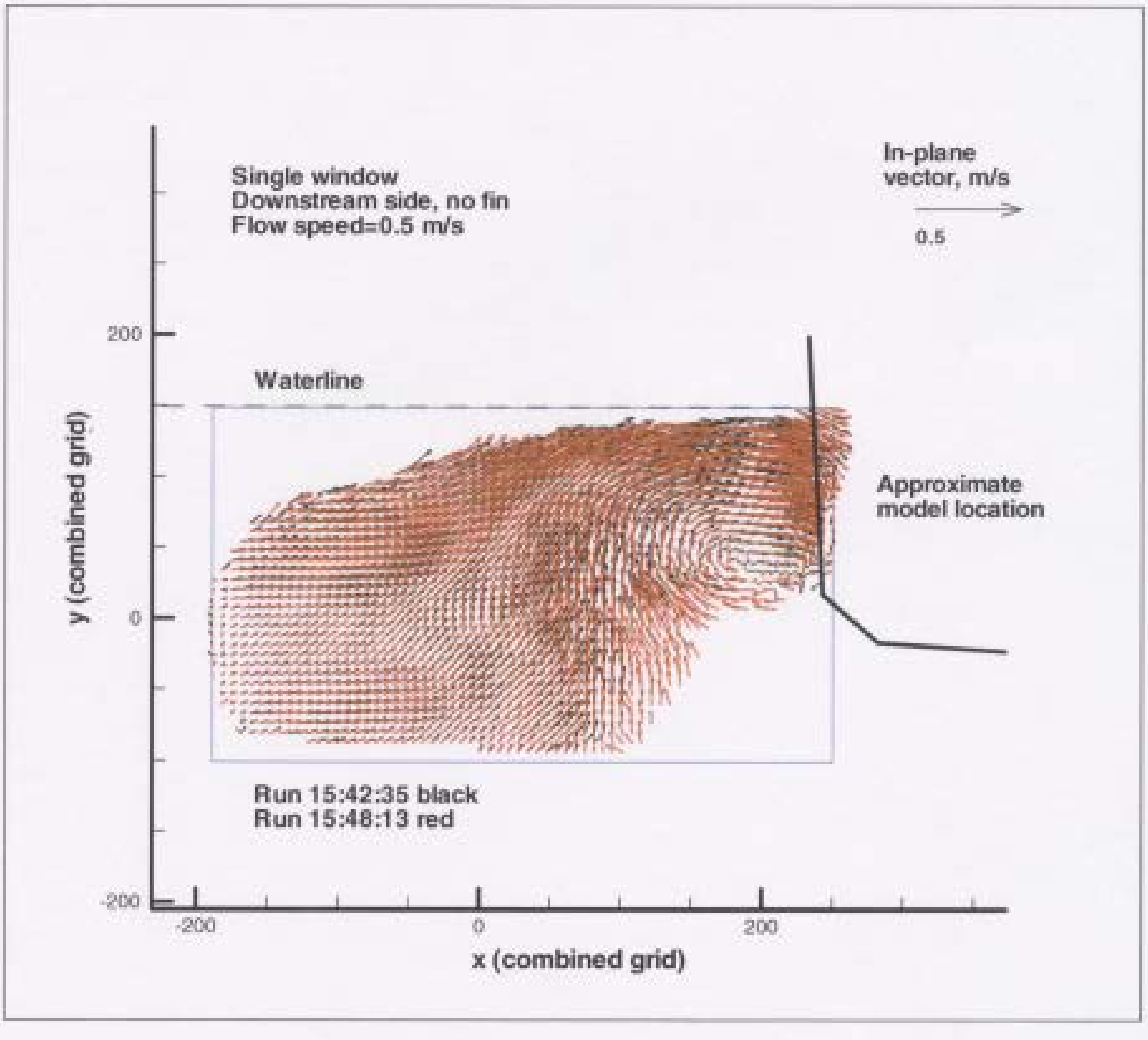

Figure 4-12, Mean in-plane flow vectors, downstream side of hull without fin, bilge to waterline, flow speed 0.5 m/s

d) Tug Without Fin, Downstream Side, Under Hull

The flow patterns for the region under the downstream bilge corner are shown in Figure 4-13. This region is under the one shown in Figure 4-12. Figure 4-13 shows that the flow has a strong upward component over almost the entire measurement window. The only area where the flow changes direction is on the downstream corner of the bilge, where the upward flow vectors are redirected into an almost horizontal direction when the flow encounters the hull. It is likely that this strong horizontal flow, off the downstream bilge corner is the major contribution to the formation of the vortex shown in Figure 4-12. Other than this redirection of the flow in the top right-hand corner of the window, the flow is almost uniformly upwards.

For the view in Figure 4-13, the horizontal seeding rake used was located well under the model. The view given in Figure 4-13 shows that the flow entering the region, which was undefined in Figure 4-12 is coming from a completely different direction than the rest of the flow in Figure 4-12. The full definition of vectors within the window given in Figure 4-12 would have required two seeding rakes to be operated simultaneously.

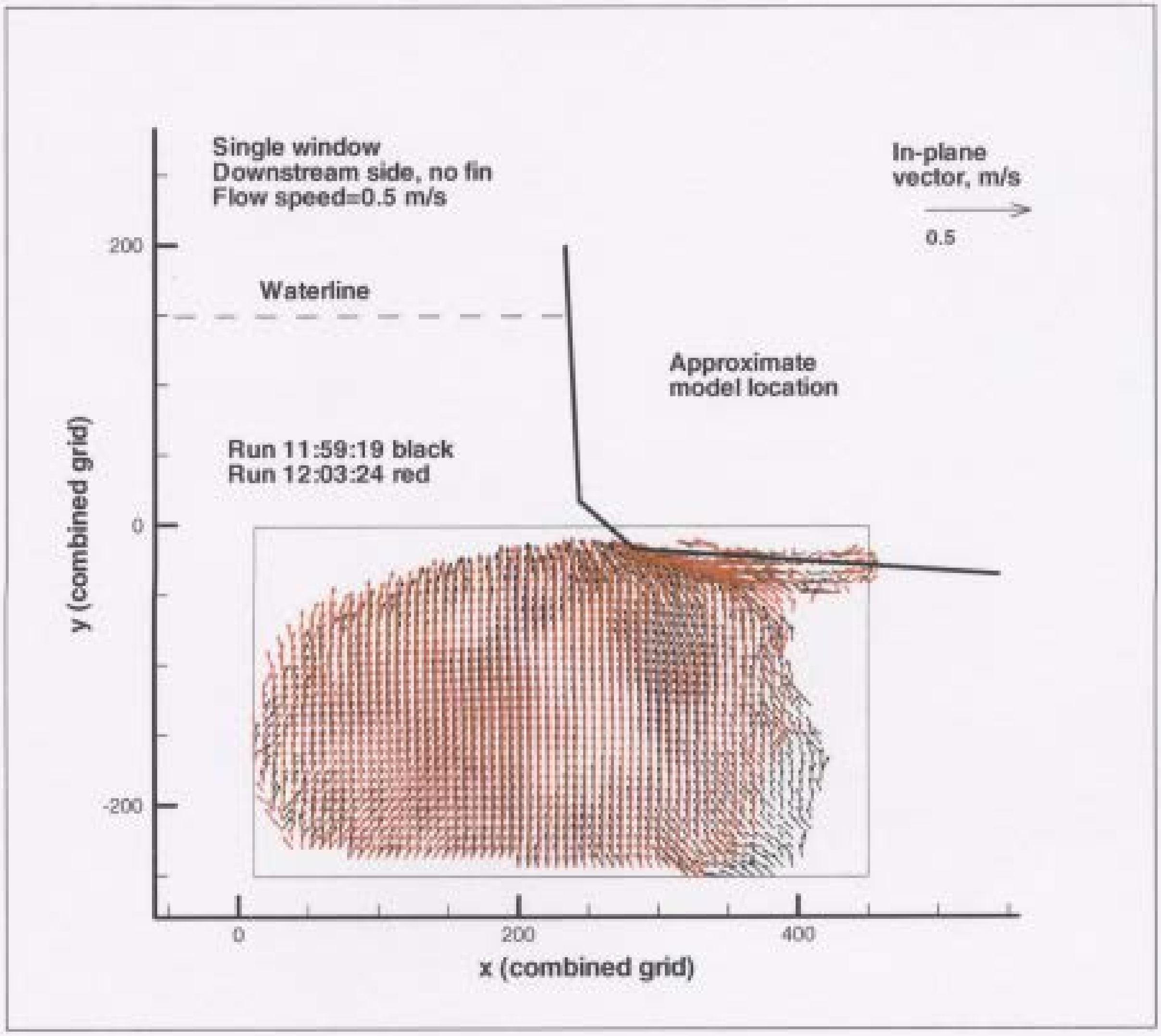

Figure 4-13, Mean in-plane flow vectors, downstream side of hull without fin, under hull, flow speed 0.5 m/s

e) Tug With Fin, Downstream Side, Close to Waterline

The flow patterns on the downstream side of the hull with the fin fitted, between the waterline and the bilge corner, are shown in Figure 4-14. The flow is relatively uniform with an upstream component (from left to right) back towards the hull, with some curvature, so that the flow is upwards on the left hand side, but horizontal on the right hand side.

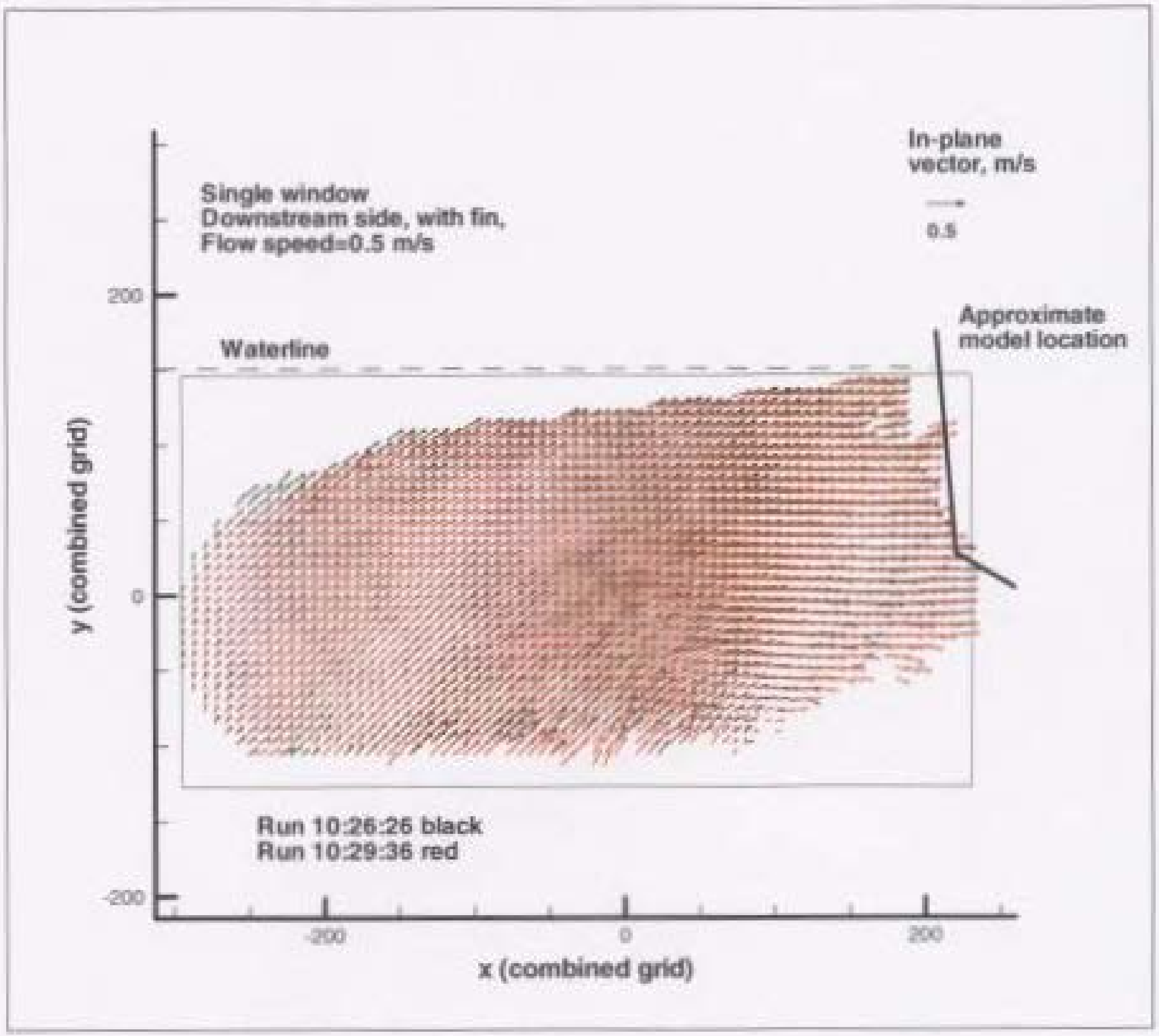

Figure 4-14, Mean in-plane flow vectors, downstream side of hull with fin, bilge to waterline, flow speed 0.5 m/s

Comparing Figures 4-12 and 4-14 shows the effect of the fin on the flow in this region, between the waterline and the downstream bilge. Figure 4-14 shows no sign of the vortex caused by flow separating off the bilge corner that was seen in Figure 4-12.

f) Tug With Fin, Downstream Side, Under Hull

The flow patterns under the hull, on the downstream side, are shown in Figure 4-15. This figure shows the presence of a large vortex, centred under the edge of the hull. This vortex was contained within a single measurement window, and the two different data sets give the core at approximately the same location. Comparing Figure 4-15 with Figure 4-13 shows one effect of fitting the fin, as this large vortex was not seen in Figure 4-13.

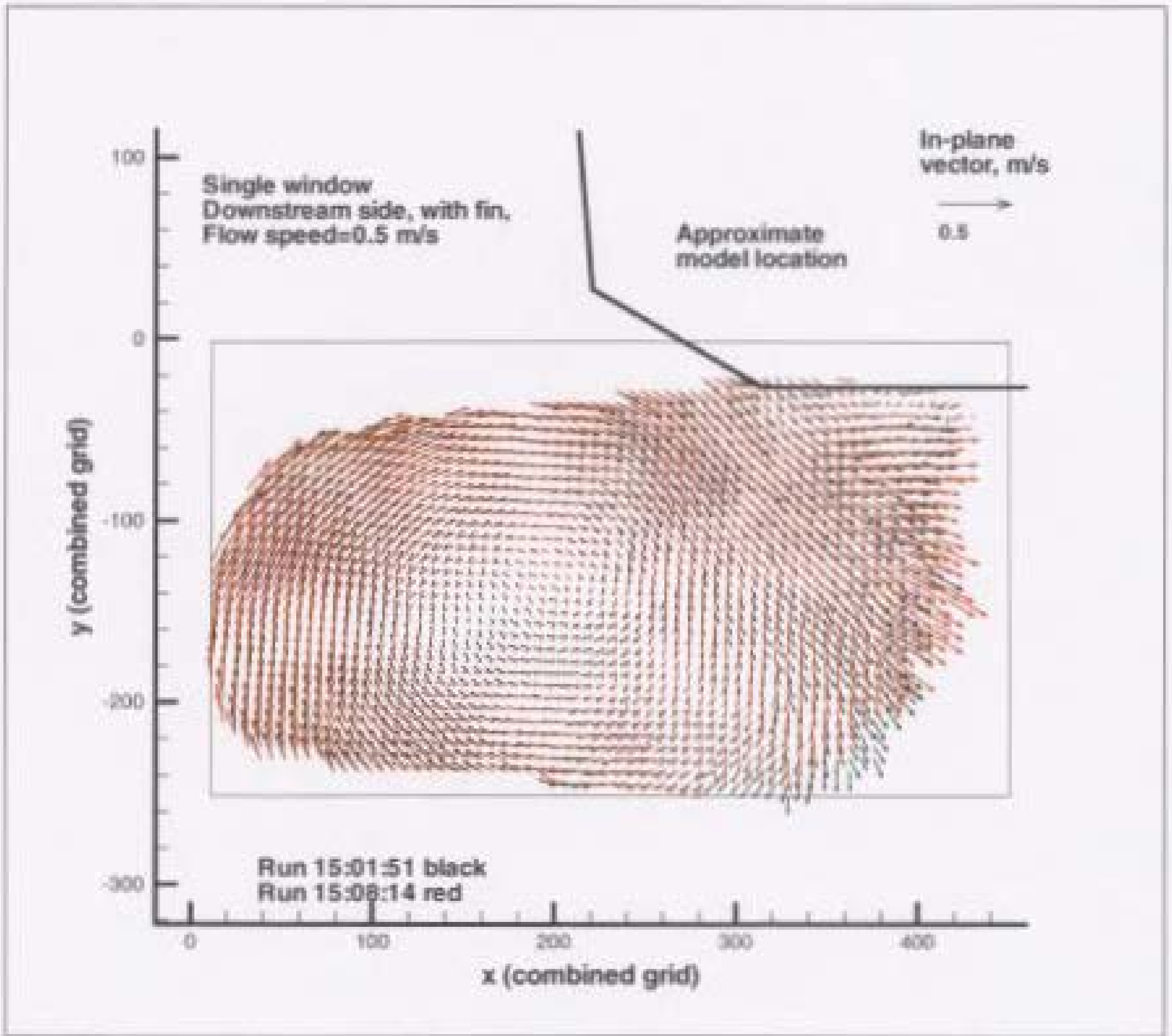

Figure 4-15, Mean in-plane flow vectors, downstream side of hull with fin, under hull, flow speed 0.5 m/s

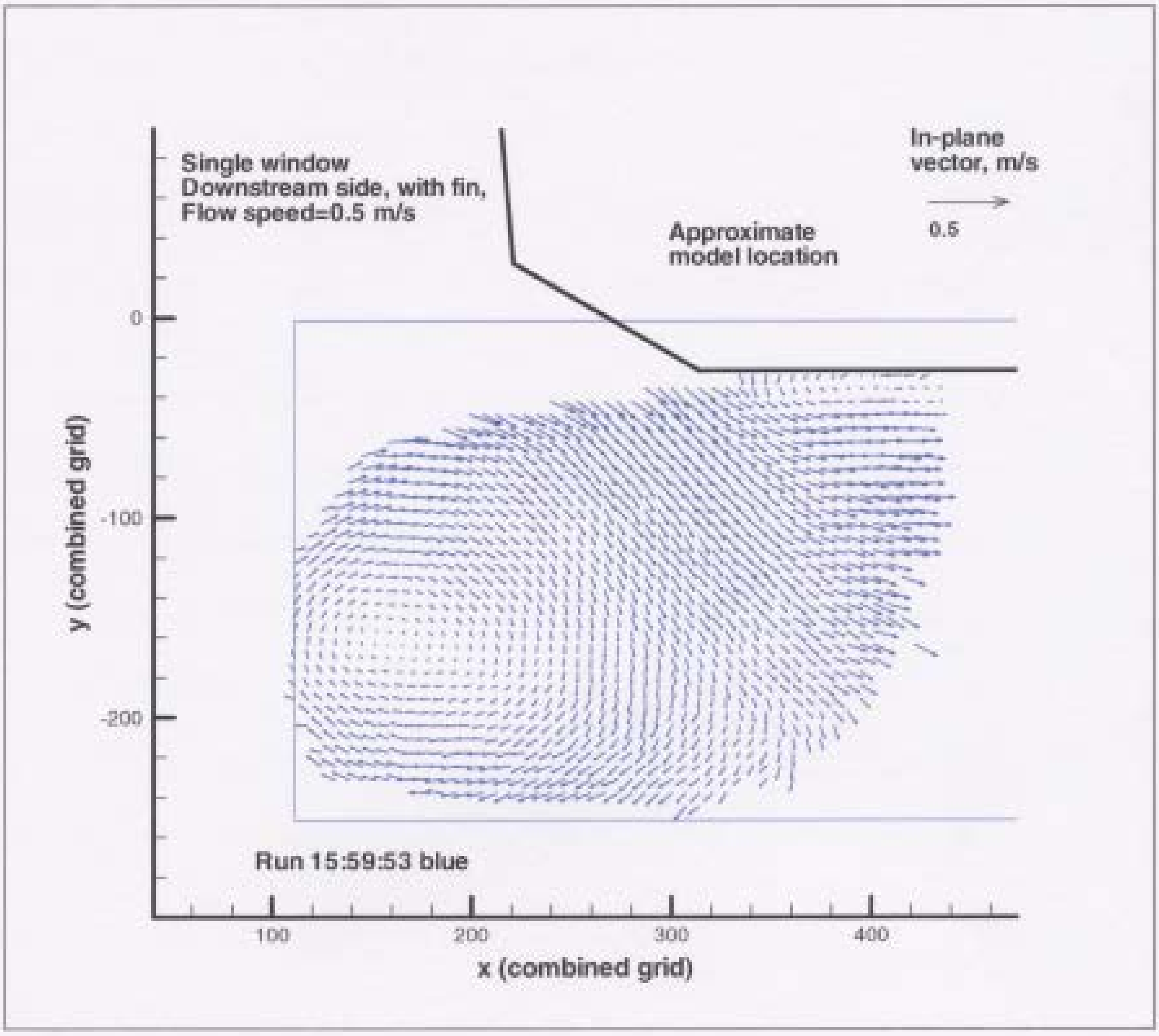

Figure 4-16, Mean in-plane flow vectors, downstream side of hull, with fin, under hull, flow speed 0.5 m/s

A second view of the flow in this condition is shown in Figure 4-16. The location for this view was even further under the hull than the view given in Figure 4-15. Only one experiment was available for this location but it is included in the discussion because it shows some complex flow patterns. The upstream flow component at the top of the vortex can be seen to separate off the downstream bilge corner, so the flow away from the hull is moving upstream, but the flow close to the hull is moving downstream. This is the opposite direction to the vortex observed on the upstream side of the bilge, so this indicates the presence of two regions of separated flow on the underside of the hull caused by the bilge corners when the fin is fitted. The seeding rake location for these views was approximately the same as for the case when the fin was removed.

This location, under the hull on the downstream side, with the fin fitted, showed the greatest discrepancy between the two vector sets for different data sets. Figure 4-15 shows more difference between the two sets of vectors than any of the other cases presented, as can be seen when Figure 4-15 is compared to the other figures. The extent of the unsteadiness in the flow at this location will be discussed below. The more turbulent flow actually aided seeding, since it tended to mix the seed particles, and resulted in a relatively even particle distribution over the measurement window.

4.5 OVERLAPPED PIV WINDOWS

4.5.1 Data Analysis

The complete flow pattern for the area of interest around the escort tug model was larger than a single window of the PIV system. Extending the measurement area beyond a single window required several movements of the model relative to the PIV system, and two depths of submergence for the PIV system within each plane. The increments of model movement in each direction were approximately one third of the dimension of the window (100mm). As a result a small area of the flow, relative to the model, should occur in at least three separate measurement windows.

The first step in the process of combining all the data within a measurement plane was to add the shift of the model (relative to the PIV measurement space) to the x and y coordinates obtained from the PIV window. The specific movement of each PIV system window to convert all the data from one measurement plane into a common grid system is given in Appendix 2.

The flow patterns obtained from different measurement windows at the same coordinates in the measurement plane were then compared. This was done by plotting the overlapped windows and comparing the measured velocity components. An example of some overlapped windows, for flow measurements on the downstream side of the hull, with no fin, is given in Figure 4-17. The vectors given were the average values for each window, using the thresholds discussed above. In general, the agreement between flow measurements for overlapped windows was very good, even when the flow conditions were highly unsteady.

The *DaVis* analysis software gave zero values for points where there was insufficient seeding to define the flow. These points had to be removed before integrating the data from different windows, otherwise the interpolation routine would include erroneous zero values for an area in one window where the same area had a valid non-zero value in another window covering the same area, but where the seeding was present. To remove these zero values, the magnitude of the flow velocity at each grid point was calculated, and points with zero flow magnitude were removed.

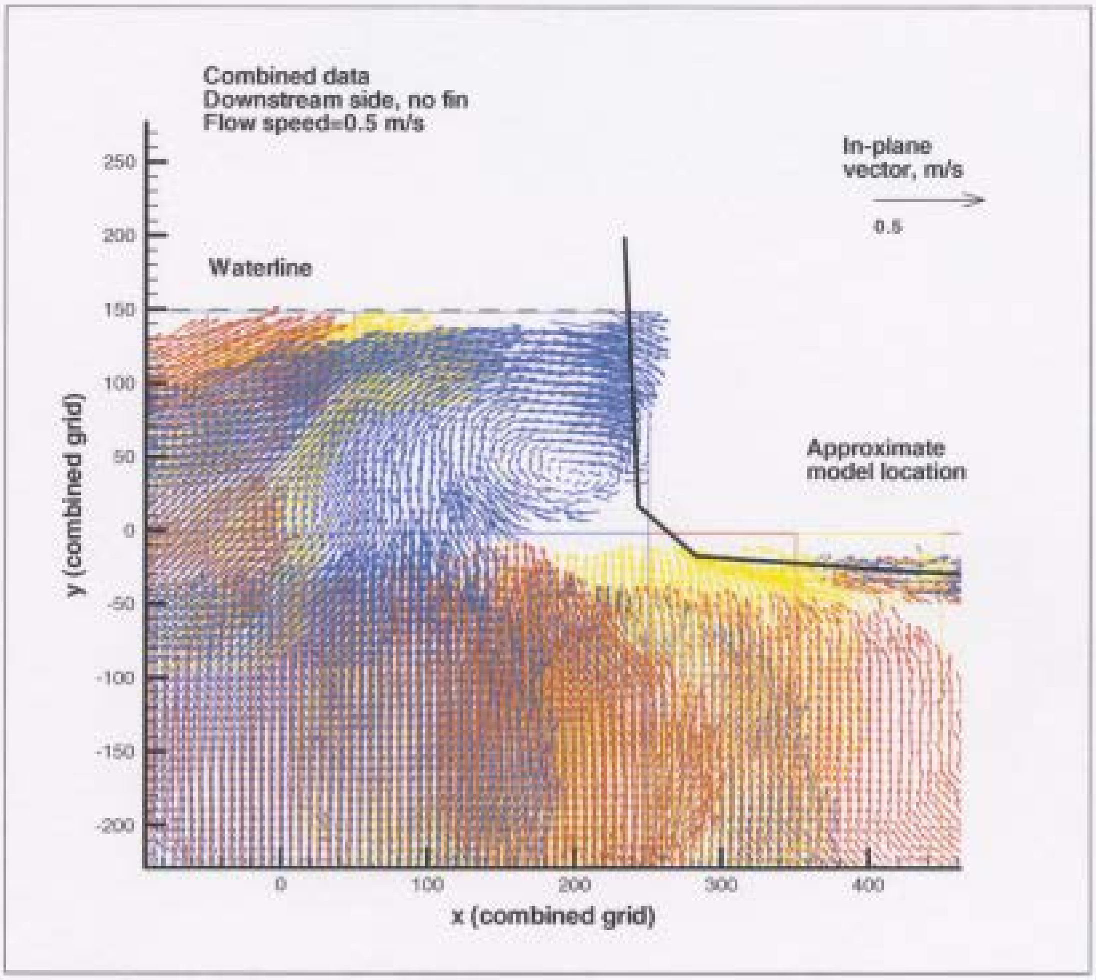

Figure 4-17, Example of overlapped windows, mean vectors for in-plane flow

The reduced data sets (excluding the zero flow magnitude cases) were combined and plotted as contours of velocity component (V_x, V_y, V_z). Examples of contour plots of the combined data for flow measurements on the downstream side of the hull with no fin, at a flow speed of 0.5 m/s are given in Figures 4-18a) to c).

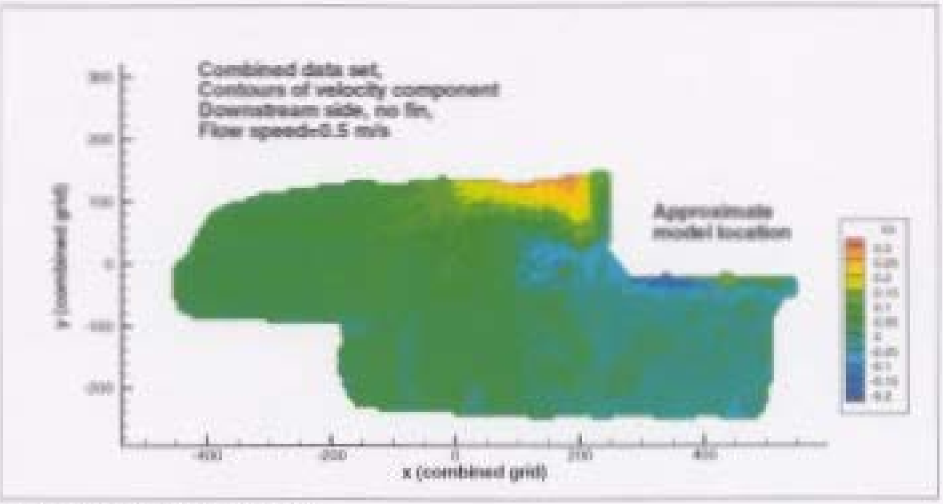

a) x-velocity component

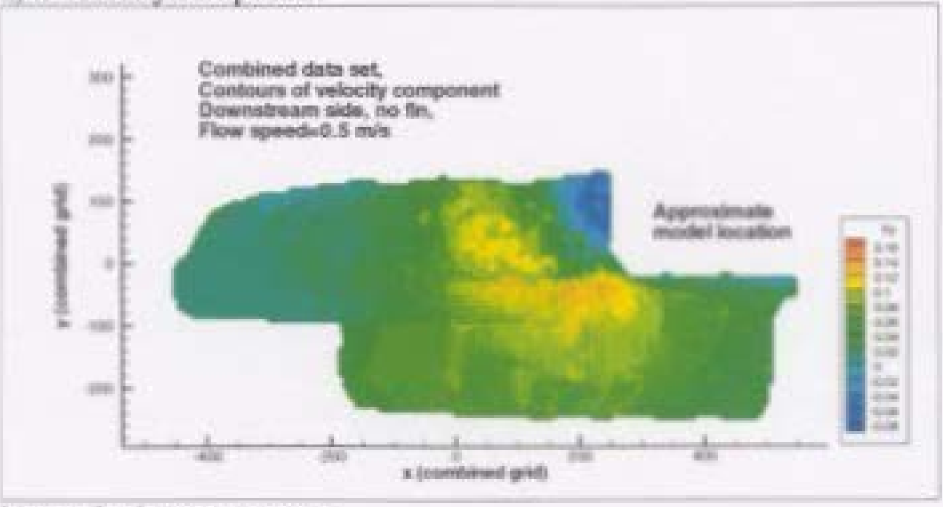

b) y-velocity component

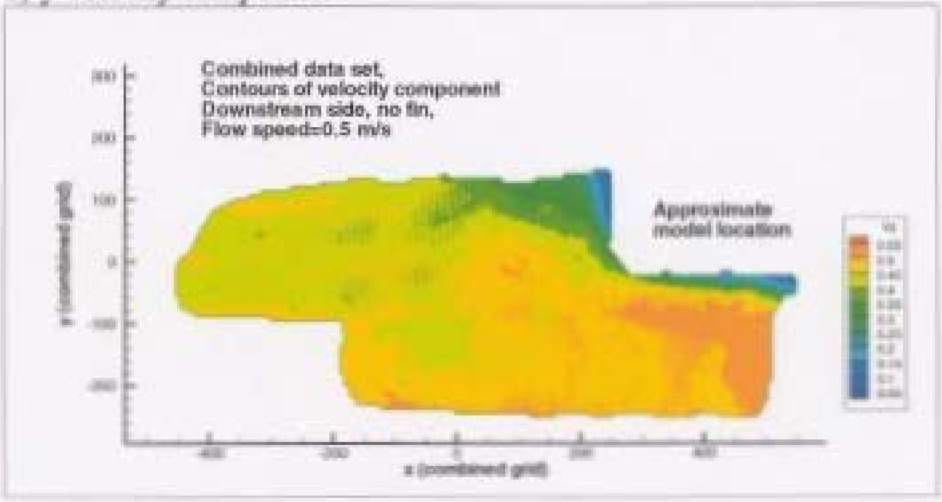

c) z-velocity component

Figure 4-18, Contours of velocity component, from overlapped windows

The contour values were interpolated on a larger scale grid, which extended over the full measurement space. The interpolated velocity components were re-combined into three-dimensional vectors and compared with the original data to check for any significant errors or discrepancies. An example of the comparison between the interpolated vectors for the in-plane flow and the vectors obtained from the PIV system is shown in Figure 4-19, which is for the same flow conditions shown in Figures 4-18a) to c). The data interpolation was carried out using *IGOR* (Wavemetrics, 2004) and the display of the final combined data set on the revised grid was made with *Tecplot*.

The grid size can be chosen depending on the nature of the flow being studied. For all the cases given here, the grid spacing presented was on 20mm squares. This grid can be used as the basis for detailed comparisons of the vectors calculated from the PIV experiments with CFD predictions for the flow, using the methods developed in Chapter 2.

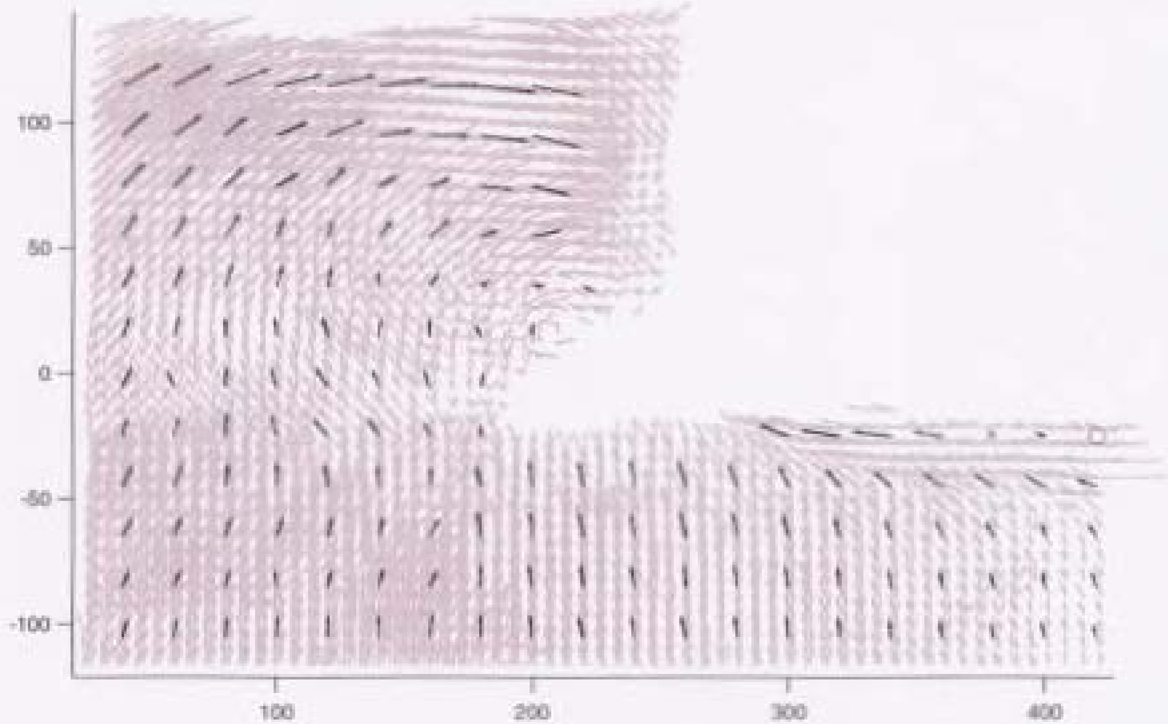

Figure 4-19, Comparison of in-plane vectors from combined experiment data (grey) with interpolated vectors (black), downstream side without fin, flow speed=0.5 m/s.

4. 5.2 Discussion Of Results

a) Upstream Side, Without Fin

The combined results for the upstream side of the hull, without the fin fitted are shown in Figures 4-20 and 4-21. Figure 4-20 includes the results for the cases shown in Figures 4-10 and 4-11. The combined results show the in-plane flow features, such as the flow away from the hull surface in the region of the flow close to the hull and the waterline, the separation of the flow from the upstream bilge corner and the upstream flow component close to the underside of the hull that have already been discussed. Also shown in Figures 4-20 and 4-21 are contours of through plane velocity. The through plane velocity is very low, close to the hull surface, but accelerates as it passes the underside of the hull.

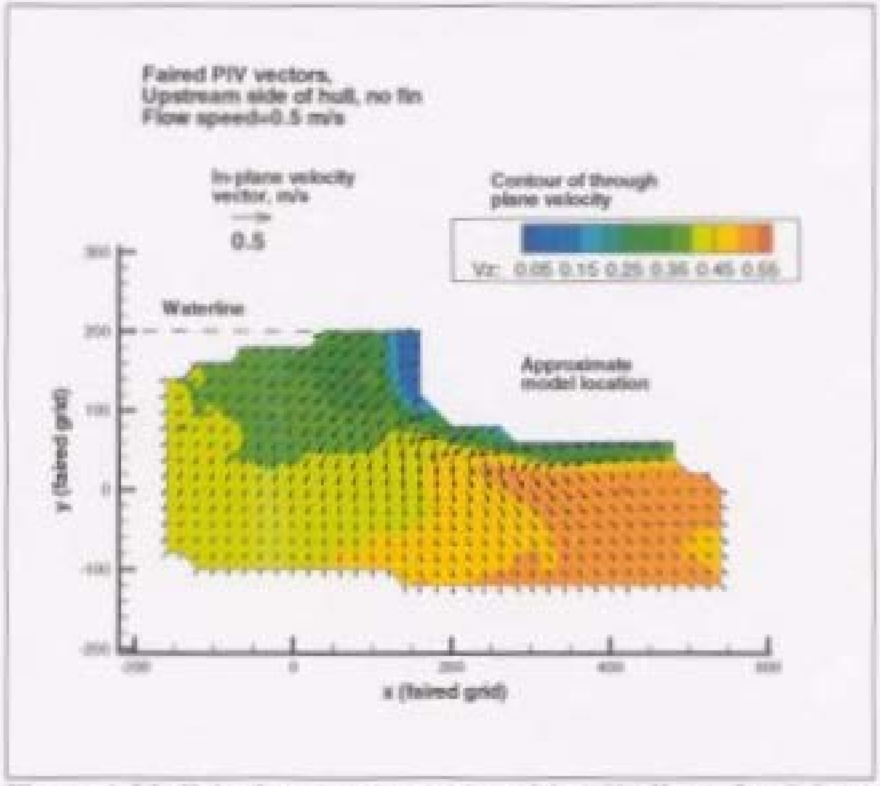

Figure 4-20, Faired vectors, upstream side of hull, no fin, 0.5 m/s

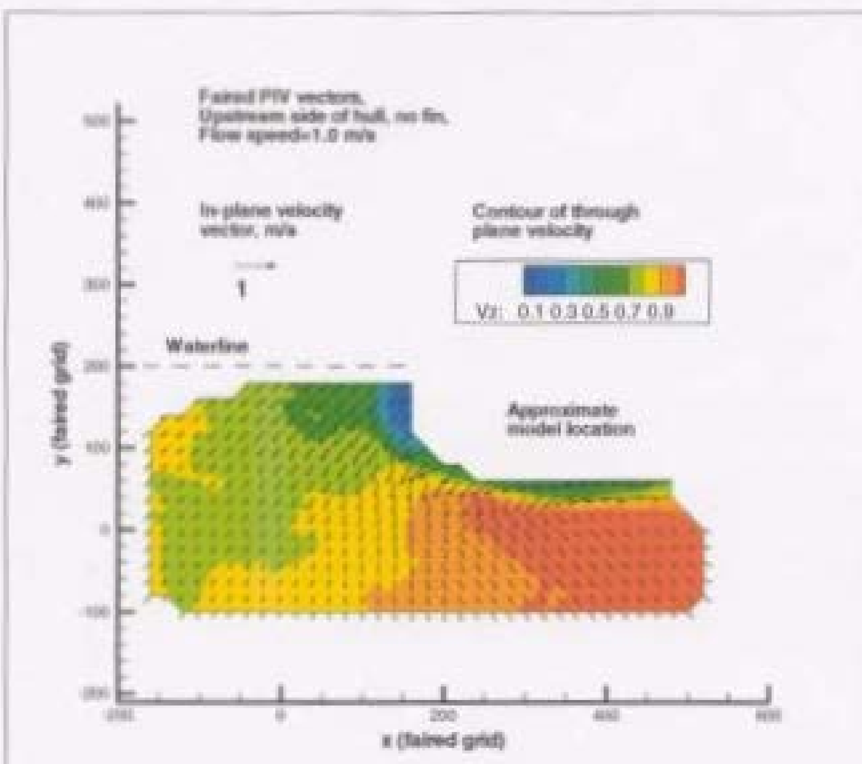

Figure 4-21, Faired vectors, upstream side of hull, no fin, 1.0 m/s

b) Downstream Side, Without Fin

The combined results for the downstream side of the tug, without the fin, are shown in Figures 4-22 and 4-23 for vectors of in plane flow components and contours of through plane flow speed. There are two dominant flow directions in these figures. One is an upward vertical flow under the hull, and away from the hull in the lower region of the measurement space. The other is a horizontal flow towards the hull, which was strongest close to the model and the water surface, which decreases in strength further away from the hull. Figures 4-22 and 4-23 also show the presence of a vortex on the downstream side of the hull, caused by the flow separating off the downstream bilge corner. This vortex extends from the underside of the hull to the waterline. Figure 4-22 includes the results shown in Figures 4-12 and 4-13.

c) Downstream Side With Fin

The combined results for the downstream side, with the fin fitted are shown in Figures 4-24 and 4-25. Both figures show the presence of a well-defined vortex located under the bilge corner, which extends the full depth of the combined measurement window. Figures 4-24 and 4-25 also show that the in-plane velocities towards the hull close to the water surface are stronger than for the case for the hull without the fin. When the fin is fitted, the effects of the hull on the flow are seen further away from the hull than when the fin is removed.

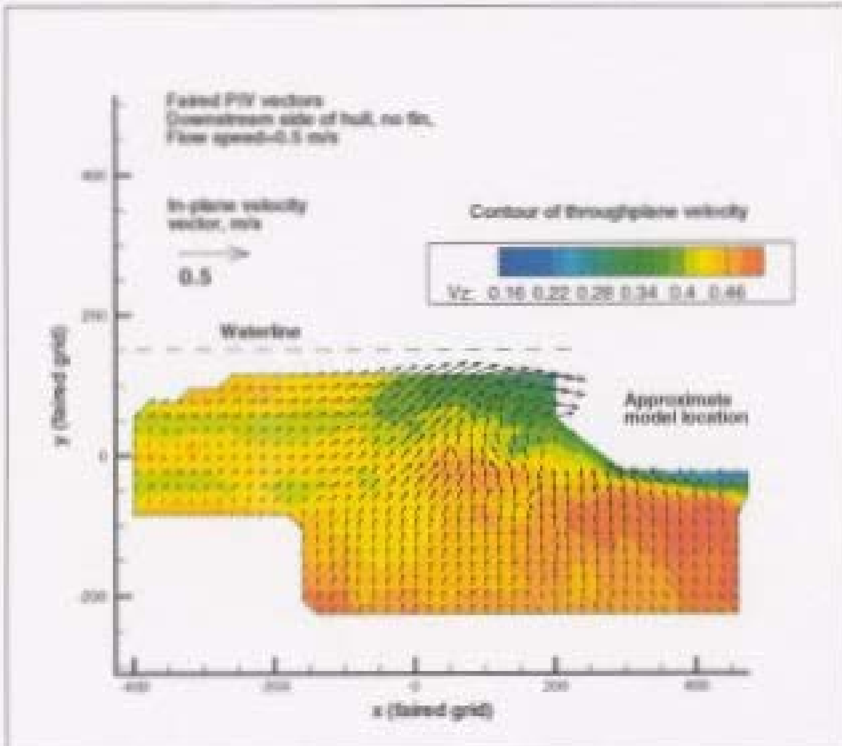

Figure 4-22, Faired vectors, downstream side, no fin, 0.5 m/s

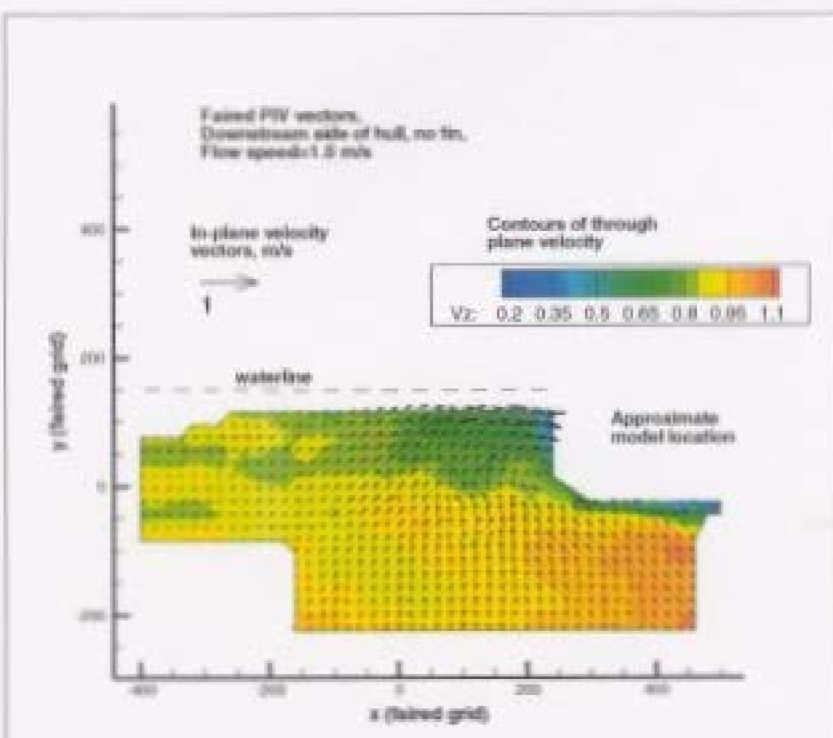

Figure 4-23, Faired vectors, downstream side, no fin, 0.5 m/s

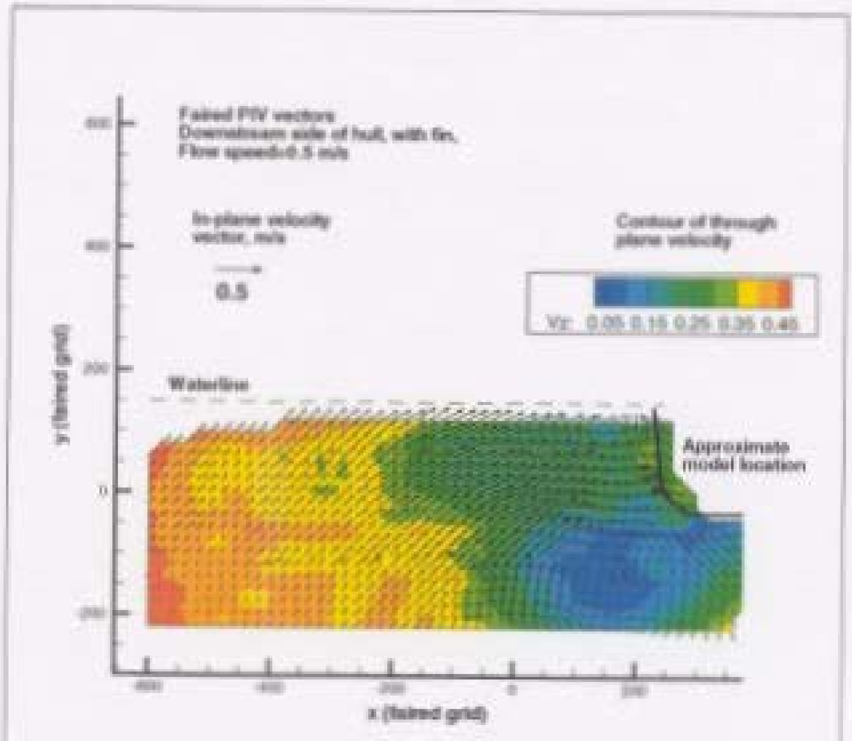

Figure 4-24, Faired vectors, downstream side, with fin, 0.5 m/s

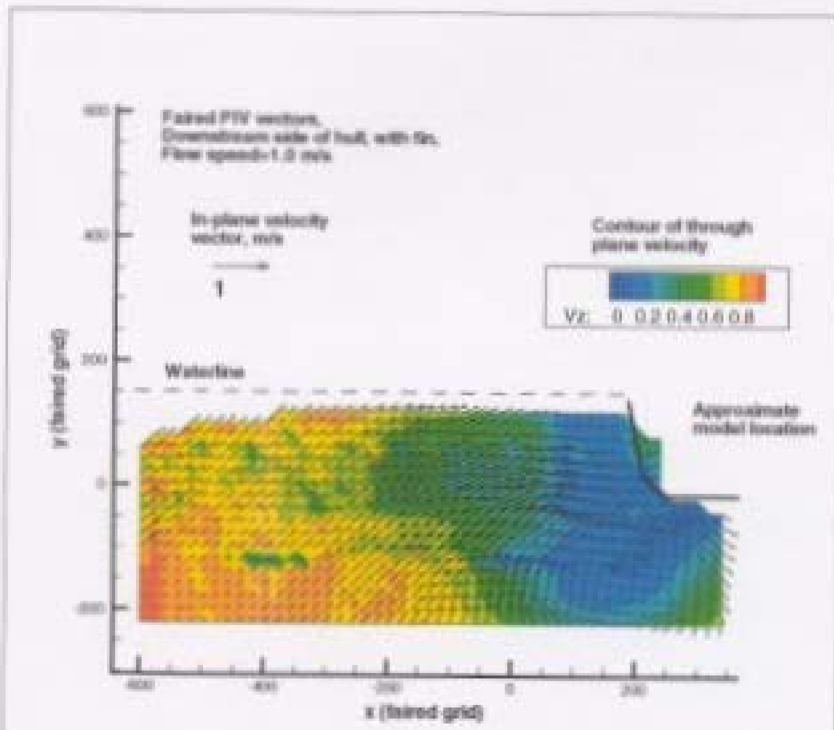

Figure 4-25, Faired vectors, downstream side, with fin, 1.0 m/s

Overall there was little change in the mean direction of the flow vectors with speed for the two speeds tested, but the magnitudes of the vector components changed with the undisturbed flow speed. The biggest difference was for the case shown in Figures 4-24 and 4-25 for the downstream side of the hull with the fin fitted. Here, the region of low speed flow extended further away from the hull at 1 m/s than at 0.5 m/s. Figure 4-24 includes the results shown in Figures 4-14, 4-15 and 4-16.

d) Fairing of Multi-Windowed PIV Data

Overall, the fairing process retained the essential features of the flow based on the vectors derived from the single PIV windows discussed above. There was some smoothing of the flow patterns when compared to the single windows. An example of this is the flow on the downstream side of the hull with the fin removed (Figure 4-22), which can be compared to the raw data (Figure 4-12). The flow within the vortex shown in Figure 4-22 has been smoothed out because the faired flow was based on the average vectors from several overlapped windows.

The advantage of the faired data was that it was based on vectors averaged over several overlapped analysis windows. As a result small variations in the flow patterns caused by distortions of the PIV image close to the edge of an analysis window, or differences in flow patterns caused by different rake designs and locations will be averaged out.

The smoothing process does result in the occasional vector that does not match the size or direction of those around it. This was caused when overlapping windows gave conflicting vector information for the same location. This typically occurred in regions where the flow was sparsely defined and the vectors from different windows were in different directions. This could have been caused by two factors. One factor was that the flow was unsteady and different average vectors were obtained for the same region with different experiments, as was the case in Figure 4-15, where although the vortex was well defined in each experiment, the centre of the vortex was not at exactly the same location.

Another factor was that the same region could be have been seeded with different seeding rakes, and in some cases, the change in seeding rake may have changed the resulting local flow vectors, if it was too close to the measurement region. These slight anomalies could be removed with further processing. This would require comparing each vector with its nearest neighbours and only allowing certain variations in the flow pattern in a manner similar to that used in the post-processing of the PIV data.

The loss of detail in some parts of the combined flow vectors flow can be overcome by reducing the area of comparison to the area of a single window in the region of interest. And refining the grid used for comparison. The analysis of the complete data set was required to check the consistency of the results over the full measurement space, which was much larger than the single measurement window.

The combined results discussed in this section were compared with CFD predictions for steady flow conditions over the same spatial region. This comparison is described in Chapter 5.

4.6 UNSTEADY FLOW

The average vectors for run 15:01:51 are shown in Figure 4-26. This shows the flow patterns on the downstream side of the hull, for the case when the fin was fitted. The vortex shown in this figure was also shown in the results of run 15:08:14, which was obtained at exactly the same location. The two results are shown together in Figure 4-15.

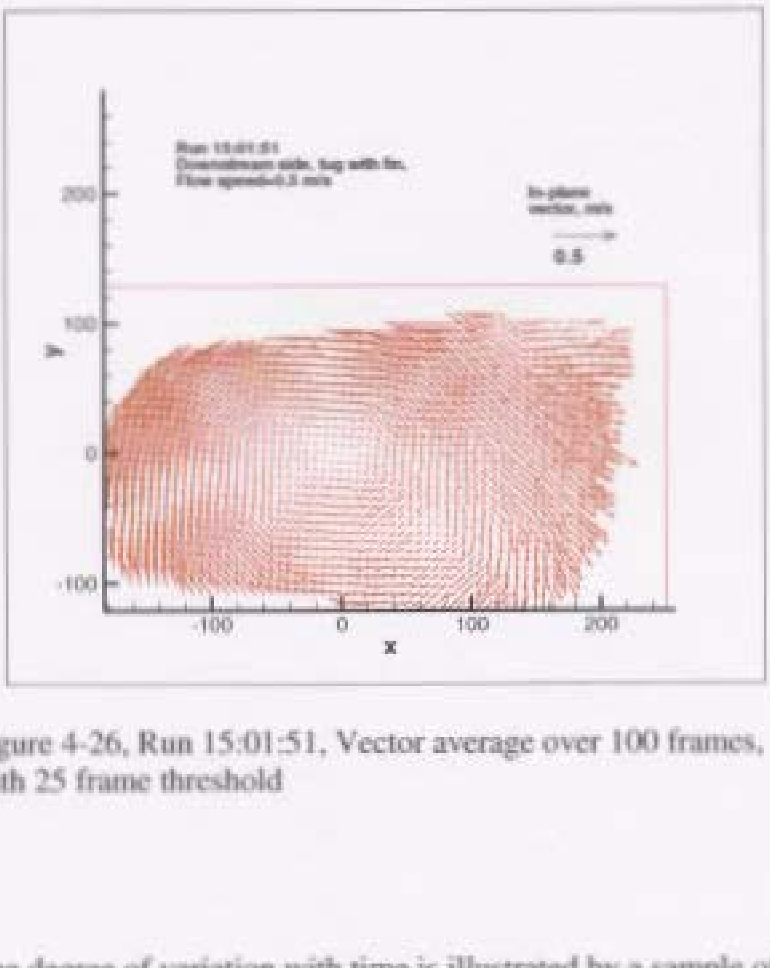

Figure 4-26, Run 15:01:51, Vector average over 100 frames, with 25 frame threshold

The degree of variation with time is illustrated by a sample of twelve consecutive vector images taken from run 15:01:51 and shown in Figures 4-27(a) to 4-27(l). These figures show that a vortex is visible in some figures, for example Figures 4-27(d) to 4-27(h). In some of the other figures the vortex is not seen at all, for example Figures 4-27(i) to 4-27(l). These twelve images when combined with the rest of the data set show that the average pattern is the well-defined vortex shown in Figure 4-26. So even though the flow was unsteady, the long-term average was relatively stable, which is the classical definition of turbulent flow, and provides a justification for using RANS codes to analyze the flow conditions.

It was expected that the flow around the escort tug hull would be unsteady, based on visual observations made during earlier experiments (Molyneux, 2003, Molyneux and Xu, 2005) but a numerical quantification of the level of unsteadiness was unknown. It is generally accepted that PIV systems are unsuitable for providing a numerical definition of turbulence in a fluid (Van den Braembussche, 2001) because the sampling rates are too low to capture high frequency variations. The sampling rate between image pairs for the PIV system used in these experiments was 5 Hz. Even though this sampling rate was relatively low, one measure of the unsteadiness in the flow that was obtained from the *DaVis* software (LaVision, 2005) is the RMS value of the vector components. Areas of flow with high RMS values will be areas of high turbulence although a true numerical estimate of the turbulence cannot be made.

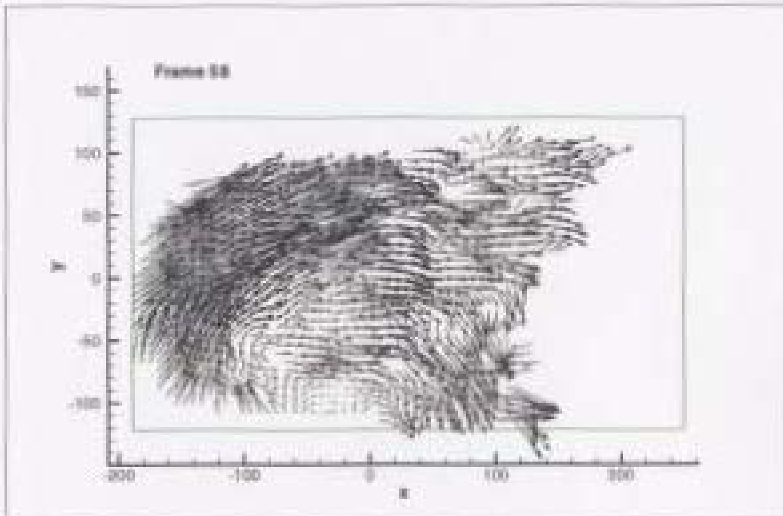

a)

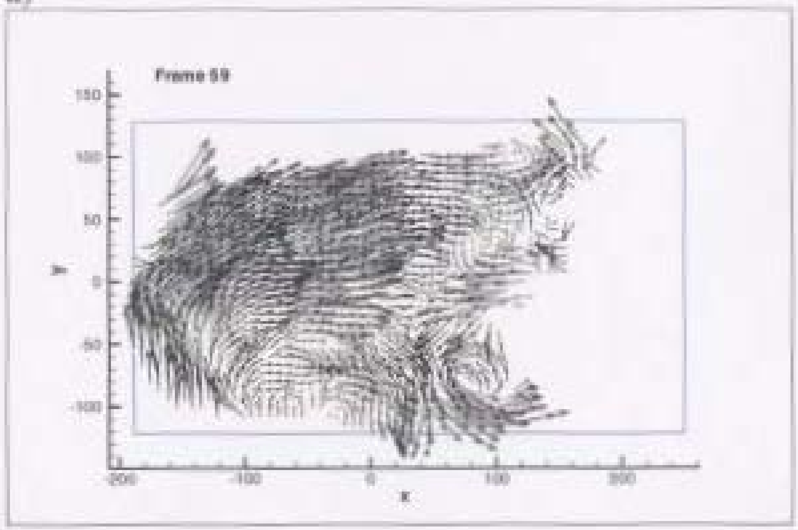

b)

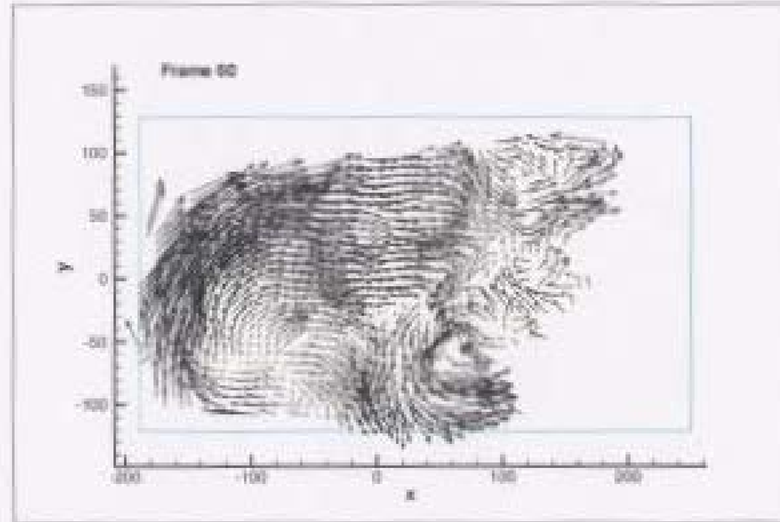

c)

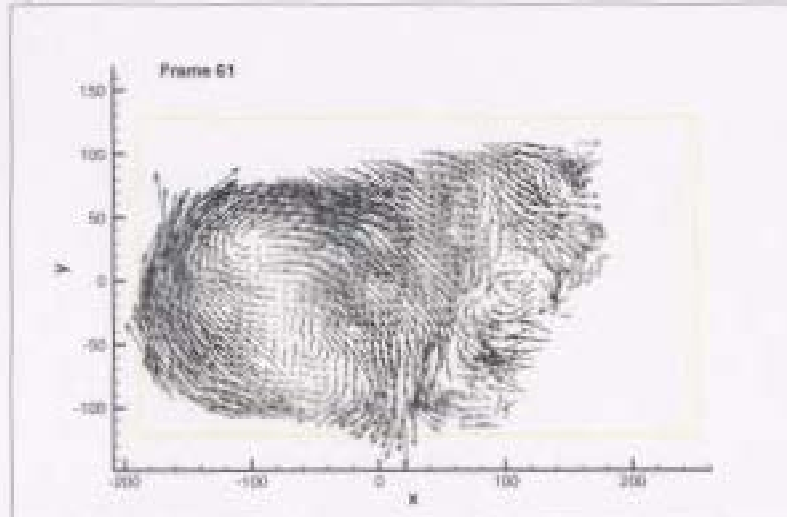

d)

Figure 4-27, Run 15:01:51, Consecutive time steps at 1000 μs intervals

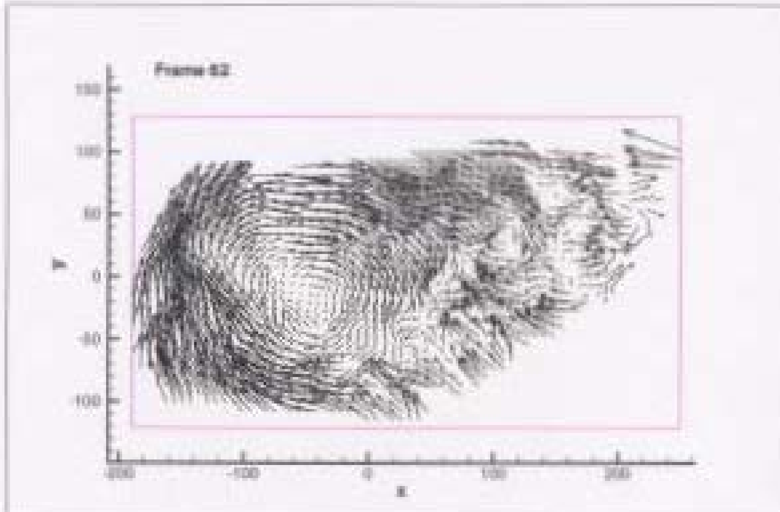

e)

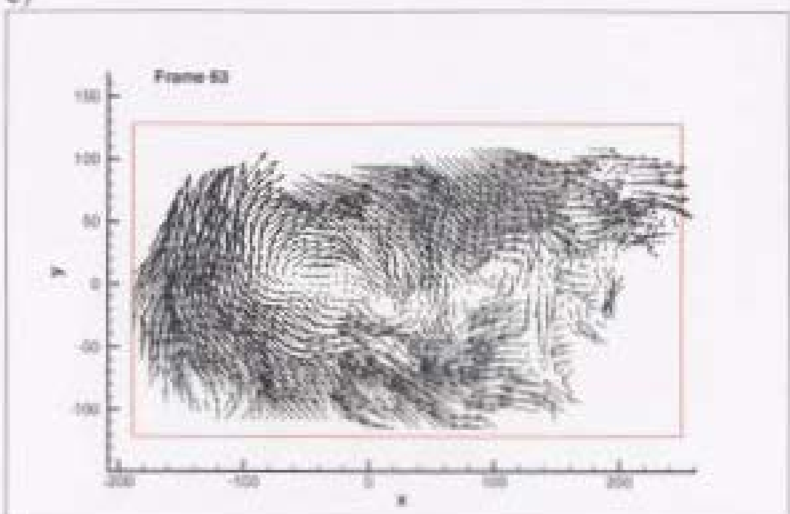

f)

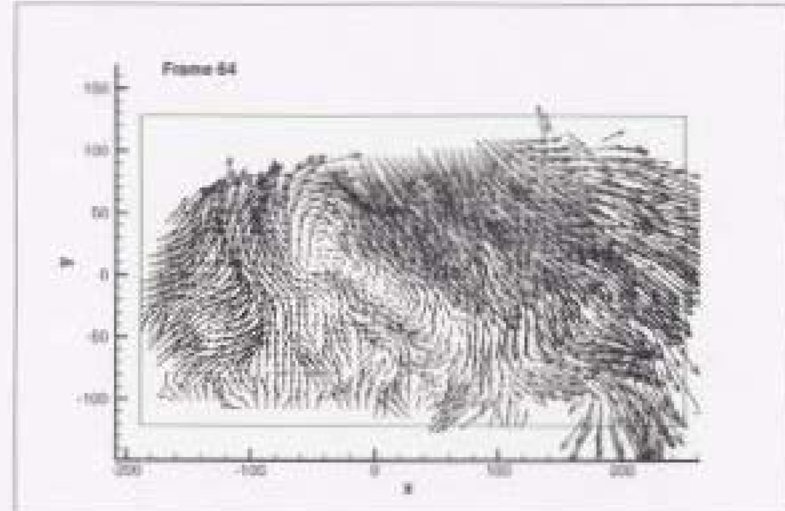

g)

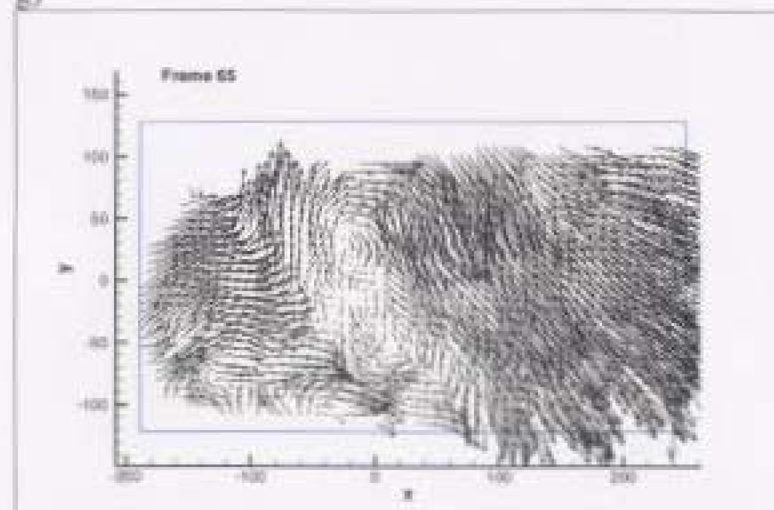

h)

Figure 4-27, Run 15:01:51, Consecutive time steps at 1000 μs intervals

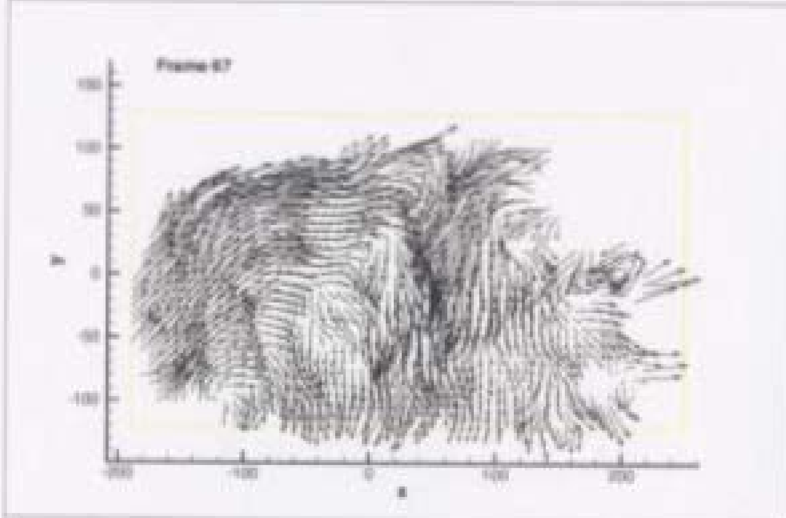

i)

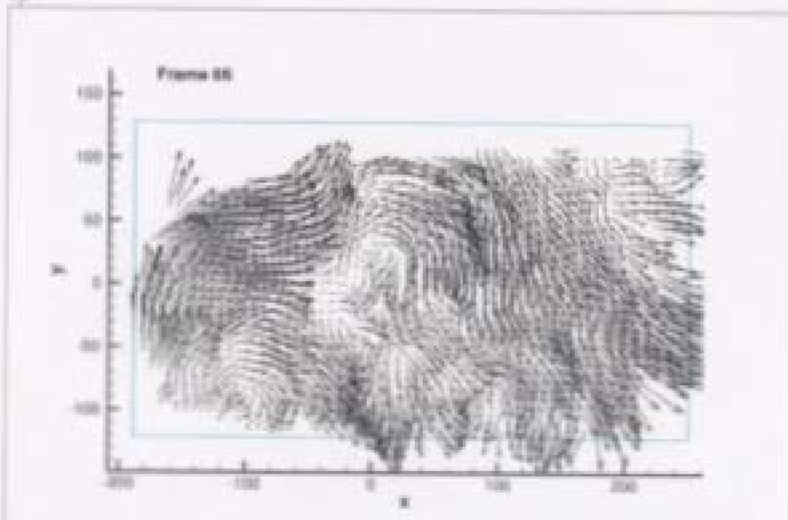

j)

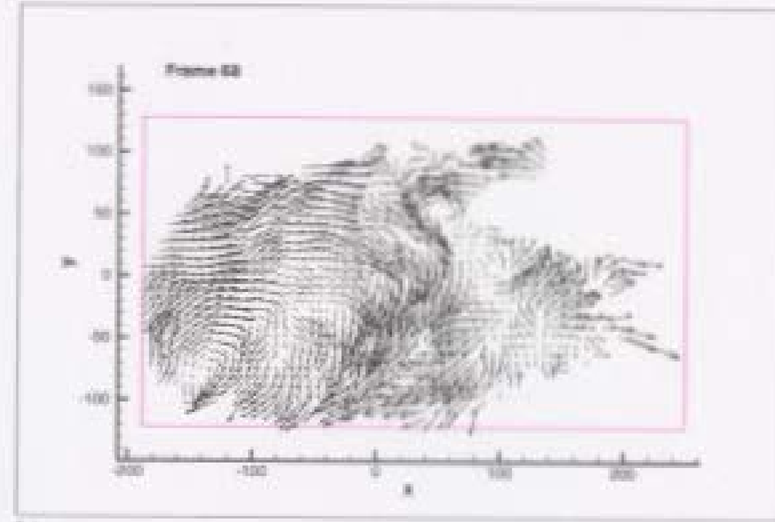

k)

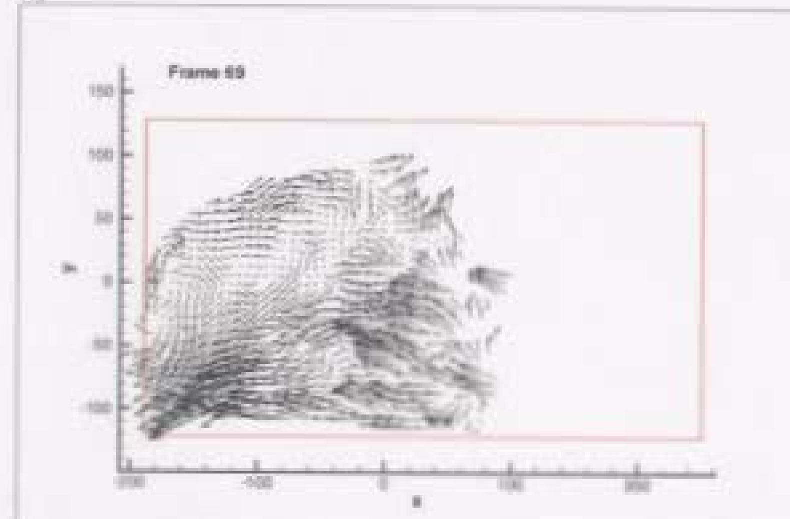

l)

Figure 4-27, Run 15:01:51, Consecutive time steps at 1000 μs intervals

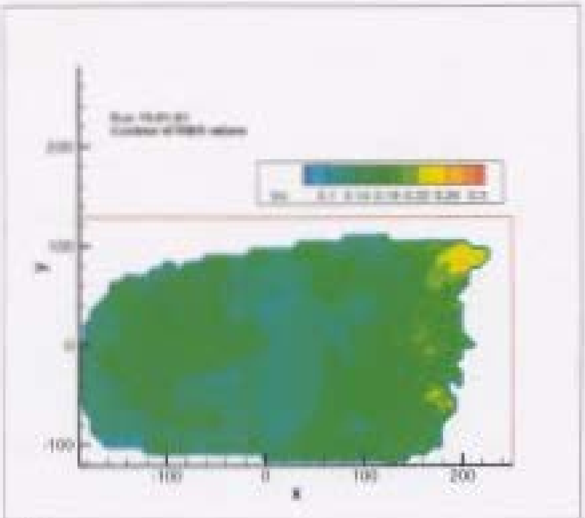

a) Vx

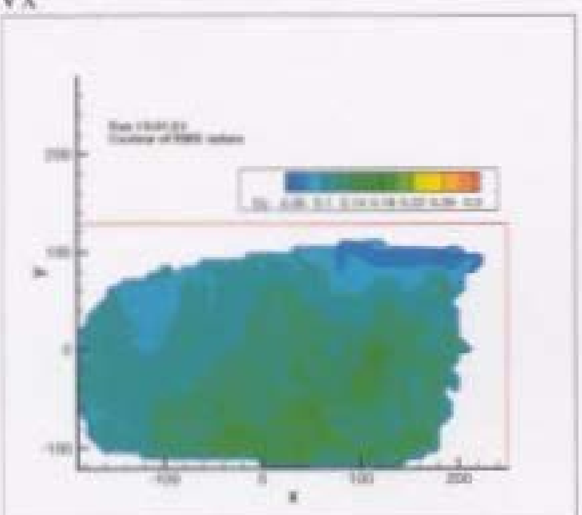

b) Vy

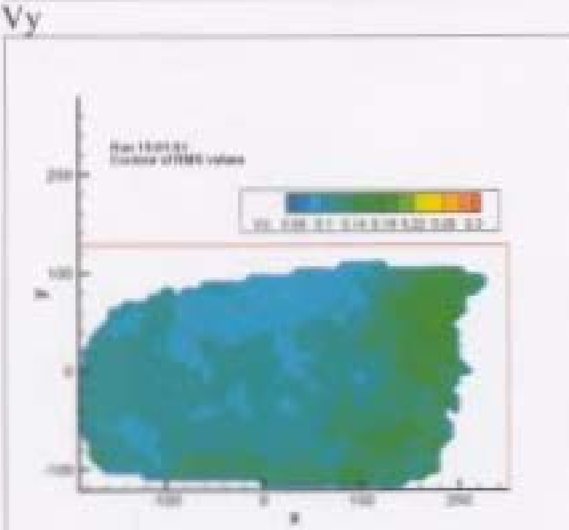

c) Vz

Figure 4-28, Run 15:01:51, Contours of RMS velocity component

Contours of RMS value for each velocity component over Run 15:01:51 for the complete sequence of time steps are shown in Figures 4-28(a) to 4-28(c). These figures show that the *x*, *y* and *z* components have similar values of RMS flow component, especially in the centre of the measurement window and the magnitude of the RMS value is mostly between 0.10 and 0.14, for an undisturbed flow speed of 0.5 m/s. The only exception is the very top right hand corner for the *x* velocity component, and this region is calculated from a smaller number of valid vectors.

The RMS values for the individual windows were combined using the same approach as the one used for the flow vectors. RMS values for each velocity component were placed on a common grid and points within the PIV mesh where no vectors were calculated were removed. The combined data were plotted as contours and interpolated on the same grid used for the velocity components. The resulting values are shown in Figures 4-29 to 4-34.

RMS values for the upstream location at midships are shown in Figures 4-29 and 4-30, for flow speeds of 0.5 and 1.0 m/s respectively. The highest turbulence was observed close to the hull and close to the free surface.

The downstream location with no fin is shown in Figures 4-31 and 4-32 for flow speeds of 0.5 m/s and 1.0 m/s. The highest areas of turbulence are close to the downstream bilge. In this measurement area the free surface had less effect on the unsteadiness in the flow.

Figures 4-33 and 4-34 show the RMS values for the case when the fin was fitted. The area of the highest turbulence extended the full depth of the measurement area and was in the same location as the vortex caused by the fin. A major effect of the fin was to increase the amount of turbulence in the flow.

In all cases, the level of turbulence does not change significantly between velocity components.

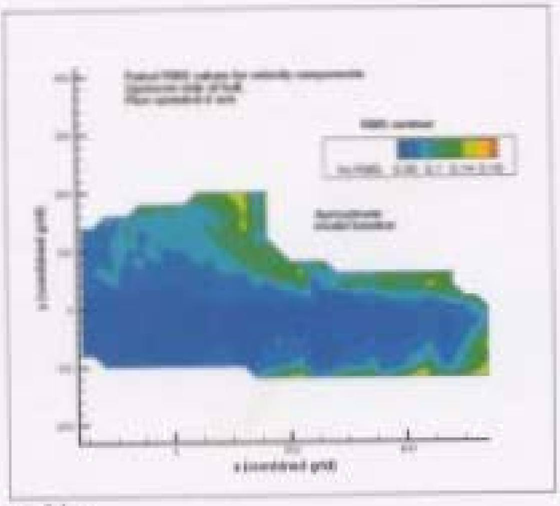

a) Vx

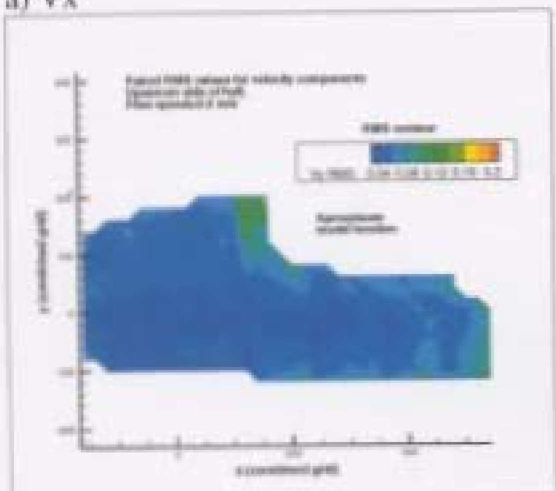

b) Vy

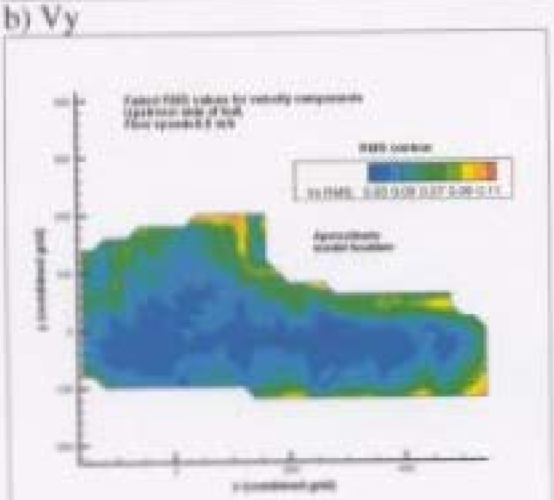

c) Vz

Figure 4-29. Contours of RMS for flow component, upstream, 0.5 m/s

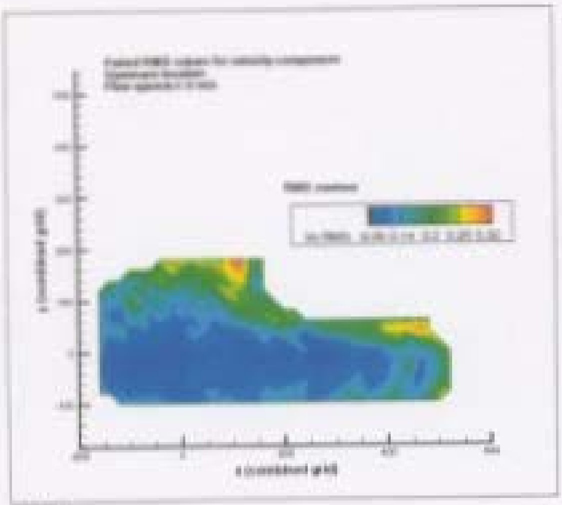

a) Vx

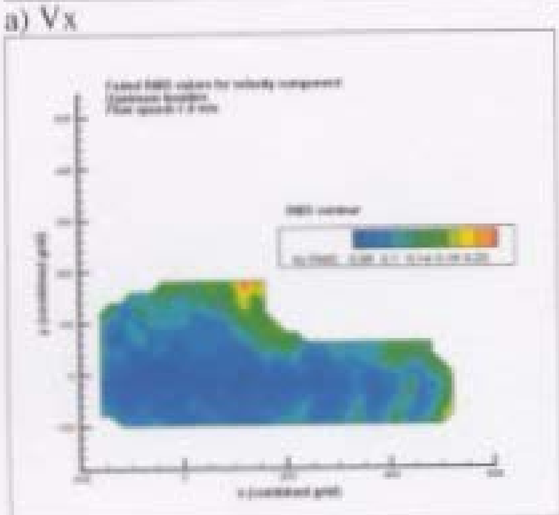

b) Vy

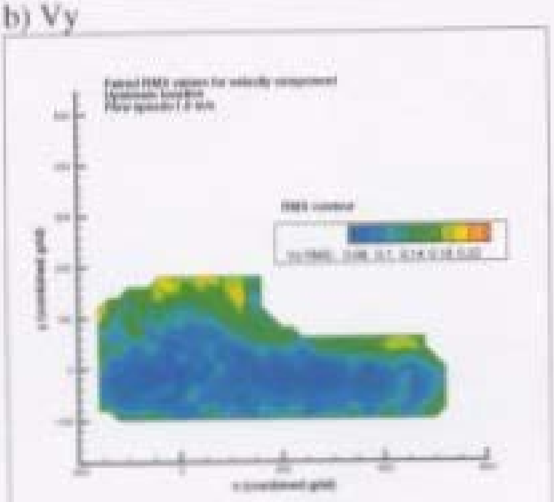

c) Vz

Figure 4-30. Contours of RMS for flow component, upstream, 1.0 m/s

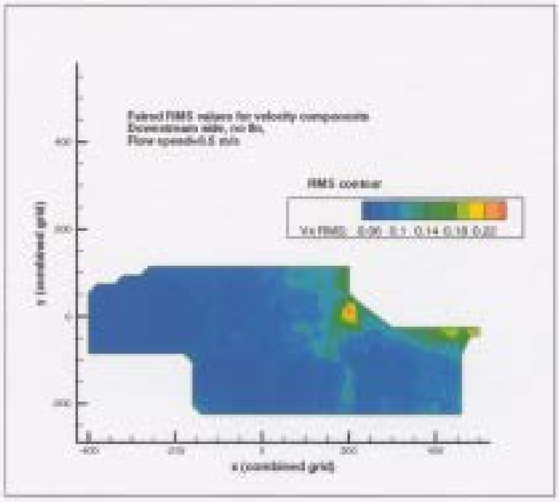

a) Vx

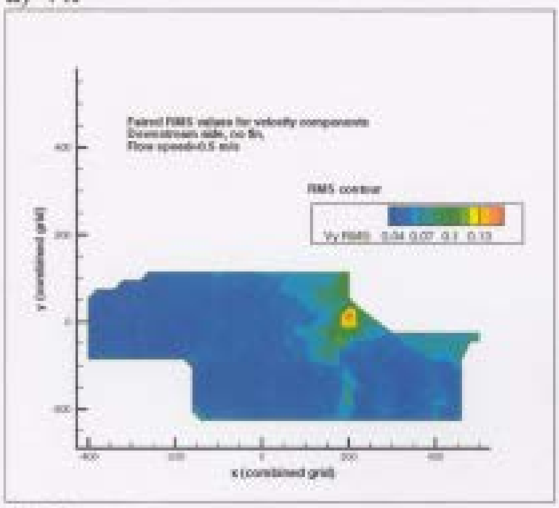

b) Vy

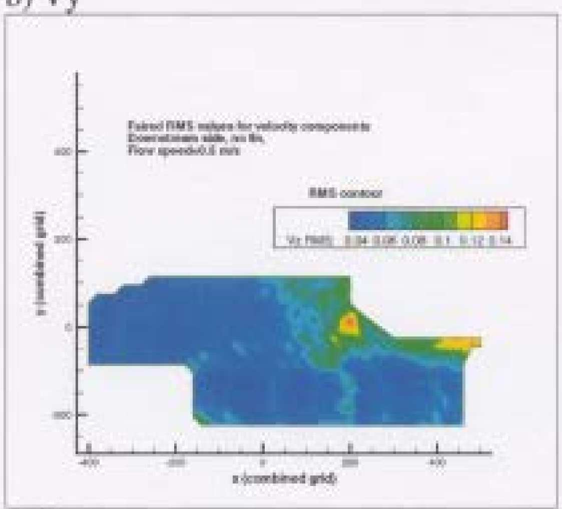

c) Vz

Figure 4-31, Contours of RMS for flow component, downstream, no fin, 0.5 m/s

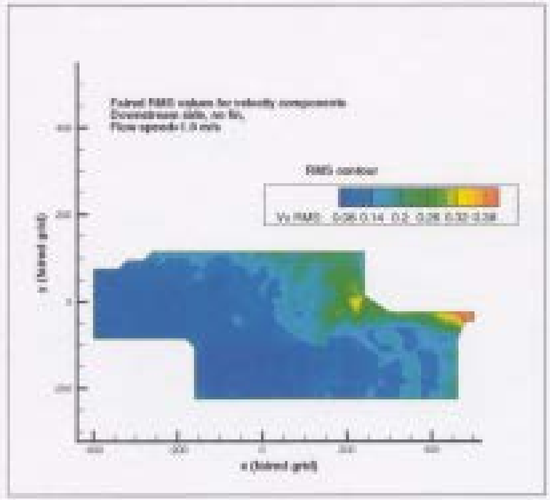

a) Vx

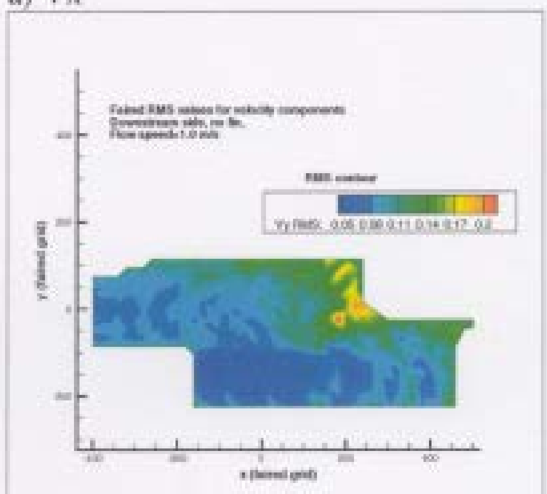

b) Vy

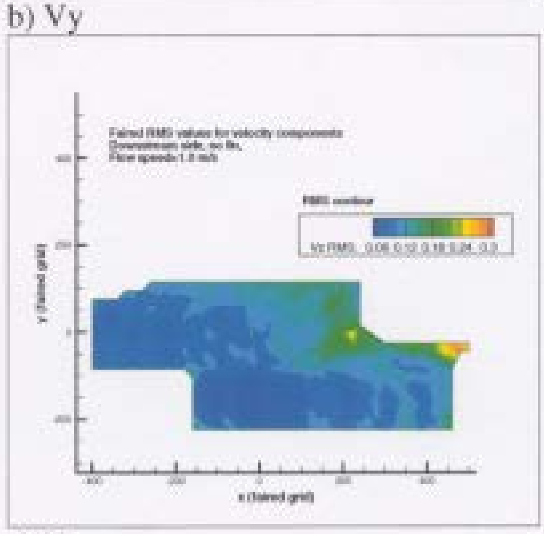

c) Vz

Figure 4-32, Contours of RMS for flow component, downstream, no fin, 1.0 m/s

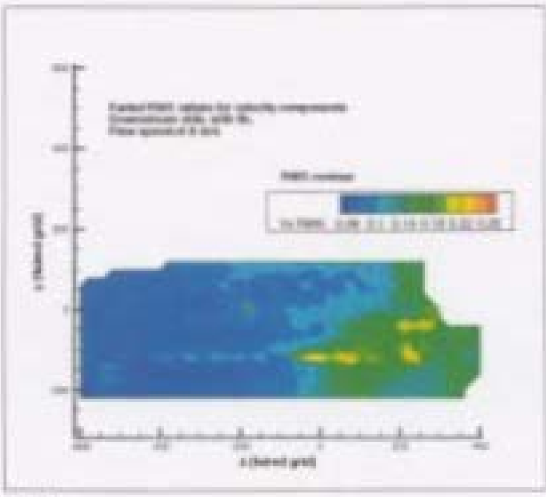

a) Vx

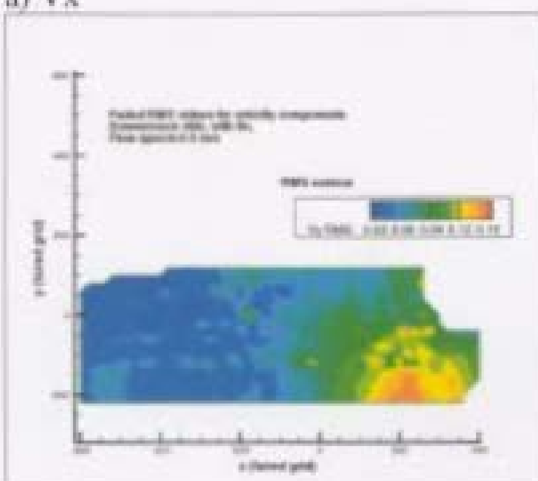

b) Vy

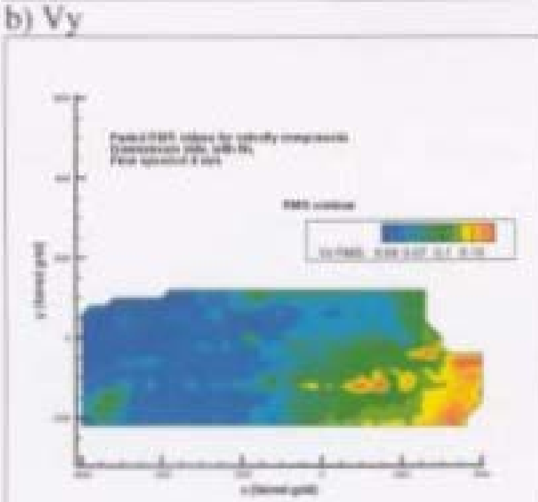

c) Vz

Figure 4-33, Contours of RMS for flow component, downstream, with fin, 0.5 m/s

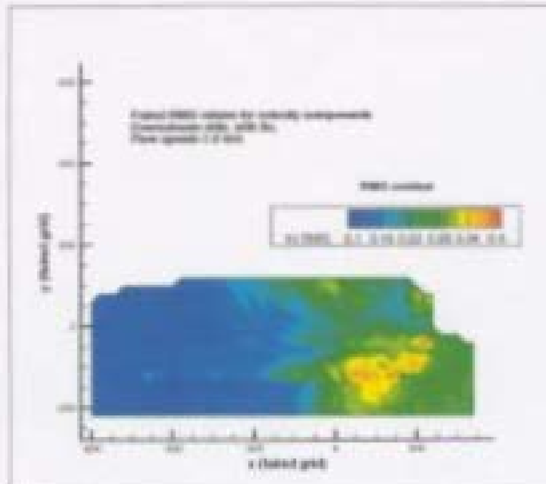

a) Vx

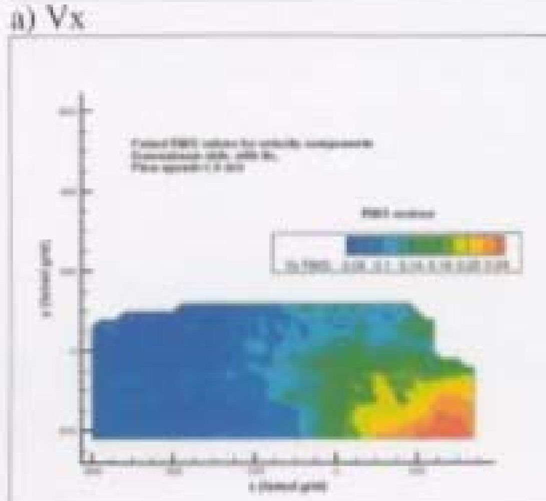

b) Vy

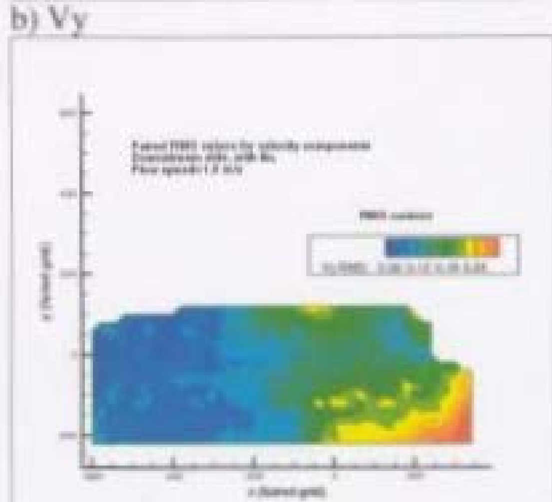

c) Vz

Figure 4-34, Contours of RMS for flow component, downstream, with fin, 1.0 m/s

4.7 RECOMMENDATIONS FOR FURTHER WORK

The three-dimensional calibration of the measurement space using the purpose made stepped plate is very efficient. However, when examining the flow around a specific geometry, there needs to be an accurate method for locating the measurement space in relation to the geometry. The test plan developed using the IOT ice tank addressed the need to overlap multiple windows, but in the detailed analysis it would have been helpful to have a more accurate method for locating the model hull within the measurement plane. One method of doing this would have been to put more reference points on the model, and then applying the calibration functions to these known points. In some locations, this could be done with the set-up used, because the chine at the bilge was clearly identifiable, but in other locations there were no reference points. Fortunately the edge of the model could be located from the vector patterns when all the windows were combined.

The seeding system would benefit from further refinement. The flow pattern around the tug at a yaw angle of 45 degrees was very complex, with high flow gradients and flow from the underside of the hull mixing with flow coming along the downstream side of the hull. All of the results were obtained with a single seeding rake, but the location of the rake relative to the model was moved for each measurement location. A refinement would have been to have two separate seeding rakes, so that different regions of the flow could be seeded at the same time.

4.8 CONCLUSIONS

Particle Image Velocimetry was successfully used to determine the flow velocities around an escort tug with a typical operating yaw angle of 45 degrees. One measurement direction was used, which was a plane normal to the direction of the undisturbed flow, which intersected with the tug's hull at midships. Measurements were made on the upstream and downstream sides of the tug. The total measurement area required to define the flow patterns around the hull was much larger than a single PIV measurement window (approximately 400 mm by 250 mm). In order to extend the measurement area beyond the singe window, the model was moved relative to the PIV system, by less than the dimensions of the window. As a result, the same area, relative to the model was seen in at least three measurement windows. The flow vectors from multiple views of the same location were averaged to obtain flow vectors over the complete measurement space.

Detailed measurements of the flow velocities around an escort tug model, operating at 45 degree of yaw is a hydrodynamic condition that has not been studied before. The key flow features identified were:

1) The separation of the incoming flow on the upstream side of the hull at the corner of the bilge and the reverse flow under the hull.

2) The formation of a vortex on the downstream side of the hull, which extended between the bottom of the hull and the waterline for the tug without the fin.

3) The formation of a large vortex on the downstream side of the hull when the fin was fitted. For a section at midships, the core of the vortex was located at approximately the mid-depth of the fin and the maximum beam of the model. This vortex changes the flow patterns close to the surface, and the smaller vortex seen when the fin was absent is not present at all.

The results of the PIV experiments can be compared with CFD predictions for the same flow conditions. The development of the CFD simulations and the comparison will be described in Chapter 5.

The speeds for which the experiments were carried out covered the typical operating speeds of a tug, using Froude scaling. The direction of the flow vectors relative to the hull changed very little with the speed of the undisturbed flow, although the magnitude of the velocity components changed with the magnitude of the undisturbed flow.

Even though the flow around the tug model was turbulent, the average flow vectors at a particular location relative to the hull were stable between experiments. This was determined by using the longest practical time sequence of 100 image pairs, repeating measurements for given flow speeds and window locations, and overlapping measurement windows so that at least three views were obtained of key flow features.

CHAPTER 5

COMPARISON OF CFD PREDICTIONS AND EXPERIMENTAL DATA FOR AN ESCORT TUG WITH YAW ANGLE

5.1 INTRODUCTION

Classical ship hydrodynamics focuses on ships moving forward in a straight line, or turning slowly under the action of a foil like rudder in calm water. These are generally considered to be the design conditions, and the ‘off-design’ conditions, where these assumptions are no longer valid have been seldom studied. An escort tug is a case where ‘off-design’ hydrodynamics are an essential part of the ship’s operational profile (Allan & Molyneux, 2004). In this situation, the tug’s hull and propulsion system are positioned to create a hydrodynamic force, which is used to bring a loaded oil tanker under control in an emergency. The tug is attached to a towline at the stern of the tanker, and by using vectored thrust, it is held at a yaw angle of approximately 45 degrees. The maximum practical speed of operation for escort tugs is about 10 knots. The designs of escort tugs to date have not been developed with a full understanding of the hydrodynamics of the situation. Without understanding the flow around a ship with a large yaw angle, it is unlikely that escort tugs can be developed to their full potential.

One method of trying to understand the flow around a hull with a large angle of attack (yaw angle) is to use computational fluid dynamics (CFD). The basic equations of fluid motion can be combined with the hull geometry and some assumptions about the turbulence in the flow to give mathematical predictions of the pressure on the hull surface and the flow vectors within the fluid. Very little research has been carried out into the hydrodynamics of hull shapes designed to operate at large yaw angles, and so the accuracy of numerical methods in fluid dynamics in these situations is unknown.

An earlier study of the ability of a commercial Reynolds Averaged Navier-Stokes (RANS) CFD code to predict flow patterns around a Series 60 C_B=0.6 hull with yaw, described in Chapter 2, concluded that there was very little difference in the predicted flow patterns between an unstructured mesh made from tetrahedral elements and a structured mesh made from hexahedral elements, when each was compared with experiment data. The Series 60 hull was not designed for large angles of attack to the flow and there was no force data available for the hull above 10 degrees of yaw, so the comparison was incomplete. It was recommended in Chapter 2 that the conclusions on the best meshing strategy for the Series 60 hull should be checked using hull forms designed to operate at yaw angles over 30 degrees. This approach required data for forces and flow patterns measured in experiments to compare with the CFD predictions.

An example of this type of hull is shown in Figures 4-1 and 4-2. This hull was a preliminary design for a tractor tug, developed by Robert Allan Ltd. of Vancouver, B. C (Allan et al. 2000). The 1:18 scale model was tested (Molyneux, 2003) at the NRC Institute for Ocean Technology (IOT). The focus of this experiment program was to obtain lift and drag forces for the hull in combination with different appendages. The range of ship speeds was from 4 to 12 knots (with model speeds based on Froude scaling). Yaw angle was varied between zero and 105 degrees. A summary of the principle particulars is given in Table 5-1.

Table 5-1, Summary of principle particulars for escort tug

Appendage option	Hull only	Hull and fin
Lwl, m	38.19	38.19
Bwl, m	14.2	14.2
T (max), m	3.8	6.86
Displacement, tonnes S.W.	1276	1276
Lateral area, m^2	125.4	157.1

The 1:18 scale model of this tug was tested at IOT over a range of propulsion and appendage configurations, which included the case of the hull with and without the fin (Molyneux, 2003). These data can be used to compare the forces measured in experiments with CFD predictions for the same flow conditions. Particle Image Velocimetry experiments to measure flow vectors around the same tug at a yaw angle of 45 degrees are described in Chapter 4. These data can be used to compare flow measurements with the predicted flow vectors.

This chapter describes the development of CFD predictions for the forces and flow patterns for an escort tug at typical operating angles to the flow and the comparison of these predictions with data from model experiments. Some conclusions are made on the effectiveness of commercial RANS based CFD codes within the design process for ship hulls that are required to operate at large yaw angles. In the case of an escort tug this angle can be up to 45 degrees.

5.2 MODEL EXPERIMENTS TO MEASURE HYDRODYNAMIC FORCES

Experiments to measure hull forces were carried out in the Ice Tank of the National Research Council's Institute for Ocean Technology (Molyneux, 2003). The objective of these tests was to measure hydrodynamic forces and moments created by the hull and the appendages on a 1:18 scale model of the ship. No propellers were fitted for these experiments. The yaw angles tested covered the full range likely to be encountered during escort operation. The results of these experiments allowed basic force data for different hull configurations to be compared, in much the same way as a resistance experiment can give a measure of merit for different hulls at zero yaw angle. The test method was very similar to that proposed by earlier researchers (Hutchison et al., 1993). The fin was at the upstream end of the hull, for all cases when it was fitted. The hull remained in the same orientation when the fin was removed.

The models were fixed at the required yaw angle and measurements were made of surge force, fore and aft sway forces and yaw moment using a Planar Motion Mechanism (PMM). The load measurement system was connected to the tug on an axis along its centreline, at the height of the towing staple on the tug. The model was free to roll about the axis through the towing staple, and free to pitch and heave. Pitch angle, roll angle, heave amplitude and carriage speed were measured, in addition to the surge force F_x and sway force F_y.

A small negative value of yaw angle (usually five or ten degrees) was used to check the symmetry of the results, and if necessary make a small correction to yaw angle to allow for any small misalignment of the model on the PMM frame. Prior to each days testing, the PMM system was checked using a series of static pulls which included surge only, sway only and combined surge and sway loads. Also individual data points were tared using data values for transducers obtained with the model stationary before the experiment began.

Figure 5-1, Model tested on PMM (10 knots)

The speeds tested corresponded to 4, 6, 8, 10 and 12 knots, using Froude scaling. At the high speeds of 10 and 12 knots, yaw angles tested varied from a small negative value to approximately 45 degrees. For speeds of 4, 6 and 8 knots, yaw angles varied from a small negative value to 105 degrees. Figure 5-1 shows the model being tested on the PMM.

Forces and moments were measured in the tug-based coordinate system and non-dimensionalized using the coefficients given below

$$C_l = \frac{F_x}{0.5\rho A_L V^2} \qquad C_q = \frac{F_y}{0.5\rho A_L V^2}$$

C_q is the force coefficient normal to the tug centerline (sway) and C_l is the force coefficient along the tug's centerline (surge). A_L is the underwater lateral area of the hull and fin (if the fin was fitted), ρ is the density of the water (kg/m^3) and V is the speed of the ship (m/s). The area of the guard was not included in the analysis, since the flow around the guard would be changed when the propellers were operating. Results for a nominal speed of 0.728 m/s (6 knots) are shown in Figure 5-2 as force coefficient against yaw angle.

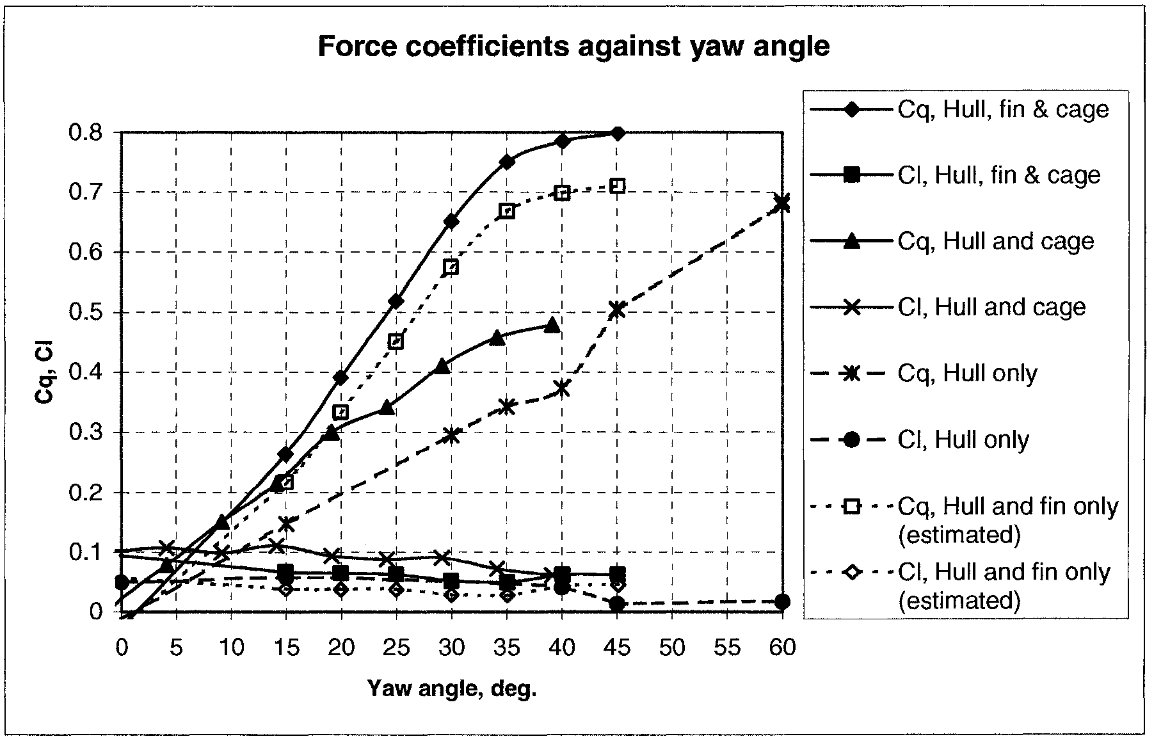

Figure 5-2, Force coefficients for an escort tug hull with different appendages for a flow speed of 0.728 m/s

When the measured force values were non-dimensionalized, the results for all speeds reduced to small variations about a mean value of the coefficient (Molyneux, 2003). This implies that free surface wave effects are small for the range of speeds typically found in escort tug operation. This observation simplifies the CFD predictions since only the hull below the design waterline needs to be considered, and the free surface effects can be ignored.

5.3 CFD PREDICTIONS OF HYDRODYNAMIC FORCES

5.3.1 Domain Dimensions

The surfaces used to the construct the 1:18 scale physical model (Molyneux, 2003) were trimmed to the nominal waterline. The trimmed surfaces were imported as IGES files and cleaned up using the utilities available within *GAMBIT* (Fluent Inc., 2005a), the program used for creating the meshes. The origin for the original hull surfaces was on the centreline, at the level of the keel, with the longitudinal position given by at the extreme aft end of the hull (above the waterline). This point was initially retained as the origin for the mesh. Dimensions for the surfaces were originally given in inches at model scale. The mesh was re-scaled in *FLUENT* (Fluent Inc., 2005b) to have units of metres, model scale and an origin at the leading edge of the waterline for the hull. All dimensions given in this report are metres, model scale.

A rectangular 'tank' was constructed around the hull. This had to be a compromise between being large enough that the boundaries had little effect on the results, and small enough that it converged to a solution in a reasonable time. A summary of the volume of fluid used as the domain is given in Table 5-2. The same domain size was used for tetrahedral and hexahedral meshing strategies. Both meshes were created using *GAMBIT 2.1*. The domain size in relation to the ship model hull is shown in Figure 5-3. A mesh sensitivity study, described in Appendix 3, showed that the predicted forces in the x and y directions were not significantly affected by the number of elements in the mesh.

Table 5-2, Summary of overall domain dimensions

	x_{max} m	x_{min} m	y_{max} m	y_{min} m	z_{max} m	z_{min} m
Original (imported)	5.715	-4.318	4.318	-4.318	0.211	-1.948
Final	7.974	-2.059	4.318	-4.318	0.000	-2.159

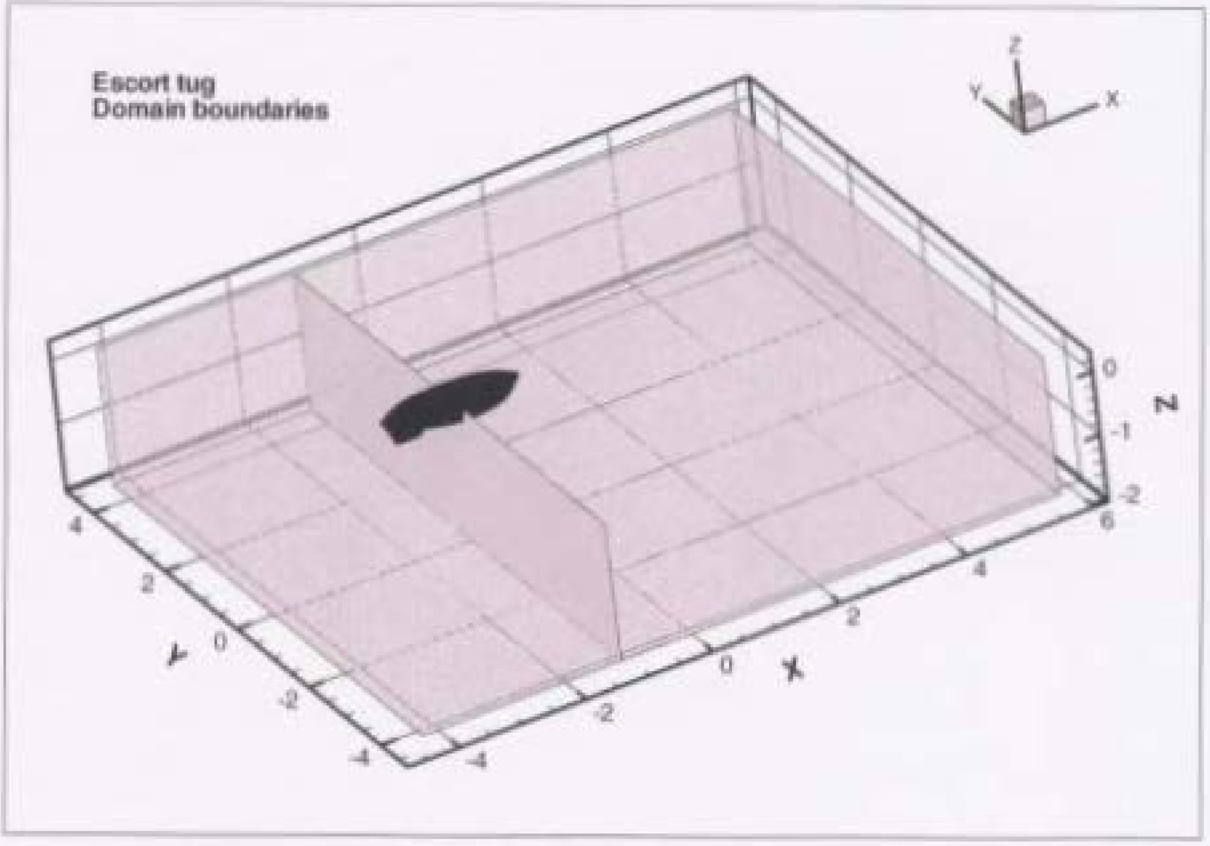

Figure 5-3, Scope of mesh (shown for tetrahedral mesh and tug with fin)

5.3.2 Tetrahedral Mesh

For the tetrahedral mesh, two volumes were created around the hull. The inner volume, close to the hull had a constant mesh size at all the boundaries. The outer volume had larger mesh elements at the outer surface than at the inner surface. The overall mesh geometry was the same for the tug with and without the fin.

The geometry for the tetrahedral mesh is summarized in Table 5-3. The total number of elements within the mesh was 2,170,899. Sections from the mesh are shown in Figures 5-4 to 5-6. These show different views to illustrate how the individual cells relate to the hull geometry. The same basic mesh geometry was used for the hull with and without the fin, and so views are shown for the case with the fin only.

Table 5-3, Summary of mesh dimensions

	x_{max} m	x_{min} m	y_{max} m	y_{min} m	z_{max} m	z_{min} m	Mesh size* m	Number of elements
Inner mesh	0.508	-2.667	1.016	-1.016	0.211	-0.297	0.03175	482,260
Outer mesh	5.715	-4.318	4.318	-4.318	0.211	-1.948	0.1016	1,688,639

* at surface

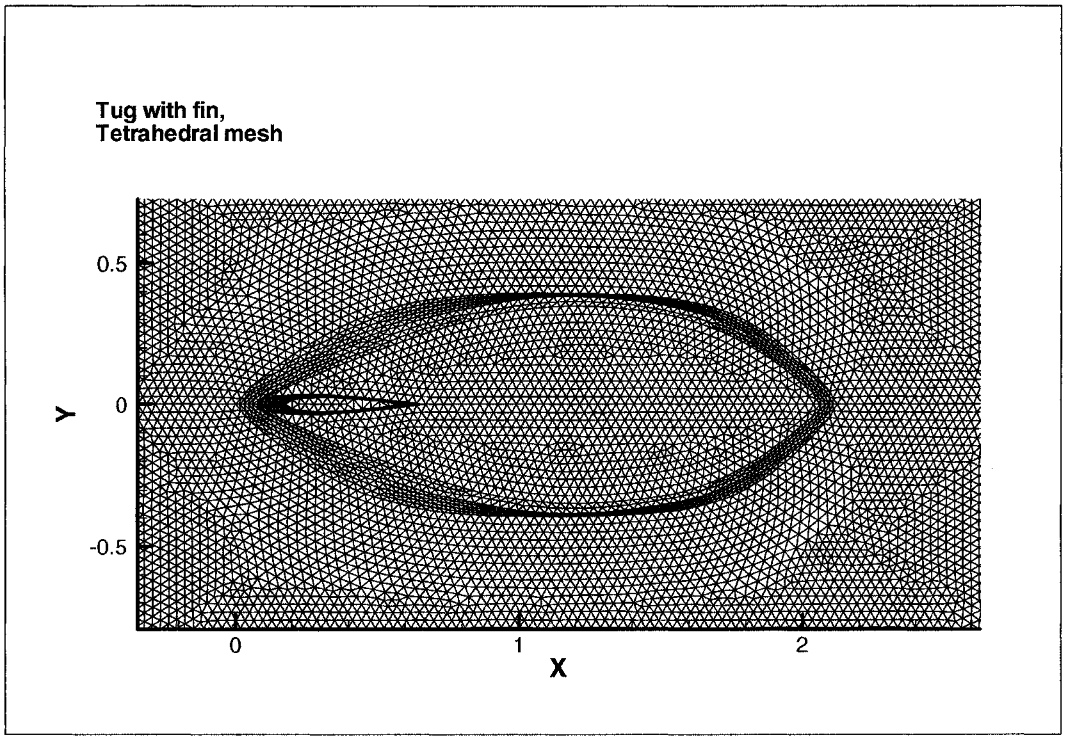

Figure 5-4, Tetrahedral mesh for escort tug, with fin, waterline view

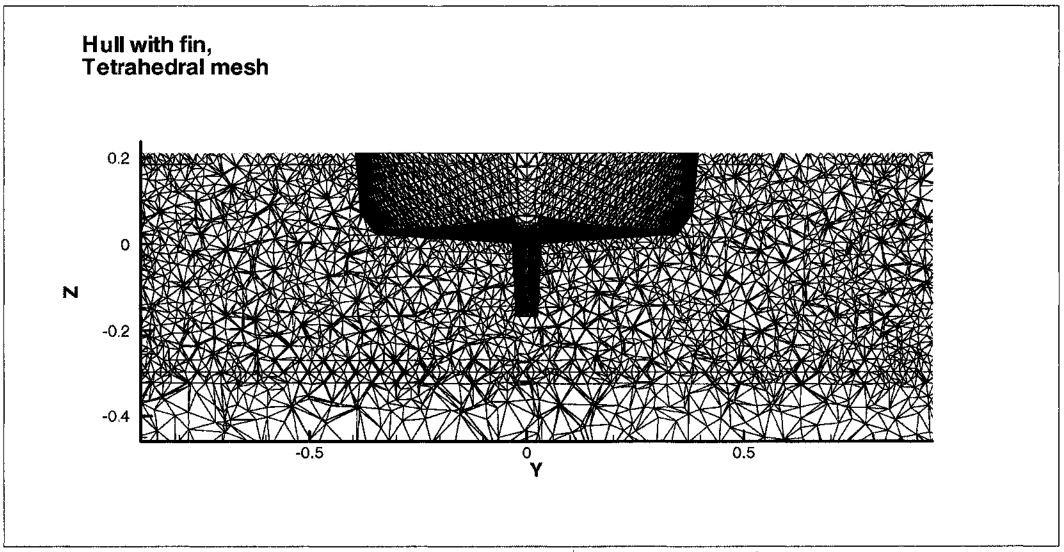

Figure 5-5, Tetrahedral mesh at midship section

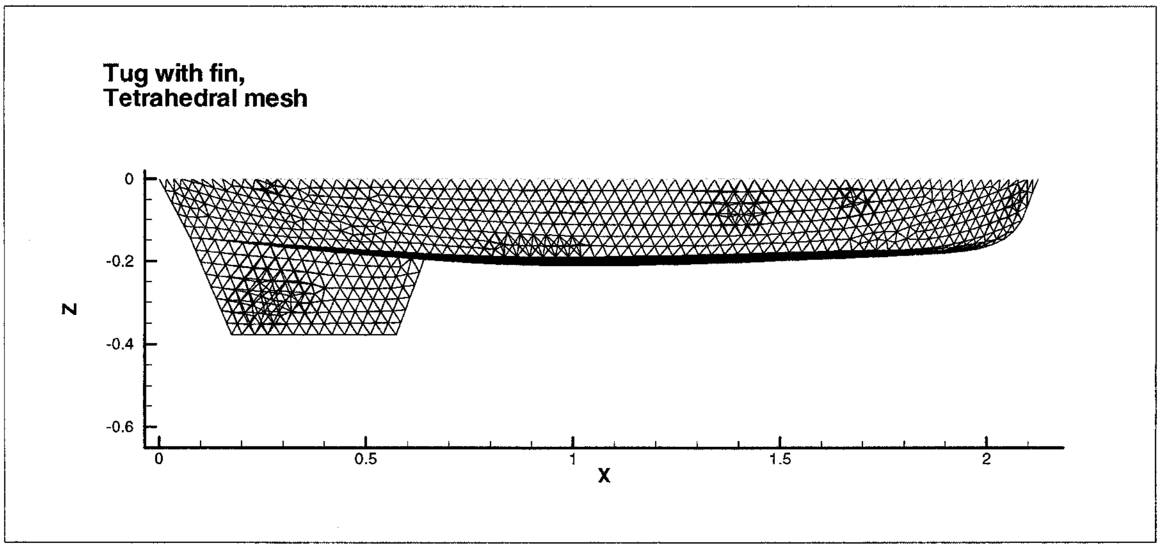

Figure 5-6, Tetrahedral mesh for escort tug, profile view

5.3.3 Hexhedral Mesh

The surface file used to create the hexahedral mesh was the same as the one used for the tetrahedral mesh. For the hexahedral mesh the additional step of creating new surfaces so that the hull could be defined completely in four-sided elements was required. This was done within *Gambit.*

Again the mesh was divided into two regions. One region was close to the hull surface, and one was sufficiently far from the hull surface, that flow conditions were not changing significantly. The hull and fluid volume were defined using a more elaborate system of construction planes along the length of the hull, especially close to the bow and the stern.

Once the inner mesh was successfully defined, the cells in the planes were extruded to the inlet, outlet and bottom wall boundaries. The mesh was symmetrical about the centreline of the ship.

The total number of elements within the mesh was 986,984, which was less than one half of the number used for the tetrahedral mesh.

Views of the hexahedral mesh close to the hull are shown in Figures 5-7 to 5-9.

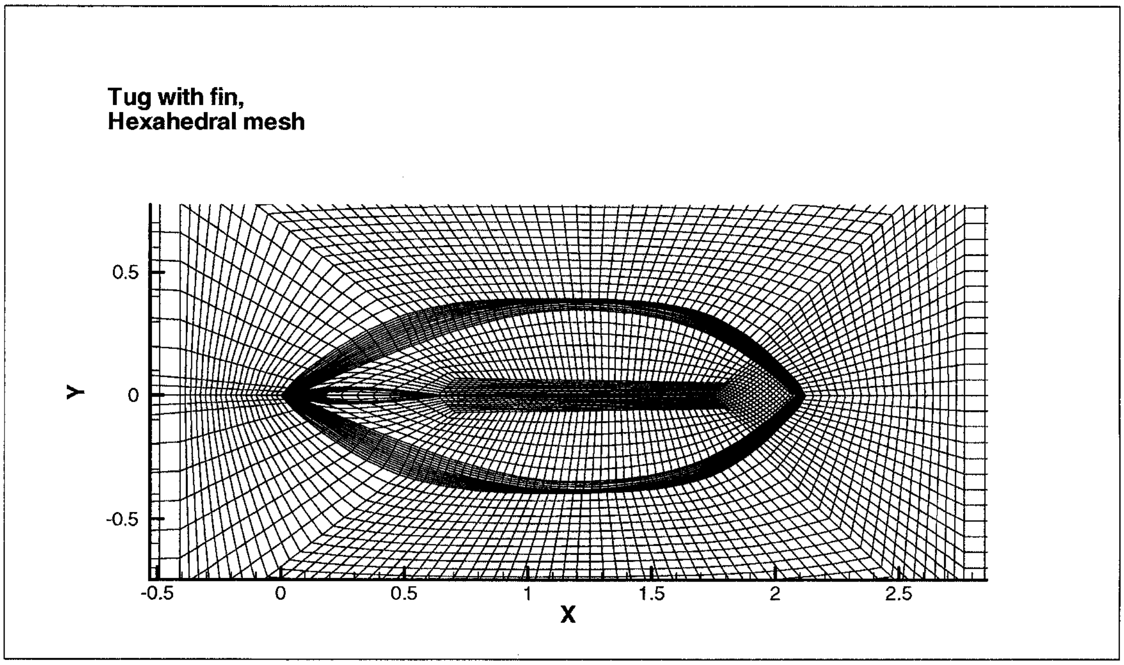

Figure 5-7, Hexahedral mesh for escort tug, waterline view

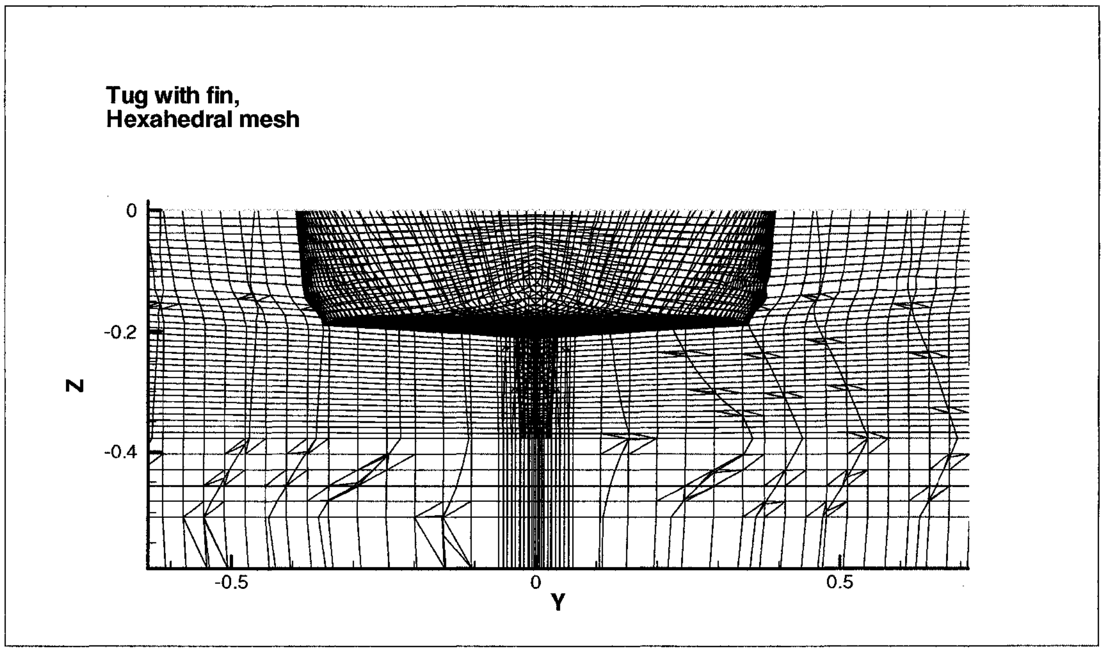

Figure 5-8, Hexahedral mesh at midship section

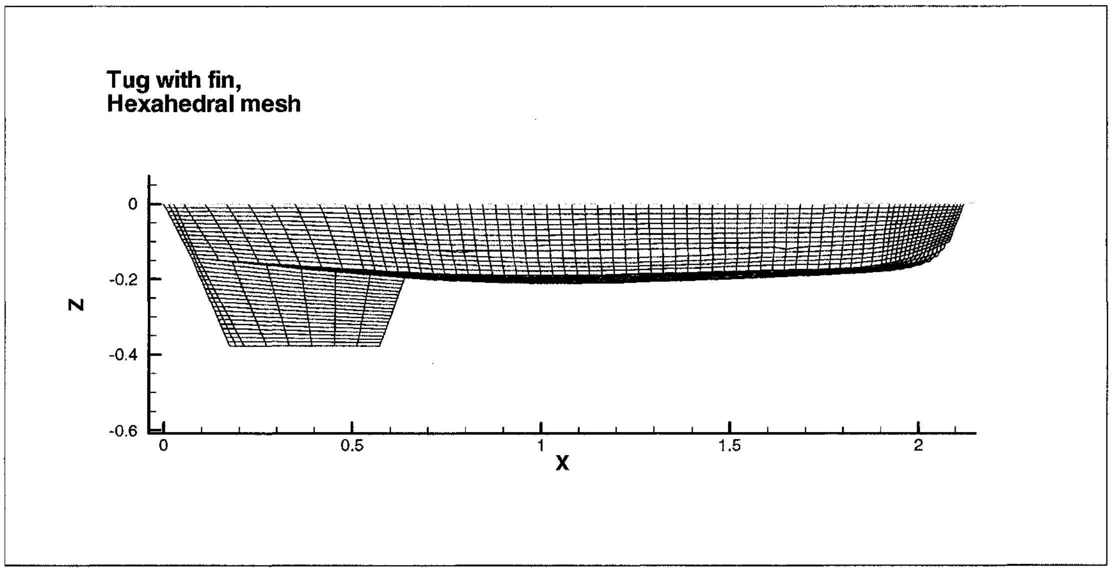

Figure 5-9, Hexahedral mesh for escort tug, profile view

5.3.4 CFD Solver

For both meshes the boundary conditions were set as velocity inlets on the two upstream faces, and pressure outlets at the two downstream faces. The upper and lower boundaries were set as walls with zero shear force. The hull surface was set as a no-slip wall boundary condition.

The CFD solver used was *FLUENT 6.1.22*. Uniform flow entered the domain through a velocity inlet on the upstream boundaries and exited through a pressure outlet on the downstream boundaries. Flow speed magnitude was set at 0.728 m/s, which corresponded to 6 knots at 1:18 scale, based on Froude scaling. The fluid used was fresh water.

The angle between the incoming flow and the hull (yaw angle) was set by adjusting the boundary conditions, so that the velocity at the inlet planes had two components. The cosine component of the angle between the steady flow and the centreline of the hull was in the positive x direction for the mesh and the sine component in the positive y direction. The pressure outlet planes were set so that the backflow pressure was also in the same direction. The advantage of this approach was that one mesh could be used for all the yaw angles. Yaw angles from 10 degrees to 45 degrees were simulated.

The turbulence model used was a $\kappa-\omega$ model with the default parameters given in Table 5-4. Turbulence intensity and turbulent viscosity ratios were set at 1% and 1 respectively.

The flow was solved for the steady state case. The non-dimensional residual for each of the solution variables (continuity, x, y and z velocity components, κ and ω) were set to 10^{-3} (default values). All flow conditions reported came to a solution within these tolerances. Results were presented as forces acting on the hull (including the fin if it was present) and as flow vectors within the fluid.

Table 5-4, Parameters for κ–ω turbulence model

α^*_∞	1.0
α_∞	0.52
α_0	0.111
β^*_∞	0.09
β_i	0.072
R_β	8
ζ^*	1.5
M_{t0}	0.25
TKE Prandl number	2
SDR Prandl number	2

5.4 COMPARISON OF CFD PREDICTIONS WITH EXPERIMENT DATA FOR FORCE COEFFICIENTS AT YAW ANGLES

5.4.1 Hull Only

Force components and non-dimensional coefficients derived from the results of the CFD simulations for the tug hull (without the fin) are given for the tetrahedral and hexahedral meshes in Table 5-5. The results of the simulations are compared with the experiments in Figure 5-10.

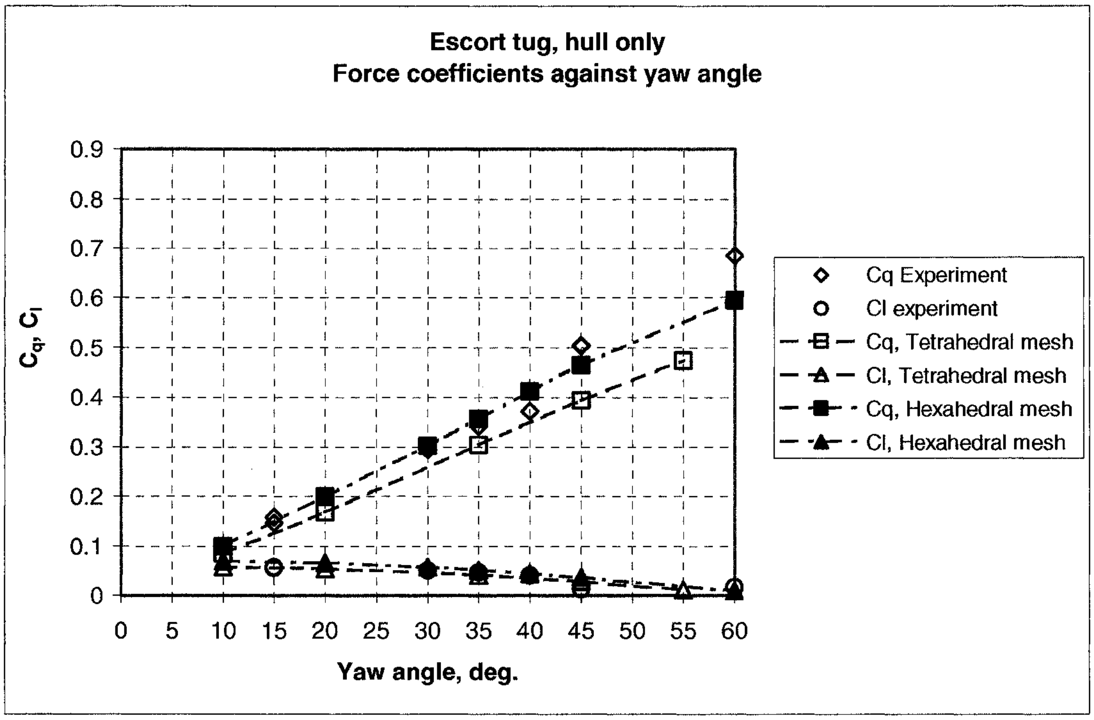

Figure 5-10, Comparison of CFD predictions for force coefficients with experiment values, hull only

Table 5-5, Comparison of CFD predictions of hydrodynamic forces, tug with no fin

			ρ	998.2	kg/m^3	
			A_L	0.387	m^2	
Tetrahedral mesh						
Yaw angle deg.	V, m/s	Surge N	Sway N	C_q	C_l	# iterations
10	0.728	5.916	8.761	0.086	0.058	170
20	0.728	5.535	17.298	0.169	0.054	195
35	0.728	4.262	31.25	0.305	0.042	225
45	0.728	2.921	40.415	0.394	0.029	233
55	0.728	1.175	48.65	0.475	0.011	232
Hexahedral mesh						
Yaw angle deg.	V, m/s m/s	Surge N	Sway N	C_q	C_l	# iterations
10	0.728	7.198	10.262	0.100	0.070	75
20	0.728	6.79	20.524	0.200	0.066	82
30	0.728	5.936	31.032	0.303	0.058	89
35	0.728	5.326	36.589	0.357	0.052	93
40	0.728	4.588	42.244	0.412	0.045	98
45	0.728	3.751	47.735	0.466	0.037	103
60	0.728	0.99	60.942	0.595	0.010	118

When the force coefficients derived from experimental measurements were compared to the values predicted by CFD, the hexahedral mesh gave the most accurate predictions for the tug with no fin. The average discrepancy between the predicted side force component and the measured value was 6 percent and the maximum discrepancy was 13 per cent. The largest discrepancy between measured and predicted values occurred at 60 degrees of yaw. For the tetrahedral mesh the predicted forces are consistently under predicted by an average of 18 percent when compared to the measured values, with the maximum discrepancy being 24 per cent.

For the longitudinal force component, which was much smaller than the side force component at the operating yaw angles, the tetrahedral mesh had an average discrepancy of 1 percent and the hexahedral mesh had an average discrepancy of 4 percent.

Comparisons were made on the basis of the difference between the measured and predicted value of the force component non-dimensionalized by the total measured force $((F_x^2+F_y^2)^{0.5})$.

5.4.2 Hull & Fin

Force components and non-dimensional coefficients derived from the results of the CFD simulations for the combined hull and fin are given for the tetrahedral and hexahedral meshes in Table 5-6. The results of the simulations are compared with the experiments in Figure 5-11.

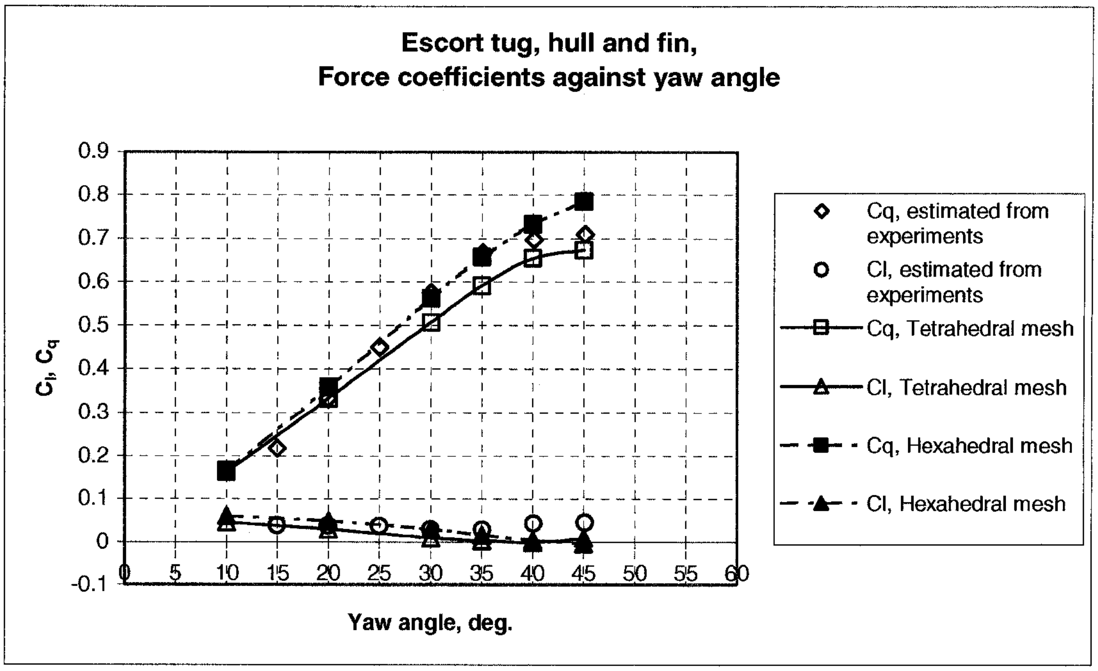

Figure 5-11, Comparison of CFD predictions for force coefficients with experiment values, hull and fin

It is important to note that experiment force data for the hull and fin condition was not available, since this was not a condition required for the original project. All of the experiments with a fin included the protective cage. The effect of the cage was estimated from the complete data set by subtracting the force components for the cage (estimated from the hull only condition and the hull and cage condition) from the hull, fin and cage condition.

Table 5-6, Comparison of CFD predictions of hydrodynamic forces, tug with fin

			ρ	998.2	kg/m^3	
			A	0.4849	m^2	
Tetrahedral Mesh						
Yaw angle, deg	Speed, m/s	Surge, N	Total sway, N	C_q	C_l	# iterations
10	0.728	5.878	20.856	0.162	0.046	224
20	0.728	3.752	42.822	0.334	0.029	259
30	0.728	1.22	65.079	0.507	0.010	284
35	0.728	0.418	75.998	0.592	0.003	293
40	0.728	-0.127	84.03	0.655	-0.001	310
45	0.728	1.146	86.53	0.674	0.009	428
Hexahedral Mesh						
Yaw angle, deg	Speed, m/s	Surge, N	Total sway, N	C_q	C_l	# iterations
10	0.728	7.712	21.346	0.166	0.060	89
20	0.728	6.173	45.906	0.358	0.048	102
30	0.728	3.721	72.174	0.562	0.029	115
35	0.728	2.065	84.407	0.658	0.016	119
40	0.728	0.523	94.16	0.733	0.004	128
45	0.728	-0.556	100.707	0.784	-0.004	145

The same observations about the accuracy of the predicted forces apply to the tug with a fin as for the tug without the fin, but the differences between the meshes are smaller. The hexahedral mesh resulted in predicted forces that were typically within 5 percent of the measured values, and never more than 10 percent different, whereas for the tetrahedral mesh, the typical agreement was within 7 percent and the maximum discrepancy was within 12 per cent. The force coefficients predicted from the hexahedral mesh were all within 5 percent of the experiment data for yaw angles between 30 and 40 degrees and within 10 percent at 45 degrees. The forces predicted by the tetrahedral mesh over this range were typically within 10 percent of the measured forces over the same range of yaw angle, but were consistently under predicted relative to the measured values. The force coefficients predicted by the hexahedral mesh were a good mean fit to the measured values up to 35 degrees of yaw, but above that the forces predicted by CFD are over predicted relative to the measured values.

The predicted normal force (pressure) and tangential force (viscous) components acting on the hug hull (fitted with the fin) from the hexahedral mesh are given in Table 5-7. These data show that as the yaw angle was increased, the proportion of viscous force to total force decreased. At zero yaw, the viscous force was approximately 25% of the total force, whereas at 10 degrees yaw, this had dropped to 9%, and at 30 degrees yaw it had dropped to 2%. At high yaw angles very little error in the forces at the hull would be expected by ignoring the viscous forces completely. One important element of including the viscosity forces within the fluid is to ensure the formation of vortices within the flow. It is important to check the predicted fluid flow patterns as well as the resulting forces.

Table 5-7, Comparison of pressure and viscous forces acting on tug and fin (hexahedral mesh)

Yaw Angle Degrees	Pressure Force N	Viscous Force N	Total Force N		Viscous/Total
0	6.07	2.06	8.13		0.254
10	22.11	1.93	22.73		0.085
20	46.08	1.71	46.32		0.037
30	72.16	1.45	72.27		0.020
40	94.05	1.14	94.16		0.012
50	102.91	0.88	103.11		0.008

5.5 CFD PREDICTIONS OF FLOW PATTERNS AT 45 DEGREES YAW

Particle Image Velocimetry experiments were carried out to measure the flow around the same tug model at speeds of 0.5 and 1.0 m/s, with a yaw angle of 45 degrees. These experiments are described in Chapter 4. Measurements were made within a plane, normal to the direction of the incoming flow, at two locations on the hull. One location was a plane that intersected with the midship section on the upstream side of the hull, and the second location was a plane that intersected the midship section on the downstream side of the hull. These planes are shown in relation to the CFD grid (for the hexahedral mesh) and the flow direction in Figure 5-12. The PIV experiments were carried out on the upstream side of the hull for the hull without the fin, and on the downstream side of the hull, with and without the fin.

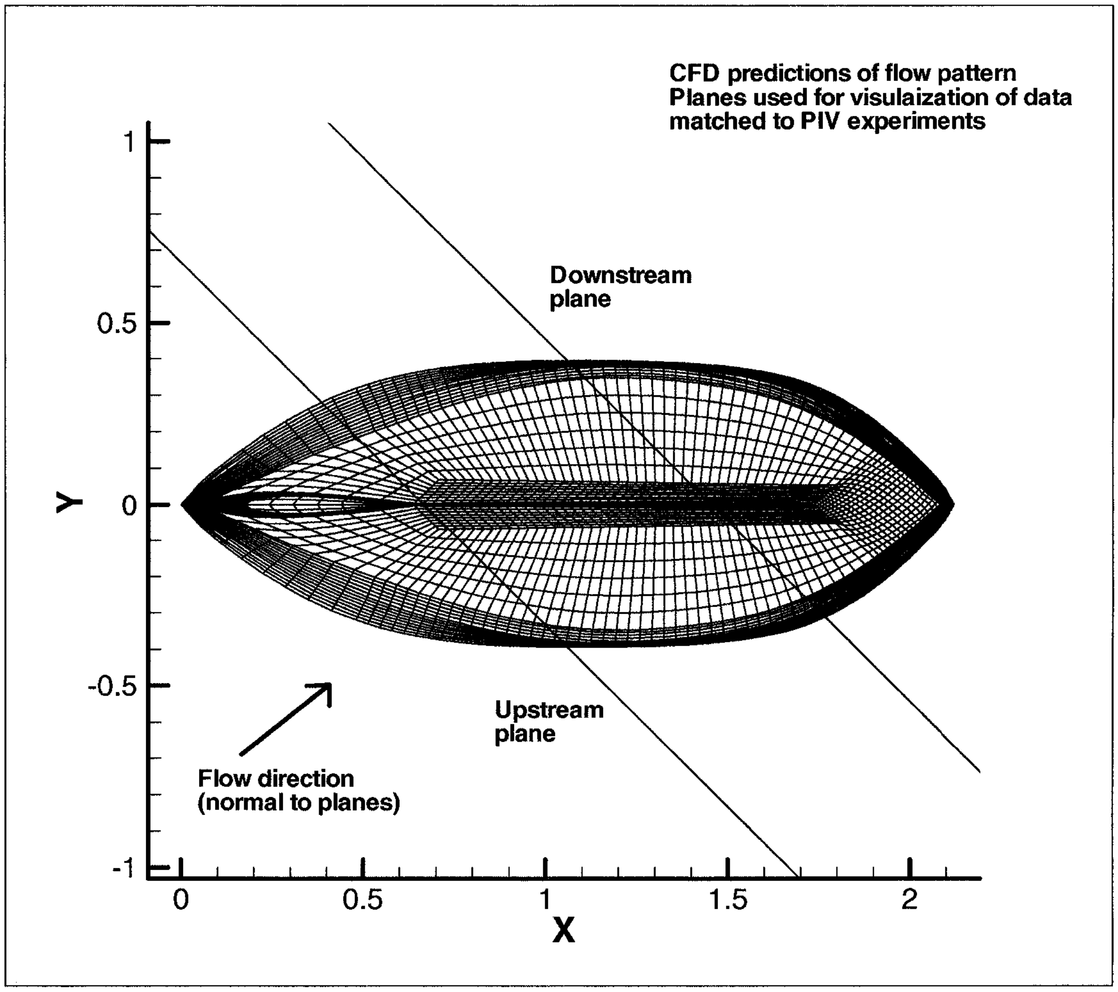

Figure 5-12, Planes used for comparing predicted flow patterns with PIV measurements

Since the grid for the CFD simulations had been created using ship-based coordinates, it was necessary to use the transformations given below, to convert the coordinates and vectors within the CFD simulations to the same flow based coordinate system as the PIV experiments.

$$x_f = (x_s \mathrm{Cos}\,\theta + y_s \mathrm{Sin}\,\theta)$$
$$y_f = (-x_s \mathrm{Sin}\,\theta + y_s \mathrm{Cos}\,\theta)$$

where;

x_f and y_f are in the flow based coordinates
x_s and y_s are in the ship based coordinates
θ is the angle between the flow direction and the ship based coordinates.

Since the transformation about the vertical axis was purely rotation, the third axis (z in the experiment notation) was unchanged.

The CFD predictions of flow vectors within the plane and contours of velocity through the plane for the three regions where PIV experiments were carried out are shown below. Figures 5-13 and 5-14 show the upstream bilge, Figures 5-15 and 5-16 show the downstream bilge, with the fin removed and Figures 5-17 and 5-18 show the downstream bilge with the fin present. In each pair of figures, the first figure shows results for the tetrahedral mesh and the second shows results for the hexahedral mesh.

One notable difference between the results given by the two meshes was that the hexahedral mesh showed a contour of 0.55 m/s, which extended under the hull, whereas this contour is missing from the results with the tetrahedral mesh.

5.5.1 Upstream Side, Without Fin

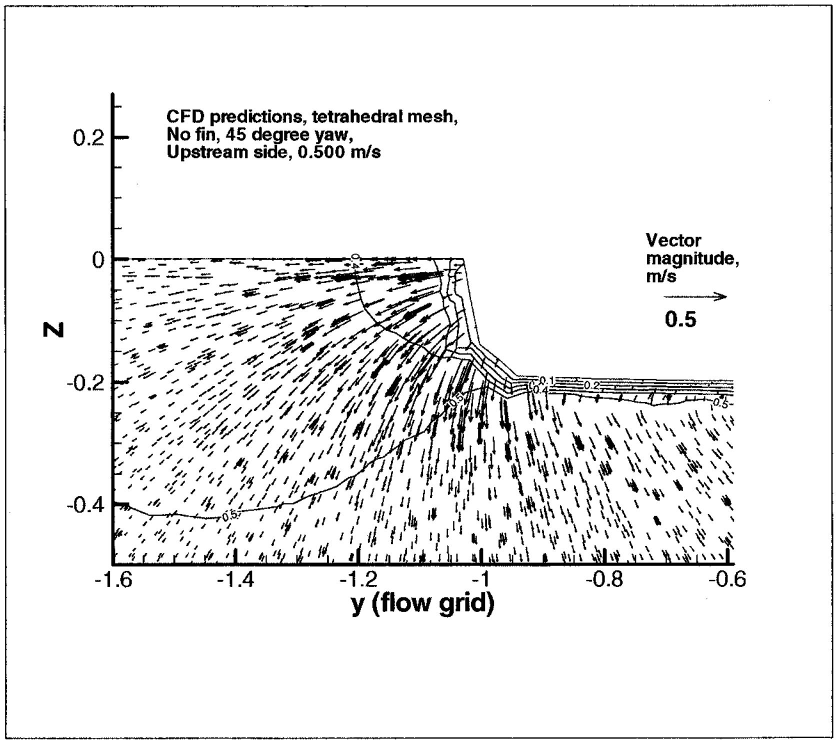

Figure 5-13, Flow vectors for tetrahedral mesh

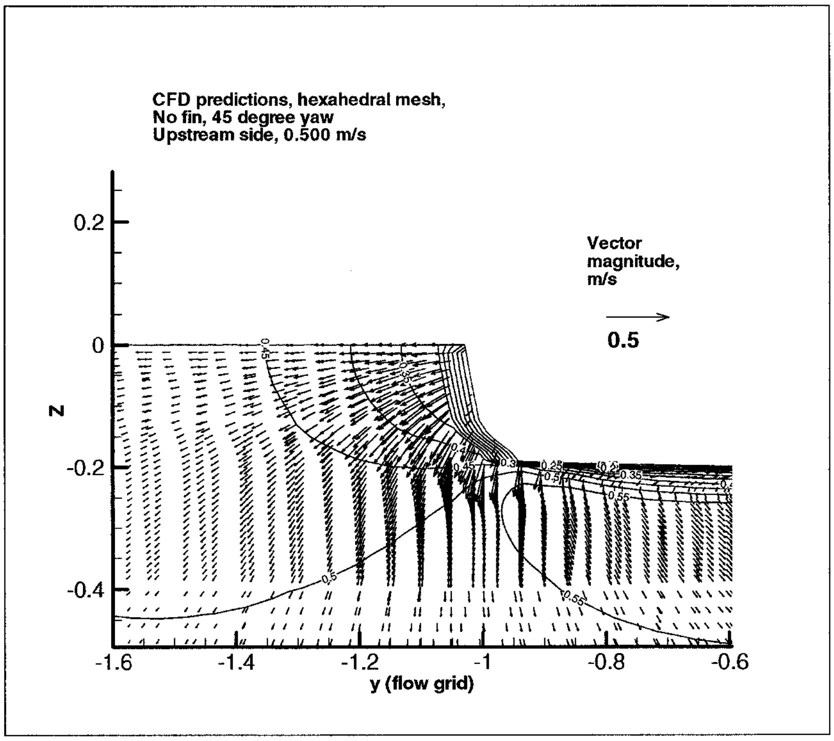

Figure 5-14, Flow vectors for hexahedral mesh

5.5.2 Downstream Side, Without Fin

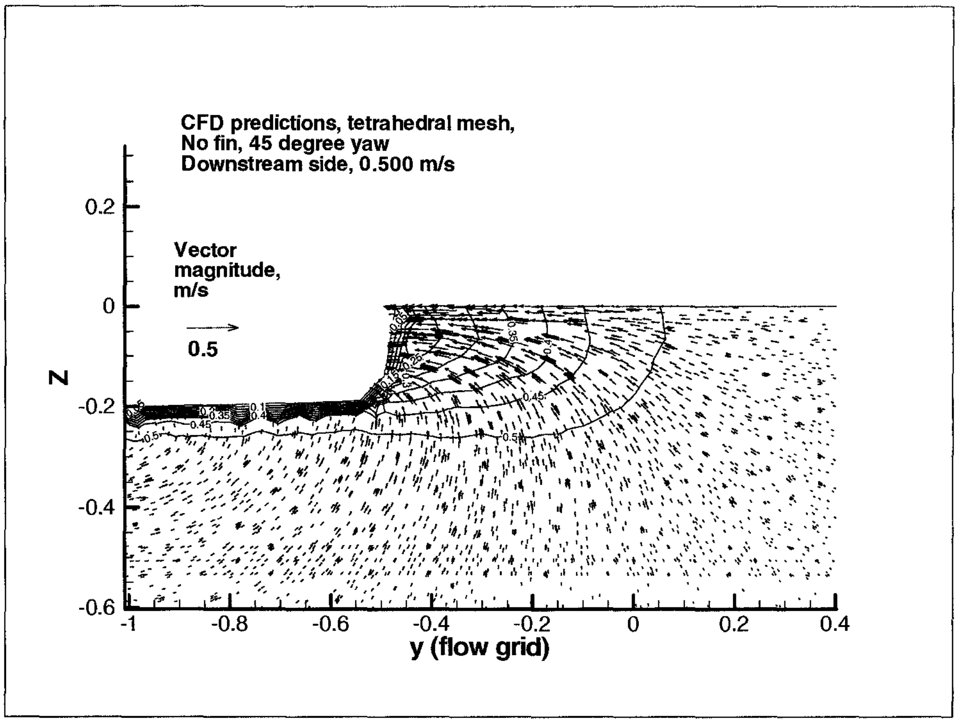

Figure 5-15, Flow vectors for tetrahedral mesh

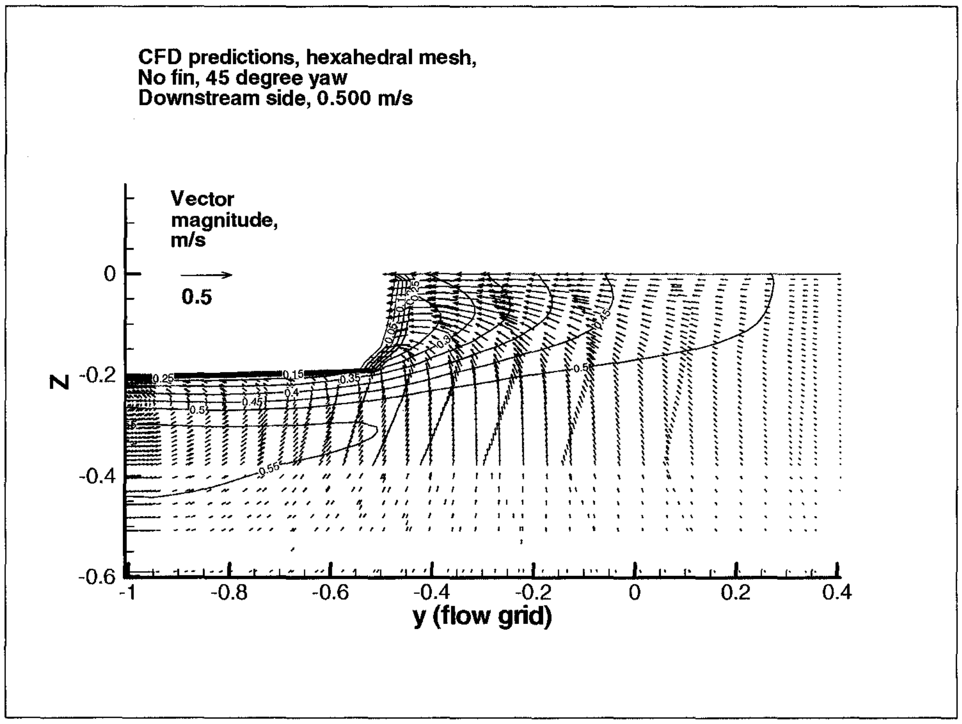

Figure 5-16, Flow vectors for hexahedral mesh

5.5.3 Downstream Side, With Fin

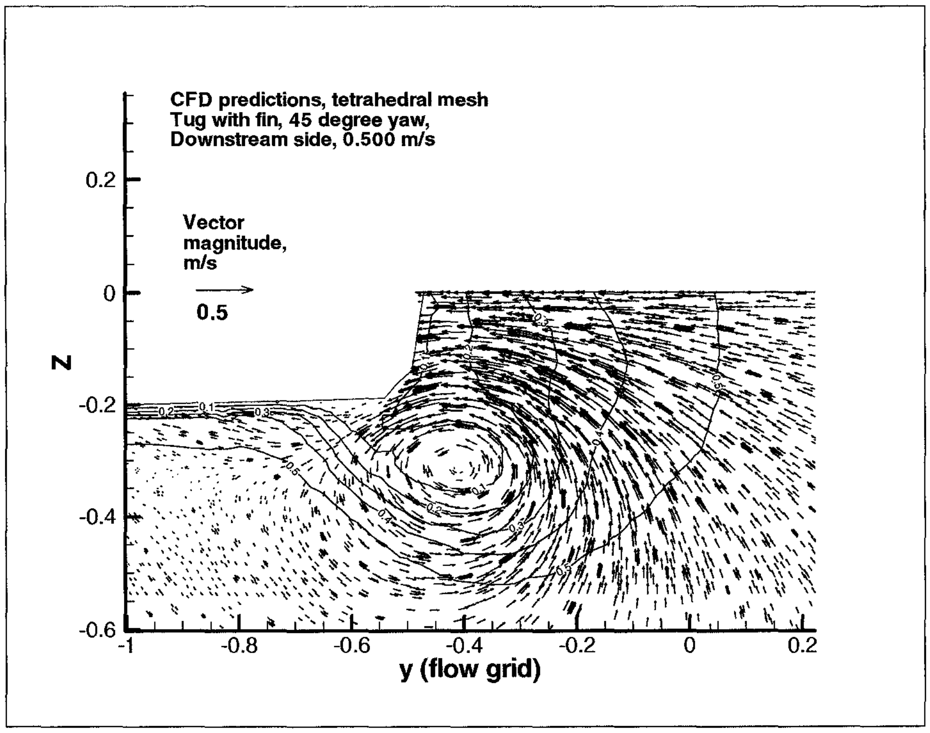

Figure 5-17, Flow vectors for tetrahedral mesh

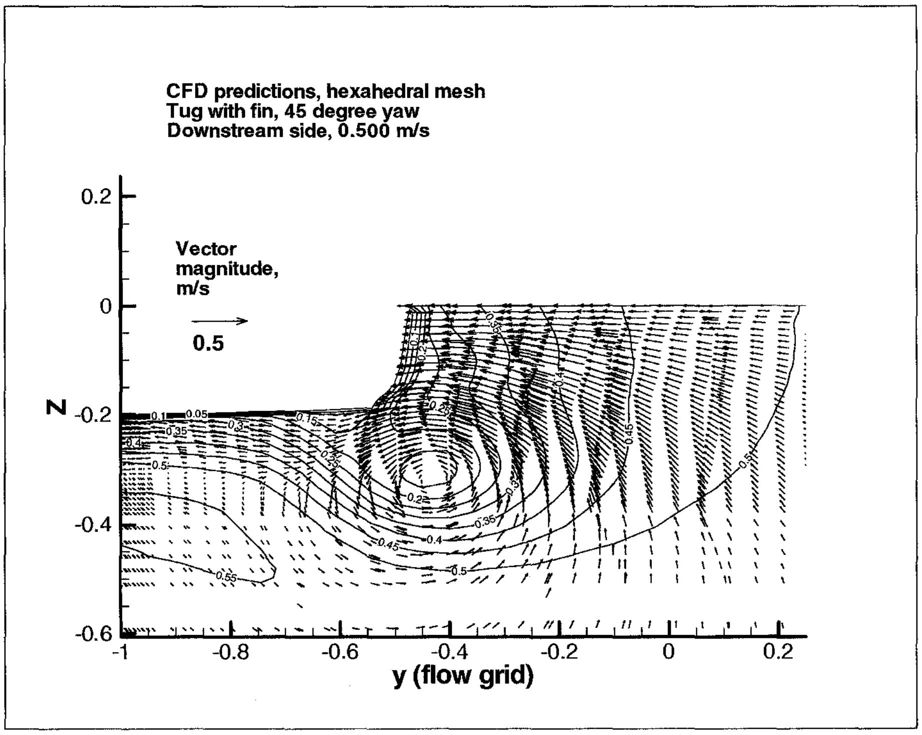

Figure 5-18, Flow vectors for hexahedral mesh

5.6 COMPARISON OF FLOW PATTERNS FROM CFD SIMULATIONS WITH RESULTS OF PIV EXPERIMENTS

Before carrying out the numerical analysis to compare the flow patterns, the original axis system used for the PIV experiments was renamed to match the axis system used in the CFD simulations. For the PIV experiments, the model was rotated to obtain upstream and downstream measurement planes on the same side of the model. For the comparison with the CFD simulations, the x-values from the PIV experiments made on the downstream side of the hull were reflected, so that the results of the PIV experiments matched the CFD simulations. The equivalent names are given in Table 5-8.

Table 5-8, Renamed axis system between CFD simulations and PIV experiments

PIV measurements	CFD simulations	Comparison
$-x$*	y_f	y_f
y	z_f	z_f
z	x_f	x_f
$-Vx$	Vy_f	Vy_f
Vy	Vz_f	Vz_f
Vz	Vx_f	Vx_f

* Downstream values only

In addition to renaming the axes, it was also necessary to convert the PIV grid, measured in millimetres, to metres and to shift the origin for the PIV experiments within the final y_f-z_f plane, to match the origin used in the CFD simulations. The shift of each axis is given in Table 5-9.

Table 5-9, Shift of origin in PIV measurements

Flow Condition	y_f shift, m	z_f shift, m
Upstream, no fin	-1.200	-0.270
Downstream, no fin	-0.250	-0.175
Downstream, with fin	-0.260	-0.175

The CFD predictions are compared to the PIV measurements for a flow speed of 0.5 m/s in Figures 5-19 to 5-24. Each figure shows the CFD predictions (for tetrahedral and hexahedral meshes) as black vectors with the PIV measurements superimposed as red vectors. When in-plane vector magnitude was very small, relative to the unit vector, the data points are shown as crosses. The PIV data used in the comparison was the combined data, based on time averaged flow vectors for all overlapped measurement windows. The measured data were presented on 0.200m square grid points.

5.6.1 Upstream Side, Without Fin

The results of the PIV experiments showed that the incoming flow separated at the corner of the bilge and the flow under the hull had a component moving towards the upstream bilge. This condition is compared with the CFD predictions in Figures 5-19 and 5-20, for the tetrahedral mesh and the hexahedral meshes respectively. Both meshes give subjective agreement in the size and direction of the in-plane flow velocities. Both meshes predict the flow separating off the upstream bilge, but neither mesh gives a complete prediction of the observed flow under the hull. For the flow under the hull, the tetrahedral mesh shows no upstream flow component at all, but the hexahedral mesh shows a weak upstream flow component close to the underside of the hull.

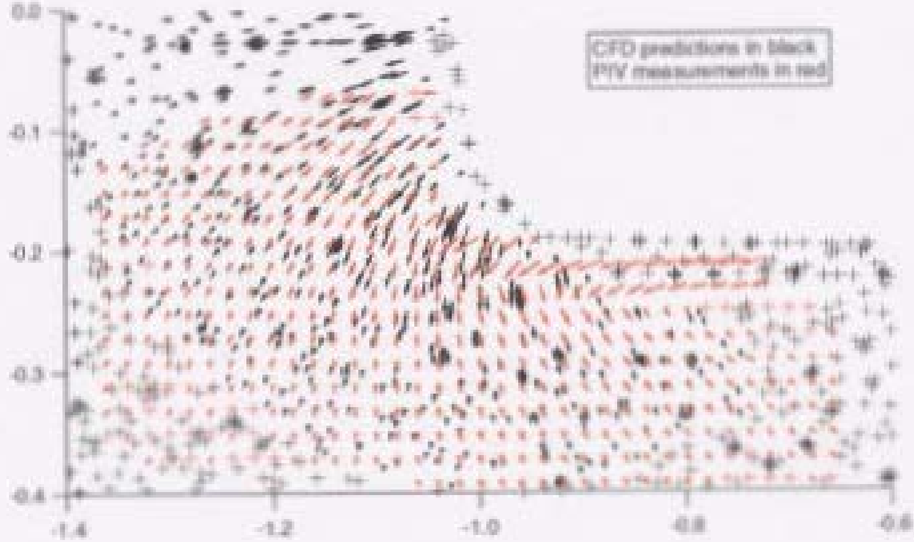

Figure 5-19, In-plane vector comparisons, upstream side without fin, tetrahedral mesh

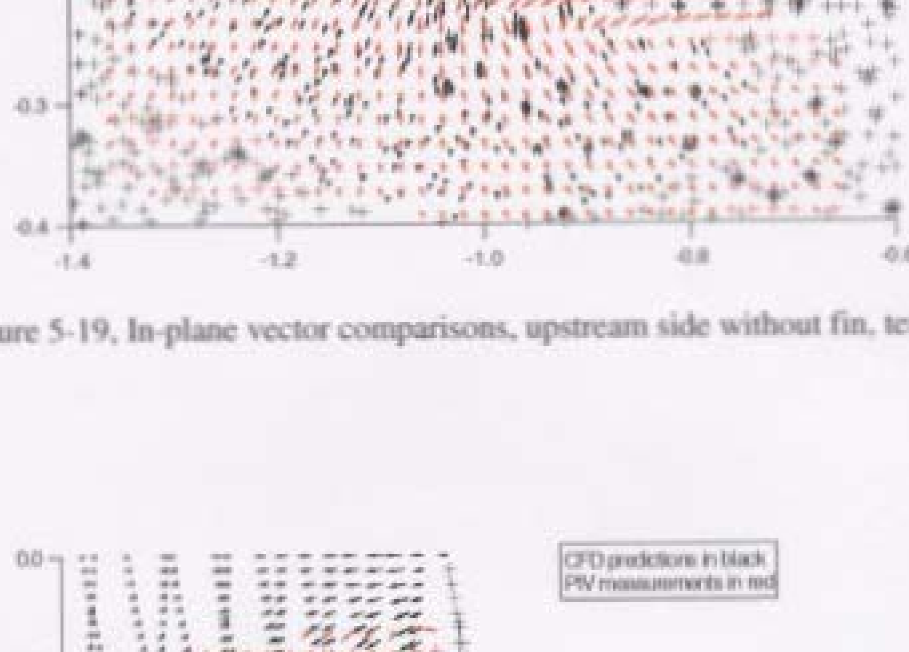

Figure 5-20, In-plane vector comparisons, upstream side without fin, hexahedral mesh

5.6.2 Downstream Side, Without Fin

The results of the PIV experiment are compared with the CFD predictions in Figures 5-21 and 5-22. On the downstream side of the hull, for the case with the fin removed, the PIV experiments showed the formation of a vortex on the downstream side of the hull, which extended from the keel to the water surface. The flow at the surface was towards to hull, but the flow well below the hull was almost vertical. For this condition both meshes show good subjective agreement for the magnitude and direction of the in-plane vectors predicted by CFD when compared to the results of the experiments. The hexahedral mesh gives slightly better definition of the local flow around the core of the vortex, which was located just downstream of the corner of the bilge.

5.6.3 Downstream, With Fin

The results of the PIV experiment are compared with the CFD predictions in Figures 5-23 and 5-24. In this condition, the PIV experiments showed that the dominant feature of the flow was the formation of a large vortex, with its core located at approximately mid-depth of the fin, and just downstream of the corner of the bilge. The upper part of this vortex separated on the bilge corner, resulting in a region of slow moving flow under the hull. Both CFD meshes showed good subjective agreement with the results of the PIV experiments. Both meshes gave good predictions for the location the core of the vortex, and in general predicted the magnitude and direction of the flow vectors throughout the region where measurements were made.

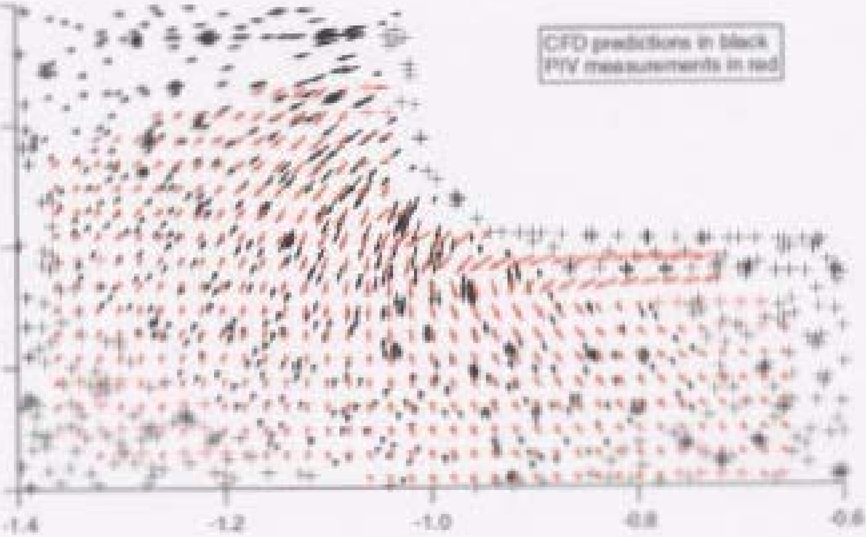

Figure 5-19, In-plane vector comparisons, upstream side without fin, tetrahedral mesh

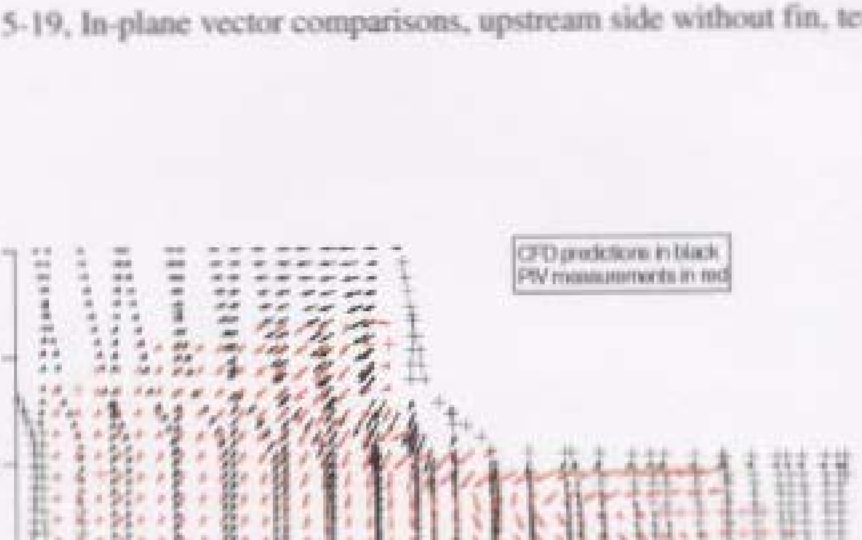

Figure 5-20, In-plane vector comparisons, upstream side without fin, hexahedral mesh

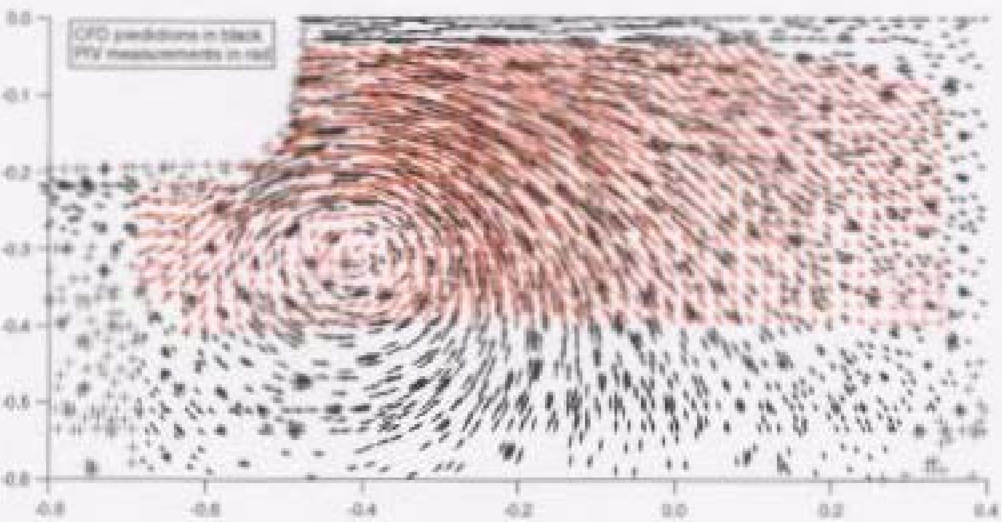

Figure 5-23, In-plane vector comparisons, downstream side with fin, tetrahedral mesh

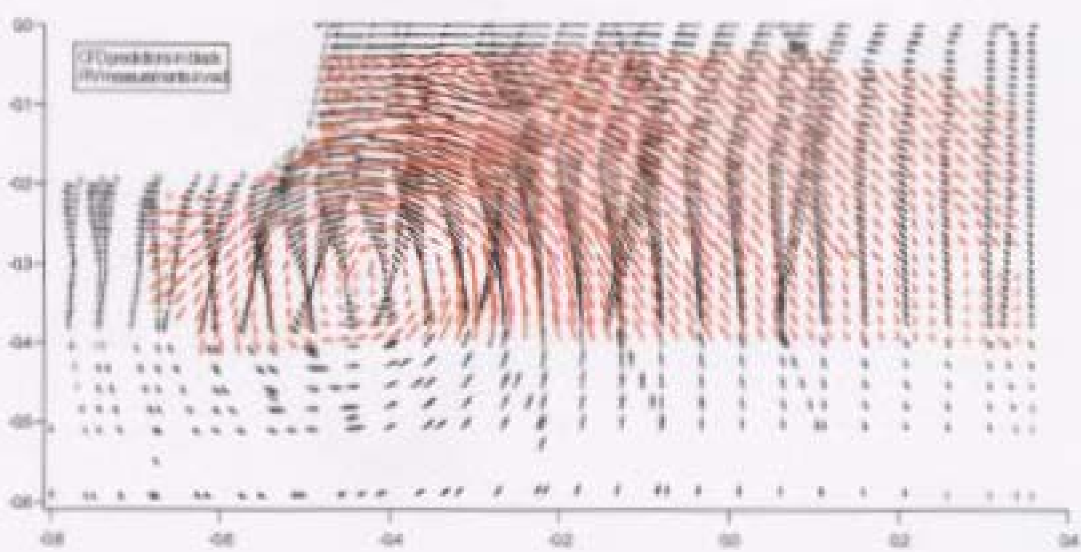

Figure 5-24, In-plane vector comparisons, downstream side with fin, hexahedral mesh

5.7 NUMERICAL ANALYSIS OF FLOW PATTERNS PREDICTED BY CFD AGAINST MEASURED PIV DATA

A numerical method was developed in Chapter 2 for comparing measured flow pattern data with the flow patterns predicted using CFD. This data compared the 3-dimensional flow vectors measured in experiments with CFD predictions for the same components over a common plane. The grid used for the comparison was the grid for the PIV experiments shown in Figures 5-19 to 5-24.

The steps in the process were the same as those used for the Series 60 data described in Chapter 2, which consisted of the following steps. The CFD data was reduced to a plane larger than the area covered by the measurements, but smaller than the complete plane within the CFD simulations. Each velocity component (V_x, V_y, V_z) was plotted as a contour over the reduced plane, and interpolated on the same grid as the one used for the PIV experiments. The in-plane velocity components (V_y, V_z) were combined into vectors. The difference between the vectors derived from the PIV experiments and the CFD simulations on the same y, z coordinate locations was calculated, using the expression

$$\overline{V_{error}} = \overline{V_{\text{expt}}} - \overline{V_{cfd}}$$

and graphed to show the errors in velocity magnitude and direction.

The following parameters were also used part of the numerical evaluation of the difference between the experiment values and the CFD predictions:

$$ErrorV_x = Vx_{expt} - Vx_{cfd}$$
$$ErrorV_y = Vy_{expt} - Vy_{cfd}$$
$$ErrorV_z = Vz_{expt} - Vz_{cfd}$$

$$Error_{2D} = \sqrt{ErrorV_y^{\ 2} + ErrorV_z^2}$$
$$Error_{3D} = \sqrt{ErrorV_x^2 + ErrorV_y^2 + ErrorV_z^2}$$

The results of the numerical analysis for the six flow conditions shown in Figures 5-19 to 5-24 are shown in Figures 5-25 to 5-36, and summarized in Tables 5-9 to 5-14.

In each set of results, the first figure shows $\overline{V_{error}}$ (magnitude and direction), the second shows $ErrorV_x$ and the table summarizes the results. All results presented are for the measured or predicted values of the flow speed, and have units of m/s for magnitude and radians for direction.

5.7.1 Upstream side, without fin, tetrahedral mesh

Table 5-10, Summary of error in CFD prediction

	Average	Standard Deviation	Minimum	Maximum	Range
In-plane					
Error Vy	-0.001	0.068	-0.346	0.134	0.480
Error Vz	-0.005	0.023	-0.085	0.162	0.247
Error 2d	0.042	0.059	0.001	0.347	0.345
Through plane					
Error Vx	-0.066	0.035	-0.238	0.137	0.375
Error 3d	0.086	0.058	0.019	0.347	0.328

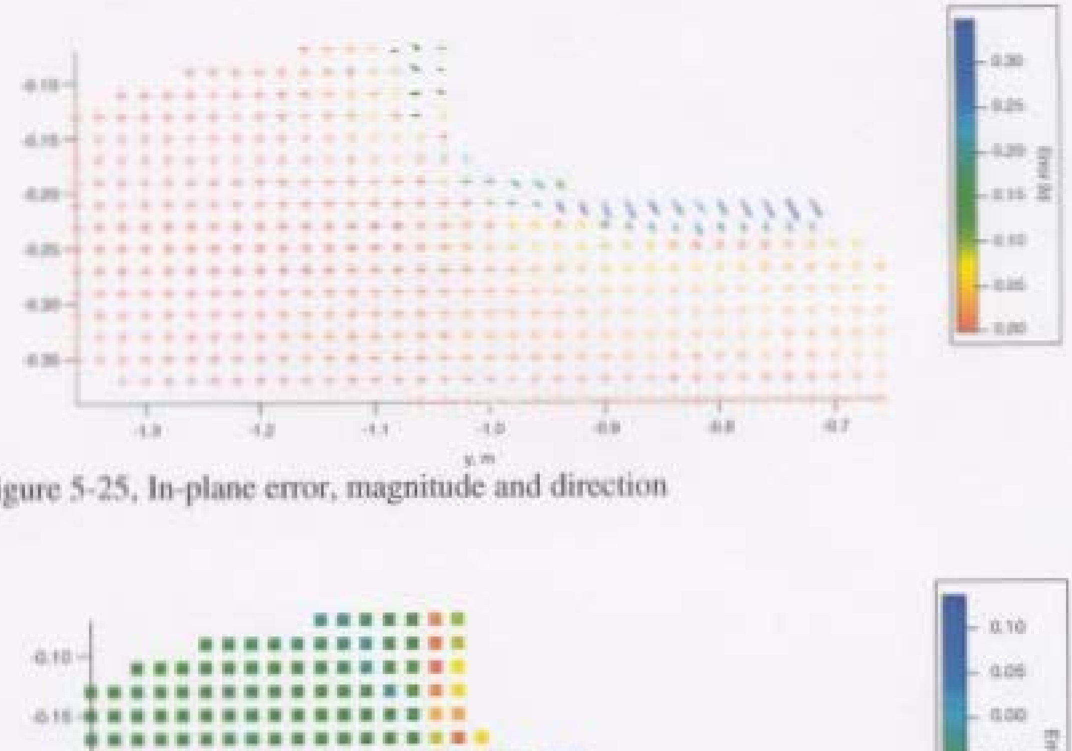

Figure 5-25, In-plane error, magnitude and direction

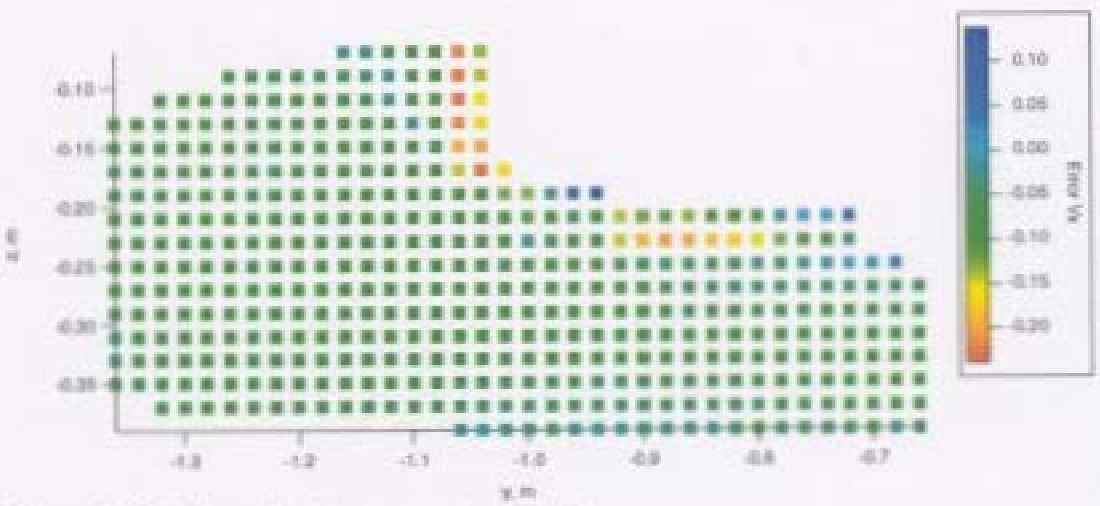

Figure 5-26, Through plane error, magnitude

5.7.2 Upstream side, without fin, hexahedral mesh

Table 5-11, Summary of error in CFD prediction

	Average	Standard Deviation	Minimum	Maximum	Range
In-plane					
Error Vy	0.001	0.061	-0.282	0.136	0.418
Error Vz	0.001	0.023	-0.064	0.142	0.205
Error 2d	0.038	0.053	0.001	0.282	0.281
Through plane					
Error Vx	-0.069	0.041	-0.300	0.115	0.415
Error 3d	0.085	0.060	0.018	0.372	0.354

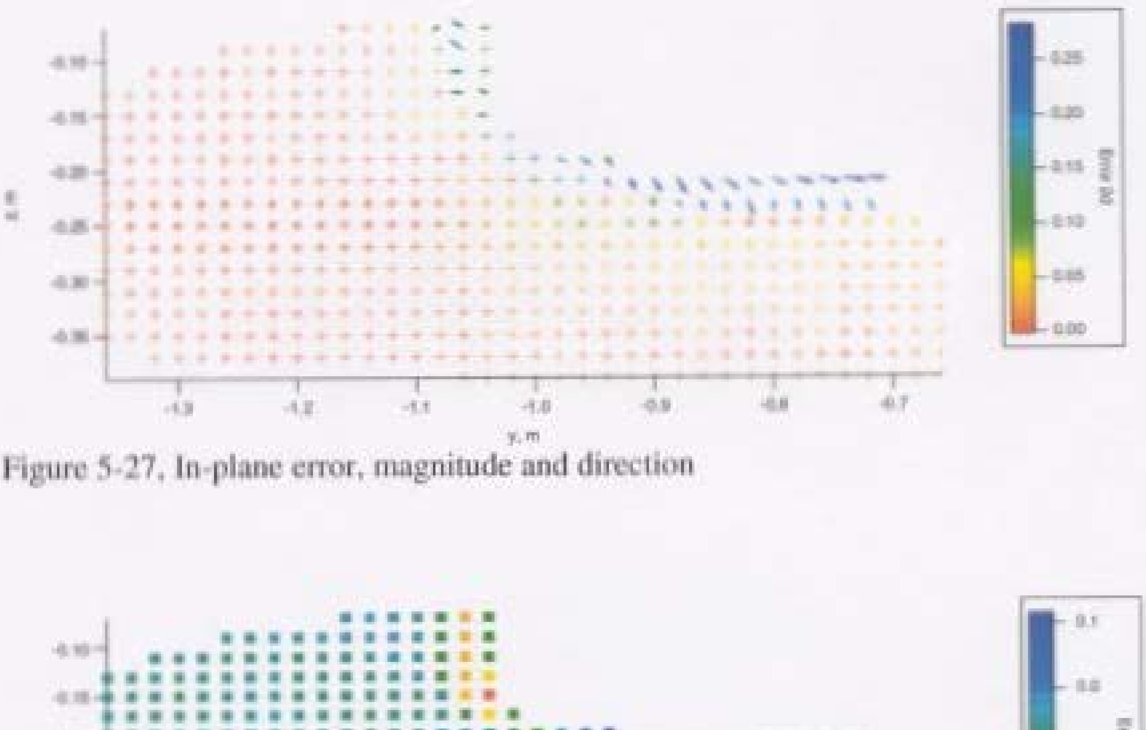

Figure 5-27, In-plane error, magnitude and direction

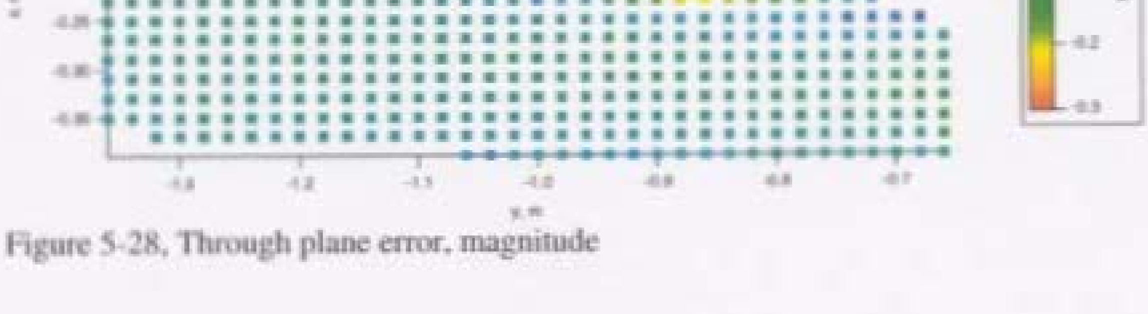

Figure 5-28, Through plane error, magnitude

5.7.3 Downstream side, without fin, tetrahedral mesh

Table 5-12, Summary of error in CFD prediction

	Average	Standard Deviation	Minimum	Maximum	Range
In-plane					
Error Vy	0.012	0.035	-0.072	0.174	0.246
Error Vz	0.005	0.024	-0.048	0.064	0.112
Error 2d	0.037	0.024	0.002	0.175	0.172
Through plane					
Error Vx	-0.034	0.050	-0.137	0.187	0.324
Error 3d	0.070	0.027	0.007	0.221	0.215

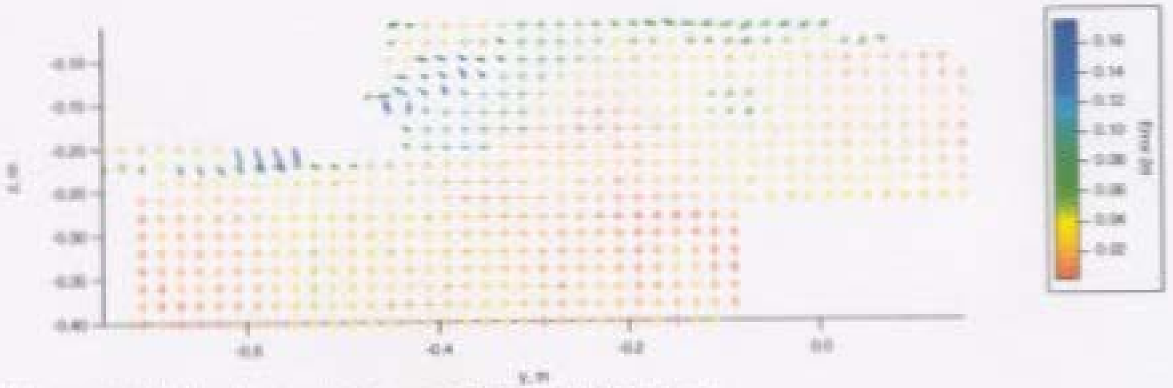

Figure 5-29, In-plane error, magnitude and direction

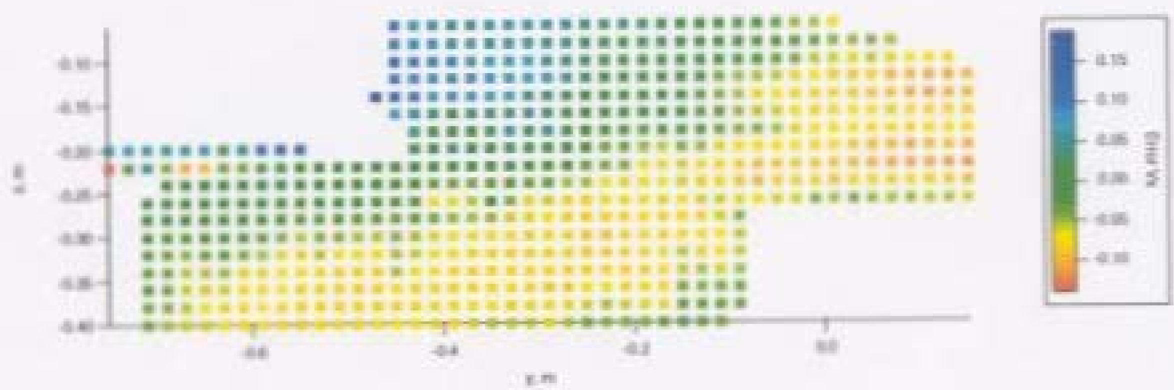

Figure 5-30, Through plane error, magnitude

5.7.4 Downstream side, without fin, hexahedral mesh

Table 5-13, Summary of error in CFD prediction

	Average	Standard Deviation	Minimum	Maximum	Range
In-plane					
Error Vy	0.013	0.040	-0.052	0.200	0.252
Error Vz	0.001	0.022	-0.045	0.063	0.108
Error 2d	0.039	0.028	0.002	0.200	0.198
Through plane					
Error Vx	-0.040	0.055	-0.110	0.206	0.316
Error 3d	0.078	0.028	0.012	0.219	0.207

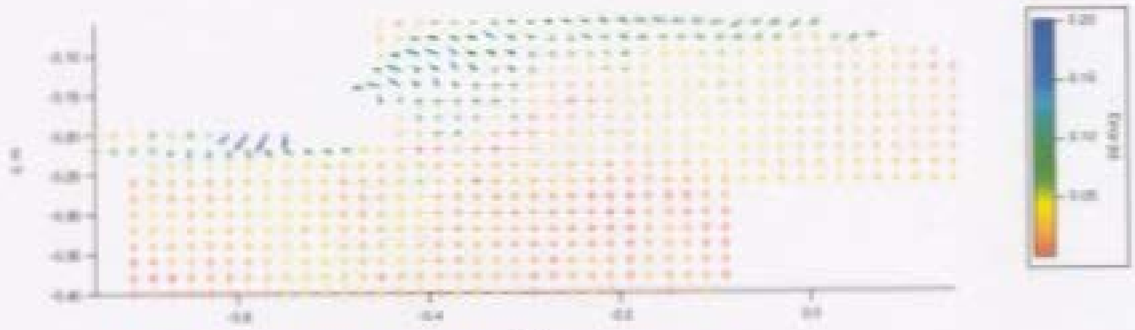

Figure 5-31, In-plane error, magnitude and direction

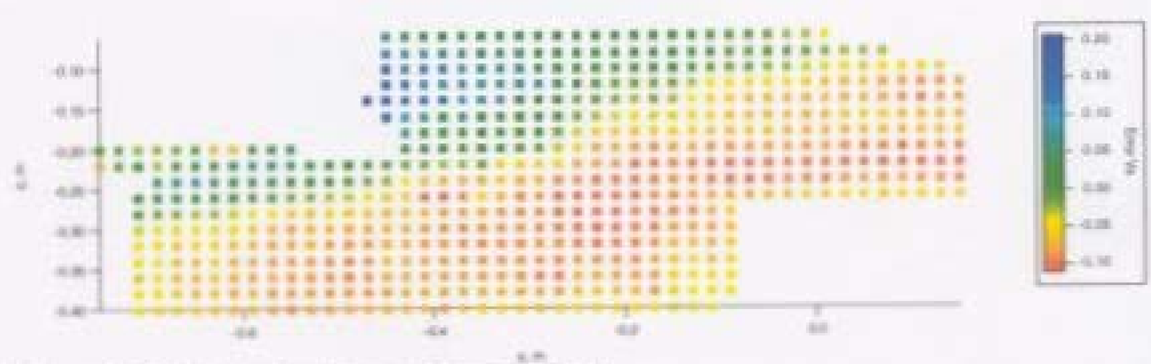

Figure 5-32, Through plane error, magnitude

5.7.5 Down stream side, with fin, tetrahedral mesh

Table 5-14, Summary of error in CFD prediction

	Average	Standard Deviation	Minimum	Maximum	Range
In-plane					
Error Vy	-0.005	0.043	-0.131	0.240	0.371
Error Vz	0.020	0.033	-0.094	0.114	0.208
Error 2d	0.049	0.032	0.002	0.254	0.252
Through plane					
Error Vx	-0.062	0.068	-0.185	0.307	0.492
Error 3d	0.100	0.044	0.010	0.397	0.388

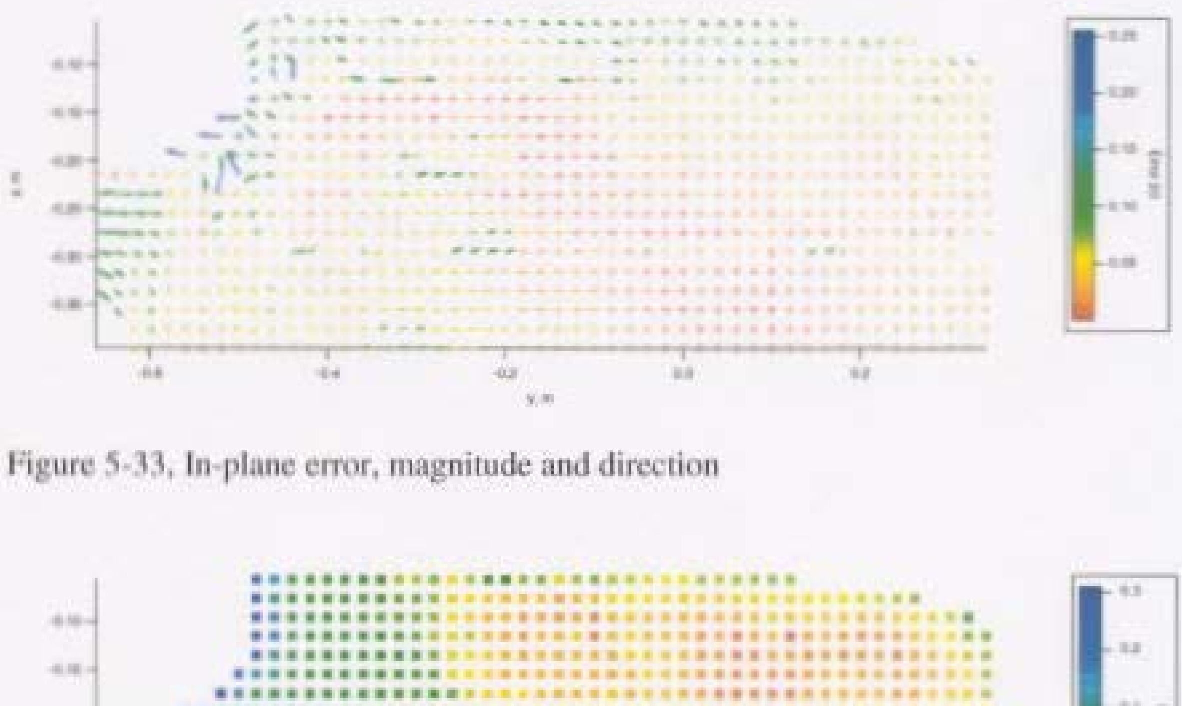

Figure 5-33, In-plane error, magnitude and direction

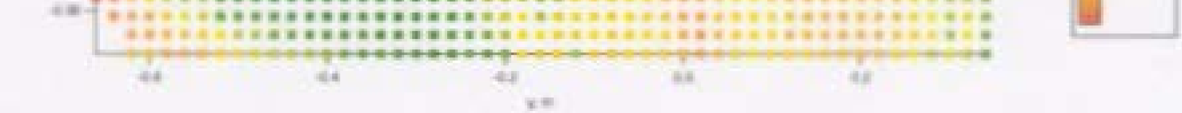

Figure 5-34, Through plane error, magnitude

5.7.6 Down stream side, with fin, hexahedral mesh

Table 5-15, Summary of error in CFD prediction

	Average	Standard Deviation	Minimum	Maximum	Range
In-plane					
Error Vy	0.007	0.048	-0.128	0.278	0.406
Error Vz	0.021	0.034	-0.116	0.116	0.232
Error 2d	0.051	0.037	0.000	0.290	0.290
Through plane					
Error Vx	-0.088	0.052	-0.200	0.278	0.478
Error 3d	0.113	0.039	0.034	0.388	0.354

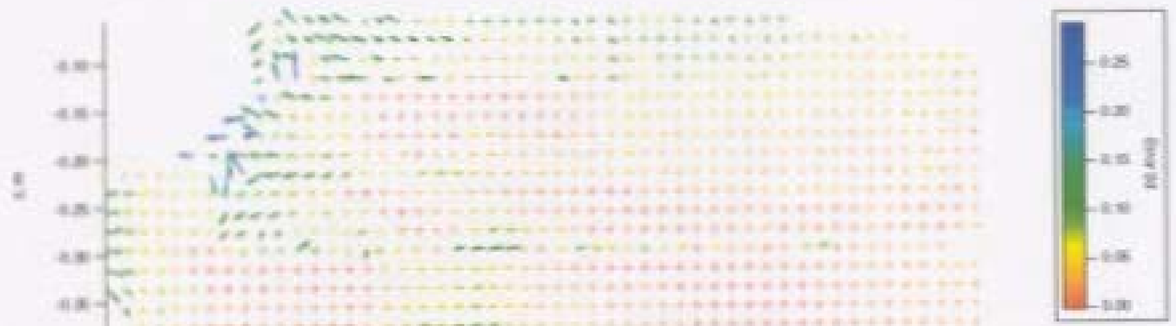

Figure 5-35, In-plane error, magnitude and direction

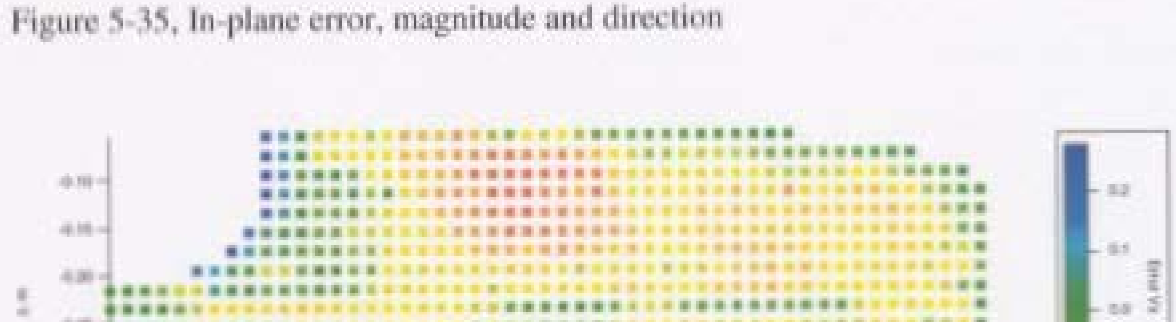

Figure 5-36, Through plane error, magnitude

5.8 DISCUSSION OF EXPERIMENTAL RESULTS

5.8.1 Through Plane Velocity Components

Table 5-16 shows a summary of the non-dimensional errors in the through plane velocity components for each of the locations around the tug. In this table, the non-dimensional parameter $Error_u$ was calculated from Tables 5-10 to 5-15 by non-dimensionalizing the values of $ErrorV_x$ with the free stream flow speed.

Table 5-16, Non-dimensional values of $Error_u$

Flow region	Tetrahedral mesh	Hexahedral mesh
Upstream, no fin	-0.133	-0.138
Down stream, no fin	-0.068	-0.080
Downstream, with fin	-0.124	-0.175

From these values it can be seen that the value of $Error_u$ is consistently negative. This means that the flow component from the CFD predictions was consistently higher than the observed values in the experiments. The difference was consistent with the values of the wake from the seeding rake used for these experiments (described in Chapter 3), which was seen to be between 10 and 12 percent of the free stream flow. It was expected that the wake from the seeding rake was reducing the flow speed, relative to the case when the rake was not present. It was also shown that the rake had negligible effect on the in-plane flow measurements, so comparison between the CFD simulations and the PIV experiments should be focussed on the in-plane flow patterns.

5.8.2 In-plane Velocity Components

Three numerical values were picked to compare the PIV experiments with the tetrahedral and hexahedral meshes. These were the mean value and standard deviation of $Error_{2D}$ and the fraction of the data where the error between the CFD predictions and the experiments (for the in-plane flow components) were within 10% of the free stream speed. The values were non-dimensionalized based on the free stream speed of 0.5 m/s. The results are given in Tables 5-17 to 5-19.

Table 5-17, Non-dimensional mean, $Error_{2D}$

Flow region	Tetrahedral mesh	Hexahedral mesh
Upstream, no fin	0.083	0.076
Down stream, no fin	0.074	0.078
Downstream, with fin	0.097	0.101

Table 5-18, Non-dimensional standard deviation, $Error_{2D}$

Flow region	Tetrahedral mesh	Hexahedral mesh
Upstream, no fin	0.117	0.107
Down stream, no fin	0.049	0.055
Downstream, with fin	0.064	0.074

Table 5-19, Fraction of data set where $Error_{2D}$ was within 10% of free stream speed

Flow region	Tetrahedral mesh	Hexahedral mesh
Upstream, no fin	0.827	0.840
Down stream, no fin	0.820	0.785
Downstream, with fin	0.623	0.598

These tables show that there was very little effect of the mesh type on the predicted flow patterns, when compared to the observed flow patterns from the PIV experiments. The hexahedral mesh had a small advantage on the upstream side of the tug model, but on the downstream side, the tetrahedral mesh had a slight advantage. In general, the best predictions were for the upstream side of the tug and the worst predictions were for the downstream side of the tug, with the fin.

For the flow on the upstream side of the hull (Figures 5-25 and 5-27), both meshes gave similar errors, with the worst predictions of flow vectors close to the hull and the accuracy of the predictions improving as the distance from the hull increased. PIV measurements close to the hull will likely be the most difficult to obtain accurately, because the hull, even when painted black, reflects the light and a bright band is seen in the pictures of the particles where the laser beam cuts the hull. Even though the analysis software includes a filter to reduce this effect, the experiment results obtained in this region may be subject to error.

On the downstream side of the hull without the fin, (Figures 5-29 and 5-31) the highest errors were seen on the underside of the hull, just before the corner of the bilge, and on the top of the vortex caused by the flow separation at the bilge. In the region under the hull, the CFD did not predict the observed speed of the flow, especially for the tetrahedral mesh. In this case the predicted flow was almost stationary, whereas the PIV measurements showed it was not. The hexahedral mesh gave slightly smaller error in this region.

The other area where the predicted flow did not match the observed flow was on the downstream side of the hull, between the bottom of the hull and the waterline. This was the region where the strongest flow velocities occurred. These high velocities were the result of the vortex caused by the flow separation off the corner of the bilge. Again the hexahedral gave smaller errors in this region but the difference was not significant relative to the tetrahedral mesh.

When the fin was present (Figures 5-33 and 5-35) and the very large vortex was generated, the worst comparison between the experiment data and the CFD predictions occurred close to the hull on the downstream side between the bottom of the hull and the waterline, and under the hull. Both meshes showed relatively small errors in the flow around the vortex, but the hexahedral mesh gave relatively poor prediction of the flow patterns close to the waterline, compared to the tetrahedral mesh.

Based on the numerical analysis, both meshes gave similar predictions of the flow patterns around the hull of an escort tug with a yaw angle of 45 degrees, and neither approach had a significant advantage in any of the conditions investigated.

The non-dimensional values for the errors between the PIV experiments and the CFD predictions for the escort tug at 45 degrees yaw are compared to the Series 60 model at 35 degrees yaw taken from Chapter 2 in Table 5-20 for the tetrahedral mesh and Table 5-21 for the hexahedral mesh. These tables show that the accuracy of the CFD predictions for the escort tug was better than for the Series 60 model, and the CFD predictions showed less variation with the type of the mesh.

Table 5-20, Comparison between Series 60 and escort tug, tetrahedral mesh

Parameter	Series 60, C_B=0.6 Yaw angle 35 degrees, Midship section	Escort tug, no fin Yaw angle 45 degrees, Midship section	Escort tug, with fin Yaw angle 45 degrees, Midship section
$Error_v$	0.091	0.024	-0.01
$Error_w$	0.013	0.010	0.040
$Error_{2D}$	0.241	0.070	0.098

Table 5-21, Comparison between Series 60 and escort tug, hexahedral mesh

Parameter	Series 60, C_B=0.6 Yaw angle 35 degrees, Midship section	Escort tug, no fin Yaw angle 45 degrees, Midship section	Escort tug, with fin Yaw angle 45 degrees, Midship section
$Error_v$	0.053	0.027	0.014
$Error_w$	0.049	0.003	0.042
$Error_{2D}$	0.164	0.078	0.102

These differences may be due to the significant differences in the hull shapes between the escort tug and the Series 60 hull. The escort tug was proportionally much wider (L/B=2.69) and shallower (B/T=3.74) compared to the Series 60 hull with L/B=7.5 and B/T=2.5. The flow on the downstream side of the escort tug (between the waterline and the keel) was proportionally faster than the flow on the downstream side of the Series 60 hull, while the flow over the bottom was approximately the same. As a result, there was less of a shear force gradient on the tug and so when the vortex forms it will not be as strong as the vortex on the Series 60.

5.9 RECOMMENDATIONS FOR FURTHER STUDY

There are some improvements that could be made to the CFD mesh that might improve the level of prediction of the forces and flow patterns. The first major refinement would be to include the free surface waves generated by the hull. This was ignored from the current meshes, on the basis that the effect of the free surface on the forces measured in the model experiments was seen to be small. The free surface of the water will distort and may affect the flow patterns close to the surface. This effect will become more noticeable as yaw angles and flow speeds increase.

Another refinement would be to make the mesh elements smaller in key areas of the flow. The most likely areas for refinement are where vortices are generated in the flow. The most noticeable vortices observed in the PIV experiments were around the downstream bilge for the hull without the fin, and the large vortex generated by the fin when it was fitted. The refined mesh could be compared with the single measurement window PIV data, instead of the coarser data spacing that was used for the complete data set. The data from the single measurement windows shown in Chapter 4 is available on very fine grid points, but a complete grid with cells at a similar spacing would be exceedingly large and require a very long time to come to a solution.

5.10 CONCLUSIONS

A commercial RANS Computational Fluid Dynamics (CFD) code was used to predict the forces generated by an escort tug hull, and the same hull fitted with a low aspect ratio fin, over the typical operating range of yaw angles, from 10 to 60 degrees. Two types of mesh were used. One type was a tetrahedral mesh, consisting of elements with four, three sided faces. The other type was a hexahedral mesh, consisting of elements made of six four sided faces. The most accurate force predictions were obtained using the mesh made entirely of hexahedral elements. This mesh gave force predictions that on average were within 5-6 % of measured values for the same flow conditions, and never exceeded 10%. The number of elements for the hexahedral mesh was less than one half of the number in the tetrahedral mesh, which resulted in a faster solution time.

The flow patterns around the hull predicted by both meshes at 45 degrees yaw were compared to PIV measurements taken at two planes around the hull. A subjective comparison of the results indicated that the hexahedral mesh gave slightly better predictions of the flow patterns, especially for the flow conditions across the bottom of the hull. A numerical analysis comparing the two meshes over the complete measurement region indicated that the differences were very localized and numerically very small. The average difference between the measured and predicted in-plane flow velocity vector magnitudes was between 8 and 10 per cent.

When the data for forces and flow patterns were combined, the best approach for creating a CFD simulation of an escort tug operating at a large yaw angle was to use a hexahedral mesh. Earlier CFD studies on the Series 60, described in Chapter 2, indicated that neither meshing approach had a significant advantage, but this conclusion was based principally on flow data and only included force measurements at 10 degrees of yaw. The different shape of the hull for the escort tug may have an effect on the accuracy of the predictions for different meshes, since this hull was wide and shallow with a high degree of curvature, whereas the Series 60 was relatively narrow with very sharp waterlines in the bow and stern.

CHAPTER 6

DISCUSSION ON THE APPLICATION OF CFD TO HULLS OPERATING AT LARGE YAW ANGLES

6.1 INTRODUCTION

For a practising naval architect, an important aspect of a CFD computer code is its potential ability to predict fluid pressure acting on a ship's hull, flow velocities within the fluid around the hull and integrate the pressure to obtain global forces. These results can be interpreted to refine the design of the hull being developed. The areas of investigation can be the hull form as a whole or studies of localized parts of the hull, such as a fin on an escort tug, or a rudder on a conventional ship.

The discussion in the previous chapters focused on validating CFD simulations against experiment data, based on measured planes at specific locations within the fluid. Little about the expected flow patterns around the complete hull has been discussed. Since it was extremely time consuming to carry out flow measurements in each case, it has to be assumed that if the flow predicted by CFD was validated at certain locations, and the level of accuracy was found to be acceptable, then the flow at other locations is predicted to approximately the same level of accuracy. The CFD code can then be used with some level of confidence to interpret the flow around the complete hull.

Data showing an overview of the force and velocity magnitude comparisons for tetrahedral and hexahedral meshes is given in Table 6-1 for the Series 60 and the escort tug (with and without fin). This table shows the difference between predicted and measured forces (as a percentage of the measured values) and errors in velocity magnitude (as a fraction of the free stream velocity). For the velocity magnitude, the error for the in-plane velocity components has been used, since this was available for all of the cases studied.

The research described in the earlier chapters determined the accuracy of a commercial Reynolds Averaged Navier-Stokes (RANS) type CFD code for predicting forces and flow patterns around a hull when there was a yaw angle. Force predictions were determined to be within 5 percent of experiment values for the Series 60 hull at 10 degrees yaw and on average within 6 per cent for a range of yaw angles from 10 to 60 degrees for an escort tug hull (without a fin). The magnitude of the in-plane flow velocity from flow measurement experiments and CFD predictions can also be compared. For the Series 60 the differences were on average 4.5% at 10 degrees yaw and 15% at 35 degrees yaw. For the escort tug at 45 degrees, the average value of the difference between measured and predicted flow magnitude was 8.5%.

Table 6-1, Summary of differences between CFD predictions and experiments for hulls with yaw angle

Tetrahedral mesh

Error $_{2d}$, non-dimensionalized by free stream speed

Hull	Number of elements	Yaw angle	Force	Section			
				20%L	60%L	90%L	
Series 60	1,760,000	10	+5%	0.050	0.038	0.069	
					50%L	90%L	
Series 60	1,760,000	35	N/A		0.241	0.102	
					50%L (DS)		50%L (US)
Escort tug							
No fin	2,171,000	20	-15.0%				
No fin	2,171,000	35	-11.0%				
No fin	2,171,000	45	-22.0%		0.074		0.084
With fin	2,171,000	20	0.3%				
With fin	2,171,000	35	-11.4%				
With fin	2,171,000	45	-5.1%		0.097		

Hexahedral mesh

Error $_{2d}$, non-dimensionalized by free stream speed

Hull		Yaw angle	Force	Section			
				20%L	60%L	90%L	
Series 60	423,000	10	+14%	0.047	0.039	0.044	
					50%L	90%L	
Series 60	423,000	35	N/A		0.164	0.142	
					50%L (DS)		50%L (US)
Escort tug							
No fin	987,000	20	-0.30%				
No fin	987,000	35	4.0%				
No fin	987,000	45	-7.60%		0.078		0.076
With fin	987,000	20	-0.30%				
With fin	987,000	35	-1.80%				
With fin	987,000	45	+10.5%		0.101		

This chapter presents the results of some CFD simulations using a commercial RANS CFD code for ship hulls with a yaw angle, and discusses some possible areas of application where CFD can be used to improve escort tug design. The effects of some of the assumptions made to simplify the calculations, such as steady flow conditions and that the free surface has a negligible effect on the results, are also discussed.

6.2 HULL FORM DESIGN

Four hull forms were chosen for the study described in this section. Three of the hull forms used have already been discussed in Chapters 2, 4 and 5. These were the Series 60 hull form, the escort tug without a fin and the escort tug with a fin. The Series 60 hull shape is typical of a high-speed merchant ship hull form, designed for minimum resistance in a straight line. The escort tug is a specialized design where operation in the 'off-design' condition of a high yaw angle is an important part of its operational profile. The fourth hull, the Wigley hull was a simple hull shape defined by second order functions for section shapes and waterlines. This hull form has been previously used for validation of numerical methods in ship hydrodynamics when the hull was at a yaw angle (Tahara and Longo, 1994). For consistency, all simulations were carried out using hexahedral meshes with no free surface. The four different hull shapes are summarized in Table 6-2.

Table 6-2 Hull forms used in yaw angle study

Design	L/B	B/T	Yaw angle range, degrees
Wigley	10.00	1.60	0 to 25
Series 60, C_B=0.6	7.50	2.49	0 to 25
Escort tug, no fin	2.69	3.74	0 to 40
Escort tug, with fin	2.69	2.07	0 to 40

A mesh for the Wigley hull was created to predict the effect of a free surface on the flow patterns and forces for a hull with a yaw angle (Collier and Molyneux, 2006). This mesh was shown to give predictions of forces that were within 4 percent of experiment measurements and wave patterns that matched the significant features of the experiment values at Froude number 0.30 at zero yaw angle. No experimentally measured force data was found for this hull with a yaw angle, but a comparison of the CFD predictions with the measured wave profiles at the hull for 10 degrees yaw showed that the principal features of the results had been predicted.

The predicted forces for each hull are given in Table 6-3. The flow speeds used were those used for the original study in each case. The predicted side force coefficient C_q is shown plotted against yaw angle for each hull in Figure 6-1.

Table 6-3, Predicted side force coefficients for four hull forms

Hull	Yaw angle, degrees	V, m/s	A, m^2	ρ, kg/m^3	Surge, N	Sway, N	C_q	C_l
Wigley hull	10	1.1827	0.250	998.2	2.154	19.428	0.111	0.012
Wigley hull	15	1.1827	0.250	998.2	2.081	37.598	0.215	0.012
Wigley hull	20	1.1827	0.250	998.2	1.921	60.195	0.345	0.011
Wigley hull	25	1.1827	0.250	998.2	1.599	85.658	0.491	0.009
Series 60	10	0.875	0.496	998.2	3.404	15.180	0.080	0.018
Series 60	15	0.875	0.496	998.2	3.569	29.356	0.155	0.019
Series 60	20	0.875	0.496	998.2	3.675	45.632	0.241	0.019
Series 60	25	0.875	0.496	998.2	3.634	63.220	0.333	0.019
ET, no fin	10	0.728	0.387	998.2	7.198	10.262	0.100	0.070
ET, no fin	20	0.728	0.387	998.2	6.79	20.524	0.200	0.066
ET, no fin	30	0.728	0.387	998.2	5.936	31.032	0.303	0.058
ET, no fin	35	0.728	0.387	998.2	5.326	36.589	0.357	0.052
ET, no fin	40	0.728	0.387	998.2	4.588	42.244	0.412	0.045
ET, no fin	45	0.728	0.387	998.2	3.751	47.735	0.466	0.037
ET, no fin	60	0.728	0.387	998.2	0.99	60.942	0.595	0.010
ET with fin	10	0.728	0.485	998.2	7.712	21.346	0.166	0.060
ET with fin	20	0.728	0.485	998.2	6.173	45.906	0.358	0.048
ET with fin	30	0.728	0.485	998.2	3.721	72.174	0.562	0.029
ET with fin	35	0.728	0.485	998.2	2.065	84.407	0.658	0.016
ET with fin	40	0.728	0.485	998.2	0.523	94.160	0.733	0.004
ET with fin	45	0.728	0.485	998.2	-0.556	100.707	0.784	-0.004
ET with fin	50	0.728	0.485	998.2	0.33	103.109	0.803	0.003

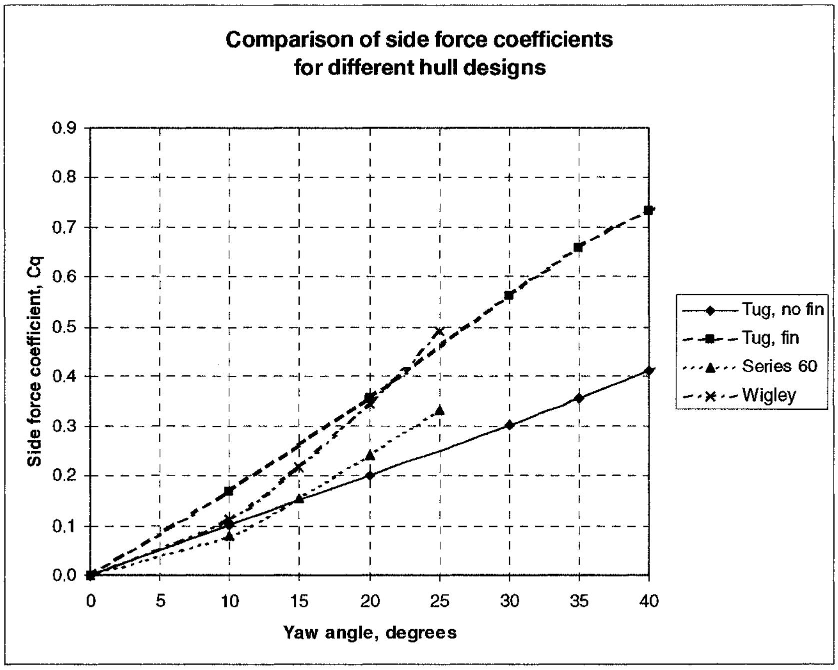

Figure 6-1, Predicted side force coefficient against yaw angle, four hull forms

Figure 6-1 shows that the fin is an essential element for generating side force on the escort tug and that the tug hull without the fin is not very efficient at generating a side force. For yaw angles below 15 degrees, the Series 60 hull had the lowest side force coefficient, but above this yaw angle the lowest side force coefficient was for the tug without the fin. The Wigley hull had the highest side force coefficient for a hull without a fin for yaw angles of 10 degrees and above, and at 25 degrees yaw the Wigley hull had a higher side force coefficient than the tug with the fin. For yaw angles below 22.5 degrees, the tug with the fin had the highest predicted side force of all the designs studied.

The high value of side force coefficient for the Wigley hull and the low value of side force coefficient for the tug without the fin can be understood by considering the flow patterns around the hull. Contours of non-dimensional flow velocity magnitude (local velocity magnitude divided by free stream velocity) are shown for each of the four hulls at a yaw angle of 20 degrees in Figures 6-2 to 6-5.

Figure 6-2 shows contours of non-dimensional flow velocity for the Wigley hull. This figure shows a vortex developing on the downstream side of the hull at the bow and its diameter expands as it moves downstream. The Wigley hull form contains a sharp discontinuity at the keel. Figure 6-3 shows the same flow conditions for the Series 60 hull, and a similar pattern was observed. The main difference being that the vortex was generated from the keel at the bow, in a similar manner to the Wigley hull, but as the flow moved further aft, the vortex formed at the bilge radius rather than the keel. For the tug with no fin (Figure 6-4), there was no vortex generated at the bow. In this case, the main feature was the flow separation on the downstream side of the hull, starting just ahead of the section at 70%L. When the fin was fitted (Figure 6-5), the flow around the fin created a large vortex, which extended under the hull, for the full depth of the fin.

A practical escort tug design must include features other than those directly related to hydrodynamics. The tug must have sufficient initial stability, large angle stability and freeboard to be able to withstand the overturning moments created by the tow force. One method of obtaining a high degree of initial stability is to have a relatively wide and shallow hull form, which has a high ratio of the transverse moment of inertia of the water plane to the volume of displacement. This has been achieved by using a hull shape with relatively blunt waterlines, compared to the Series 60 hull form or the Wigley hull form.

The resulting hull form has a lower tendency for the flow to separate at the bow, and as a result, the side force coefficient for this type of hull is low, relative to designs, which have finer waterline angles at the bow and stern.

In order to be effective at generating a high value of side force coefficient, an escort tug must have some additional appendage, which is very effective at creating the side force component. The case investigated used a low aspect ratio fin, which generated approximately half of the total side force, but there may be alternatives, which are equally effective.

The high value of the side force coefficient for the Wigley hull has some potential applications within escort tug design. The simple hull shape is unacceptable for practical tug design since it does not have the displacement or stability characteristics necessary for tug operation. Fitting it with a propulsion system would also be challenging given the high degree of curvature of the hull surfaces. Although unsuitable for a complete hull, the Wigley shape may make an effective keel design for an escort tug. A long shallow keel shaped like a Wigley hull, under a conventional tug hull form, may result in a tug with the same side force coefficient, but a shallower draft than the escort tug that was tested.

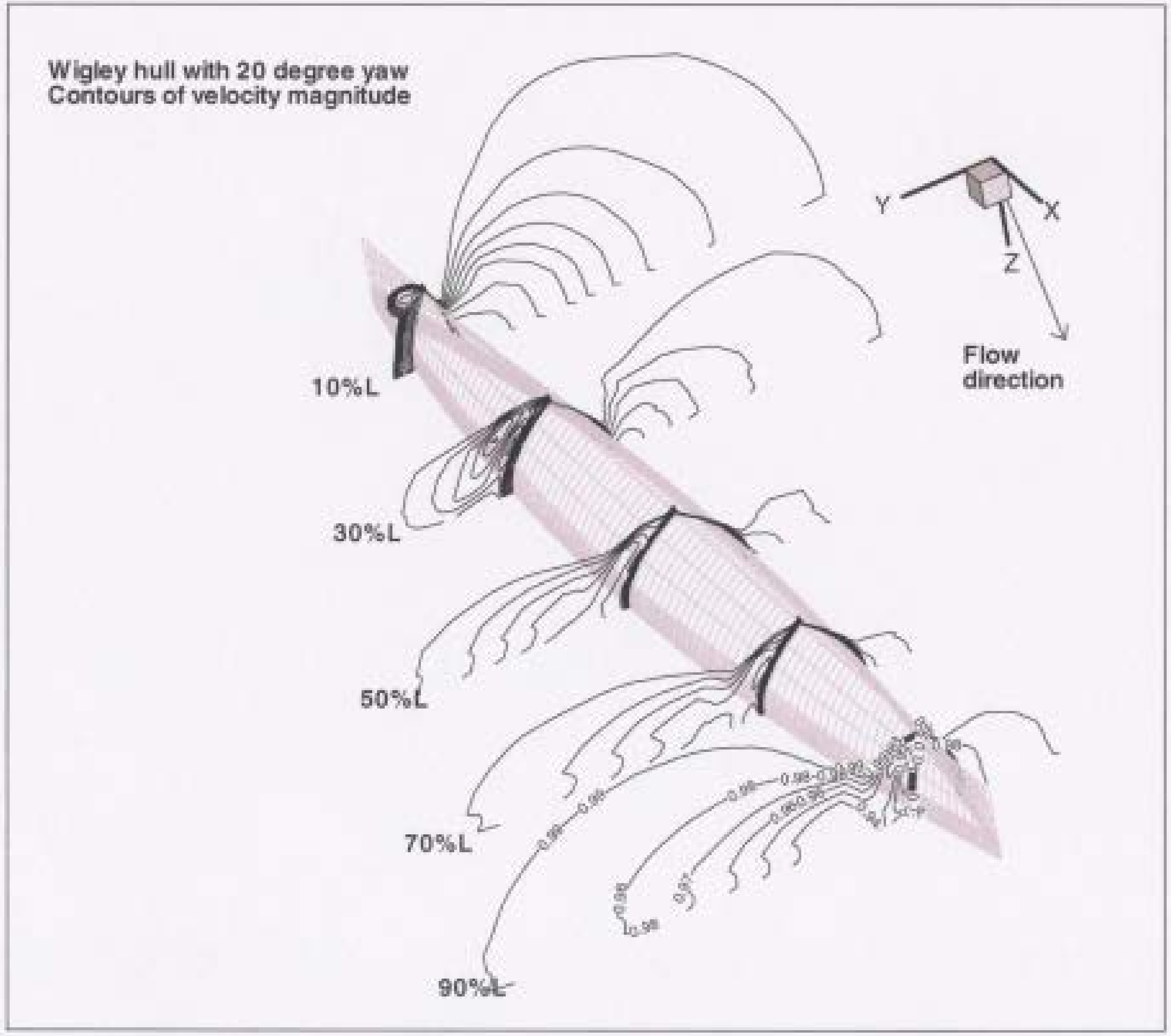

Figure 6-2, Predicted non-dimensional velocity magnitude around Wigley hull at 20 degrees yaw

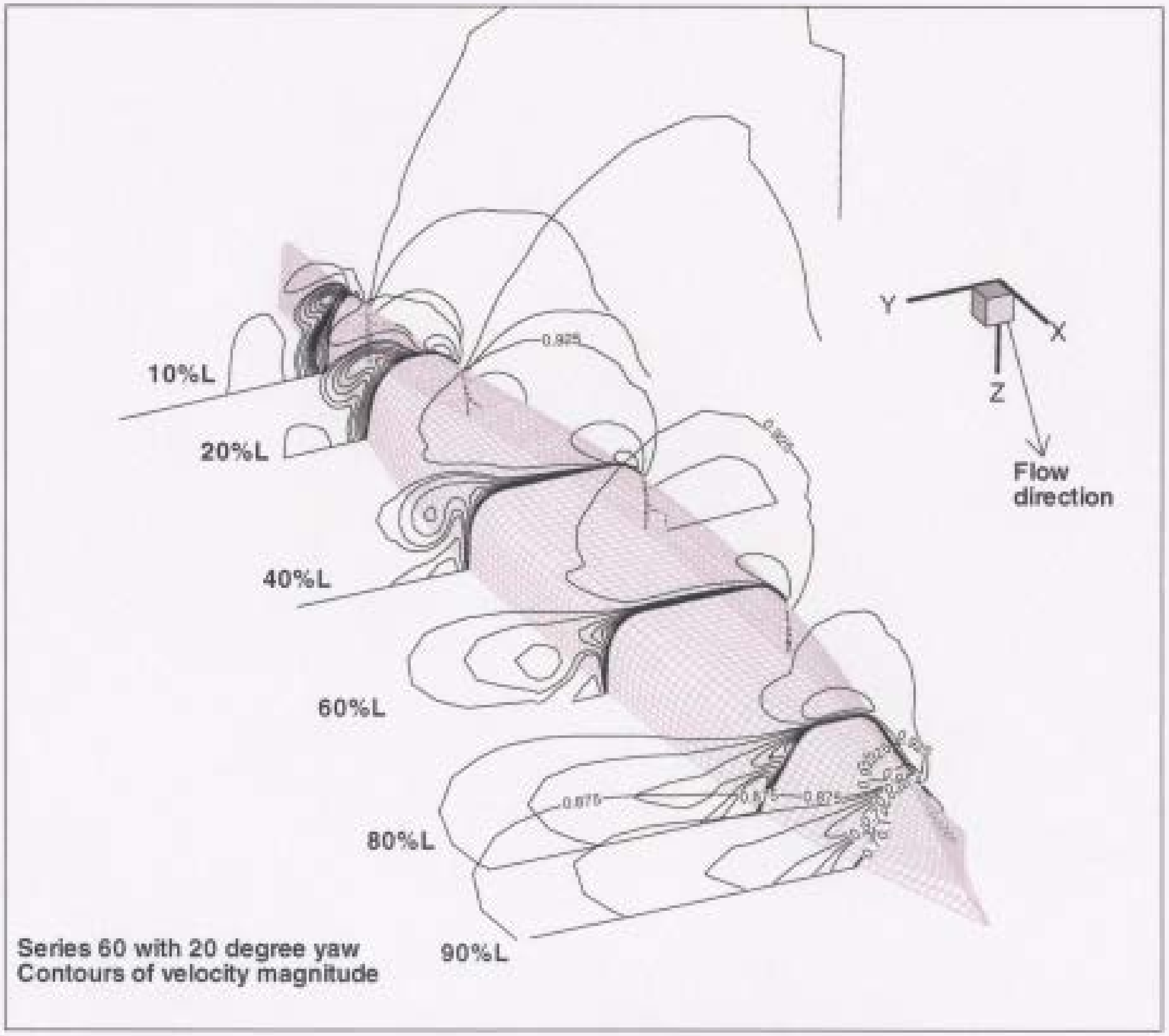

Figure 6-3, Predicted non-dimensional velocity magnitude around Series 60 hull at 20 degrees yaw

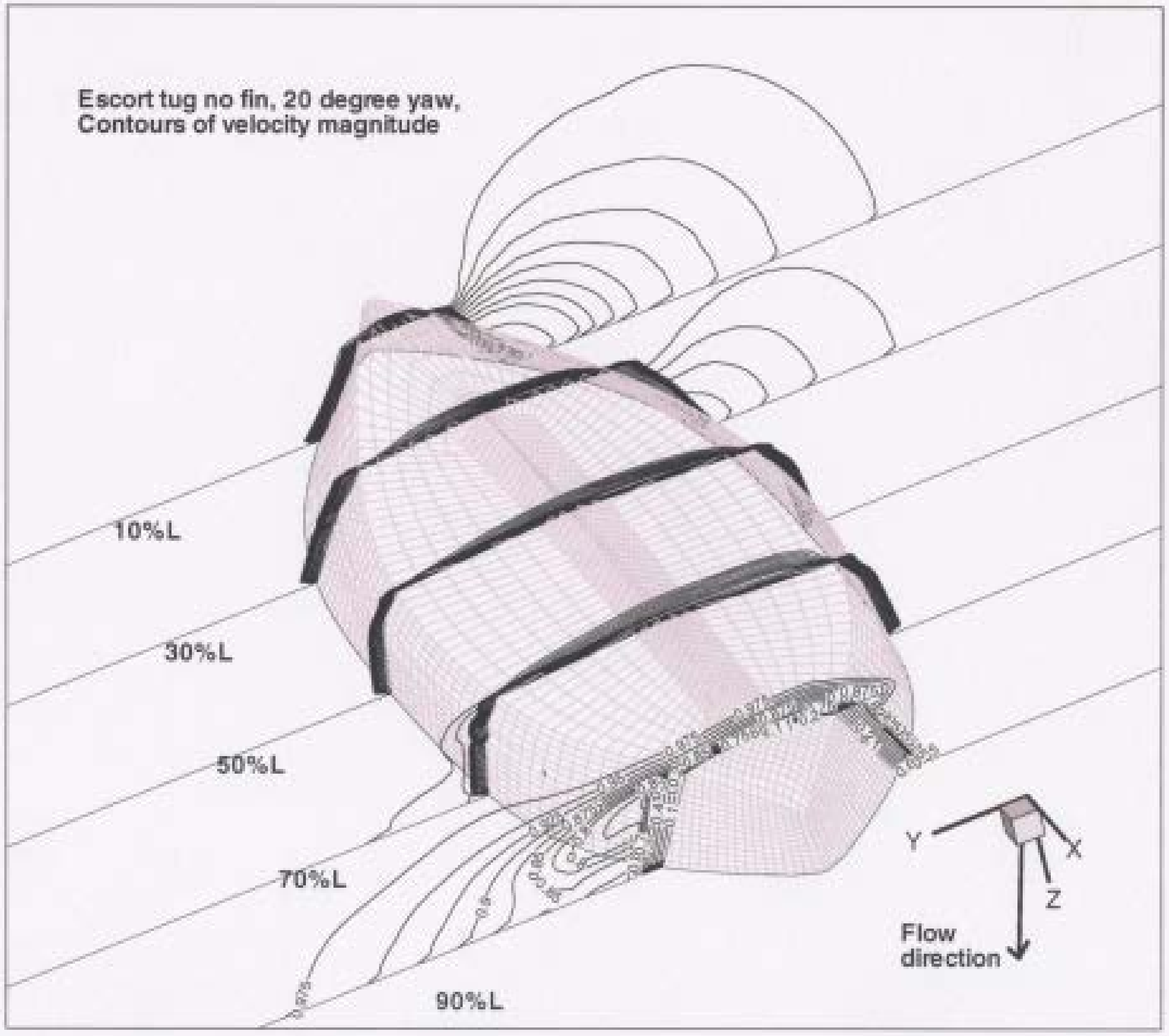

Figure 6-4, Predicted non-dimensional velocity magnitude around escort tug (without fin) at 20 degrees yaw

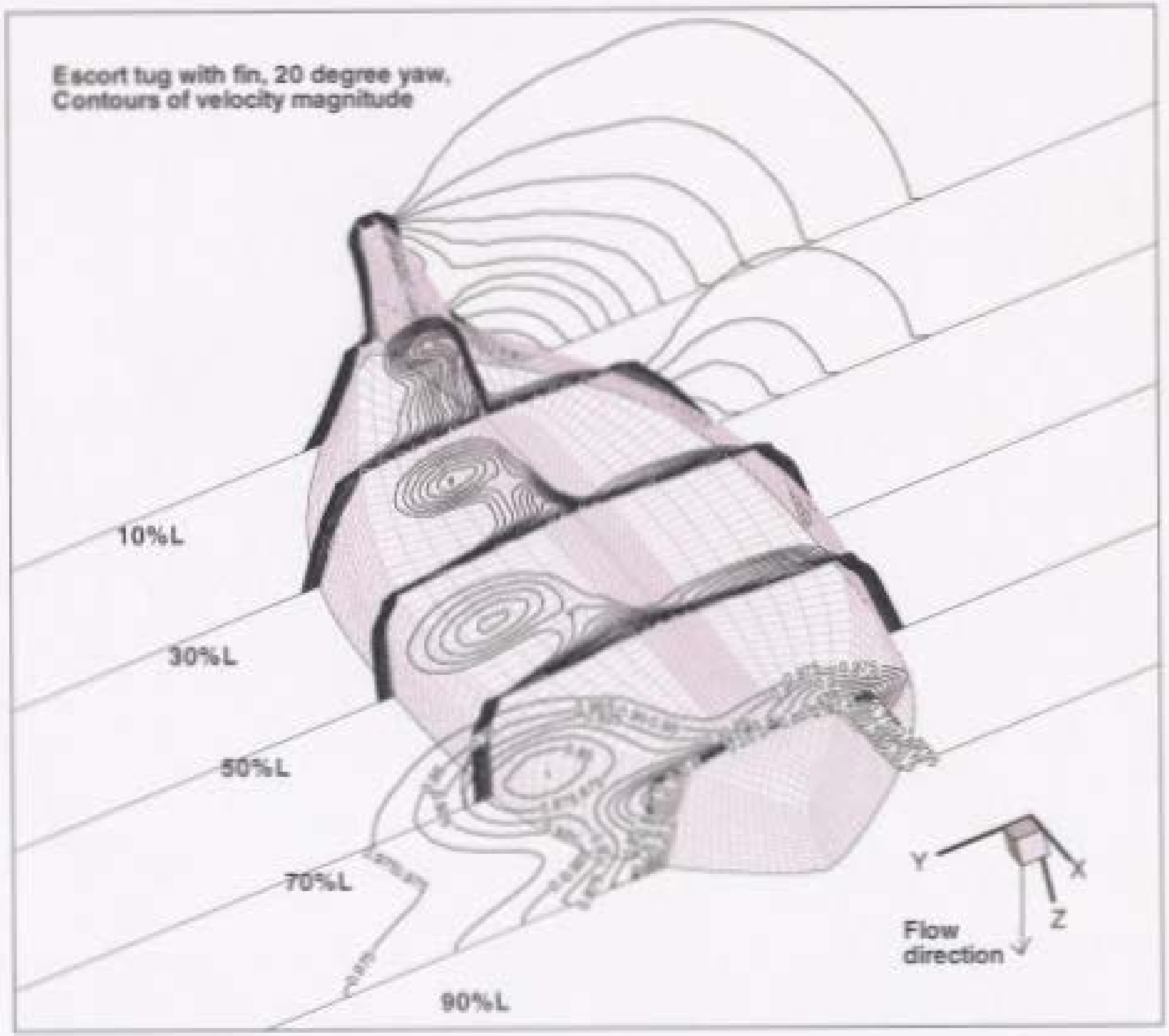

Figure 6-5, Predicted non-dimensional velocity magnitude around escort tug (with fin) at 20 degrees yaw

6.3 APPENDAGE DESIGN

The comparison between measured and predicted forces for the escort tug with a yaw angle, discussed in Chapter 5, showed that the effect of the fin on the escort tug was well predicted by the CFD code. The CFD code allows the user to determine forces on sections of the hull, so in the case of the tug with the fin, the force components can be determined for each part separately. Figure 6-6 shows the predicted lift and drag coefficients for the fin, when fitted to the hull, as a function of yaw angle. This figure shows that the fin stalls at 38 degrees. Experimental values for the combined fin and hull show that the local maximum for the side force occurs at 45 degrees (Molyneux, 2003), which was confirmed by the CFD predictions.

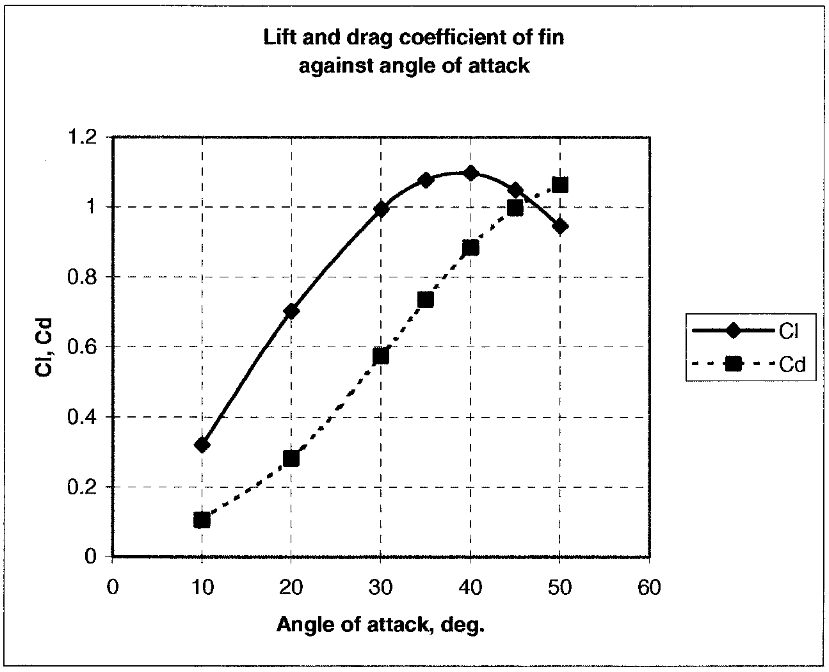

Figure 6-6, Calculated lift and drag coefficient for a low aspect ratio fin fitted to an escort tug hull.

The predicted flow patterns around the fin for yaw angles of 20, 35 and 45 degrees are shown in Figures 6-7 to 6-9. Each figure shows vectors of in-plane flow and contours of velocity magnitude, in a plane at mid-fin depth parallel to the design waterline. These figures show that at 20 degrees, the flow is still attached to the upper (low pressure) side of the fin. At 35 degrees the flow has begun to separate and at 45 degrees, the flow has completely separated.

This leads to another application for the CFD code, which would be to optimize the design of the fin for an escort tug. This approach would require separate meshes for each fin design attached to the same hull. Design factors of the fin that could be studied with CFD are the aspect ratio, thickness-chord ratio and profile. More complex fin geometries, such as trim tabs or flaps could also be studied. Using CFD enables the forces generated by the fin to be evaluated without carrying out model experiments for each fin design.

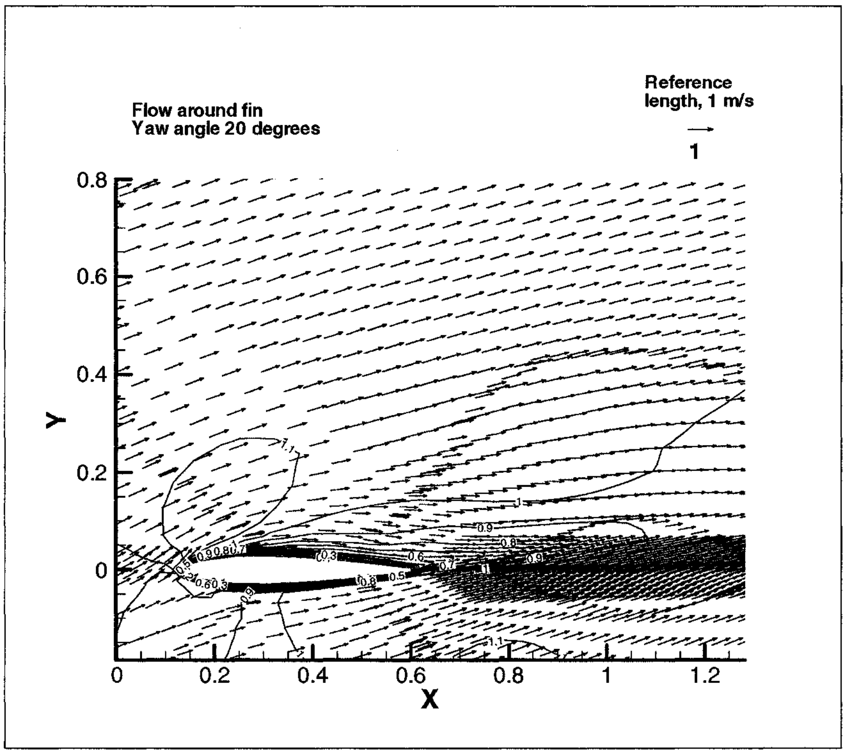

Figure 6-7, Flow around fin, yaw angle 20 degrees

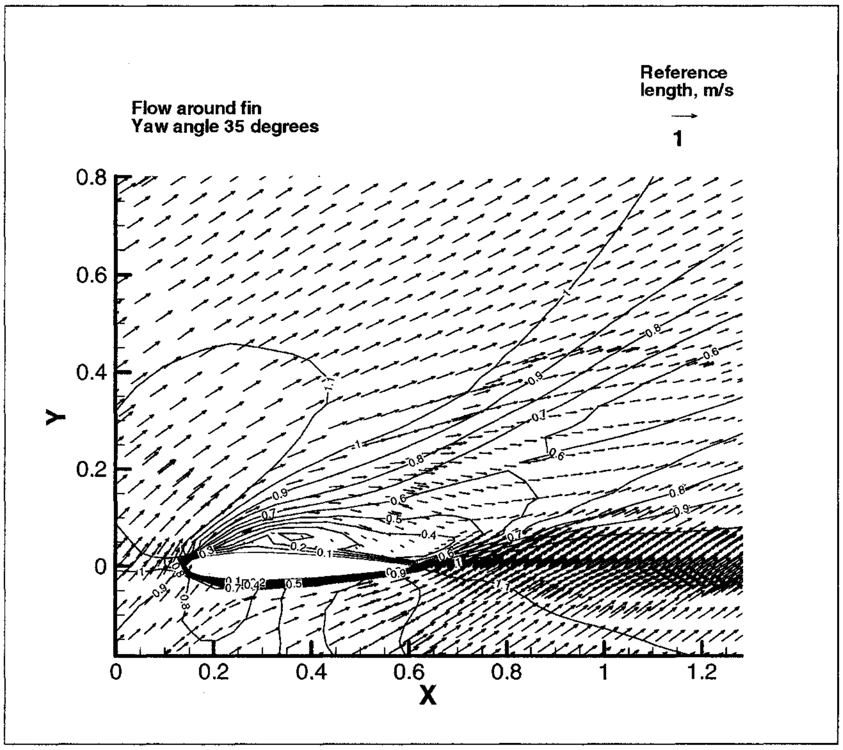

Figure 6-8, Flow around fin, yaw angle 35 degrees

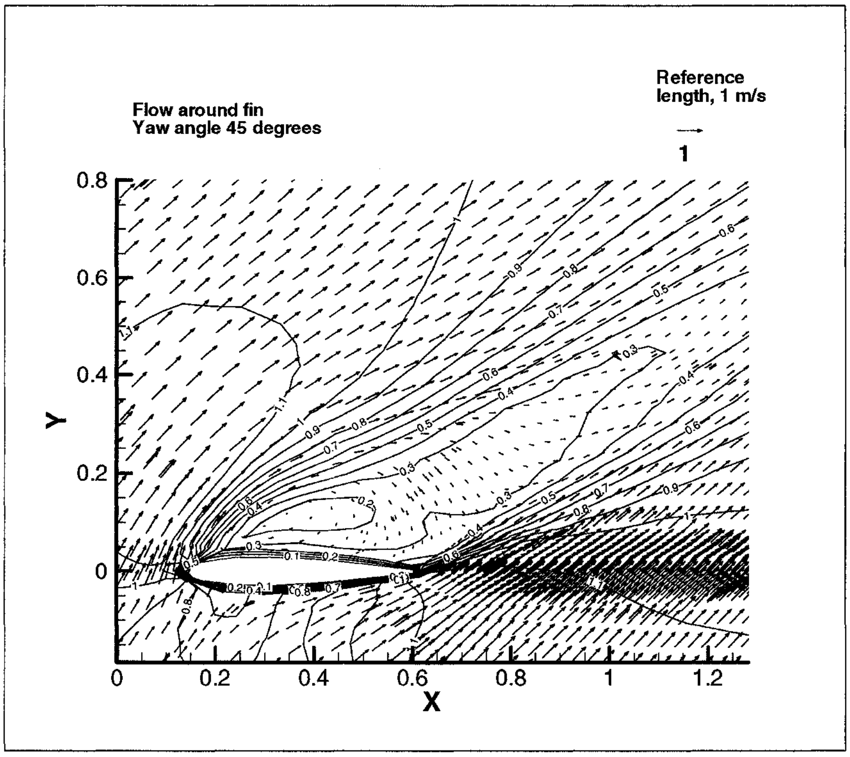

Figure 6-9, Flow around fin, yaw angle 45 degrees

6.4 UNSTEADY FLOW

One of the assumptions within the CFD solutions discussed above was that the flow was steady and the time dependent terms in the Navier-Stokes equations could be ignored. The experiment data used for comparison with the CFD results was all based on time-averaged flow velocities, and so there was no data with which to compare with any time varying CFD solutions. There was also a computational advantage, since the solution was obtained in a shorter time.

Figure 6-10. Aerial view of oil spill from *'Argo Merchant'* courtesy of NASA

During the PIV experiments discussed in Chapter 4, it was observed that there was a periodic shedding of a vortex off the bow and the stern of the model. This type of flow can be clearly seen in Figure 6-10, which shows oil leaking from a grounded tanker, with a current assumed to be flowing from the top left corner to the bottom right corner of the picture. The oil slick downstream of the tanker shows periodic patterns within the flow.

To illustrate the effect of time dependent flow on the results a simplified flow problem was considered. A two-dimensional model was created, using the design waterline of the 1:18 scale model tug at two different yaw angles. The domain was 15.2 m wide, and extended 7.6 m upstream and 20.4m downstream of the tug. Uniform flow at 0.728m/s entered the domain on the left hand edge, and exited from the right hand edge. The upper and lower boundaries and the hull were defined as walls with zero shear force at the wall. The two yaw angles considered were 20 degrees and 45 degrees. The time domain case was solved for steps of 0.1 seconds and results were presented as contours of velocity magnitude.

Results for the hull with 20 degree yaw are shown in Figures 6-11 to 6-13, at time steps of 50, 60 and 70 seconds. At 20 degrees yaw, there is some unsteadiness on the downstream flow patterns, but it was restricted to the region close to the hull on the downstream side.

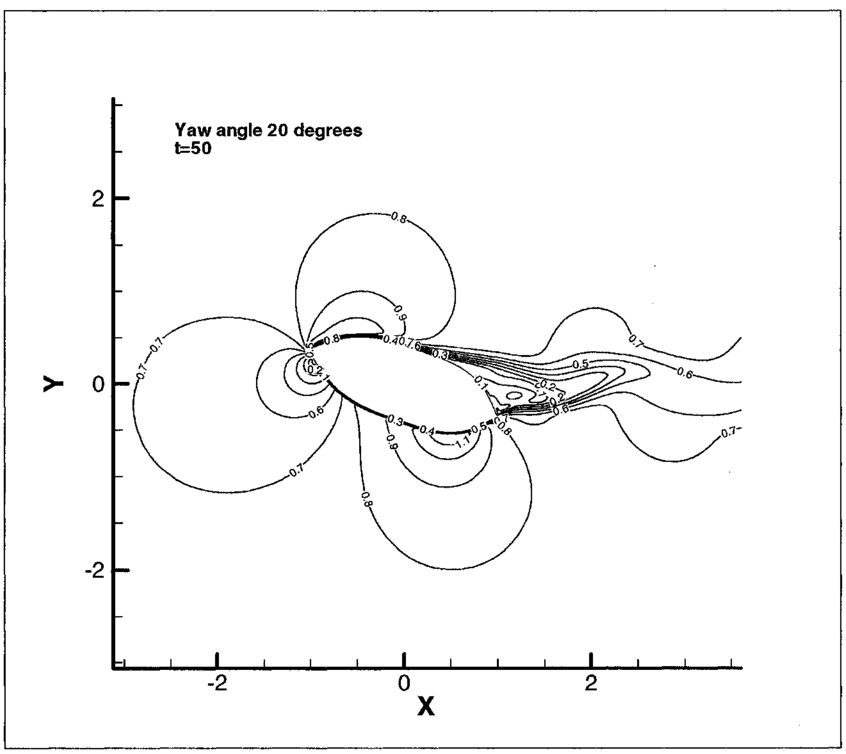

Figure 6-11, Two-dimensional flow, based on escort tug waterline, yaw angle 20 degrees, flow speed=0.728 m/s t=50 seconds

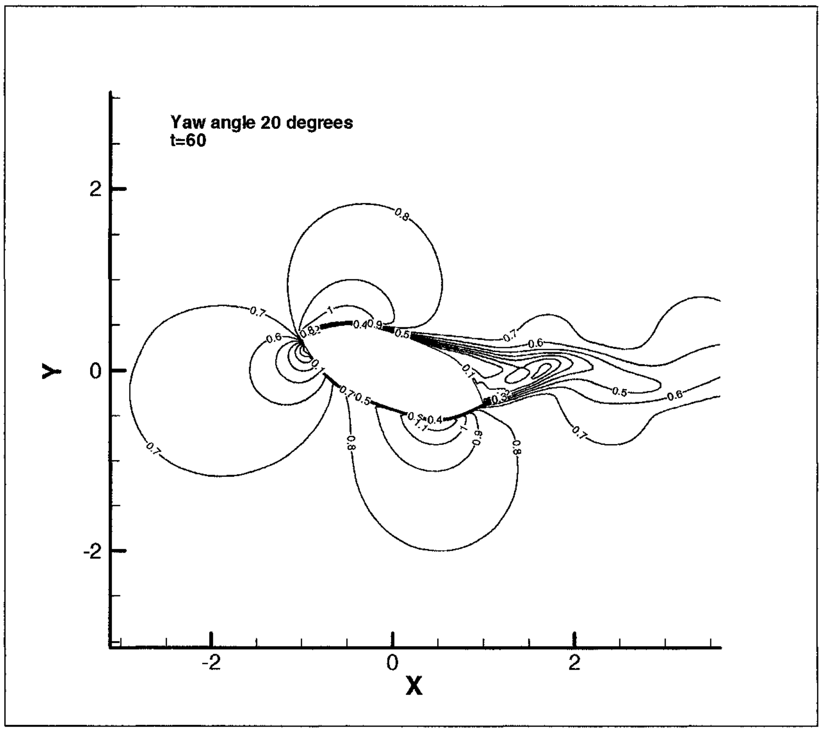

Figure 6-12, Two dimensional flow, based on escort tug waterline, yaw angle 20 degrees, flow speed=0.728 m/s t=60 seconds

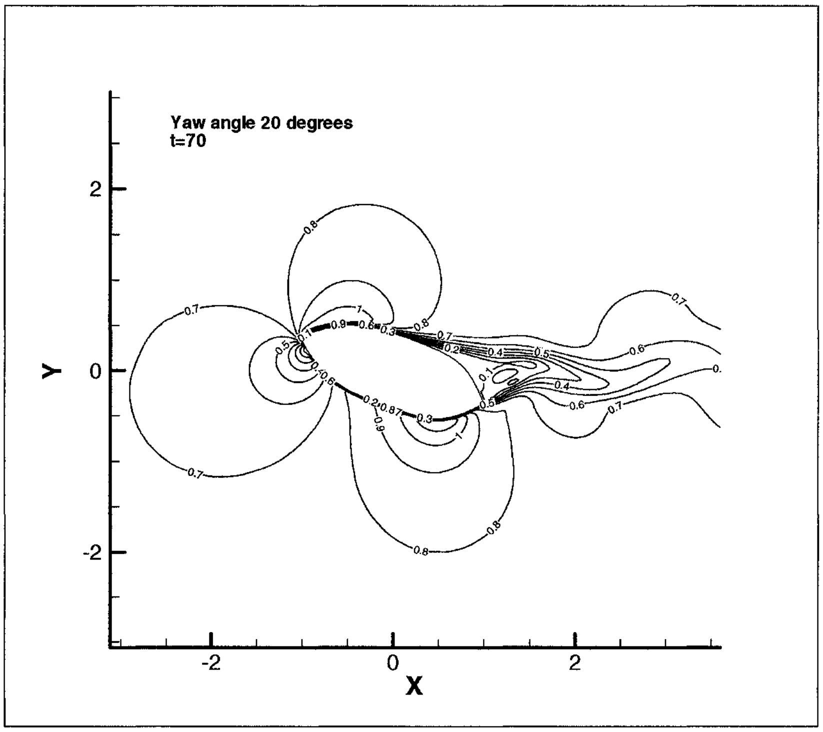

Figure 6-13, Two dimensional flow, based on escort tug waterline, yaw angle 20 degrees, flow speed=0.728 m/s t=70 seconds

Results for the hull at 45 degrees of yaw are shown in Figures 6-14 to 6-18, for times of 50, 54, 58, 62 and 66 seconds within the solution. At 66 seconds the flow pattern starts to repeat again, so the figures show every one-quarter of the periodic flow cycle. This yaw angle shows a high degree of unsteadiness in the flow and clearly shows that vortices are being shed periodically at the bow and stern.

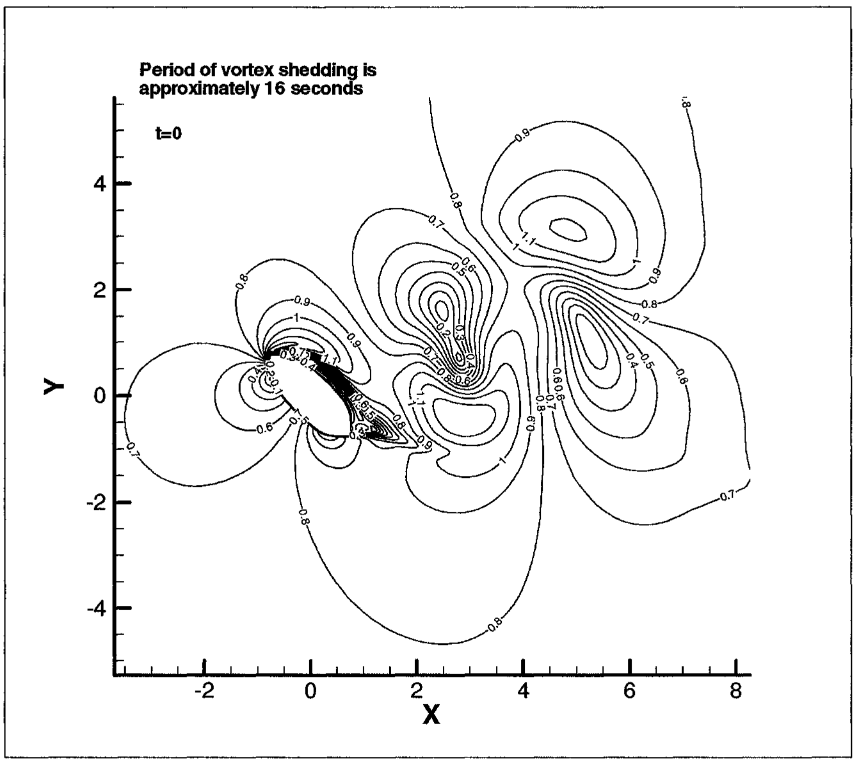

Figure 6-14, Two dimensional flow, based on escort tug waterline, yaw angle 45 degrees, flow speed=0.728 m/s t=50 seconds

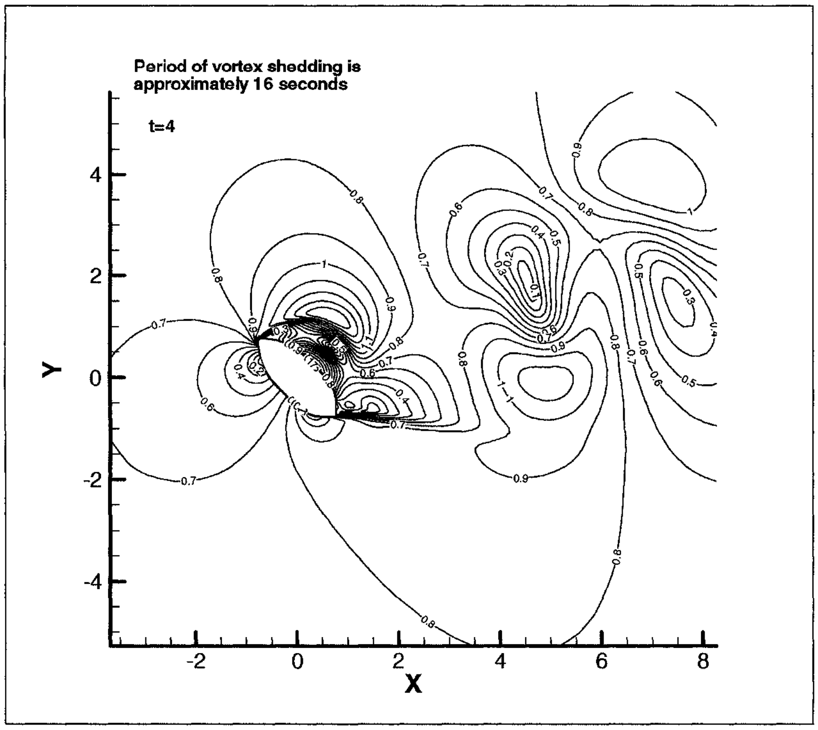

Figure 6-15, Two dimensional flow, based on escort tug waterline, yaw angle 45 degrees, flow speed=0.728 m/s t=54 seconds

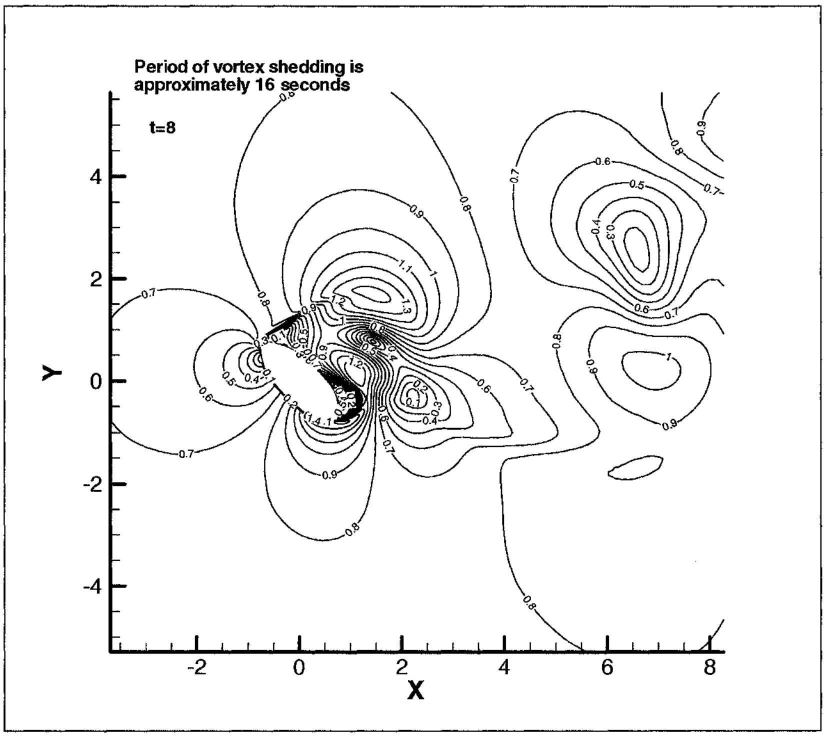

Figure 6-16, Two dimensional flow, based on escort tug waterline, yaw angle 45 degrees, flow speed=0.728 m/s t=58 seconds

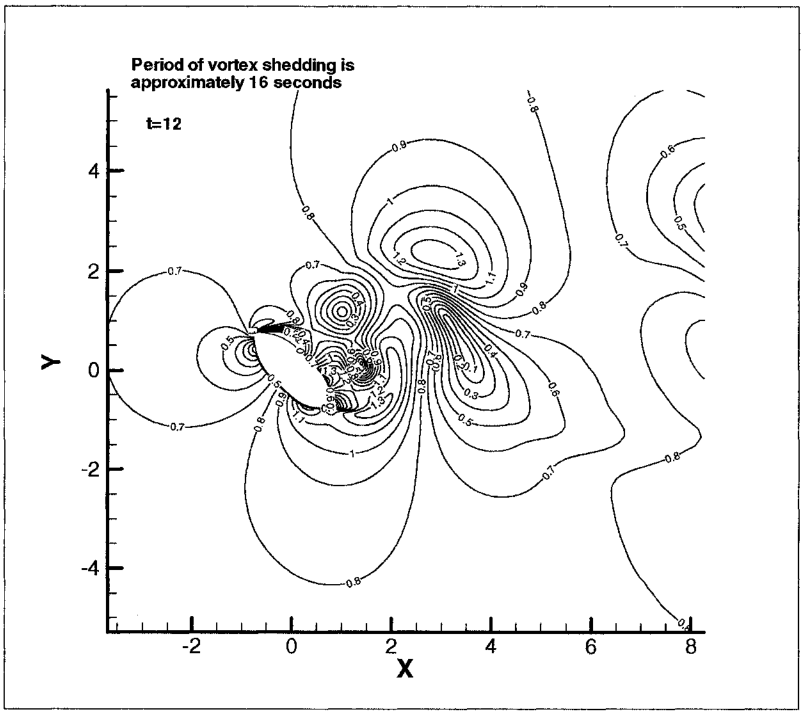

Figure 6-17, Two dimensional flow, based on escort tug waterline, yaw angle 45 degrees, flow speed=0.728 m/s t=62 seconds

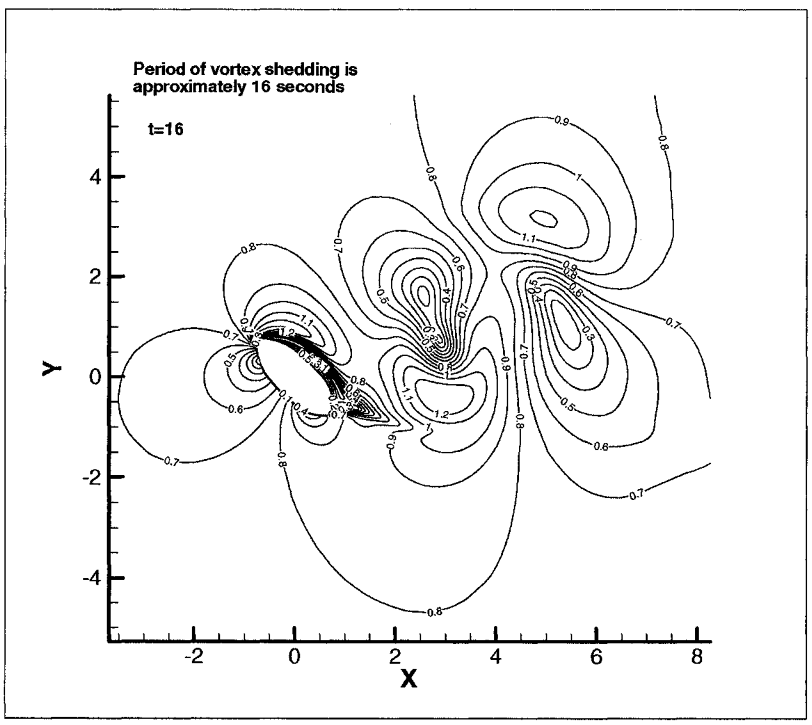

Figure 6-18, Two dimensional flow, based on escort tug waterline, yaw angle 45 degrees, flow speed=0.728 m/s t=66 seconds

The periodic vortex shedding is a real part of the flow around an escort tug and would be an interesting flow pattern to study. Unfortunately the PIV system used for this research cannot give good underwater measurements in a plane parallel to the waterline. Using the view directly out of the bottom of the borescopes results in an unacceptable distortion of the image, since this view does not include any optical correction. An alternative approach, which should be feasible, would be to make the measurements using the cameras in air, without the borescopes and seed the flow at the free surface.

6.5 FREE SURFACE WAVES

The most obvious potential shortcoming in the CFD solutions was the omission of the free surface within the solution. In order to address this issue some simulations for the Wigley hull were carried out with and without a free surface for yaw angles between zero and 40 degrees (Collier and Molyneux, 2006). The only data found for validating these simulations were experimental measurements of forces and wave profiles along the hull at zero yaw, and measurements of wave profile at 10 degrees yaw, so any comparison of the effect of waves on the forces and flow patterns can only be based on the results of un-validated CFD simulations. Despite this limitation, the results gave some insight into the effect of including a free surface on the calculated forces and flow patterns.

Flow speed for the comparison between the cases with and without the free surface was made at a Froude number (based on ship length) of 0.267. This was the Froude number used for a comparison between the model experiments and CFD simulations at 10 degrees yaw angle (Tahara and Longo, 1994).

The effect of free surface on a Wigley hull was evaluated at the highest speeds expected for escort tug operation. Based on the hull geometry and operating speeds given in Chapter 5, the maximum Froude number for an escort tug would be approximately 0.30. The model experiments and CFD validation for force measurements on the escort tug (described in Chapter 5) were made at a Froude number of 0.16. Force measurements made during experiments at other speeds showed that the side force coefficients varied much more with yaw angle than with flow speed. The flow measurements for the escort tug using PIV (described in Chapter 4) were made at Froude numbers of 0.110 and 0.219. All of the validation of the CFD predictions for the escort tug was carried out close to the mid-range of escort tug speeds.

6.5.1 Predicted Forces

A summary of the force predictions for each case, with and without the free surface is given in Table 6-4.

Table 6-4, Comparison of force components from CFD simulations for Wigley hull, with and without free surface

			# Iterations		F_x **(N)**		F_y **(N)**	
Yaw Angle degrees	**Speed (m/s)**	F_n	**FS**	**nFS**	**FS**	**nFS**	**FS**	**nFS**
0	1.18266	0.267	1031	205	2.2427	2.1772	-0.0094	0.0002
10	1.18266	0.267	1045	200	2.2670	2.1677	18.977	18.811
15	1.18266	0.267	1067	207	2.0334	2.0720	35.292	35.447
20	1.18266	0.267	1314	250	2.0135	1.8823	53.874	57.515
30	1.18266	0.267	1645	609	1.9054	0.8516	89.267	112.83
40	1.18266	0.267	1675	935	1.7097	-1.101	119.52	155.43

FS includes fluid free surface
nFS has boundary condition of a plane at level of nominal free surface

In terms of the effect of the free surface on the forces, there was a very small difference between the two sets of predicted forces in the x direction (along the centreline of the hull) throughout the yaw angle range. For yaw angles up to 20 degrees, the difference was less than 0.25N and within 3N at 40 degrees (for a model with a nominal length of 2 metres). The predicted force values in the y direction (normal to the centreline of the hull) show a greater variation. Up to 15 degrees yaw the difference was negligible, but as the yaw angle increased, the forces predicted with a free surface were consistently lower than the cases without the free surface. At 30 degrees yaw, the predicted forces for the free surface were 20 percent lower than the case without the free surface, and at forty degrees, the predicted values for the free surface case were 30 percent lower. At a yaw angle of 40 degrees, the difference between the side forces was reduced to 2 percent, if the flow speed was reduced to a Froude number of 0.11.

Adding a free surface to the CFD problem increased considerably the number of iterations that the program takes to come to a solution. At small yaw angles the solution including the free surface takes five times as many iterations, and at larger yaw angles it takes almost twice as many.

6.5.2 Predicted Flow Patterns

The predicted flow patterns within a plane at the midsection of the hull at 10 degrees yaw are shown with and without the free surface in Figures 6-19 and 6-20, and at 40 degrees

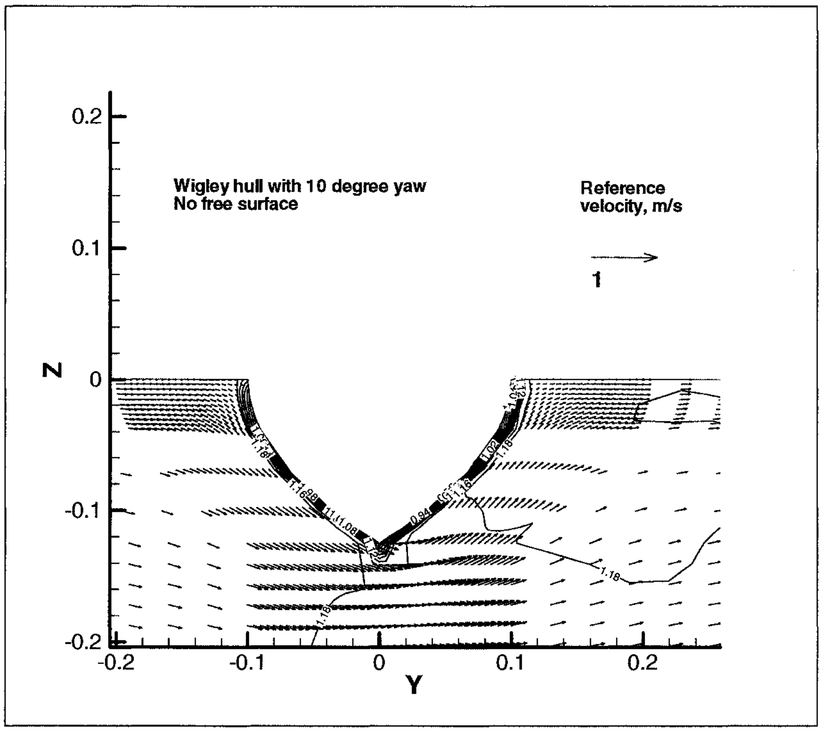

Figure 6-19, Flow patterns at 50%L with free surface ignored, yaw angle 10 degrees

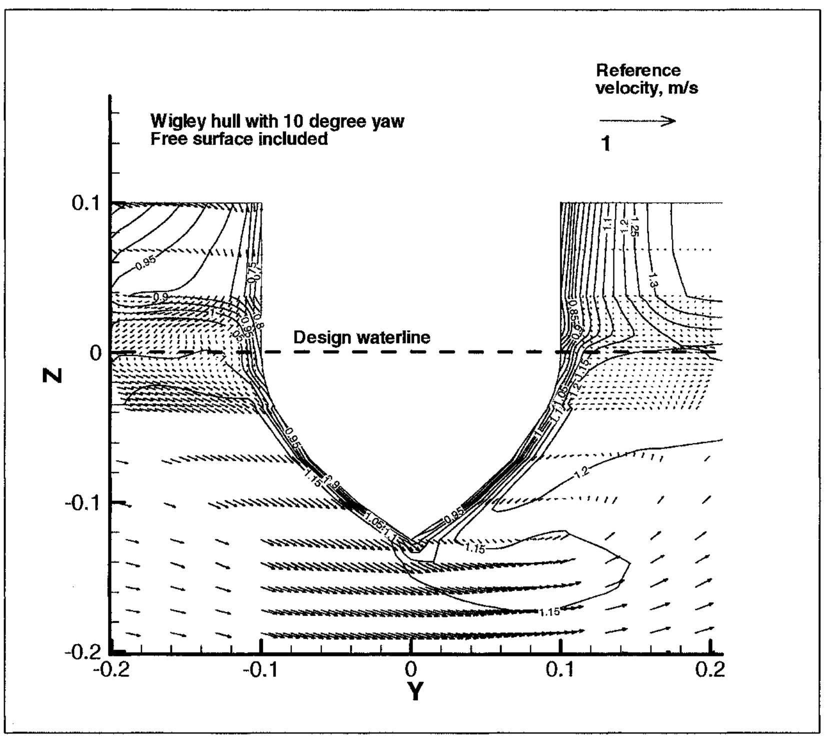

Figure 6-20, Flow patterns at 50%L with free surface included, yaw angle 10 degrees

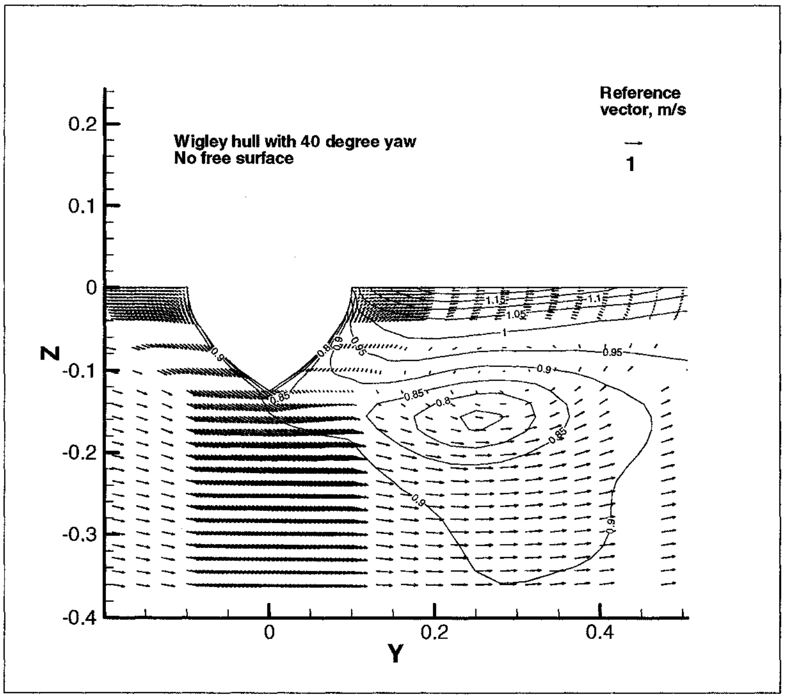

Figure 6-21, Flow patterns at 50%L with free surface ignored, yaw angle 40 degrees

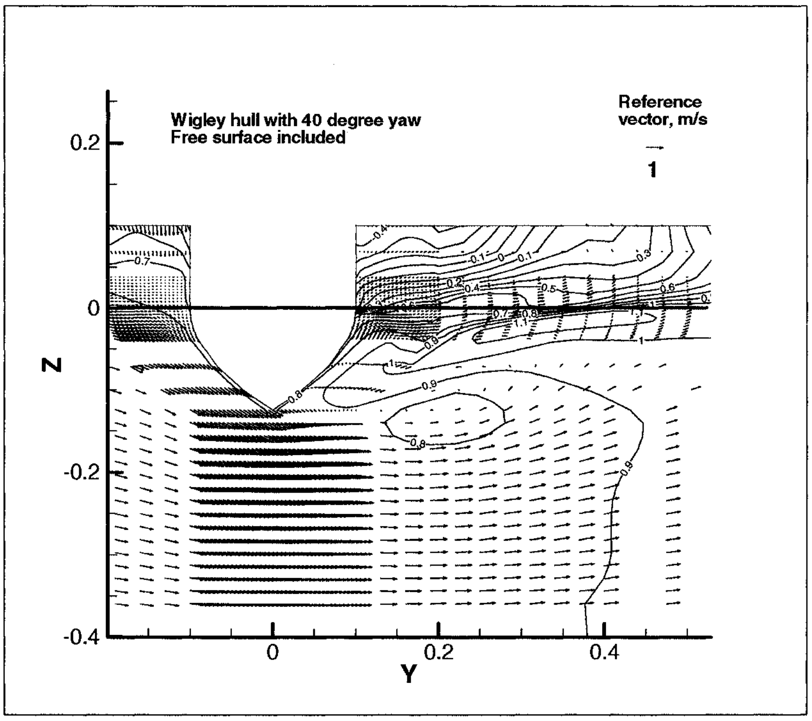

Figure 6-22, Flow patterns at 50%L with free surface included, yaw angle 40 degrees yaw in Figures 6-21 and 6-22. These figures show vectors of in-plane flow (magnitude and direction) and contours of through-plane flow.

There was clearly some effect of the free surface on the flow patterns. At 10 degrees yaw a small vortex was predicted on the downstream side of the hull when the free surface was present, but this was not seen when the free surface was ignored. At 40 degrees of yaw, both methods showed a vortex developing on the downstream side of the hull, but the location of the core was in a slightly different location. The contours of through plane flow were also slightly different in each case.

The numerical method developed in Chapter 2 for comparing CFD predictions with measured flow data was used to compare the different CFD grids. In this case, the basis for the comparison was the grid for the hull with no free surface, and the numerical difference between the CFD predictions of flow patterns for the hull with and without a free surface were calculated.

The difference between the in-plane predictions for 10 degrees of yaw is shown in Figure 6-23 and the through-plane predictions are given in Figure 6-24. The numerical values from these figures are summarized in Table 6-5. The analysis shows that the numerical difference between the flow patterns predicted with and without the free surface, is on average within 4 per cent. This difference is smaller than the difference between the experiments and the CFD predictions for the Series 60 model at 10 degrees yaw. The

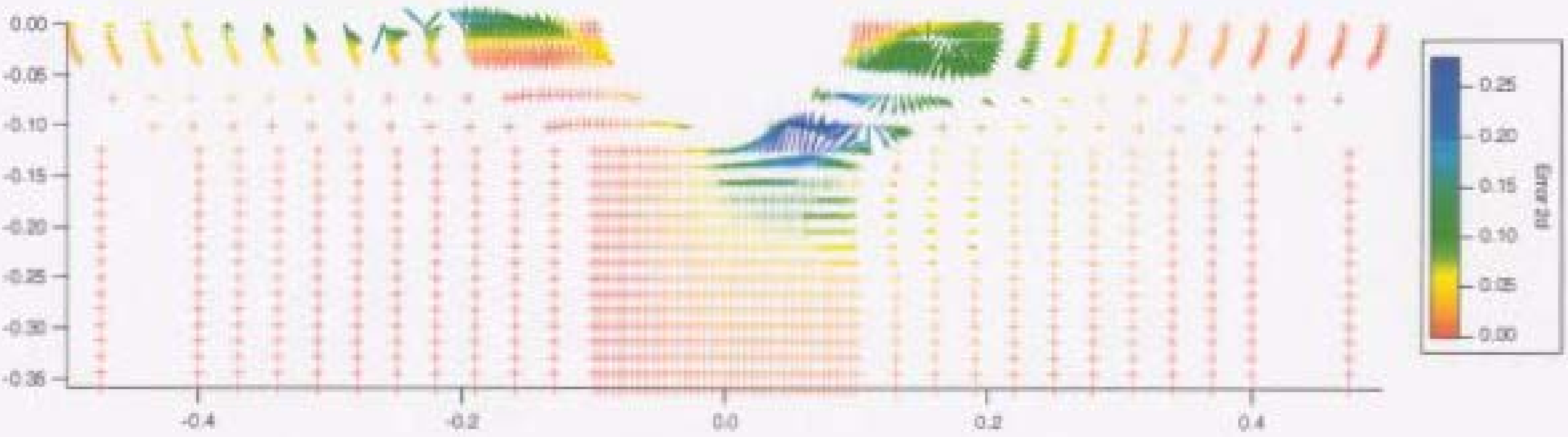

Figure 6-23, Errors in in-plane velocity, yaw angle 10 degrees

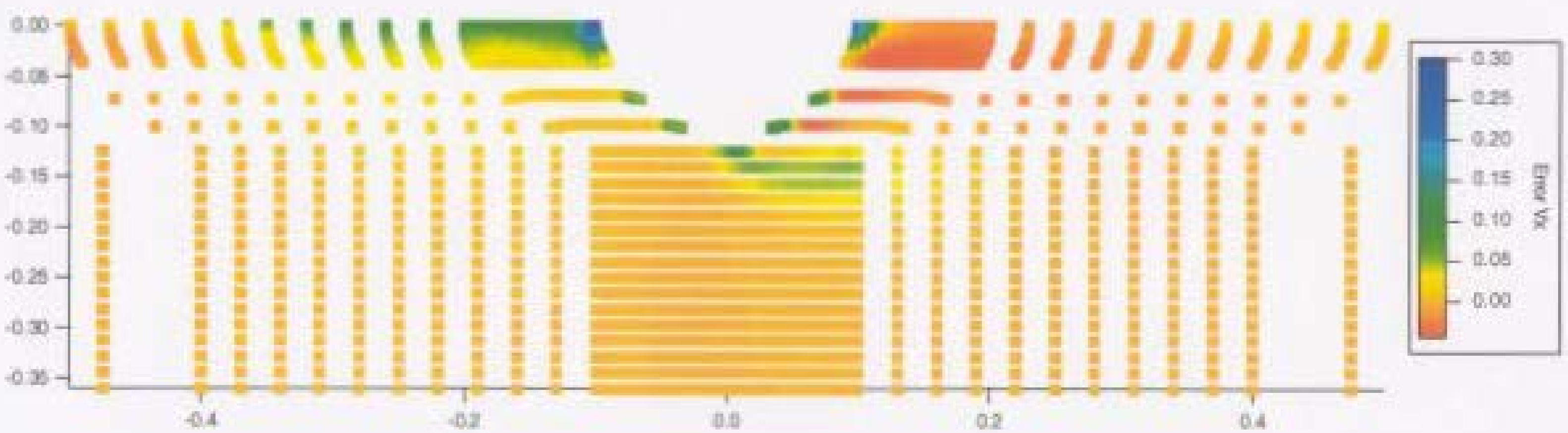

Figure 6-24, Errors in through-plane velocity, yaw angle 10 degrees largest differences between the two simulations for the Wigley hull with a yaw angle of 10 degrees occurred on the downstream side of the hull, close to the keel.

Table 6-5, Comparison of CFD predictions for Wigley hull, with and without free surface, yaw angle 10 degrees

Wigley hull, midsection
10 degree yaw

In-plane velocities

	Average	Std. Devn.	Min.	Max.	Range
Error V_y/V	0.018	0.038	-0.060	0.167	0.228
Error V_z/V	0.008	0.029	-0.068	0.166	0.233
Error 2d/V	0.035	0.038	0.001	0.235	0.234
Through plane velocity					
Error V_x/V	0.007	0.027	-0.036	0.254	0.289
Error 3d/V	0.041	0.043	0.003	0.254	0.251

At forty degrees of yaw, the differences in the predicted flow patterns due to the free surface are shown plotted in Figures 6-25 and 6-26, and summarized in Table 6-6. The differences shown in this table are much larger than those observed at 10 degrees, and larger than the differences between the experiments and CFD predictions for both the Series 60 model at 35 degrees yaw and the escort tug at 45 degrees yaw. The largest errors were very close to the top of the grid on the downstream side of the model. In this case, using the full mesh for the 'no free surface' case may not be a fair comparison, since when the flow within this region of the 'free surface' case contained a mixture both fluids.

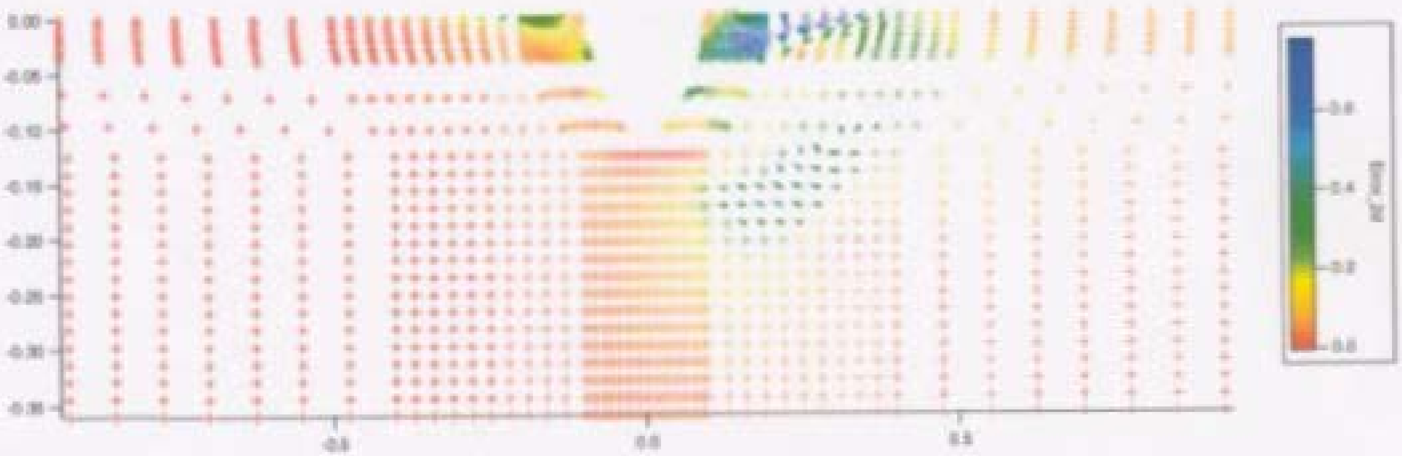

Figure 6-25, Errors in in-plane velocity, yaw angle 40 degrees

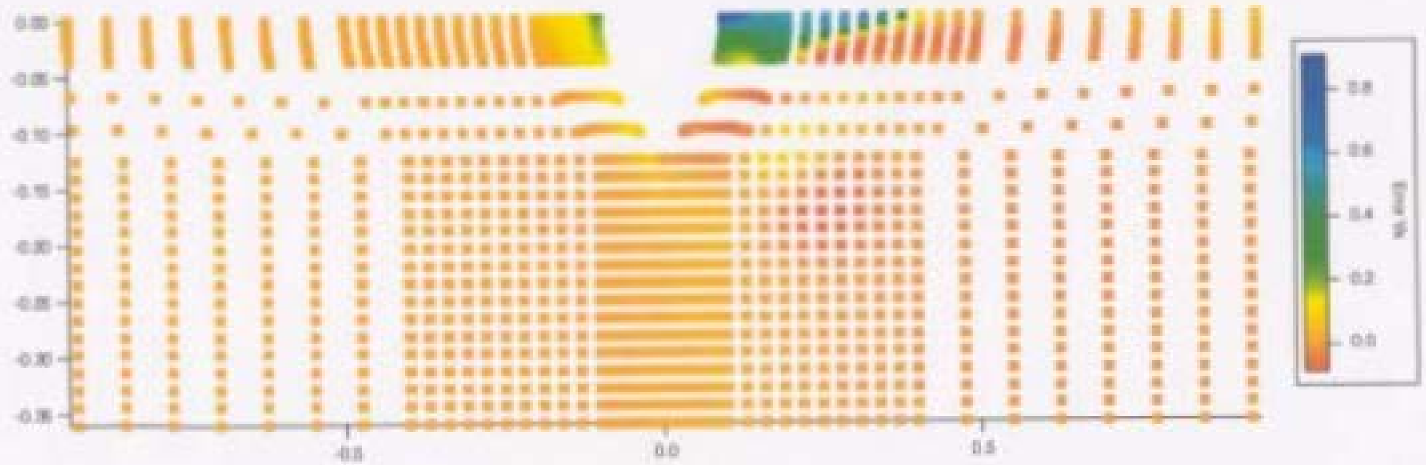

Figure 6-26, Errors in through-plane velocity, yaw angle 40 degrees

Table 6-6, Comparison of CFD predictions for Wigley hull, with and without free surface, yaw angle 40 degrees, full grid

In-plane velocities	Average	Std. Devn.	Min.	Max.	Range
Error V_y/V	-0.060	0.139	-0.655	0.248	0.903
Error V_z/V	-0.029	0.058	-0.309	0.077	0.385
Error 2d/V	0.110	0.123	0.000	0.658	0.657
Through plane velocity					
Error V_x/V	0.054	0.108	-0.071	0.765	0.836
Error 3d/V	0.131	0.157	0.001	0.832	0.832

To ensure that the comparison was based on a single fluid, the maximum z value was reduced from zero to 0.02 m. The revised numerical analysis is given in Table 6-7. This shows that the comparison between the two meshes was improved, and the difference between the predicted flow patterns was now close to the observed differences between experiment and CFD predictions for the three hulls for which data was available (Series 60 at 35 degrees yaw and escort tug at 45 degrees yaw).

Table 6-7, Comparison of CFD predictions for Wigley hull, with and without free surface, yaw angle 40 degrees, reduced grid

In-plane velocities	Average	Std. Devn.	Min.	Max.	Range
Error V_y/V	-0.053	0.105	-0.547	0.191	0.738
Error V_z/V	-0.032	0.060	-0.309	0.063	0.372
Error 2d/V	0.082	0.105	0.001	0.635	0.634
Through plane velocity					
Error V_x/V	0.028	0.056	-0.071	0.344	0.415
Error 3d/V	0.097	0.114	0.001	0.635	0.635

Based on this analysis, it can be seen that the calculated forces and flow patterns around a Wigley hull were affected by the presence of the free surface. The degree of difference between them depended on the speed of the flow and the yaw angle of the hull. At low yaw angles the difference was within 1 percent on forces and, on average, within 4 percent on flow velocity. As the speed and yaw angle was increased, then the differences became more pronounced. The largest differences in the flow patterns between the two meshes occurred close to the free surface. If the region close to the free surface was removed from the comparison, then the difference between the two sets of results was reduced.

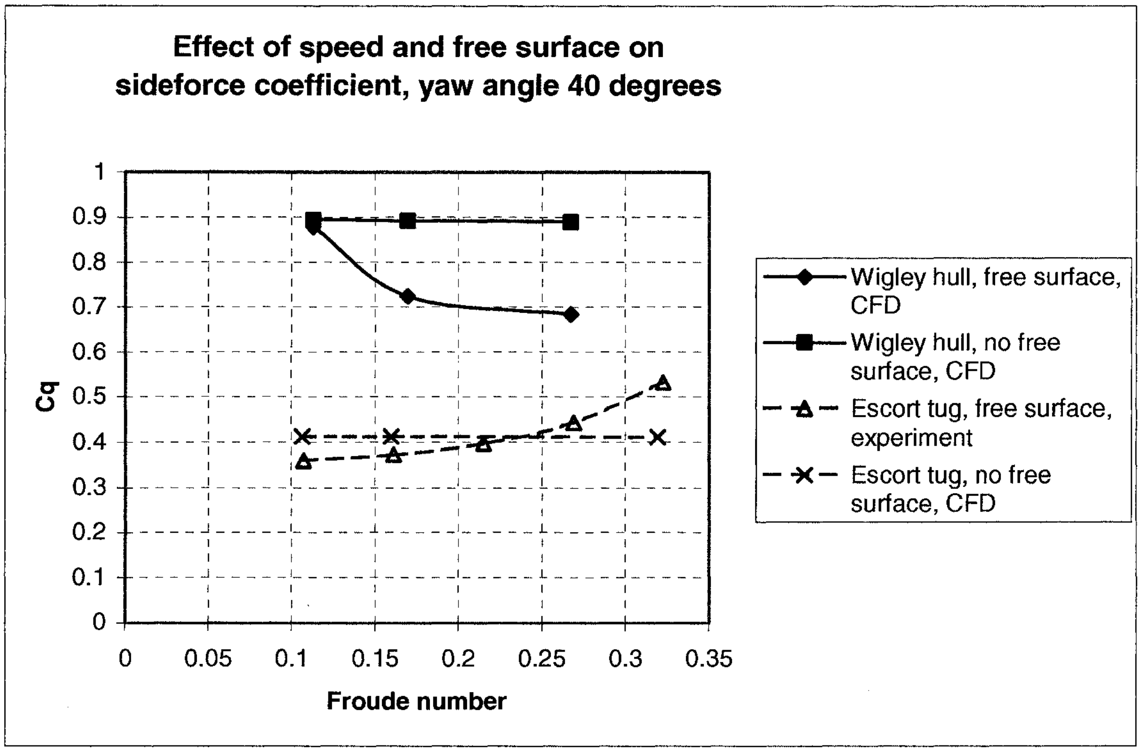

Figure 6-27, Effect of speed and free surface on side force coefficient at 40 degree yaw, Wigley hull and escort tug, without fin

It is also likely that the shape of the hull has some effect on the results too. Figure 6-27 shows a comparison of the calculated side force coefficient for the Wigley hull, with and without the free surface, with the escort tug. For the escort tug, the 'free surface' values were derived from forces measured during experiments, and the 'no free surface' case was taken from CFD predictions. The tug without the fin was chosen for this comparison for two reasons. Firstly, measured force values were available for this configuration, whereas the forces were estimated for the hull with the fin, as discussed in Chapter 5. Secondly, the comparison should give a better understand the effect of hull shape, since the Wigley hull did not have a fin.

Figure 6-27 shows that the trend of side force coefficient against Froude number for the tug is the opposite of the Wigley hull. For the tug, the highest coefficient was seen at the high Froude numbers, but for the Wigley hull, the highest force coefficient was seen at the lowest Froude number. For the escort tug, the CFD case with no free surface had approximately the same value as the arithmetic mean of the values for all the cases with a free surface. The effect of the free surface on the escort tug could be confirmed by running a CFD simulation including the free surface.

The shape of the Wigley hull resulted in a high degree of flow separation off the keel. When the free surface was present this resulted in a lot of mixing of the air and water, and a poorly defined free surface on the downstream side of the hull. This was not seen in the escort tug experiments, and may explain the opposite trend in the results.

6.6 CONCLUSIONS

Results from a commercial RANS CFD code showed differences in the predicted force components and flow velocity distributions that depended on the hull shape and the type of appendages fitted. The results can give the naval architect some insights into how the flow patterns around a hull at a yaw angle are formed, and the features of the hull that influence the magnitude of the resulting hydrodynamic forces. Sharp waterlines at the bow, or a large appendage are required to generate high values of side force coefficient.

In practice, the flow around a hull with a yaw angle is unsteady with time, but the degree of unsteadiness will depend on the yaw angle and flow speed. Checking the accuracy of the time dependent results of the CFD code will require additional experiment data, since all data up to this point has been obtained for time-averaged flow patterns.

The free surface will have some effect on the predicted flow patterns, but the amount of difference will likely depend on the hull shape, the flow speed and the yaw angle. Small yaw angles and low flow speeds will be the cases where the assumptions will have the least effect on the predicted forces and flow patterns. Based on analysis of a Wigley hull, the difference between the predicted forces was within 1 per cent at 10 degrees yaw increasing to 30 per cent at 40 degrees. The magnitude of the difference between the flow patterns depended on the region used for analysis, but if the comparison was restricted to areas where a single fluid was present, the difference between the in-plane velocity magnitudes was less than 10 percent for yaw angles up to 40 degrees.

It is likely that the effect of the free surface on the escort tug will be smaller than for the Wigley hull, especially for the flow speeds used for the comparison of forces and flow patterns. At low speeds, measured forces for the escort tug showed less variation with flow speed, when compared to the equivalent values for the Wigley hull. This could be confirmed by running a CFD simulation, including the free surface, for the escort tug model.

CHAPTER 7

CONCLUSIONS

7.1 RESEARCH OBJECTIVES

In Chapter 1 it was identified that there was very little information available to help naval architects understand the flow velocities and the forces that result when a ship's hull operates at a large yaw angle (20 to 45 degrees). Escort tugs operate at these yaw angles, and the hydrodynamics of these hull shapes have not been analyzed in detail. This lack of knowledge may be preventing escort tugs from reaching their optimum hydrodynamic performance. It was also speculated that commercial RANS based CFD codes should be able to make predictions of forces and flow patterns for a hull in this yaw angle range, but the accuracy that could be obtained for these conditions was unknown.

Predicted forces and flow patterns could be compared against experimental measurements (if there were any available) to check the accuracy of the CFD predictions. Data was published for the Series 60 hull at 10 degrees yaw (Longo and Stern, 1996, 2002), which was below the yaw angle range of interest, and at 35 degrees (Di Felice and Mauro, 1999), which was within the range of interest.

The overall objective of this research was to determine how accurate RANS CFD codes were at predicting the forces and flow patterns around a hull shape at a high yaw angle and especially hulls shapes typical of those designed for high yaw angle operation. If it was found that an acceptable level of accuracy could be achieved, then the CFD code can be used for analyzing hull designs at high yaw angles. In order to reach this objective three key elements were needed, that were not available from the literature, each having several sub elements. These key elements and sub-elements were:

a) Develop a method for comparing CFD predictions of flow velocities against measured data.

A combined numerical and graphical method was required to reduce the level of subjectivity when comparing CFD predictions of flow vectors with measured data.

This involved the following steps:

i) Make CFD predictions for Series 60 hull to use as test case against published experiment data.

ii) Develop a numerical and graphical method for comparing CFD predictions against experiment data.

iii) Use this method to analyze the accuracy of CFD predictions for Series 60.

iv) Evaluate the most accurate CFD modelling technique based on Series 60 results.

The Series 60 hull was narrower and deeper, with much finer waterlines, than a hull typically used for high yaw angle operation. The conclusions developed on this hull shape may not apply to all hulls at high yaw angles. In order to address this concern, two additional steps must be taken.

b) Obtain measurements of flow velocities around a hull designed for operation at a large yaw angle.

Measured flow data for hulls designed to operate at yaw angles between 20 and 45 degrees (such as escort tugs) were not available.

This involved the following steps:

i) Commission a PIV system.

ii) Develop techniques for seeding the flow in a towing tank suitable for a hull with a yaw angle.

iii) Develop a test plan to obtain data over a suitable measurement area.

iv) Carry out experiments.

v) Analyze and interpret results.

c) Determine accuracy of CFD predictions for a hull designed for large yaw angles.

Assess the accuracy of CFD codes for predicting forces and flow velocities for a hull designed to operate with a high yaw angle.

This involved the following steps:

a) Make CFD predictions for an escort tug hull over a range of yaw angles.

b) Analyze the accuracy of CFD predictions for an escort tug hull against PIV data (using methods developed above).

c) Determine the most accurate CFD modelling technique based on escort tug results.

d) Assess the effect of the simplifying assumptions within the CFD methods.

Conclusions were determined at each stage of the research and the significant conclusions from the research are given below.

7.2 METHODS FOR ASSESSING ACCURACY OF CFD PREDICTIONS OF FLOW VELOCITIES AGAINST EXPERIMENT DATA

An evaluation method, based on numerical analysis and graphical presentations, was developed that allowed comparisons to be made between experimental measurements of fluid velocity and predictions of the same flow conditions made using CFD. It was assumed that flow measurements were made on a constant plane within the fluid. The method required the definition of an area over which the evaluation was to be made, and a grid of comparison points within this area. The analyst must decide on the most appropriate measurement area and grid pattern. Both of these choices can be specific for the flow patterns being studied. The same general approach can also be used for comparing flow vectors predicted by different CFD meshes against each other.

In order to make the comparison, each of three orthogonal velocity components (for experimental measurements and CFD predictions) was interpolated on a common comparison grid. The assessment of the accuracy of the CFD prediction was based on the statistics of the differences between the two sets of data. A perfect prediction would have a zero value for the difference between the flow vector measured in the experiments and the flow vector obtained from the CFD predictions.

Measured flow data is typically presented as in-plane flow components and through plane flow components, regardless of how the measurements were made. For this reason it was found to be helpful to consider flow within the measurement plane and the flow through the measurement plane separately. If two-dimensional measurements were made, then only the in-plane values needed to be considered, and the third dimension can be ignored.

A graphical presentation was developed that showed the error in magnitude and direction of flow velocities between the predicted and measured vectors within the plane. The accuracy of the CFD predictions over the complete comparison area was visualized, based on the magnitude and direction of the 'error' between the measured values and the CFD predictions. The accuracy of the predictions was mapped relative to the geometry of the hull or key features within the flow, such as a vortex or a boundary layer.

Numerical quantities were also used in the analysis and the most useful parameters were found to be the magnitudes of the mean error in the individual orthogonal velocity components, the magnitude of the in-plane velocity component, as well as the maximum and minimum errors.

The main advantage of the approach was that it gave a numerical measure of the accuracy of the CFD predictions of flow vectors against measured data. It provided a numerical index of the accuracy of the predictions and reduced the level of subjectivity required when assessing predicted flow vectors against experiment data. Subjectivity was not removed completely, since the analyst must pick the region where the comparison is being made, and the density of the comparison points. Other parameters can be added to the comparison between CFD predictions and experimental results, such as Reynolds stresses and vorticity, without changing the principles of the method.

7.3 APPLICATION OF PIV METHODOLOGY TO TOWING TANKS

A preliminary study (Molyneux and Xu, 2005) showed that it was necessary to use a seeding rake when carrying out experiments using PIV to measure the flow vectors around a ship model with a yaw angle in a towing tank. Without active seeding of the flow, it was not possible to make consistent measurements of flow velocity, especially on the downstream side of the hull, because the seed particle concentration was too low. A method was needed to deliver seeding particles into the flow and maintain the minimum concentration required for accurate measurements. Ideally the delivery system should have had no effect on the flow, but this was impossible to achieve. The next best option was to ensure that the disturbance to the flow caused by the rake was distributed uniformly across the measurement window of the PIV system, and that the magnitude of the disturbance be as small as possible.

The multi-fingered rakes used for the experiments described in Chapters 3 and 4 were shown to creat a uniform disturbance across the measurement area, but reduced the mean flow speed by between 12 and 15%, depending on the flow speed. The disturbance of the in-plane flow vectors caused by the rake was shown to be small (less than 2% of the free stream flow at 1 m/s) and this number did not change for cases when the seeding rake was removed.

The location of the seeding rake relative to the measurement area (which was varied between 720 mm and 3600 mm ahead of the laser light sheet) had little effect on the measured mean flow speed, but the particle concentration decreased as the distance was increased. Based on this observation, the recommended location for the seeding rake was to be just far enough away from the model, so that uniform particle concentration was obtained. Beyond this distance, the level of disturbance to the flow due to the rake did not decrease, but the particle concentration decreased significantly.

Since the area of the rake was large, in relation to the measurement area, it affected all of the flow being studied in a single PIV measurement window. As a result, if the same rake and relative location were used, then flow patterns measured for different geometric arrangements of a ship model should be comparable, but with a similar bias to the results, caused by the presence of the seeding rake.

The estimated uncertainty for the PIV velocity analysis was between 8% and 16%. The 8% values of uncertainty are estimated for a flow speed of 1.0 m/s with laser pulse times of 1000 μs. The 16% value of uncertainty was estimated for a flow speed of 0.5 m/s, with a laser pulse time of 500 μs. This level of uncertainty was relatively high compared to other PIV systems (Lawson and Wu (1997b), Soloff et al. (1997), Di Felice and De Gregorio (2000), Gui et al. (2001, Calagno et al. (2002)), who claimed values of up to 5%. The high level of uncertainty was a result of the relatively short pulse times required to obtain a measurement with the strongest flow component through the plane of the laser sheet.

The design of the seeding rake could be further refined. The system used for these experiments was based on simple circular section pipes, typically used in domestic plumbing. They had the advantage of being cheap and readily available, but may have had a higher wake than a section with a lower drag coefficient, such as an airfoil. A revised rake design using lower drag section pipe should be built and tested with the objective of reducing the level of disturbance to the flow in the direction of the main flow component, without loosing seeding concentration.

7.4 PIV EXPERIMENTS ON AN ESCORT TUG MODEL

PIV was successfully used to determine the flow velocities around an escort tug model with a typical operating yaw angle of 45 degrees. One measurement orientation was used, which was a plane normal to the direction of the undisturbed flow. This plane intersected with the tug's hull at midships. Measurements were made on the upstream and downstream sides of the tug.

Detailed measurements of the flow velocities around an escort tug model, operating at 45 degrees of yaw was a hydrodynamic condition that had not been studied before. The key flow features identified were:

1) The separation of the incoming flow on the upstream side of the hull at the corner of the bilge and the reverse flow under the hull.

2) The formation of a vortex on the downstream side of the hull, which extended between the bottom of the hull and the waterline, for the tug without the fin.

3) The formation of a large vortex on the downstream side of the hull when the fin was fitted. For a section at midships, the core of the vortex was located at approximately the mid-depth of the fin and the maximum beam of the model. This vortex changes the flow patterns close to the surface, and the smaller vortex seen when the fin was absent was not observed at all.

The vortex in the second case discussed above was not as well defined by the PIV measurements as the other two cases. This region included a mixing of the flow from two distinctly different directions. One flow component along the side of the hull and one was under the hull. If two separate seeding systems had been used simultaneously, a more complete definition of the flow would have been obtained.

The speeds for which the experiments were carried out covered the typical operating speeds of a tug, using Froude scaling. The direction of the flow vectors relative to the hull changed very little with the speed of the undisturbed flow, although the magnitude of the velocity components changed with the magnitude of the undisturbed flow. Only carrying out experiments at one speed could have reduced the number of experiments.

Preliminary CFD simulations (Molyneux, 2005) had shown that the total measurement area required to define the flow patterns around the hull was much larger than a single PIV measurement window (approximately 400 mm by 250 mm). In order to extend the measurement area beyond the single window, the model was moved relative to the PIV system, by less than the dimensions of the window. As a result, the same area, relative to the model was seen in at least three measurement windows. The model was moved relative to the PIV system to adjust the measurement location, since this method kept the PIV measurement window fixed in space, and removed the need to re-calibrate the it with each new measurement location.

The flow around the tug model was observed to be turbulent, but the mean flow vectors at a particular measurement window were found to be stable. This was determined by averaging the calculated flow vectors at each location within the measurement window over each time step for the complete sample of image pairs within an experiment. The mean flow vectors were then compared to the mean flow vectors with other experiments for the same flow conditions at the same window location. In addition the measurement windows were converted to a common grid, referenced to the model geometry, and mean flow vectors from overlapped windows were included in the comparison. As a result, at least six separate views were obtained of key flow features. This comparison showed that the flow features were stable (based typically on 100 image pairs and six views of a measurement point).

The nature of the expected flow patterns around the escort tug required that the relatively high uncertainty (discussed above) be accepted for two reasons. The first was the desire for a large measurement area from a single field of view to maximize the data collected in unsteady flow conditions. The second requirement was for the measurement plane to be oriented across the strongest flow direction, since this was the primary plane of interest for the flow measurements. This orientation resulted in the need for relatively short laser pulse times to ensure the same particles were kept within the measurement space for both image pairs.

It would have helped in the analysis of the PIV experiments to have exact locations on the model hull identified within the measurement window when the viewing area was close to the hull. This could have been achieved with contrasting marks on the model hull at pre-determined locations. These locations could then be transposed into the undistorted viewing window, by using the calibration functions.

7.5 ESTIMATED ACCURACY OF CFD PREDICTIONS FOR HULLS WITH YAW ANGLE

Most of the applications of Computational Fluid Dynamics (CFD) to ship hydrodynamic studies have used a hexahedral mesh, where six four-sided faces define elemental volumes of fluid. In principle, these cell shapes give the best predictions when the viscous shear forces within the boundary layer have a significant impact on the total forces. It is theoretically more accurate to compute shear forces on cells of this shape when the shear forces are important relative to the pressure forces. This is typically the case for a ship hull at a small yaw angle.

An alternative approach is to use elements made of four three-sided faces. This approach may be just as accurate when the effect of the viscous shear forces is diminished, such as the case when a ship hull is operating at a large yaw angle. One objective of this research was to evaluate the most accurate meshing strategy for solving flow patterns of this type.

In practice, the flow around a hull with a yaw angle will be unsteady with time, but the degree of unsteadiness will depend on the yaw angle and flow speed. Checking the accuracy of the time dependent results of the CFD code will require additional experiment data, since all data up to this point that is suitable for comparing with CFD predictions has been obtained for time-averaged flow patterns.

All of the CFD predictions for the Series 60 hull and the escort tug were for the simplified case of fluid flow with a flat boundary at the nominal waterline and flow that was assumed to be steady. These assumptions were found to be reasonable for low speed flow at moderate yaw angles. As the speed of the flow or the yaw angle increased these assumptions would become less valid. For the Series 60 case, the free surface was not relevant (either because the Froude number was low or the model was symmetrical about the design water line). For the escort tug, the Froude number used for validating the forces was approximately 0.15 and flow patterns were compared at a Froude number of 0.10.

For the Series 60 hull, the tetrahedral mesh gave the most accurate force prediction at 10 degrees yaw. This was within 5% of the value measured by experiments. For the escort tug, the hexahedral mesh gave consistently more accurate predictions of forces throughout the range of yaw angles, for both cases, with and without the fin. Up to 35 degrees yaw, CFD predictions of forces were within 4% of the values measured in experiments and within 10.5% at 45 degrees yaw.

The difference between the force predictions for the two hull forms was due to the local flow conditions. The Series 60 hull form was deeper and narrower than the escort tug, with much finer waterlines. Flow on the downstream side of the Series 60 hull was moving more slowly than on the downstream side of the escort tug. As a result the viscous forces between grid elements were less significant. The high number of elements in the tetrahedral mesh may also have contributed to a more accurate solution. In the escort tug case, with faster flow on the downstream side of the hull, the hexahedral mesh gave more accurate results with the higher speed flow.

Neither meshing approach gave consistently more accurate predictions of the in-plane flow vectors. For the Series 60 hull with 10 degrees of yaw both meshes gave predicted velocity vectors that, on average, were within 5 percent of the measured values, except for the section at 90%L with the tetrahedral mesh, which was within 7%. At 35 degrees yaw, the quality of all the predictions deteriorated. The highest error was for the tetrahedral mesh in the plane at 50%L, where the error was on average 24% of the free stream flow. All of the other locations gave predictions with average error values between 10 and 16% of the free stream flow. For the escort tug at 45 degrees yaw, with or without the fin, all of the average flow vector magnitudes were between 7% and 10% of the measured values, with no observable difference between the meshing strategies.

Based on this analysis it should be practical to obtain predictions of in-plane flow vectors, which on average are within 8 per cent of measured values. The uncertainty estimates for the PIV experiments indicated that flow velocities can be measured to within 16% for a flow speed of 0.5 m/s and 8% for flow speeds of 1.0 m/s. Given this level of accuracy of the experiments, CFD code can be used to estimate the flow vectors within a fluid moving around a hull with a yaw angle to within this level of confidence.

In general a tetrahedral mesh required a lower level of skill to create than the hexahedral mesh, although it took longer to solve a single iteration within the solution. The number of elements for the tetrahedral mesh was typically much higher than for the equivalent mesh made with hexahedral elements, which was the biggest factor in determining the solution time. Even with the higher number of elements required for tetrahedral mesh, a solution for a single yaw angle and flow speed combination could be obtained overnight using a PC workstation.

It should be noted that the assessment for the escort tug, described above, was based on averaged flow velocity data from multiple PIV windows, interpolated on 20 mm grid squares. The CFD grid for the tetrahedral and hexahedral meshes was approximately this density. The PIV data, in its raw form, was available for grid spacing approximately three times more dense (6.7 mm grid squares). To match this density in the CFD would require a mesh that had 27 times the number of elements in the region of interest. This was not attempted.

Selecting the type of CFD mesh is important if comparing measured and predicted forces is the primary objective, but the optimum choice will depend on the hull geometry and the flow conditions. For the escort tug, which was relatively wide and shallow with full waterlines, a hexahedral mesh was more accurate for yaw angles up to 45 degrees. For the

Series 60, which was narrow and deep, with sharp waterlines, the tetrahedral mesh was the most accurate (based on measured force data at 10 degrees yaw only). This difference in the most effective type of mesh is related to the flow conditions around the hull. The shallow escort tug hull had much less tendency to slow down the flow on the downstream side of the hull.

It can be concluded that the best mesh for CFD predictions of forces for a hull with a yaw angle will depend on the expected flow conditions and hull geometry. A hexahedral mesh will give the best predictions for wide, shallow hulls, whereas a tetrahedral mesh will give the best predictions for narrow, deep hulls.

If comparing flow patterns is the primary objective, the selection of the type of mesh does not appear to be significant. Neither the tetrahedral mesh nor the hexahedral mesh showed a significant advantage over the other for any of the cases where experiment and CFD predictions were available.

7.6 APPLICATION OF CFD TO THE DESIGN OF ESCORT TUGS

The level of accuracy of the CFD predictions, discussed in the previous section, indicates that the results of the RANS CFD code can be used to predict the flow patterns and resulting forces around a hull with a yaw angle with a reasonable degree of confidence.

Forces can be predicted to within 4% for yaw angles up to 35 degrees and flow velocities can be predicted to within 10%.

From the CFD predictions for the escort tug, with and without the fin, it was seen that the fin was an essential element in generating the obtained level of side force coefficient, even when the fin was stalled. The high side force coefficient for the escort tug with the fin was due to the formation of a large vortex that formed downstream from the low aspect ratio fin fitted at the bow. This vortex was observed in the PIV experiments and predicted by the CFD code. The side force component due to the fin was approximately 50% of the total force generated by the tug.

Without this fin, the tug hull alone had a relatively low value of side force coefficient. A higher value of side force coefficient was obtained for the Series 60 hull and the Wigley hull than for the escort tug without the fin. This higher value of side force coefficient was due to the formation of a vortex at the bow for the Wigley and Series 60 hulls, which expanded as it moved downstream. For the escort tug without the fin, this vortex was not predicted for yaw angles up to 45 degrees.

The CFD predictions made for this research have given some useful insights into the forces generated by a low aspect ratio fin, and may be used to assess alternatives to this design, which will create the same level of side force coefficient, but from different geometrical dimensions.

From the research described in this thesis, it can be seen that RANS CFD codes can be used to predict the flow patterns and forces for a hull with a yaw angle up to 45 degrees and that analyzing the flow for different tug geometries using RANS CFD codes can lead to more effective tug designs in the future. Areas for future research include a detailed assessment of the effect of the free surface on CFD predictions of escort tug performance and the solving the resulting forces and flow patterns in the time domain.

REFERENCES

Allan, R. G, Bartells, J-E. and Molyneux, W. D. 2000 'The Development of a New Generation of High Performance Escort Tugs', Proceedings, International Towage and Salvage Conference, Jersey, May 2000.

Allan R. G. & Molyneux, W. D. 2004 'Escort Tug Design Alternatives and a Comparison of Their Hydrodynamic Performance', Paper A11, Maritime Technology Conference and Expo, S.N.A.M.E. Washington, D. C. September 30th to October 1st.

Alessandrini, B. A. and Delhommeau, G. 1996 'Viscous Free Surface Flow Past a Ship in Drift and in Rotating Motion', 22nd Symposium on Naval Hydrodynamics, Washington D.C., pp. 491-507.

Calagno, G., Di Felice, F., Felli, M, and Pereira, F. 2002 'Application of Stereo PIV: Propeller Wake Analysis in a Large Circulating Water Channel', 11th Symposium on Applications of Laser Techniques to Fluid Mechanics, Calouste Gulbenkian Foundation, Lisbon, Portugal, 8th to 11th July, Paper 26-4.

Campana, E. F., Di Mascio, A. and Penna, R. 1998 'CFD Analysis of the Flow Past a Ship in Steady Drift Motion', Proceedings of 3rd Osaka Colloquium on Advanced CFD Applications to Ship Flow and Hull Form Design, 25-26 May, Osaka, Japan, pp. 151-159.

Collier, A. and Molyneux, W. D. 2006 'Effect of Free Surface on CFD Predictions for Wigley Hull Form at Increasing Yaw Angles', NRC/IOT, SR-2006-20.

Cura Hochbaum, A. 1996 'Computation of the Turbulent Flow Around a Ship Model in Steady Turn and in Steady Oblique Motion', 22nd Symposium on Naval Hydrodynamics, Washington D.C., pp. 550-567.

Di Felice, F. and Mauro, S. 1999 'LDV Cross-Flow Survey on a Series 60 Double model at Incidence', Proceedings of 9th International Offshore and Polar Engineering Conference, Brest France, May 30-June 4, pp. 536-543.

Di Felice, F. & De Gregorio, F. 2000 'Ship Model Wake Analysis by Means of PIV in a Large Circulating Water Channel', Proceedings of 10th International Offshore and Polar Engineering Conference, Seattle, USA, May 28-June 2, pp. 392-397

Fluent Inc. 2005(a) 'Fluent 6.2 User's Guide', available on-line, July 2005. http://www.fluentusers.com/fluent/doc/ori/html/ug/main_pre.htm

Fluent Inc. 2005(b) 'Gambit 2.2 User's Guide', available on-line, June 2005 http://www.fluentusers.com/gambit/doc/doc_f.htm

Gui, L., Longo, J. and Stern, F. 2001, 'Towing Tank PIV Measurement System, Data and Uncertainty Assessment for DTMB Model 5512', *Experiments in Fluids*, Volume 31, pp. 336-346.

Hutchison, B., Gray, D. and Jagannathan S., 1993 'New Insights into Voith Schneider Tractor Tug Capability', *Marine Technology*, Vol. 30, No. 4, pp. 233-242.

LaVision GmbH, 2004 'DaVis Software Manual for DaVis 6.2', January.

LaVision Inc. 2005 'DaVis Flowmaster Software Manual for DaVis 7.1'.

Lawson, N. J. and Wu, J. 1997(a) 'Three-dimensional Particle Image Velocimetry: Error Analysis of Stereoscopic Techniques', *Measurement Science and Technology*, Volume 8, pp 894-900.

Lawson, N. J. and Wu, J. 1997(b) 'Three-dimensional Particle Image Velocimetry: Experimental Error Analysis of a Digital Angular Stereoscopic System', *Measurement Science and Technology*, Volume 8, pp 1455-1464.

Löhner, R., Yang, C., Oñate, & Idelssohn, S. 1999 'An Unstructured Grid-based Parallel Free Surface Solver', *Applied Numerical Mathematics*, Vol. 31, pp 271-293.

Longo, J. & Stern, F. 1996 'Yaw Effects on Model-Scale Ship Flows', Proceedings, 21st Symposium on Naval Hydrodynamics, June 24-28, Trondheim, Norway, pp. 312-327.

Longo, J. and Stern, F. 2002 'Effects of Drift Angle on Model Ship Flow', *Experiments in Fluids*, Vol. 32, pp. 558-569.

Longo, J. Stern, F. & Toda, Y. 1993 'Mean-Flow Measurements in the Boundary Layer and Wake and Wave Field of a Series 60 C_B=0.6 Ship Model-Part 2: Scale Effects on Near-Field Wave Patterns and Comparisons with Inviscid Theory', *Journal of Ship Research*, Vol. 37, No. 1. January, pp. 16-24.

Molyneux, W. D. 2003 'A Comparison of Hydrodynamic Forces Generated by Three Different Escort Tug Configurations', NRC/IOT TR-2003-27.

Molyneux, W. D. 2005 'Plan for Particle Image Velocimetry Experiments of Flow Around a Model of an Escort Tug', IOT/NRC, TR-2005-15.

Molyneux, W. D., and Xu, J. 2005 'Particle Image Velocimetry Experiments to Measure Flow Around and Escort Tug', IOT/NRC, TR-2005-10.

Potters Industries Inc 2005 Product Specification Sheet, http://www.pottersbeads.com/literature/SC_Hollow_Glass_Spheres.pdf, May.

Rhee, S. H. 2005, Lead Consulting Engineer, Fluent Inc., Private correspondence by email, 11 July.

Soloff, S. M., Adrian, R. J. and Liu, Z-C. 1997 'Distortion Compensation for Generalized Stereoscopic Particle Image Velocimetry', *Measurement Science and Technology*, Volume 8, pp 1441-1454.

Tahara, Y. and Longo, J. 1994 'Non-linear Free Surface Flow Around a Yawed Ship', Proceedings of the 9th International Conference on Boundary Element Technology, Orlando, FL, USA, pp 121-128.

Tahara, Y., Longo, J. & Stern, F. 2002 'Comparison of CFD and EFD for the Series 60 C_B=0.6 in Steady Drift Motion', *Journal of Marine Science and Technology*, Vol. 7, pp. 17-30.

Toda, Y., Stern, F. & Longo, J. 1992 'Mean-Flow Measurements in the Boundary Layer and Wake and Wave Field of a Series 60 C_B=0.6 Ship Model-Part 1: Froude Numbers 0.16 and 0.316', Journal of Ship Research, Vol. 36, No. 4, December, pp. 360-377.

Todd, F. H. 1963 'Series 60 Methodical Series Experiments with Models of Single Screw Merchant Ships', David Taylor Model Basin Report 1712.

Turnock, S. 2006, Senior Lecturer in Ship Science, University of Southampton, Private correspondence by email, 7 April.

Van den Braembussche, R. A. (editor) 2001 '*Measurement Techniques in Fluid Dynamics*', Von Karman Institute for Fluid Dynamics, 2nd Revised Edition.

Wavemetrics Inc. 2004 'Igor Pro Version 5 Users Guide'.

Xu, J., Molyneux, W. D. and Bose, N. 2005 'A Versatile Particle Image Velocimetry System for Flow Measurements in Water Tanks', 7th Canadian Marine Hydromechanics and Structures Conference, Halifax, N. S. September.

Yang, C. & Löhner, R. 1998 'Fully Non-linear Ship Wave Calculation Using Unstructured Grid and Parallel Computing', Proceedings of 3rd Osaka Colloquium on Advanced CFD Applications to Ship Flow and Hull Form Design, 25-26 May, Osaka, Japan, pp. 125-150.

APPENDIX 1

RESULTS OF MESH SENSITIVITY STUDY

SERIES 60 HULL

A mesh sensitivity study was carried out for the Series 60 hull form, within the overall boundaries given in Chapter 2. For the tetrahedral mesh, the number of elements was varied by changing the size of the elements at the surface boundaries. For the hexahedral mesh, the number of elements in the region close to the hull was varied. In each case, the size of the elements far away from the hull was unchanged.

The results show that for each mesh, the differences in calculated forces within 1 Newton.

Table A1-1, Results of mesh sensitivity study, effect of number of elements on calculated forces

Yaw =10 degrees V 0.875 m/s

	Iterations	number of elements, 000's	Fx	Fy	Ft	Ct	Cs
Tetrahedral mesh	171	577	3.57	14.66	15.09	5.917	24.297
Tetrahedral mesh	177	1,131	3.513	13.993	14.43	5.822	23.191
Tetrahedral mesh	176	1,760	4.51	13.56	14.29	7.471	22.474
Hexahedral mesh	119	248	3.40	15.18	15.55	5.642	25.152
Hexahedral mesh	116	423	3.46	15.05	15.44	5.741	24.938
Hexahedral mesh	118	774	3.37	15.64	16.00	5.580	25.919

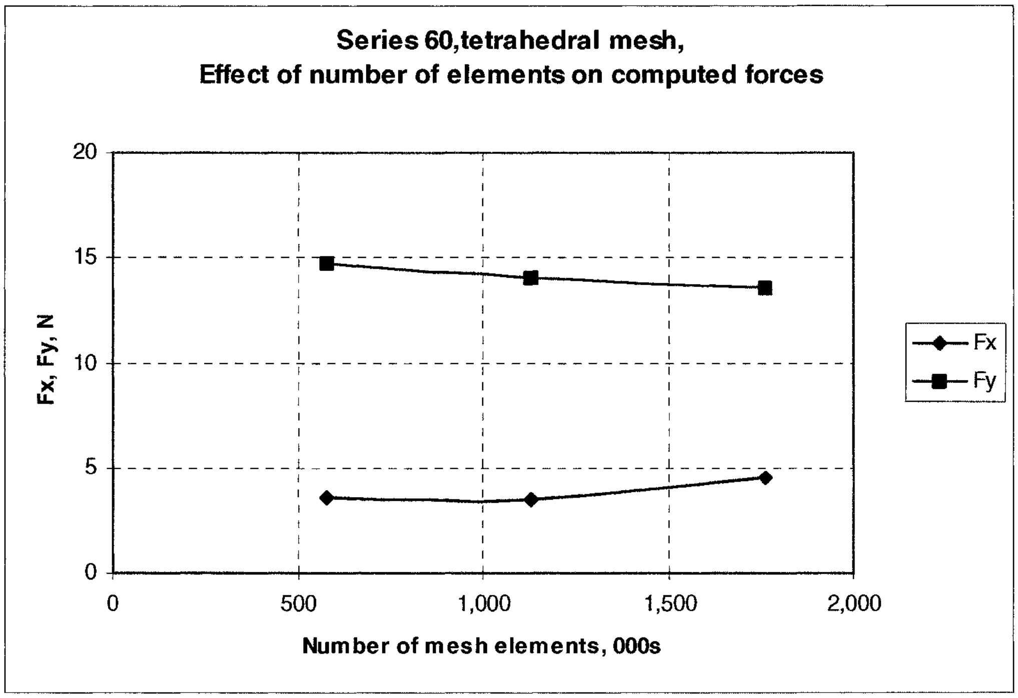

Figure A1-1, Effect of number of mesh elements on calculated forces, tetrahedral mesh

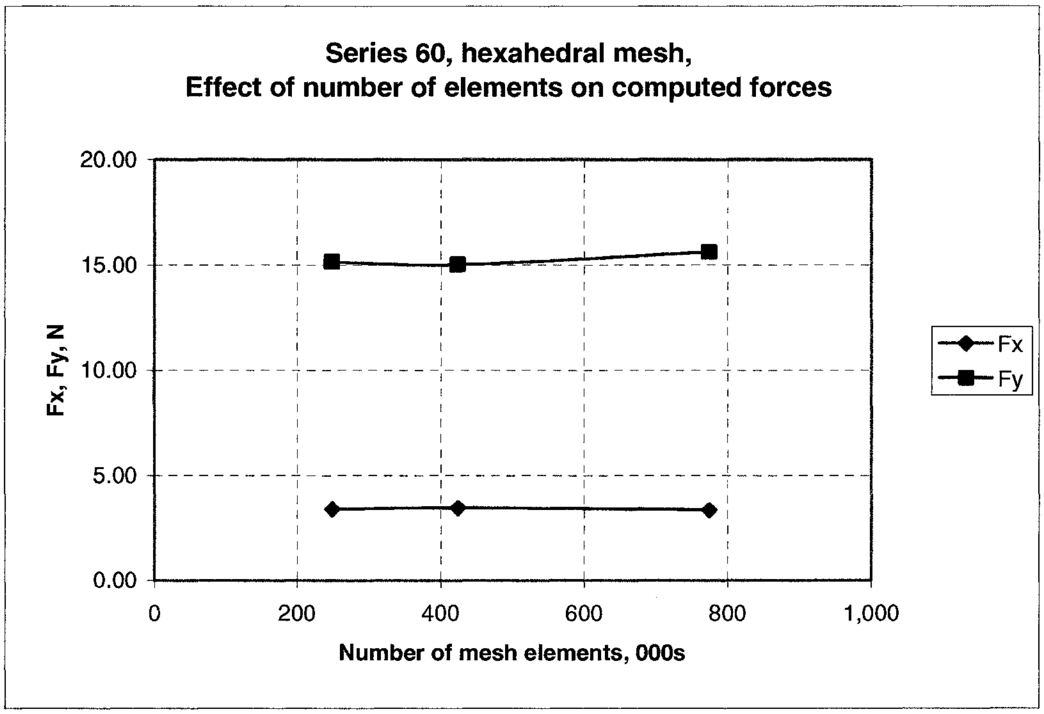

Figure A1-2, Effect of number of mesh elements on calculated forces, hexahedral mesh

APPENDIX 2

PARTICLE IMAGE VELOCIMETRY MEASUREMENTS FOR

FLOW AROUND AND ESCORT TUG MODEL

TEST LOG

Table 1: Upstream side, no fin

Test date	Time	δt, μs	Speed, m/s	Beam to centreline, mm laser	model	borescope height, mm	x correction mm	y correction mm	# frames	Threshold	Notes
30-Jan-06	14:20:08	1000	0.50	300	0	0	0	0	100	25	
	14:37:15	1000	0.50	300	0	0	0	0	100	25	
	14:44:17	1000	0.50	300	0	0	0	0	100	25	
	14:49:19	500	1.00	300	0	0	0	0	100	25	
	14:52:51	500	1.00	300	0	0	0	0	100	25	
30-Jan-06	15:03:22	1000	0.50	200	0	0	100	0	100	25	
	15:11:44	1000	0.50	200	0	0	100	0	100	25	
	15:18:06	500	1.00	200	0	0	100	0	100	25	Not used
	15:22:42	500	1.00	200	0	0	100	0	100	25	Not used
30-Jan-06	15:35:09	1000	0.50	200	0	0	100	0	100	25	Not used
	15:38:59	1000	0.50	200	0	0	100	0	100	25	Not used
	15:42:33	1000	0.50	200	0	0	100	0	100	25	Not used
	15:47:13	1000	0.50	200	0	0	100	0	100	25	Not used
	15:53:43	1000	0.50	200	0	0	100	0	100	25	Not used

Table 1 continued: Upstream side, no fin

Test date	Time	δt, μs	Speed, m/s	Beam to centreline, mm laser	model	borescope height, mm	x correction mm	y correction mm	# frames	Threshold	Notes
31-Jan-06	9:28:44	1000	0.50	200	0	0	100	0	100	25	
	9:33:31	1000	0.50	200	0	0	100	0	100	25	
	9:37:50	500	1.00	200	0	0	100	0	100	25	
	9:43:55	500	1.00	200	0	0	100	0	100	25	
	9:48:32	500	1.00	200	0	0	100	0	100	25	
31-Jan-06	10:01:01	1000	0.50	100	0	0	200	0	100	25	
	10:06:57	1000	0.50	100	0	0	200	0	100	25	
	10:14:27	500	1.00	100	0	0	200	0	100	25	
	10:19:16	500	1.00	100	0	0	200	0	100	25	
31-Jan-06	10:30:05	1000	0.50	0	0	0	300	0	100	25	
	10:34:41	1000	0.50	0	0	0	300	0	100	25	
	10:41:12	500	1.00	0	0	0	300	0	100	25	
	10:45:37	500	1.00	0	0	0	300	0	100	25	
31-Jan-06	11:09:34	1000	0.50	300	0	100	0	100	100	25	
	11:12:51	1000	0.50	300	0	100	0	100	100	25	
	11:24:20	1000	0.50	300	0	100	0	100	100	25	
	11:28:55	500	1.00	300	0	100	0	100	100	25	
	11:33:48	500	1.00	300	0	100	0	100	100	25	
	11:38:32	1000	0.50	300	0	100	0	100	100	25	
	11:41:00	1000	0.50	300	0	100	0	100	100	25	
	11:46:18	500	1.00	300	0	100	0	100	100	25	
	11:50:10	500	1.00	300	0	100	0	100	100	25	

Table 2, Downstream side, no fin

Test date	Time	δt, μs	Speed, m/s	Beam to centreline, mm laser	model	borescope height, mm	x correction mm	y correction mm	# frames	threshold
26-Jan-06	11:23:52	1000	0.5	100	0	-130	300	-130	100	25
	11:26:53	1000	0.5	100	0	-130	300	-130	100	25
	11:29:33	500	1.0	100	0	-130	300	-130	100	25
	11:33:43	500	1.0	100	0	-130	300	-130	100	25
	11:42:02	500	1.0	100	0	-130	300	-130	100	25
26-Jan-06	11:54:39	1000	0.5	200	0	-130	200	-130	100	25
	11:59:19	1000	0.5	200	0	-130	200	-130	100	25
	12:03:24	1000	0.5	200	0	-130	200	-130	100	25
	12:17:34	500	1.0	200	0	-130	200	-130	100	25
	12:23:20	500	1.0	200	0	-130	200	-130	100	25
	12:30:24	500	1.0	200	0	-130	200	-130	100	25
	12:36:23	500	1.0	200	0	-130	200	-130	100	25
26-Jan-06	13:54:46	1000	0.5	300	0	-130	100	-130	100	25
	14:04:17	1000	0.5	300	0	-130	100	-130	100	25
	14:08:55	500	1.0	300	0	-130	100	-130	100	25
	14:12:19	500	1.0	300	0	-130	100	-130	100	25
26-Jan-06	14:20:34	1000	0.5	400	0	-130	0	-130	100	25
	14:27:11	1000	0.5	400	0	-130	0	-130	100	25
	14:30:57	500	0.5	400	0	-130	0	-130	100	25
	14:34:56	500	1.0	400	0	-130	0	-130	100	25
	14:38:19	500	1.0	400	0	-130	0	-130	100	25

Table 2 continued, Downstream side, no fin

Test date	Time	δt, μs	Speed, m/s	Beam to centreline, mm laser	model	borescope height, mm	x correction mm	y correction mm	# frames	threshold
27-Jan-06	9:59:19	1500	0.5	400	100	20	-100	0	100	25
	10:08:39	1500	0.5	400	100	20	-100	0	100	25
	10:15:31	700	1.0	400	100	20	-100	0	100	25
	10:24:33	700	1.0	400	100	20	-100	0	100	25
	10:28:38	700	1.0	400	100	20	-100	0	100	25
27-Jan-06	10:38:17	1500	0.5	400	200	20	-200	0	100	25
	10:48:40	1500	0.5	400	200	20	-200	0	100	25
	10:51:54	700	1.0	400	200	20	-200	0	100	25
	10:56:20	700	1.0	400	200	20	-200	0	100	25
27-Jan-06	11:11:08	1500	0.5	400	300	20	-300	0	100	25
	11:16:34	1500	0.5	400	300	20	-300	0	100	25
	11:22:25	700	1.0	400	300	20	-300	0	100	25
	11:26:45	700	1.0	400	300	20	-300	0	100	25
27-Jan-06	15:12:48	500	0.5	400	0	20	0	0	100	25
	15:15:16	1000	0.5	400	0	20	0	0	100	25
	15:17:59	500	1.0	400	0	20	0	0	100	25
	15:20:52	500	1.0	400	0	20	0	0	100	25
	15:27:18	1000	0.5	400	0	20	0	0	100	25
	15:30:41	1000	0.5	400	0	20	0	0	100	25
	15:33:32	1000	0.5	400	0	20	0	0	100	25
	15:39:09	500	1.0	400	0	20	0	0	100	25
	15:42:35	500	1.0	400	0	20	0	0	100	25
	15:48:13	500	1.0	400	0	20	0	0	100	25

Table 3, Downstream side, with fin

Test date	Time	δt, μs	Speed, m/s	Beam to centreline, mm laser	model	borescope height, mm	x correction mm	y correction mm	# frames	Threshold	Notes
18-Jan-06	15:29:35	1000	0.5	400	0	0	0	0	50	12	
	15:35:09	1000	1.0	400	0	0	0	0	50	12	
	15:48:14	2000	0.5	400	0	0	0	0	50	12	
	15:51:13	1000	1.0	400	0	0	0	0	50	12	
19-Jan-06	10:00:15	2000	0.5	400	100	0	-100	0	50	12	Not used
	10:06:41	2000	1.0	400	100	0	-100	0	50	12	Not used
	10:13:30	1000	1.0	400	100	0	-100	0	50	12	Not used
	10:26:17	2000	0.5	400	100	0	-100	0	50	12	
	10:29:36	2000	0.5	400	100	0	-100	0	50	12	
	10:33:14	1000	0.5	400	100	0	-100	0	50	12	
	10:39:31	1000	1.0	400	100	0	-100	0	50	12	
	10:42:39	1000	1.0	400	100	0	-100	0	50	12	
19-Jan-06	10:57:10	2000	0.5	400	200	0	-200	0	50	12	
	11:01:16	2000	0.5	400	200	0	-200	0	50	12	
	11:07:01	2000	0.5	400	200	0	-200	0	50	12	
	11:11:05	1000	1.0	400	200	0	-200	0	50	12	
	11:18:52	2000	0.5	400	200	0	-200	0	50	12	
	11:21:44	1000	1.0	400	200	0	-200	0	50	12	
	11:27:18	1000	1.0	400	200	0	-200	0	50	12	
19-Jan-06	11:40:33	2000	0.5	400	300	0	-300	0	50	12	
	12:04:06	2000	0.5	400	300	0	-300	0	50	12	
	12:10:37	2000	0.5	400	300	0	-300	0	50	12	
	12:13:36	1000	1.0	400	300	0	-300	0	50	12	
	12:18:04	1000	1.0	400	300	0	-300	0	50	12	

Table 3 continued, Downstream side, with fin

Test date	Time	δt, μs	Speed, m/s	Beam to centreline, mm laser	model	borescope height, mm	x correction mm	y correction mm	# frames	Threshold	Notes
19-Jan-06	13:43:16	2000	0.5	400	400	0	-400	0	50	12	
	13:51:39	2000	0.5	400	400	0	-400	0	50	12	
	13:56:21	2000	0.5	400	400	0	-400	0	50	12	
	13:59:51	2000	1.0	400	400	0	-400	0	50	12	Not used
	14:07:31	1000	1.0	400	400	0	-400	0	50	12	
	14:11:38	1000	1.0	400	400	0	-400	0	50	12	
	14:22:12	2000	0.5	400	500	0	-500	0	50	12	
	14:28:44	2000	0.5	400	500	0	-500	0	50	12	
	14:32:14	2000	0.5	400	500	0	-500	0	50	12	
	14:34:24	1000	1.0	400	500	0	-500	0	50	12	
	14:36:50	1000	1.0	400	500	0	-500	0	50	12	
24-Jan-06	14:40:28	1500	0.5	400	0	-130	0	-130	100	25	Not used
	14:46:39	1500	0.5	400	0	-130	0	-130	100	25	Not used
	14:53:32	700	1.0	400	0	-130	0	-130	100	25	
	15:02:23	700	1.0	400	0	-130	0	-130	100	25	
	15:12:52	700	1.0	400	0	-130	0	-130	100	25	Not used
	15:21:00	700	1.0	400	0	-130	0	-130	100	25	Not used
24-Jan-06	15:35:21	1500	0.5	400	100	-130	-100	-130	100	25	Not used
	15:44:58	1500	0.5	400	100	-130	-100	-130	100	25	Not used
	15:47:46	1500	0.5	400	100	-130	-100	-130	100	25	
	15:50:58	700	1.0	400	100	-130	-100	-130	100	25	
	15:54:59	700	1.0	400	100	-130	-100	-130	100	25	Not used

Table 3 continued, Downstream side, with fin

Test date	Time	δt, μs	Speed, m/s	Beam to centreline, mm laser	Beam to centreline, mm model	borescope height, mm	x correction mm	y correction mm	# frames	Threshold	Notes
25-Jan-06	9:51:34	1500	0.5	400	200	-130	-200	-130	100	25	
	9:56:45	1500	0.5	400	200	-130	-200	-130	100	25	
	10:01:44	1500	0.5	400	200	-130	-200	-130	100	25	
	10:04:53	700	1.0	400	200	-130	-200	-130	100	25	
	10:10:36	1000	1.0	400	200	-130	-200	-130	100	25	
25-Jan-06	10:26:00	1500	0.5	400	300	-130	-300	-130	100	25	Not used
	10:29:56	1500	0.5	400	300	-130	-300	-130	100	25	Not used
	10:33:20	1000	1.0	400	300	-130	-300	-130	100	25	Not used
	10:41:12	1500	0.5	400	300	-130	-300	-130	100	25	
	10:45:03	1500	0.5	400	300	-130	-300	-130	100	25	
	10:47:24	1500	0.5	400	300	-130	-300	-130	100	25	
	10:50:43	700	1.0	400	300	-130	-300	-130	100	25	
	10:54:50	700	1.0	400	300	-130	-300	-130	100	25	
25-Jan-06	11:03:55	1500	0.5	400	400	-130	-400	-130	100	25	
	11:07:06	1500	0.5	400	400	-130	-400	-130	100	25	
	11:11:31	700	0.5	400	400	-130	-400	-130	100	25	
	11:14:38	700	1.0	400	400	-130	-400	-130	100	25	
	11:23:05	700	1.0	400	400	-130	-400	-130	100	25	
	11:27:01	1500	1.0	400	400	-130	-400	-130	100	25	

Table 3 continued, Downstream side, with fin

Test date	Time	δt, μs	Speed, m/s	Beam to centreline, mm		borescope	x correction	y correction	# frames	threshold	Notes
25-Jan-06	11:38:00	1500	0.5	400	500	-130	-500	-130	100	25	
	11:42:01	1500	0.5	400	500	-130	-500	-130	100	25	
	11:45:24	700	1.0	400	500	-130	-500	-130	100	25	
	11:51:04	500	1.0	400	500	-130	-500	-130	100	25	Not used
	11:57:13	700	1.0	400	500	-130	-500	-130	100	25	Not used
	12:01:25	1000	1.0	400	500	-130	-500	-130	100	25	
25-Jan-06	14:25:16	1500	0.5	300	0	-130	100	-130	100	25	Not used
	14:29:41	1000	0.5	300	0	-130	100	-130	100	25	Not used
	14:29:53	1000	0.5	300	0	-130	100	-130	100	25	Not used
	14:32:41	800	0.5	300	0	-130	100	-130	100	25	
	14:35:52	1000	0.5	300	0	-130	100	-130	100	25	
	14:40:08	700	1.0	300	0	-130	100	-130	100	25	
	14:45:21	700	1.0	300	0	-130	100	-130	100	25	
25-Jan-06	15:01:51	1000	0.5	200	0	-130	200	-130	100	25	
	15:08:14	1500	0.5	200	0	-130	200	-130	100	25	
	15:12:33	1500	0.5	200	0	-130	200	-130	100	25	
	15:16:46	700	1.0	200	0	-130	200	-130	100	25	
	15:22:43	700	1.0	200	0	-130	200	-130	100	25	
25-Jan-06	15:37:17	1500	0.5	100	0	-130	300	-130	100	25	Not used
	15:59:53	1500	0.5	100	0	-130	300	-130	100	25	
	16:09:04	700	1.0	100	0	-130	300	-130	100	25	
	16:15:34	700	1.0	100	0	-130	300	-130	100	25	
	16:41:06	1500	0.5	100	0	-130	300	-130	100	25	Not used

APPENDIX 3

RESULTS OF MESH SENSITIVITY STUDY

ESCORT TUG (NO FIN)

A mesh sensitivity study was carried out for the escort tug hull form, within the overall boundaries given in Chapter 5. For the tetrahedral mesh, the number of elements was varied by changing the size of the elements at the surface boundaries. For the hexahedral mesh, the number of elements in the region close to the hull was varied. In each case, the size of the elements far away from the hull was unchanged.

The results show that for the hexahedral mesh, the differences in calculated forces are within 1 Newton, which is lower than the resolution of the PMM frame used to measure the forces in the experiments. For the tetrahedral mesh, this level of resolution was obtained once the number of mesh elements exceeded 1.8M.

Table A3-1, Results of mesh sensitivity study, effect of number of elements on calculated forces

Yaw=45 degrees V 0.728 m/s

	Iterations	number of elements, 000's	Fx	Fy	Ft	Cl	Cq
Tetrahedral mesh	181	1,618	3.94	43.58	43.76	0.0385	0.426
Tetrahedral mesh	212	1,864	3.13	41.68	41.80	0.0306	0.407
Tetrahedral mesh	233	2,171	2.92	40.42	40.52	0.0285	0.395
Hexahedral mesh	103	987	3.75	47.74	47.88	0.0366	0.466
Hexahedral mesh	145	1,307	2.89	47.53	47.61	0.0282	0.464
Hexahedral mesh	159	1,636	2.94	46.84	46.93	0.0287	0.458

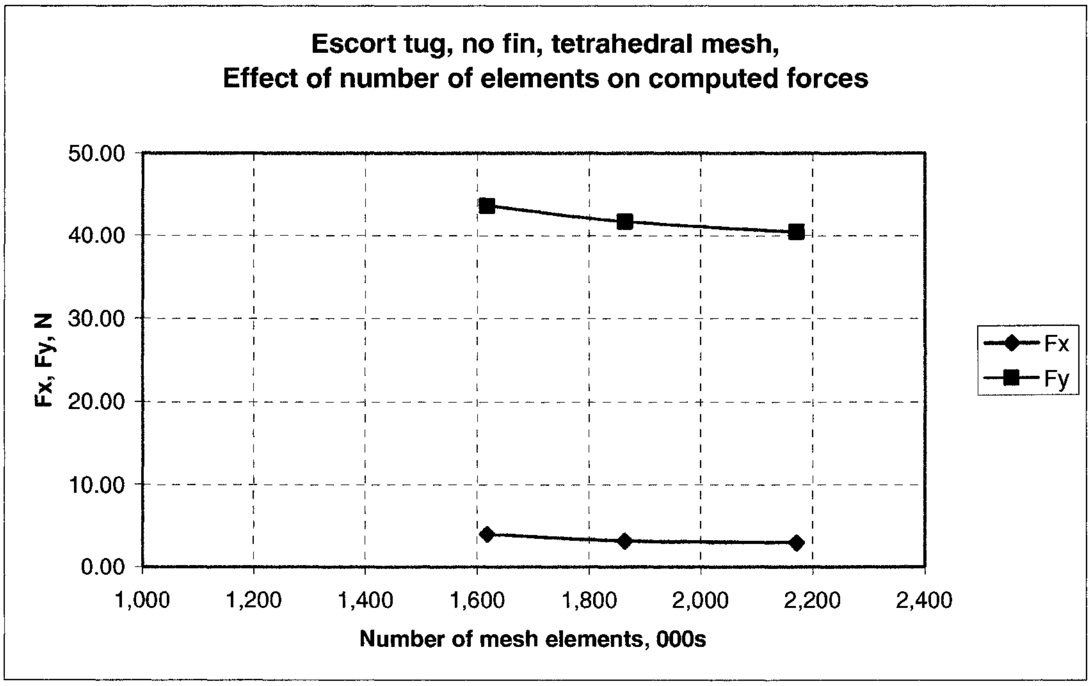

Figure A3-1, Effect of number of mesh elements on calculated forces, tetrahedral mesh

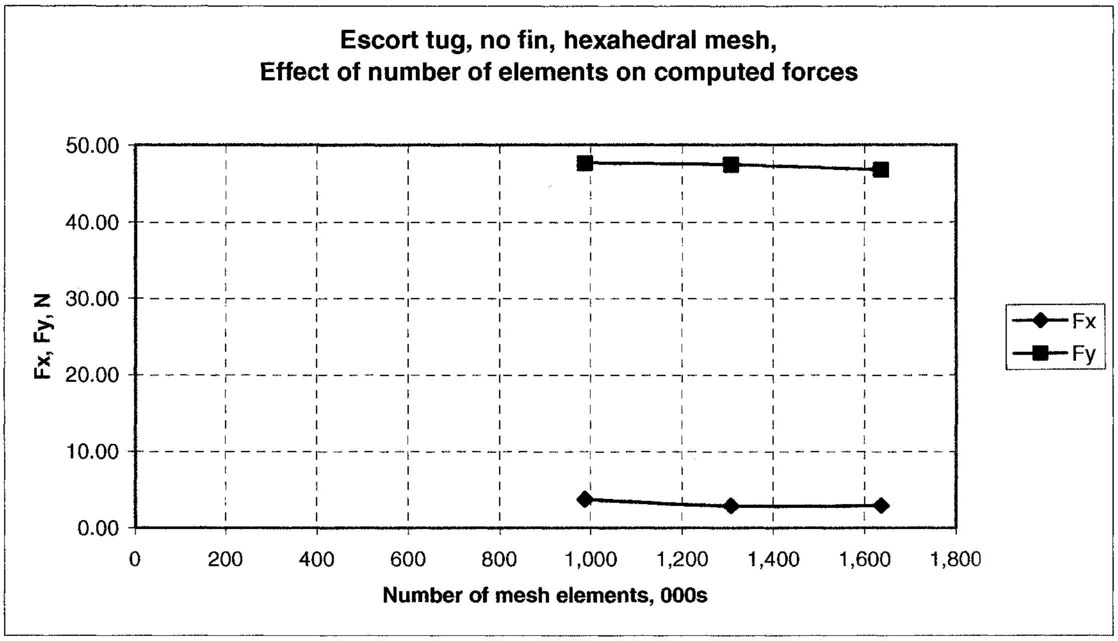

Figure A3-2, Effect of number of mesh elements on calculated forces, hexahedral mesh